The Individual Virtual Eye

Dissertation
der Fakultät für Informations- und Kognitionswissenschaften
der Eberhard-Karls-Universität Tübingen
zur Erlangung des Grades eines
Doktors der Naturwissenschaften
(Dr. rer. nat.)

vorgelegt von
Dipl.-Inform. Jens Einighammer
aus Tübingen

Tübingen
2008

Dedicated to
my father
Dr. Hans J. Einighammer

Abstract

The individual virtual eye is a computer model of a human eye with respect to the optical properties. Established schematic eyes, as Gullstrand's model eye, are intended to represent properties of an average eye based on averaged population measurements. In contrast, the individual virtual eye is based on measurements of an individual person. Therefore the geometry of the eye is important, including axial length and topographic measurements of the anterior corneal surface. All optical components of a pseudophakic eye – an eye with an artificial lens – are modeled by means of computer scientific methods. A spline-based interpolation method was developed to efficiently include data from corneal topographic measurements. Based on this virtual eye the geometrical optical properties, such as the wavefront aberration, can be simulated by using Snell's law of refraction and the method called real ray tracing. Moreover, optical components can be calculated using computer scientific optimization procedures. High value was set on the efficient implementation of the time-critical numerical ray-tracing and optimization procedures to allow for short calculation times in the range of seconds. This leads to clinical application fields in ophthalmology that have been addressed in this thesis. One application is intraocular lens calculation for cataract surgery, with the potential to overcome limitations of current calculation methods like lens calculation after refractive surgery. Also customized aspherical lenses were calculated what shows the capability of the methods to deal with advanced lens geometry. Clinically important issues as the optical effects of intraocular lens dislocation have been investigated. Furthermore, this computer model has been used to assess ablation profiles used in current refractive corneal laser surgery. One possible future enhancement of the model is the simulation of phakic eyes by incorporating a correct model of the human crystalline lens. And, so far, the individual virtual eye focused on geometrical optical properties, but may serve as a basis for including physiological properties of the retina and brain in future.

Keywords: Human optics; pseudophakic eye; computer simulation; real ray tracing; Snell's law; corneal topography; spline interpolation; wavefront aberration; optimization problem; intraocular lens calculation; ablation profiles; refractive surgery

Zusammenfassung

Das individuelle virtuelle Auge ist ein Computermodell eines menschlichen Auges zur Simulation der optischen Eigenschaften. Gängige Modellaugen wie das bekannte schematische Auge von Gullstrand basieren auf Daten von vielen Personen und zielen üblicherweise darauf ab, die Eigenschaften eines durchschnittlichen Auges zu repräsentieren. Im Gegensatz dazu basiert das individuelle virtuelle Auge auf Messwerten einer einzelnen Person. Entscheidend dabei sind geometrische Größen, insbesondere die axiale Länge und die Topographie der vorderen Hornhautoberfläche. Alle optischen Komponenten eines pseudophaken Auges – d.h. eines Auges mit einer künstlichen Linse – sind mit computertechnischen Methoden modelliert. Ein auf Spline-Interpolation basierendes Verfahren wurde entwickelt, um eine effiziente Integration von Messwerten einer Hornhauttopographie zu ermöglichen. Anhand dieses virtuellen Auges können unter Anwendung des Snell'schen Brechungsgesetzes und Ray-Tracing-Methoden geometrisch optische Eigenschaften, wie zum Beispiel die Wellenfrontaberration, simuliert werden. Darüber hinaus können mit computertechnischen Optimierungsmethoden auch optische Komponenten berechnet werden. Großer Wert wurde auf eine effiziente Implementierung der zeitkritischen numerischen Ray-Tracing- und Optimierungsmethoden gelegt, um eine kurze Berechnungszeit im Bereich von Sekunden zu erreichen. Dies führt zu klinischen Anwendungsgebieten in der Ophthalmologie, von denen einige in dieser Arbeit behandelt wurden. Dazu zählt die Intraokularlinsenberechnung für die Kataraktchirurgie, sowohl für normale als auch für schwierige Fälle wie nach refraktiver Chirurgie, bei denen bisherige Berechnungsmethoden unzulänglich sind. Ferner wurden auch individuell zugeschnittene asphärische Intraokularlinsen berechnet, und somit die Leistungsfähigkeit des Ray-Tracing-Verfahrens im Hinblick auf aufwendigere Linsengeometrien demonstriert. Als klinisch relevante Fragestellung wurde der optische Effekt einer Verdrehung oder Verkippung von Intraokularlinsen evaluiert. Darüber hinaus wurden Ablationsprofile untersucht, wie sie derzeit in der refraktiven kornealen Laserchirurgie eingesetzt werden. Eine zukünftige Erweiterungsmöglichkeit wäre die Einbeziehung eines Modells der natürlichen kristallinen Linse des Menschen, so dass auch phake Augen simuliert werden können. Auch konzentriert sich das virtuelle Auge bislang auf geometrisch optische Eigenschaften, könnte aber als Basis dienen für die Einbeziehung von physiologischen Eigenschaften von Netzhaut und Gehirn.

Schlüsselbegriffe: Optik des menschlichen Auges; pseudophakes Auge; Computersimulation; Ray Tracing; Snell'sches Gesetz; Hornhauttopographie; Spline-Interpolation; Wellenfrontaberration; Optimierungsproblem; Intraokularlinsenberechnung; Ablationsprofile; refraktive Chirurgie

Main Contributions

This is an interdisciplinary thesis combining scientific fields. The main contribution field and key discipline is computer science: computer technical structures and methods were developed and implemented for the realization of an individual virtual eye to allow for realistic simulation regarding the optical properties and furthermore allow for calculation of optical components. This leads to substantial contributions to a second discipline, medicine, as there are clinically relevant applications of the individual virtual eye in ophthalmology.

Computer Science

Contributions to computer science are located in chapter 3 that describes the computer technical development and implementation of the individual virtual eye:

- Modeling of optical components (spectacles, cornea and lens) of the virtual eye with mathematical surfaces that are feasible regarding physiology and optical properties as well as efficiently usable for computational ray tracing (section 3.1 on page 33 ff.)
- Development of a spline-based interpolation schema for corneal elevation and surface normals obtained from corneal topography measurements, especially regarding an efficient usage for ray tracing (section 3.1.1 on page 34 ff.)
- Simulation of optical performance by real ray tracing through the virtual eye based on Snell's law resulting in the geometric optical criterions spot size and wavefront aberration (section 3.2 on page 41 ff.)
- Calculation of optical components (e.g. intraocular lenses) by the formulation of optimization problems taking the geometry as input and optical quality criterions as output; solving by numerical minimization in one or more dimensions (section 3.3 on page 46 ff.)
- Implementation of the virtual eye in a way that allows for an integration into medical devices leading to practicable medical applications (Figure 1-1)

Medicine

Contributions to medicine are found in chapter 5 that shows the ophthalmological applications of the individual virtual eye:

- Calculation of intraocular lenses with the potential to overcome limitations of current calculation methods like the correct handling of refractive treated eyes what is of particular clinical interest (section 5.1 on page 55 ff.)
- Calculation of customized toric aspherical intraocular lenses what is not possible so far in clinical practice (section 5.2 on page 67 ff.)
- Analysis of ablation profiles currently used in refractive laser surgery (section 5.3 on page 98 ff.)

Software Architecture

The individual virtual eye is embedded in the real ray tracing module of the OphthaTOP (OphthaSWISS AG, Switzerland) videotopometer software developed in cooperation with the Division "Experimental Ophthalmic Surgery", University Eye Hospital Tübingen. An overview of the software architecture showing the main components is shown in Figure 1-1. All calculations performed in this thesis were done with this real ray tracing module.
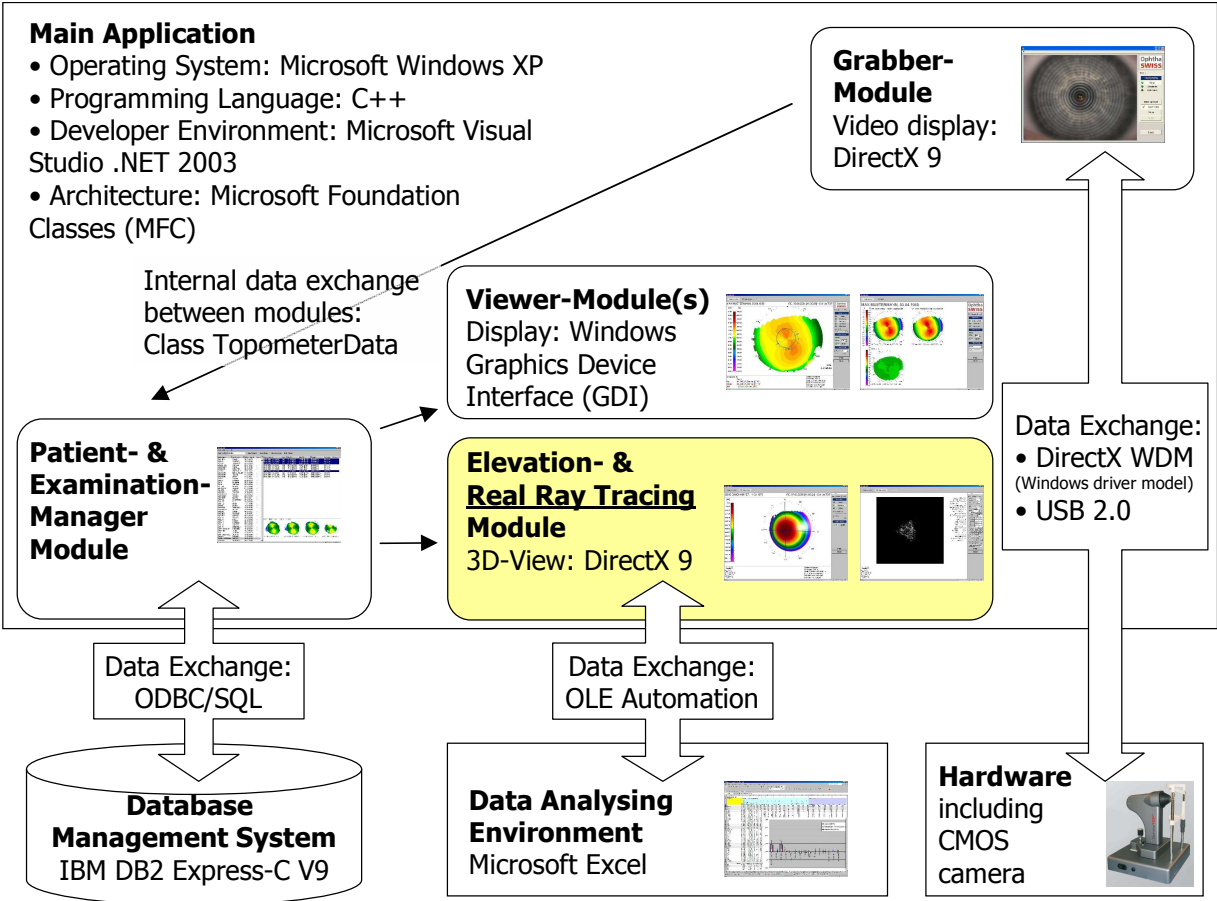

Figure 1-1: Software architecture

Contents

Abbreviations

ACD	Anterior chamber depth
ANSI	American National Standards Institute
AST	Astigmatism
AUS	Applanation US
AX	Axis
CCC	Continuous curvilinear capsulorhexis
CCD	Charged-coupled device
CLE	Clear lens extraction
CR	Corneal reflex
CSC	Corneal sighting center
CYL	Cylinder
EPI-LASIK	Epithelial laser in situ keratomileusis
FCZ	Full correction zone
FEMTO-LASIK	Laser in situ keratomileusis with femtosecond-laser flap cutting
FOZ	Functional optical zone
GRIN	Gradient refractive index
HBF	Homogeneous beam fluence
HOA	Higher order aberration
IOL	Intraocular lens
ISO	International Organization for Standardization
IUS	Water-immersion US
LASEK	Laser epithelial keratomileusis
LASER	Light Amplification by Stimulated Emission of Radiation
LASIK	Laser in situ keratomileusis
LOA	Lower order aberration
LOS	Line of sight
MAE	Mean absolute error
MNE	Mean numerical error
MRSE	Mean refractive spherical equivalent
MTF	Modulation transfer function
OCT	Optical coherence tomography
OPD	Optical path difference
OPL	Optical path length
OSA	Optical society of America
OTF	Optical transfer function
PA	Pupillary axis
PCI	Partial coherence interferometry
P-IOL	Phakic intraocular lens
PMMA	Polymethylmethacrylate
Post-op	Postoperative
Pre-op	Preoperative
PRK	Photorefractive keratectomy
PSF	Point spread function
PTF	Phase transfer function
RK	Radial keratotomy
RMS	Root mean square
RPE	Retinal pigment epithelium
RRT	Real ray tracing
SA	Spherical aberration

SD	Standard deviation
SEQ	Spherical equivalent refraction
SPH	Sphere
TSZ	Transition zone
ULIB	User Group for Laser Interference Biometry
US	Ultrasound A-scan echo-impulse technique
VBF	Variable beam fluence
VK axis	Videokeratometric axis
WFE	Wavefront error

1 Motivation

The present work deals with the construction of a computer model of the human eye. The purpose of this virtual eye is to analyze and simulate the optical properties of the eye as well as to calculate optical components and corrections.

This leads to an interdisciplinary character of this thesis. Physics is involved by providing measurement methods and the fundamental laws of optics. Mathematics provides formulae for surface and wavefront description among other things. Computer science delivers the methods and possibilities due to the computational power to simulate the physical properties and enables analysis and advanced calculation. The results are finally used in medicine, in particular ophthalmology. So far, there are schematic model eyes based on measurements of a large number of eyes that represent properties of an average eye; one such example is the popular model eye introduced at the beginning of the 20th century by Nobel prize winner Allvar Gullstrand. In contrast, the basic idea of this thesis is to construct an individual model eye to represent the properties of an *individual* eye. For this purpose biometric geometry data of human eyes obtained from advanced measurement methods are necessary. These include mainly the topography of the anterior cornea as well as segmental lengths. The individual virtual eye is constructed in three-dimensional space. The optical components relevant for the optical properties are mainly the cornea and the lens. Each of them is reconstructed computer technically – since the image formation process is dominated by the effect that light rays are refracted at boundaries separating two media with different refractive indices, this leads to the modeling of surfaces. Once the virtual eye is constructed it can be used to simulate the optical properties of the entire eye as well as one or more of its optical components.

Lens optics and paraxial optics in general provide simple formulae for optical systems but are not capable of addressing issues like complex irregular shapes or higher order aberrations. Thanks to the computational power of a computer it is possible to do a more realistic simulation of the optics by tracing many light rays through an optical system. Each real ray is refracted multiple times and obeys Snell's law of refraction. Real ray tracing (RRT) is a common method in design processes of technical optics and the same methods are adopted for the calculations in the virtual eye. The ray tracing calculations are dominated by ray-surface intersections that are solved analytically or numerically by common methods; this requires computational power. When analyzing the optical properties – for example calculating the wavefront aberration – one set of rays is traced through the eye. When actually calculating optical components (like an intraocular lens), many iterations during an optimization process are necessary; this largely increases the computational effort. However, this leads to the possibility of calculating components with advanced optical properties that cannot be retrieved with conventional calculation methods.

Chapter 2 will introduce into optics, physiology, clinical measurement methods and surgical procedures. In chapter 3 the computer technical implementation of the virtual eye is described in detail. A verification of the model is given in chapter 4: it shows a comparison of predicted and actually measured ocular errors. Chapter 5 will introduce applications of the individual virtual eye. Section 5.1 shows the capability of RRT to calculate spherical intraocular lenses – for standard patients as well as for problem cases after refractive surgery – so far a clinically unsolvable problem. Customized intraocular lenses with advanced geometry are calculated in section 5.2; moreover the influence of reference axes and effects of dislocation of intraocular lenses are investigated. In section 5.3, RRT is used to investigate ablation profiles used in current refractive laser surgery.

2 Background

2.1 Optics

Optics is a branch of physics dealing with the behavior and properties of light. Different mathematical formalisms can be used and different approximations can be made depending on the properties of interest. In *geometric optics* it is assumed that the wavelength of light is sufficiently small so that it can be described in terms of rays using only reflection and refraction. *Physical optics* or *wave optics* is the branch of optics which includes the effects of interference, diffraction and polarization. The branches of optics relevant for the optics of the human eye are outlined in the following sections and are in parts based on the complete optics reference provided by Hecht et al. (Hecht 1989).

2.1.1 Geometric Optics

In geometric or ray optics, the light propagation is described in terms of rays. These rays are assumed to travel in straight lines as long as the refractive index of a medium is homogeneous. In case of a medium where the refractive index is a function of its position, these rays may be curved. The ray in geometric optics is an abstract object which is perpendicular to the wavefront of the actual optical waves. The path of these rays is determined by refraction and reflection. Refraction occurs when a ray travels from a medium to another medium with a different refractive index. At the boundary between the media, the wave's phase velocity is altered, the wavelength increases or decreases but its frequency remains constant. As a result, the ray gets a new direction that is determined by *Snell's law* (Figure 2-1): The incoming light ray **i** travels through medium 1 and strikes the surface in point O. The angle between **i** and the surface normal **n** at point O is known as the angle of incidence θ_1. The ray continues in medium 2, and the angle between the outgoing ray **o** and the surface normal **n** is the angle of refraction θ_2. Snell's law gives the relation between the angles and the refractive indices of the media:

$$n_1 \sin \theta_1 = n_2 \sin \theta_2 \qquad\qquad (2\text{-}1)$$

In the special case that the angle of incidence is zero ($\theta_1 = 0°$; that means the incoming ray is perpendicular to the surface) the angle of refraction becomes also zero ($\theta_2 = 0°$): the ray is not bent. Snell's law also shows the reversibility of light rays: the path of the ray is the same going from left to right and vice versa.
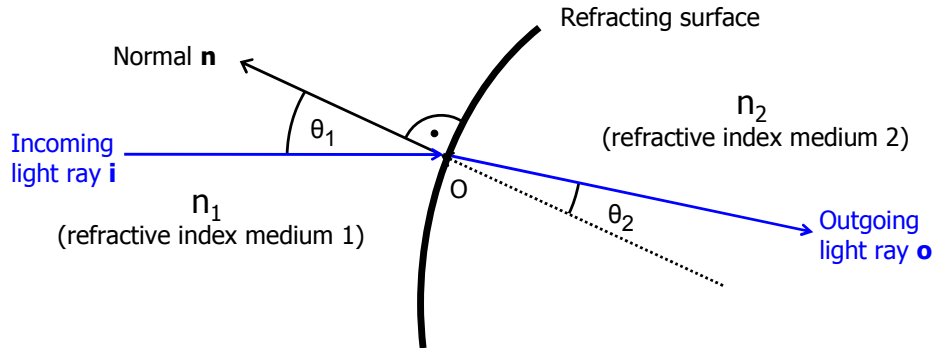
Figure 2-1: Snell's law of refraction

When moving from a dense to a less dense medium ($n_1 > n_2$) Snell's equation has no solution when θ_1 exceeds a value known as the critical angle for total internal reflection:

$$\theta_{crit} = \arcsin\frac{n_2}{n_1} \tag{2-2}$$

If $\theta_1 > \theta_{crit}$ no refraction occurs, the incident ray undergoes total internal reflection.
The law of reflection is simple: angle of incidence is the same as angle of reflection:

$$\theta_1 = \theta_2 \tag{2-3}$$

The incident ray and the surface normal define a plane. The refracted ray and the reflected ray lie in this plane, too. Snell's law as well as the law of reflection can be derived from Fresnel equations, which directly result from Maxwell's equations.
A ray obeying Snell's law is called *exact ray* or *real ray* – as opposed to a paraxial ray. Analyzing optical systems by tracing many rays based on Snell's law is therefore known as *exact ray tracing*, *finite ray tracing* or *real ray tracing*. The term real ray tracing and its abbreviation RRT will be used throughout this thesis (Bass 1995; Arasa and Alda 2004).

Paraxial Optics

Paraxial optics is a simplification of geometric optics. It assumes rotationally symmetric refracting or reflecting surfaces having a common axis, called the optical axis. A simple lens is an example of such a centered system; multiple simple lenses are centered if they are aligned on a common axis. A ray passing through sufficiently close to the optical axis makes a small angle of incidence with the normal to any surface. Such a ray is called a *paraxial ray*, and refraction is described by the so called *paraxial approximation of Snell's law*. This approximation assumes that for small angles the sine of the angles can be satisfactorily approximated by the angles themselves, and the law of refraction becomes

$$n_1\theta_1 \approx n_2\theta_2. \tag{2-4}$$

The paraxial optics is also known as first-order approximation. Its advantage is that this model results in simple linear formulae that can easily be handled mathematically. Every point in object space can be transformed one-to-one to a point in image space. Paraxial optics gives a quick overview about the optical properties of an optical system; however it remains an idealized model.

Lens Optics

A *lens* is an optical part used to refract light rays in a desired direction. It is usually made of glass or plastic; the most common type consists of surfaces that have spherical curvature. This means that the front and rear surfaces of the lens are modeled as a part of the surface of a sphere. Each surface can be convex, concave of planar. The sings of the lens' radii of curvature indicate whether the corresponding surfaces are convex of concave. The convention is that the radius of curvature is positive, when the center of curvature is in right direction relative to the vertex. When parallel light passes through a convex lens, the rays converge; when light passes through a concave lens it diverges. Parallel rays entering a convex lens converge in the focal point. The distance from the lens is called *focal length* of the lens. The plane perpendicular to the lens axis placed at the distance of the focal length is called focal plane. Conversely, when a point source of light is placed at the focal point the rays will be converted into a collimated beam by the lens. These two cases are examples of image formation in lenses: an object at infinite distance is focused to an image at the focal point and vice versa. A lens of negligible thickness is called *thin lens*. The relation of the focal length f, the distance of the object to the left of the lens in the object space medium S_1, and the distance of the focused image to the right of the lens in the image space medium S_2 is given by an equation called *Gauss's law for thin-lens* Figure 2-2:

$$\frac{1}{f} = \frac{1}{S_1} + \frac{1}{S_2}$$
(2-5)
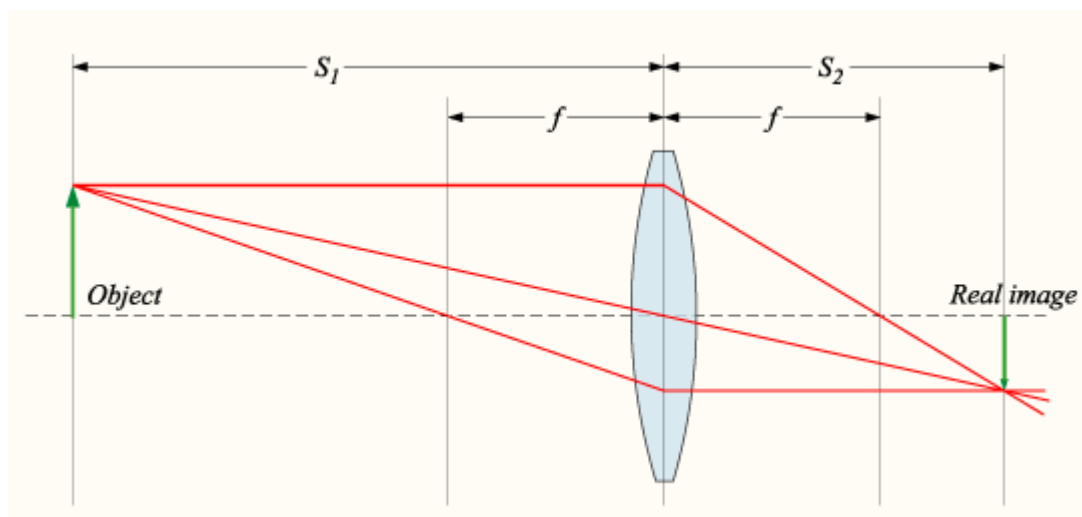
Figure 2-2: Thin lens in paraxial optics
Reference: Wikipedia [http://en.wikipedia.org/wiki/Image:Lens3.svg]

A convex lens produces a real inverted image to the right of the lens. The magnification of an image is given by:

$$m = -\frac{S_2}{S_1}$$
(2-6)

The optical power of a lens is measured in terms of *diopters* ($D = 1/m$). This is equivalent to the inverse of the focal length (given in meters).

The value of the focal length for a particular lens can be calculated from so called *lensmaker's equation*. It is provided here in a form that gives the focal length of a lens with refractive index n_L, surrounded by some material with a refractive index n_M:

$$\frac{1}{f} = (n_L - n_M)\left(\frac{1}{R_1} - \frac{1}{R_2} + \frac{(n_L - n_M)d}{n_L R_1 R_2} \right) \tag{2-7}$$

f: focal length
n_L: refractive index of the lens material
n_M: refractive index of the surrounding material
R_1: radius of curvature of the anterior surface
R_2: radius of curvature of the posterior surface
d: thickness (distance between the surface vertices)

Equation (2-7) is correct for thick lenses. When the thickness d is small compared to the radii of curvature, the thin lens approximation can be made:

$$\frac{1}{f} \approx (n-1)\left(\frac{1}{R_1} - \frac{1}{R_2} \right) \tag{2-8}$$

Lenses may be combined to form more complex optical systems. The simplest case is when thin lenses are placed in contact, the combined focal length of n lenses can be calculated by:

$$\frac{1}{f_{total}} = \frac{1}{f_1} + \frac{1}{f_2} + \dots + \frac{1}{f_n} \tag{2-9}$$

Since $1/f$ is the power of the lens, the power of thin lenses in contact is additive.

Gaussian Optics

Gaussian optics, named after Carl Friedrich Gauss, analyzes paraxial image formation of optical systems by introducing a number of special points, known as *cardinal points* or cardinal planes:

- focal points and planes
- principal points and planes
- surface vertices
- nodal points

For a thick lens there are two of each, one set for the front and one for the rear. These points and planes define the optical properties of the system. The cardinal points lie on the optical axis of the system. Each point has special properties for passing rays in the paraxial approximation. See Figure 2-3 for a schematic view. The front focal point hat the property, that all rays passing through will emerge parallel to the optical axis. All rays entering the system parallel to the optical axis are focused onto the rear focal point. The plane perpendicular to the optical axis containing a focal point is called focal plane. The extension of the incident and emerging rays in each case intersect, by definition, the principal planes which cross the axis at the principal points. The principal points are crucial in defining the optical properties of the system, since the object distance, image distance and focal length are referenced to these points and, in conclusion, determine the magnification of the system. For a thin lens surrounded by air, the principal planes both lie on the lens. For a thick lens the principal planes do not necessarily pass through the lens center, nor do they have to lie inside the lens at all. The nodal points are two axial points that have the property that a ray passing through the first nodal point appears to emerge from the second nodal point, parallel to its original direction. When the ingoing and the outgoing side of the optical system have the same refractive index, the nodal points and principal points coincide. The surface vertices are

the points where each surface crosses the optical axis. They are important because these are measurable parameters of the optical elements, and the positions of the other cardinal points must be known with respect to the vertices to describe the physical system.
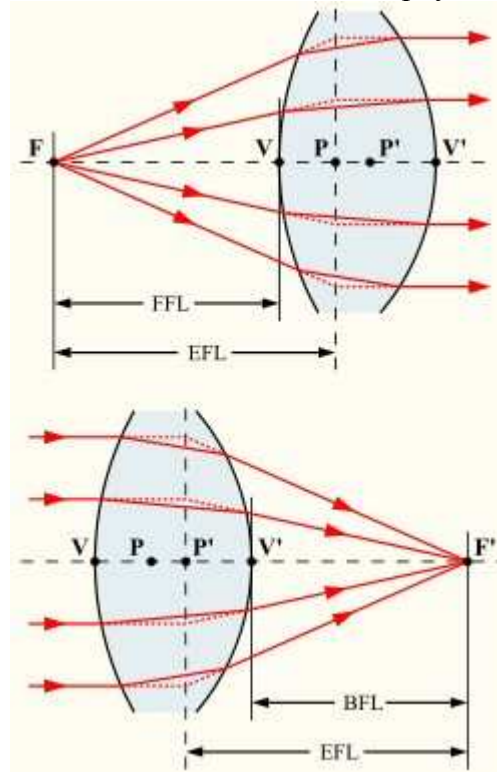

Figure 2-3: Cardinal points of a thick lens
Reference: Wikipedia [http://en.wikipedia.org/wiki/Image:Cardinal-points-1.svg]

An optical system, such as a lens, can be treated as a black box with their properties completely defined by the cardinal points. Multiples of such single components can be combined to form a more complex optical system. This allows for tracing rays through an optical system following the laws of the paraxial approximation (even if the rays are outside the paraxial region). The rays traced this way are not identical with the path of the real light rays, but are only of constructional importance (Paul 1999). Gaussian optics can be formulated using mathematical matrix formulation, known as *ray transfer matrix analysis* or ABCD matrix analysis. This provides a calculation schema that allows for easy analysis of complex optical systems (Hecht 1989) [p. 229].

Aberrations

Gaussian optics based on the paraxial approximation is only correct for rays in the paraxial region where one object point is reproduced in one image point. This is a description of perfect optical conditions, but reality is different. The deviations of the idealized case of Gaussian optics are called *aberrations*. There are two principal types of aberrations: *chromatic* and *monochromatic* aberrations. The chromatic aberration is caused by dispersion: since the index of refraction varies with the color of the light (wavelength), images are projected in somewhat different places and sizes. Chromatic aberration even occurs in the paraxial region. Monochromatic aberrations occur even when monochromatic (that means light of one wavelength) is used and arise outside the paraxial region. They can be divided in two groups: aberrations blurring the image (e.g. spherical aberration, coma and astigmatism) and aberrations deforming the image (e.g. distortion or Petzval field curvature). In other words the discrepancy of geometric optics using Snell's law and gaussian optics using the paraxial approximation of Snell's law results in aberrations.

Seidel Aberrations

The paraxial approximation assumes that $\sin(\theta) \approx \theta$ for small angles. It is therefore referred to as *first-order approximation*. The sinus can be described as a Taylor expansion:

$$\sin(\theta) = \theta - \frac{\theta^3}{3!} + \frac{\theta^5}{5!} - \frac{\theta^7}{7!} + ... \tag{2-10}$$

One gets a better approximation of Snell's law if the first two elements of Taylor's expansion are used: the *third-order approximation*. The deviation between third- and first-order approximation results in the five third-order aberrations: spherical aberration, coma, astigmatism, field curvature and distortion. They were first examined by Ludwig Seidel and are therefore called *Seidel aberrations*. The other terms of the expansion still result in deviations from true Snell's law, and are referred to as higher order aberrations.

Spherical aberration causes rays parallel to – but away from – the lens axis to be focused in a slightly different place towards the lens vertex compared to rays close to the axis. The distance of the intersection point of a ray with the optical axis and the paraxial focal point is called longitudinal spherical aberration. The distance of the intersection of a ray with the focal plane to the focal point is called transverse spherical aberration. The spherical aberration typically increases when opening the aperture.

Coma is an off-axis modification of spherical aberration. It results in a blurred image of an off-axis point that is shaped like a comet. An optical system free of both, coma and spherical aberration is called aplanatic.

Astigmatism is the difference in focal length of rays coming from different planes of an off-axis point. Like coma, astigmatism leads to a non-symmetric image around the optical axis. Astigmatism leads to the fact, that a point (not lying on the optical axis) cannot be focused onto a point in any image plane, therefore the greek name "a-stigma-tism". Seidel's astigmatism – also known as off-axis astigmatism – is not to be confused with the eye defect called astigmatism (see section 2.4), for example caused by a toric cornea that is not spherical but more curved in one plane than in another (Thibos 1999) [section 3.3].

Field curvature is the effect, that a sharp image (with a wide aperture) is derived only at a curved image surface. An object perpendicular to the optical axis is only projected onto a surface in the paraxial region. This aberration is also called Petzval field curvature.

Distortion is caused by the variation in the lateral magnification for object points at different distances from the optical axis. If magnification increases with the object point distance from the optical axis, it is called pincushion distortion. Conversely, if the magnification decreases it is called barrel distortion. As with field curvature, the image thus may be sharp, but deformed.

Chromatic Aberrations

Due to dispersion of light a lens has a different refractive index for different wavelengths. Rays of different wavelength (and therefore color) are focused at a different distance from the lens (longitudinal or axial chromatic aberration) and different positions in the focal plane (transverse or lateral chromatic aberration).

Chromatic aberration can be minimized by a combination of lenses for two (called dichromat or achromat) or more (polychromat or superachromat) wavelengths. The correction for all wavelengths is not possible due to the non-linear behavior of dispersion of optical glasses. No dispersion occurs at reflecting mirrors.

It is possible too, to transform chromatic aberrations into Seidel aberrations formally.

2.1.2 Physical Optics

Physical optics or wave optics includes phenomena for which the ray approximation of geometric optics is not valid, like *diffraction*, *interference* and *polarization*. So physical optics

may be considered as an intermediate method: it describes the light propagation more physically than geometric optics, but it is not an exact physical theory as full wave electromagnetism. Polarization and interference do not play a crucial role in human optics in the context of this thesis and are therefore not discussed furthermore.

Diffraction

The ability of light to bend around corners, a consequence of the wave nature of light, is fundamental to both interference and diffraction. Diffraction is simply any deviation from geometrical optics resulting from the obstruction of a wave front of light by some obstacle or some opening. Diffraction occurs when light waves pass through small openings, around obstacles, or by sharp edges.

When light passes through apertures the diffraction increases with decreasing aperture size. The resulting diffraction pattern of a uniformly illuminated circular aperture has a bright region in the center, known as the *Airy disc*. This disc is surrounded by concentric rings. The diameter of this disc is related to the wavelength of the illuminating light and the size of the aperture. The angle θ from the center at which the first minimum occurs is

$$\sin(\theta) = 1.22\frac{\lambda}{d}, \qquad\qquad (2\text{-}11)$$

where λ is the wavelength and d is the diameter of the aperture. Consequently diffraction limits the minimum size d of a spot of light formed at the focus of a geometrically perfect lens, known as the *diffraction limit*. The Rayleigh criterion for barely resolving two objects is that the center of the Airy disc for one object occurs at the first minimum of the Airy disc of a second object. With Huygens' principle it is possible to compute the diffraction pattern of a wave from any arbitrarily shaped aperture. If the pattern is observed at a sufficient distance from the aperture, it will appear as the two-dimensional Fourier transform of the function representing the aperture.

Diffraction takes place whenever light passes through an aperture. Since all optical systems have a limiting aperture, it is impossible to build a diffraction-free optical device. While it is possible to improve image quality by eliminating aberrations, it is impossible to exceed the limits to image quality set by diffraction. Ultimate optical quality is therefore referred to as diffraction limited (Salmon 1999) [p. 8].

2.1.3 Image Evaluation

There are different ways to assess the quality of an optical system. There may be different demands that an optical system should meet, but mostly the main goal is that a system produces an image that resembles its original as good as possible. As an image consists of arbitrary collections of objects, the evaluation can be reduced on the case of simple primitive objects as points, lines or edges.

Image evaluation can be done from geometric optics or wave optics point of view. Analysis relying on geometric optics is also called *geometric evaluation*; analysis based on wave optics is also called *diffraction evaluation*. In the following the analysis is mainly geometric evaluation, but often aspects of wave optics are incorporated.

Spot Diagrams

The straight forward result of tracing rays through an optical system is a *spot diagram*. It shows the position of the rays hitting an image plane. The spot diagram not necessarily indicates the distribution of irradiance in the image, as the plot does not show any weighting of the rays. This is only the case when the pupil is uniformly illuminated, and the rays are uniformly distributed within the pupil. In the ideal case, all rays meet in one single point in

the image plane. This is prohibited by the presence of aberrations and typical spot distributions are the result that can be interpreted with some experience.

Quantitative spot size analysis is typically done by tracing enough rays so that the data for any particular ray can be treated statistically. Each ray is considered to carry a weight proportional to the area it represents in the aperture of the system. The spot size can be calculated as the *root-mean-square (RMS) spot size*.

This evaluation is purely geometric. However this spot size can be compared to a quantity of wave optics, the size of the Airy disk. This allows for an assessment of how close a particular optical system is from diffraction limit. If the geometric spot size is much larger than the Airy disk, the performance of the system will be likely limited by geometric aberrations. In other words, if most of the hits in the spot diagram fall inside the Airy disk, the optical system tends to be diffraction limited ("OSLO Manual" 2001) [p. 179]; (Thöniß 2004).

Wavefront Aberration

For a perfect point image (absence of aberrations), in terms of geometrical optics, the corresponding wavefront is a sphere, centered on that point. The *optical path difference* (OPD) or *wavefront aberration* is the deviation of the actual wavefront from this reference sphere. Although wavefront is a term of wave optics, it can also be calculated according to the laws of geometrical optics (neglecting wave properties like diffraction in this case), resulting in a geometric wavefront. Geometrically, it is possible that all of the rays from an object point meet in a single point, but as in the case of spot diagrams, wave optics does not allow this beyond the diffraction limit. There is some freedom in choosing the reference sphere when calculating the wavefront aberration. The *root mean square (RMS) wavefront error* is the standard deviation of the wavefront aberration function. It is convenient to choose a best-fit reference sphere in the rear exit pupil of the optical system ("OSLO Manual" 2001) [p. 180]. Best-fit means in this case, that e.g. the RMS wavefront error is minimized.

It may be useful to represent the wavefront in the form of polynomials. A common set of polynomials are the *Zernike polynomials*. These polynomials have an orthogonal basis set in the polar coordinates over the interior of the unit circle. Their characteristic is that the average value of each polynomial (other than the constant term) is zero over the unit circle and each term minimizes the RMS wavefront error to the order of that term. Therefore, the RMS wavefront error cannot be decreased by changing lower order Zernike polynomial terms. This is a very compact description of a potentially complex wavefront shape ("OSLO Manual" 2001) [p. 124 ff.]; (Arasa and Alda 2004). But since a limited number of coefficients are used it remains an approximation of the actual wavefront. The following definitions are according to the Optical Society of America (OSA) (Thibos, Applegate et al. 2002)[1]. The wave aberration function is described by

$$W(\rho,\theta) = \sum_{n,m} C_n^m Z_n^m(\rho,\theta) \, , \qquad \textbf{(2-12)}$$

where C_n^m are the Zernike coefficients. The Zernike polynomials are defined as

$$Z_n^m(\rho,\theta) = \begin{cases} + N_n^m R_n^{|m|}(\rho)\cos(m\theta) & \textit{für } m \geq 0 \\ - N_n^m R_n^{|m|}(\rho)\sin(m\theta) & \textit{für } m < 0 \end{cases} . \qquad \textbf{(2-13)}$$

It can be seen that they include a sinusoidal azimuthal component and additionally include a normalization function

---

[1] Now an established standard: ANSI Z80.28-2004, Methods for Reporting Optical Aberrations of Eyes. Also proposed for ISO/DIS 24157 (Draft currently being voted on, 2007).

$$N_n^m = \sqrt{\frac{2(n+1)}{1+\delta_{m0}}}$$

(2-14)

and a polynomial radial component

$$R_n^{|m|}(\rho) = \sum_{s=0}^{(n-|m|)/2} \frac{(-1)^s (n-s)!}{s![\frac{1}{2}(n+|m|)-s]![\frac{1}{2}(n-|m|)-s]!} \rho^{n-2s} \; .$$

(2-15)

Figure 2-4 shows the Zernike coefficients and their corresponding names up to the 6th radial order. The first two orders are omitted in the diagram: Z00 is known as *piston* and only is a constant offset with no further optical relevance. Z-11 and Z11 are known as *tilt* and represent mainly a shift of the image position without further distortion. Piston and tilt are often not included when analyzing the Zernike coefficients because of their minor importance. The 2nd order coefficients are also called *lower order aberrations* (LOAs) and – though not identical – in principle correspond to a classical spectacle refraction (see section 2.4): the *defocus* corresponds to the sphere while the *vertical* and *horizontal astigmatism* coefficients correspond the cylinder (rather than to Seidel's astigmatism). 3rd order and higher coefficients are referred to as *higher order aberrations* (HOAs). Z(4,0) and Z(6,0) are sometimes combined and referred to as *spherical like aberrations*.
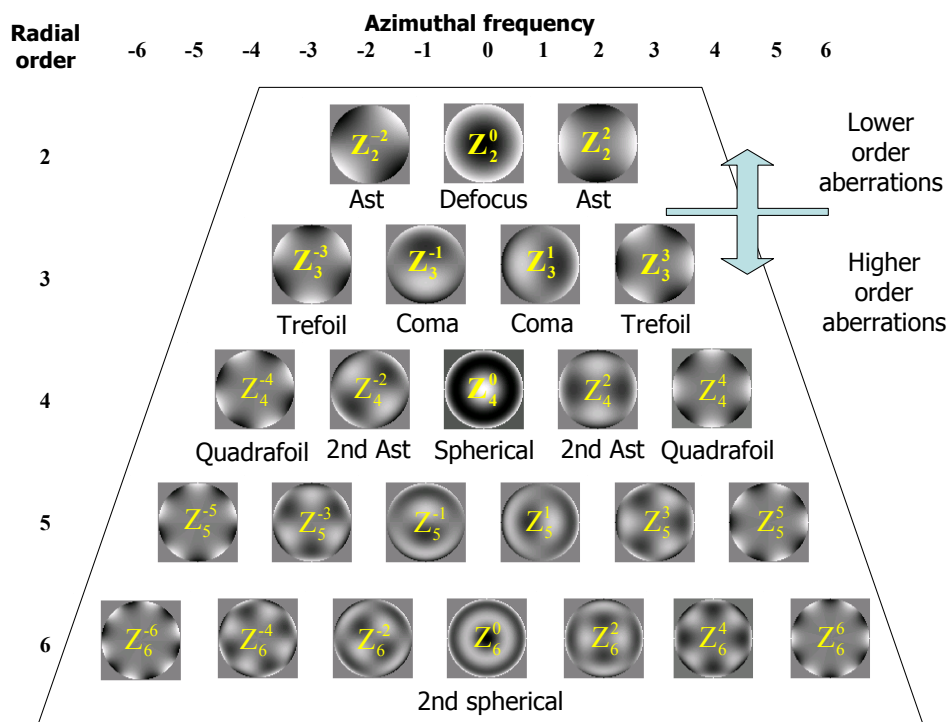
Figure 2-4: Zernike coefficients up to the 6th order

Point Spread Function

The *point spread function* (PSF) is the illuminance distribution in the image of a point source of light. In other words, it is the image of a point source. The form of the PSF depends on diffraction, defocus, aberration, scatter and the form and size of the aperture stop. Assuming a well-corrected optical system without aberrations (a diffraction limited system) and a circular aperture, the PSF is rotationally symmetric and its section follows a Bessel function of the first kind of order 1 ("OSLO Manual" 2001) [formula 7.19]. Such a diffraction limited PSF

shows that the light distribution consists of a central peak and central disk of light, the Airy disk. This is surrounded by a number of rings of light of ever-decreasing light level. If the optical system has aberrations, the PSF is broader and the peak is lowered, relative to the diffraction limited case, and is typically not rotationally symmetric any more. Due to the difficulty in comparing different PSFs or quantifying their optical performance, there are often simplifications used. The *Raleigh criterion* applies to monochromatic point sources and states, that for a diffraction limited system, two point sources can just be resolved if the peak of the PSFs lies on the first minimum of the other. In presence of aberrations and chromatic light the Airy disk may disappear, because of the lack of well-defined zeros in the PSF. Criteria useful for these cases include the half-width and the *Strehl intensity ratio*. The width of the PSF is taken as the half-width, which is the width at half the peak height. This half-width increases with aberrations. A drawback is the directional dependence in case of a non-rotationally symmetric PSF. This is not the case with the Strehl intensity ratio. It is defined to be the ratio of the maximum light level value of the aberrated PSF to the maximum light level value of the diffraction limited PSF. The Strehl ratio is always less than or equal to one. The greater the aberrations are, the lower the Strehl ratio is. A criterion for a good, near diffraction-limited system is that the Strehl intensity ratio has a value of > 0.8 (Atchison and Smith 2000) [p. 195 ff.].

There are various ways to calculate the PSF. The PSF can be calculated from the geometric wavefront; diffractive effects may additionally be included ("OSLO Manual" 2001) [p. 181]; (Atchison and Smith 2000) [p. 259]. A simpler method is to calculate the PSF from the density distribution of the spot diagram, therefore neglecting wave properties (Arasa and Alda 2004).

Optical Transfer Function

The *optical transfer function* (OTF) is the Fourier transform of the PSF and is a measure of the accuracy with which different frequency components in an object are reproduced in the image. The OTF is a complex quantity including both the *modulation transfer function* (MTF) and the *phase transfer function* (PTF). The MTF is the ratio of the modulation in the image to the modulation in the object. The PTF is a measure of the shift of that spatial frequency component from its ideal position. The OTF can be thought of being the function describing the dependency between a one-dimensional grating pattern with a light level that varies sinusoidally and its image. Even though most objects are not sine wave targets, the OTF is still useful because with Fourier analysis an arbitrary object can be represented as a superposition of several frequency components ("OSLO Manual" 2001) [p. 187 ff.].

The MTF is typically evaluated in the tangential and sagittal planes. If the MTF is calculated from geometric information, it is referred to as geometric MTF as opposed to diffractive MTF regarding physical optics (Thöniß 2004). The MTF is a very useful measure for optical performance, although drawing conclusions from an existing MTF to the present aberrations is generally difficult.

2.2 Physiological Optics
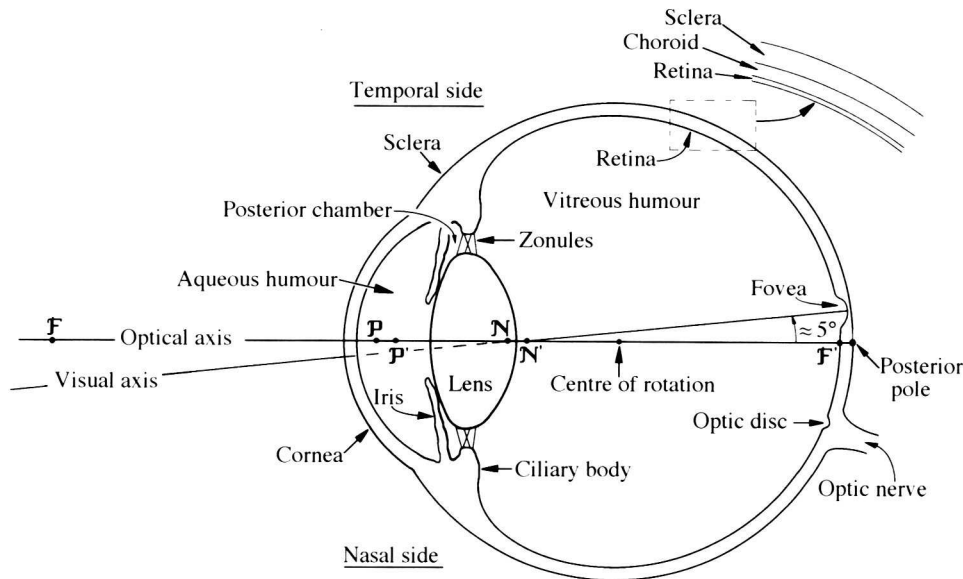
2.2.1 Anatomy and Physiology

Figure 2-5: Horizontal section of the right eye as seen from above
Reference: (Atchison and Smith 2000) [Fig. 1.1]

The description of the anatomy and physiology is provided according to Atchison et. al. (Atchison and Smith 2000) [p. 3 ff.]. An overview of the structure of the human eye is shown in Figure 2-5. The eye is wrapped in three main layers: the outer *sclera* that passes into the *cornea* at the anterior part. The cornea is the transparent part through which the light rays enter the eye. The sclera is the "white" of the eye that is mainly protective in function. The middle layer consists of the choroid that passes into the ciliary body and the *iris*. The choroid is deeply pigmented with melanin reducing reflecting stray light in the eye. The ciliary body is responsible for the accommodation of the *lens*; both, the choroid and ciliary body are important for vegetative processes. The pigmentation of the iris is responsible for the color of the eye. The size of the opening of the iris, the *pupil*, is variable and under control of the autonomic nervous system. The pupil gives the aperture of the eye and plays an important optical role. The innermost layer is the *retina*. This is an extension of the central nervous system and connected to the brain by the optic nerve. The retina contains the rods and cones and serves as the "film" of the eye. The inside of the eye can be divided into three parts: the anterior chamber between the cornea and the iris filled with a watery liquid, the *aqueous humor*. The posterior chamber is the part between the iris and the ciliary body and the lens, filled with aqueous humor, too. The third part is the vitreous chamber filled with a jellylike fluid called *vitreous humor*.

The Cornea
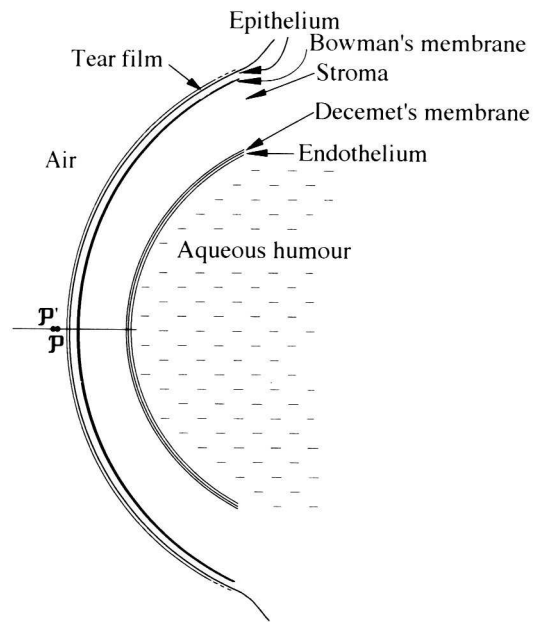
Figure 2-6: Cross-section of the cornea
Reference: (Atchison and Smith 2000) [Fig. 2.1]

The cross-sectional structure of the cornea is shown in Figure 2-6. The front surface is the tear film. It consists of oily, aqueous and mucous layers. It moistens the cornea and is important for clear vision since it smoothes the adjacent layer of epithelium cells. The epithelium protects the rest of the cornea; the innermost of multiple layers of cells is able to divide. Bowman's membrane mainly consists of collagen fibrils and passes into the stroma that is with 90 percent by far the thickest part of the cornea and consists of collagen lamellae. Following Descement's membrane the last layer of the cornea is the endothelium, which is responsible for the fluid balance of the stroma.

The Lens

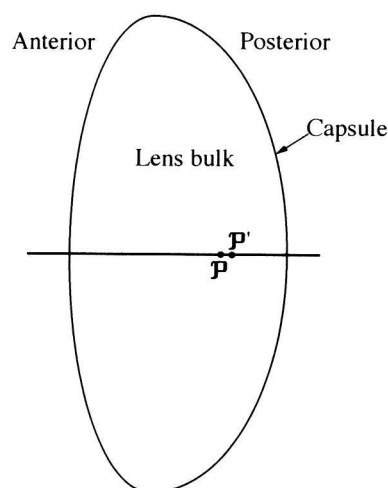**Figure 2-7: Cross-section of the crystalline lens**
Reference: (Atchison and Smith 2000) [Fig. 2.5]

The structure of the lens is shown in Figure 2-7. The lens is an elastic capsule containing cellular tissue of non-uniform gradient index. This is difficult to measure and makes it

difficult to deal with human lens parameters. The epithelium cells inside the lens are responsible for continual growth of the lens throughout life, so lens properties – even optical ones – are age-dependent. The elastic capsule is connected to the ciliary muscles by the zonules. This allows for *accommodation* of the lens: when the ciliary muscle is relaxed, the zonules are put under tension and the lens capsule flattens, leading to a decreased refraction power. When the muscle is contracted the lens capsule steepens, leading to an increased optical power. The accommodation is responsible for the ability of the eye to focus between far and near objects (Figure 2-8). The eye looses accommodation as it ages, called *presbyopia*. Additionally the aging lens eventually becomes yellowish or cloudy, called *cataract*. When the cataract becomes dense enough to interfere with the patient's vision the lens may be replaced by an artificial lens implant during cataract surgery.
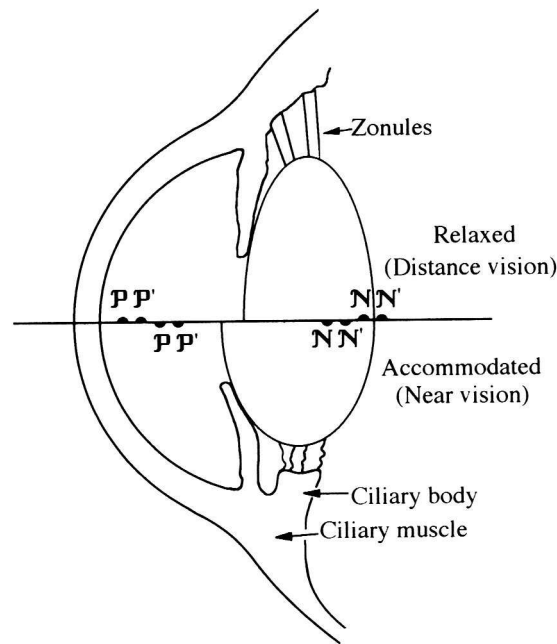

Figure 2-8: The effect of accommodation on lens shape and position
Reference: (Atchison and Smith 2000) [Fig. 2.6]

15

The Retina

Figure content with labels:
- 6. Inner nuclear layer
- 7. Inner plexiform layer
- 8. Layer of ganglion cells
- 9. Nerve fibre layer
- 10. Inner limiting membrane
- 5. Outer plexiform layer
- 4. Outer nuclear layer
- 3. Outer limiting membrane
- 2. Photoreceptors (rods and cones)
- 1. Pigment epithelium
- Bruch's membrane
- LIGHT
- Choroid
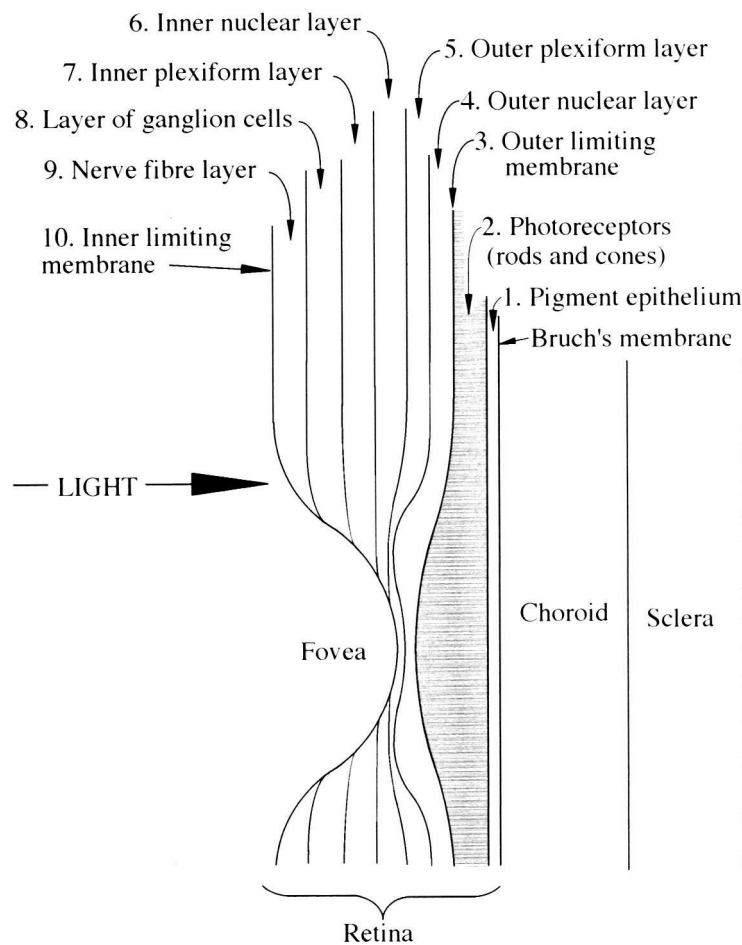- Sclera
- Fovea
- Retina

Figure 2-9: Layers at the back of the human eye
Reference: (Atchison and Smith 2000) [Fig. 1.3]

The retina is the light-sensitive part of the eye. It consists of several layers playing different roles, see Figure 2-9. The choroid connects to the *retinal pigment epithelium* (RPE) at Bruch's membrane. The pigment epithelium is fed by the blood vessels of the choroid and keeps the layer containing the photoreceptors healthy. This layer contains two types of receptor cells: the *rods* and *cones*. The rods are highly sensitive low-level light detectors responsible for vision in dim light. In contrast, the cones need higher light levels but enable higher spatial resolution and are responsible for fine and color vision. Therefore there are three types of cones absorbing long (red), middle (green) and short (blue) wavelength light. The outlying parts of the retina are responsible for peripheral vision while the center area, called *macula*, is used for fine central vision and color vision. Therefore distribution density of the cones is increasing moving towards the center of the macula, called *fovea*. The fovea is responsible for sharp daylight vision. In contrast, the rods density is decreasing moving to the fovea resulting in night blindness of the center of the fovea. Just as the axons carrying the electric signals from the nerve fiber layer to the optic nerve, the blood vessels supplying the inner part of the retina travel through the *optic disc*. Since there are no rods and cones this area corresponds to the blind spot in the visual field of the retina. The thickness of the retina varies between approximately 50 and 600 μm and is least in the fovea and biggest near the optic disc.

2.2.2 Image Formation

The image formation process of the human eye is comparable to a man-made optical camera: the entering light is refracted by the cornea, limited by the pupil, refracted by the lens and focused at the retina. The cornea has a much higher optical power than the lens. However the power of the cornea is constant, while the human lens can accommodate and its power is therefore adjustable. The size of the pupil is variable and responsible for the amount of light entering the eye. The following sections describe the main optical elements and their properties with regard to the construction of a virtual eye.

Figure 2-10: Image formation of the human eye
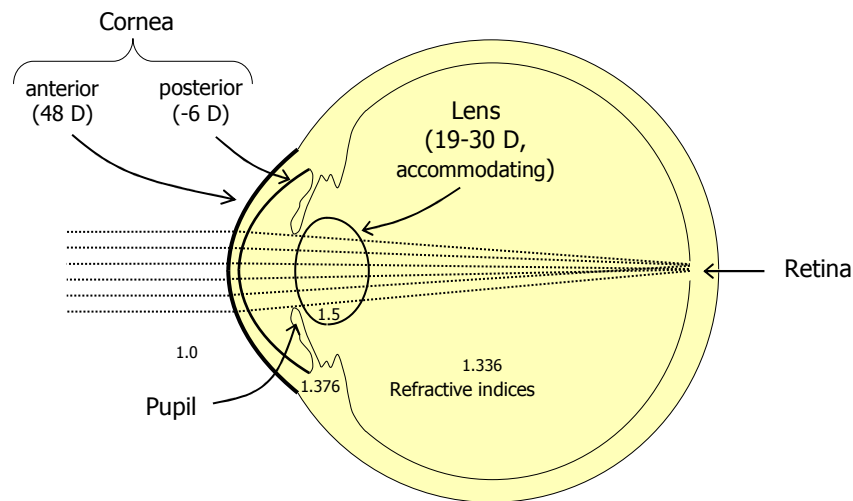
The Cornea

The paraxial region of a corneal surface can be described with an apical radius of curvature in one meridian. However this is not sufficient when moving to the periphery, since an average corneal surface is not a perfect sphere, but aspherical – it is known to flatten peripherally.
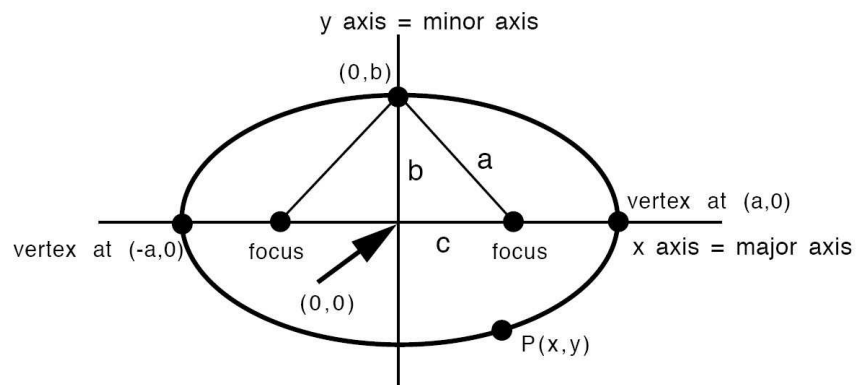

Figure 2-11: Basic geometry of an ellipse
Reference: (Salmon 1999) [Fig. 3.1]

A popular formula for describing a cross-section of a corneal surface is *Baker's equation* introducing the *shape factor* (Baker 1943):

$$pz^2 - 2Rz + r^2 = 0 \qquad\qquad \textbf{(2-16)}$$

R: apical radius
r: distance from apex
z: elevation
p: shape factor

This is in general the mathematical description of a *conic section* (the result of cutting a cone by a plane), including the special cases of *ellipses*. The *eccentricity e* describes the degree of elongation of an ellipse and may be defined by the ratio of distances of c and a, see Figure 2-11. The eccentricity of an ellipse has a value of $0 < e < 1.0$, where $e = 0$ describes a sphere, whereas $e = 1.0$ defines a parabola. However using Baker's equation and the shape factor p is more general. The shape factor can be transformed into *asphericity* $Q = p-1$. Figure 2-12 gives an overview of different values of the shape factor p, the asphericity Q, the eccentricity e (where applicable) and their corresponding shapes. The eccentricity is related to the shape factor and asphericity by $p = 1-e^2$ and $Q = -e^2$. If a corneal surface has an asphericity $Q < 0$ it is called *prolate*, if $Q > 0$ it is called *oblate*. A review of mathematical descriptors of corneal asphericity is given by Gatinel et al. (Gatinel, Haouat et al. 2002) and Calossi, recently (Calossi 2007).
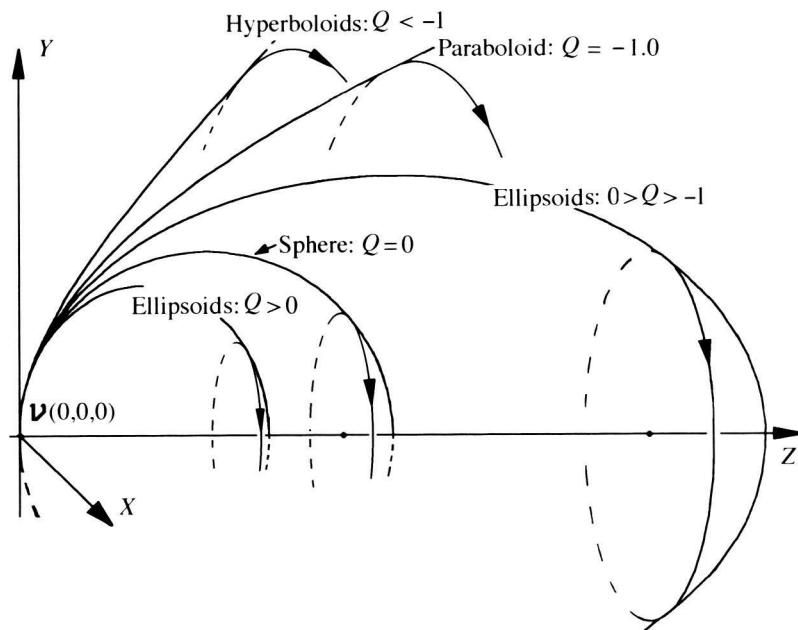
Figure 2-12: The shape of conicoids with different asphericities (same apical radii)
Reference: (Atchison and Smith 2000) [Fig. 2.2]

Baker's equation (2-16) resolved for elevation leads to:

$$z_{conic} = \frac{R - \sqrt{R^2 - (1+Q)r^2}}{(1+Q)} \qquad\qquad \textbf{(2-17)}$$

However this form is not useful for the special cases of flat surfaces ($R = \infty$) and paraboloids ($Q = -1$). But it can be transformed using the third binomial theorem in the following form that is valid for all values of parameters:

18

$$z_{conic} = \frac{r^2}{R + \sqrt{R^2 - (1+Q)r^2}}$$ **(2-18)**

This is the general formula for conics; it can be further refined by adding polynomial terms resulting in a so called *figured conic* (Atchison and Smith 2000) [p. 167]:

$$z_{figured\_conic} = z_{conic} + f_4 r^4 + f_6 r^6 + ...$$ **(2-19)**

Conic section (2D) →rotation→ Conicoid (3D, surface of revolution)

Prolate ellipsoid, Q<0
„rugby-ball"

Sphere, Q=0

Oblate ellipsoid, Q>0
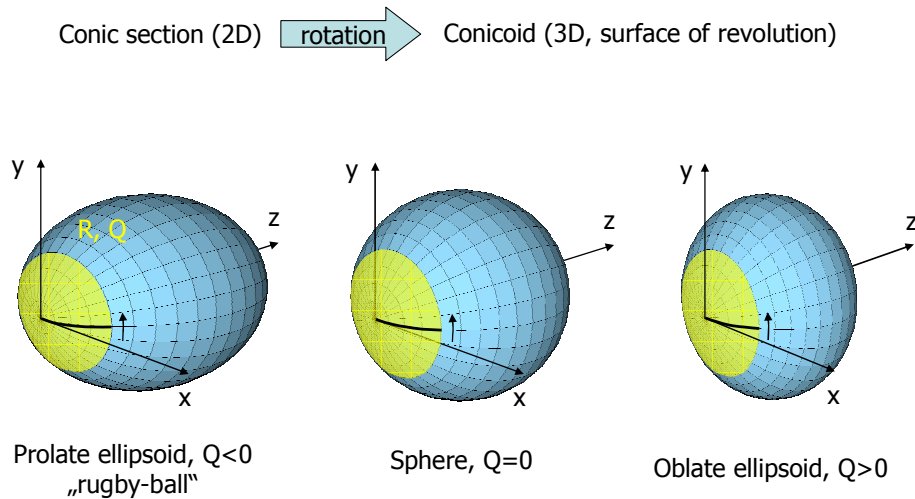
Figure 2-13: Conicoids
(graphics created with http://www.javaview.de)

The formula describing the cross-sectional shape can easily be used to define a three dimensional surface. By building the surfaces of revolution one gets the associated three dimensional objects, the conics are extended to conicoids: sphere to spheroid; ellipse to ellipsoid; parabola to paraboloid; hyperbola to hyperboloid (Figure 2-13 shows a spheroid, oblate ellipsoid and prolate ellipsoid). In a cartesian coordinate system these surfaces of revolutions based on conic sections can be expressed in the yellow marked areas in Figure 2-13 as:

$$z(x,y) = \frac{R - \sqrt{R^2 - (1+Q)(x^2 + y^2)}}{1+Q}$$ **(2-20)**

or alternatively (without gaps):

$$z(x,y) = \frac{x^2 + y^2}{R + \sqrt{R^2 - (1+Q)(x^2 + y^2)}} \qquad \textbf{(2-21)}$$

R: apical radius of curvature

Q: asphericity

However, a real cornea usually has some amount of *toricity*. Thus it cannot be described by a surface of revolution but more likely as a part of a torus (Figure 2-14), mathematically expressed as:

$$z(x,y) = R_x - \sqrt{\left(R_x - R_y + \sqrt{R_y^2 - y^2}\right)^2 - x^2} \qquad \textbf{(2-22)}$$

R_x: radius of curvature in x direction

R_y: radius of curvature in y direction
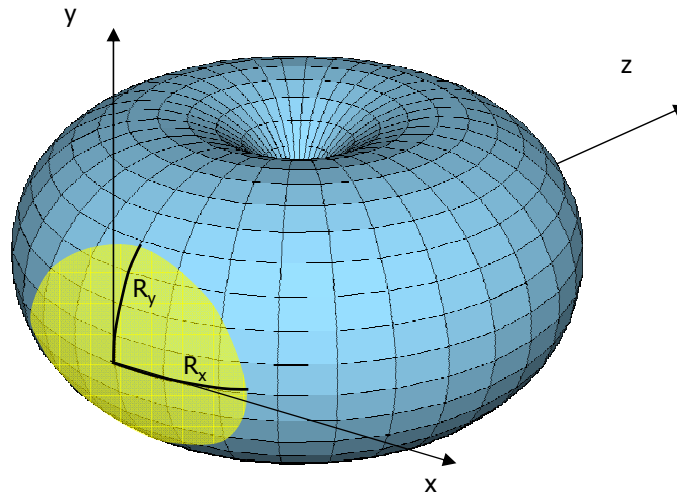
Figure 2-14: Torus
(graphics created with http://www.javaview.de)

Two different radii of curvature can be specified and therefore an astigmatic cornea can be modeled. The drawback in this expression is, that there no asphericity is included. A mathematical representation combining the capabilities of equation (2-20) and (2-22) is the so called *biconic surface*, discussed in detail in section 3.1. Therefore when looking at cross-sections of a real cornea each meridian might have its own apical radius and asphericity.

Based on Baker's equation a wide range of corneal shapes can be described. More sophisticated models are necessary when leaving the optical zone and moving to the outer periphery beyond the limbus. However this is beyond the scope of this work that focuses on optical properties. Furthermore Baker's equation is not sufficient for describing abnormally shaped corneas e.g. after corneal refractive surgery. However it is sufficient for describing normal corneas and is used by various model eyes (see following section).

This surface description is applicable to, both, the anterior and posterior corneal surface. As described before, the cornea consists of several layers, each with an own refractive index. Since the stroma is by far the thickest layer its refractive index dominates. So it is a reasonable approximation to describe the refraction process at the cornea as two refractions

according to Snell's law: a first refraction at the anterior corneal surface and a second refraction at the posterior corneal surface, assuming a constant refraction index in between.

The Lens

The optical properties of the human crystalline lens are more complex. The anterior and posterior surface may be principally described by a radius and asphericity, too. However these parameters are object to change during accommodation. Furthermore the refractive index within the lens is not constant. While the refractive index is biggest in the central region of the lens it decreases when moving to the periphery. Light rays are therefore refracted by the anterior surface and the posterior surface just as at the cornea. But in between they undergo a continuous refraction; that means their direction is not a straight line within the lens. This is comparable to man-made *gradient refractive index* (GRIN) lenses which have a continuous refractive index distribution. Computational ray tracing through gradient index media is more complex than for homogeneous refractive index media, because the classical Snell's law has to be generalized. This in principle leads to the task of solving a differential equation what can be done with various numerical methods (Langenbach 1993); ("OSLO Manual" 2001) [p. 138 f.]. However this thesis is focused on the investigation of homogeneous refractive index lenses, rather than modeling the human crystalline lens.

The Pupil

In human optics, the opening formed by the iris is known as the pupil. It is important to distinguish the *real pupil* from the *entrance pupil* and the *exit pupil*. The entrance pupil is the image of the real pupil formed by the optical elements in front of the iris; it is the image of the real pupil in object space. Accordingly the exit pupil is the image of the real pupil formed by the optical elements behind the iris; it is the image or the real pupil in image space. The exit pupil has little usage in practice. What an observer sees when looking into an eye is the entrance pupil.

The size of the pupil controls the amount of light entering the eye. As the pupil changes its size, the pupil center may also move. Most subjects show a temporal movement of the pupil center with increase in pupil size (Atchison and Smith 2000) [p. 23]. While there are other factors inducing changes of pupil size (and position), the most important factor affecting pupil size is the level of illumination.

2.2.3 Schematic Eye Models

There are various schematic eye models trying to quantify the physical dimensions and optical properties of the human eye. They are mainly based on population mean values and the construction may be done at different levels of complexity – and for different purposes. The models can be divided into two main groups, the *paraxial schematic eyes* and the more complex *finite schematic eyes*. The simple paraxial schematic eyes are only accurate in the paraxial region, for spherical refracting surfaces and all components are aligned on one optical axis according to paraxial optics. They may be used for simulating basic optical properties like magnification, retinal illumination, Purkinje surface reflections, entrance and exit pupil calculation or consideration of refractive errors. However they do not succeed in simulating advanced optical properties. The finite schematic eye are often based on paraxial ones, but introduce more sophisticated features like non-spherical refracting surfaces, gradient index lenses and components may be aligned arbitrarily. They more accurately simulate human optics, but still have to be used with caution because different models may be designed for different purpose. These more advanced models are useful for predicting retinal image sizes, predicting light levels on the retina or predicting the effects of changes in any ocular structure (like altering the corneal shape e.g. by refractive surgery) on ocular aberrations. Some eye models provide data for different levels of accommodation, while some additionally include

aging factors. Most schematic eyes are restricted to monochromatic considerations. All schematic eyes are using rotationally symmetric surfaces although it is known that the average cornea has some amount of toricity that causes a corneal astigmatism of about 0.7 diopters (Salmon 1999) [p. 24]. This corneal astigmatism seems to be compensated to some degree by an opposite astigmatism of the human lens (Mrochen, Jankov et al. 2003; Kelly, Mihashi et al. 2004). The lack of toric surfaces in model eyes may arise from the difficulties in measuring the exact properties of the human lens. (Note, that some model eyes are referenced to be not completely rotationally symmetric in the following text – this is only due to the specification of different reference axes, the individual surfaces still are rotationally symmetric.)

Paraxial Schematic Eyes
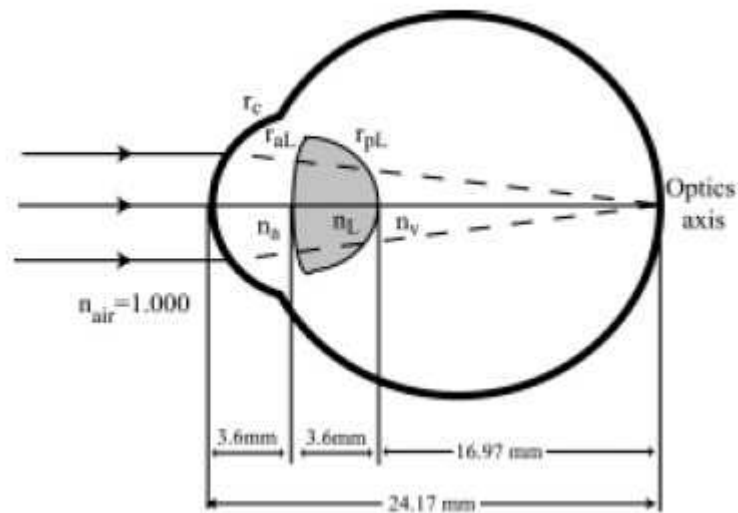
Figure 2-15: Gullstrand's three-surface simplified schematic eye
Reference: (Maheshwari and Williams 2001) [Fig. 7]

The possibly most popular eye model was presented 1909 by Gullstrand (Helmholtz, Gullstrand et al. 1909) [p. 299 ff.]; he was later rewarded with the Nobel prize of physiology for his investigations on the dioptrics of the eye. He used a comprehensive analysis of ocular data to construct two paraxial model eyes: a *six-surface exact* and a *three-surface simplified schematic eye*, both at two levels of accommodation (relaxed and maximal). The exact schematic eye consists of six refracting spherical surfaces: two for the anterior and posterior cornea; four for the lens to approximate the non-uniform gradient index of refraction by providing a central nucleus of high refractive index and a surrounding cortex of lower refractive index ((Atchison and Smith 2000) [figure 5.3]; (Helmholtz, Gullstrand et al. 1909) [p. 335]). Two sets of lens parameters are provided, one for the relaxed state, one for maximum accommodation. The simplified schematic eye uses only three surfaces: one for the cornea and two for the anterior and posterior lens surface (Figure 2-15), again for the relaxed and maximum accommodated state.

Similar to Gullstrand's model eye is the *Le Grand full theoretical eye* and *Le Grand simplified eye* (Le Grand and El Hage 1980). The full theoretical eye only has one refractive index and two surfaces for the lens (provided in relaxed and accommodated forms) and the simplified version uses a lens of zero thickness.

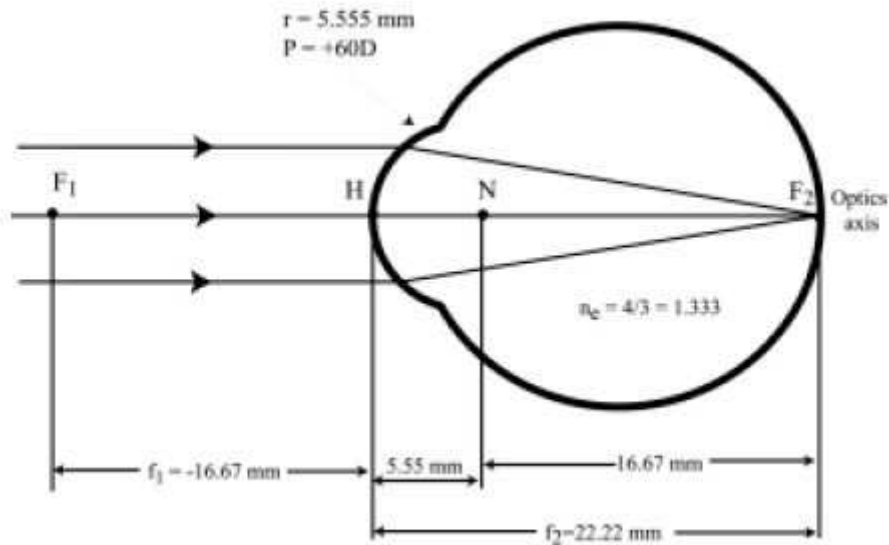**Figure 2-16: Emsley standard reduced 60-diopter eye**
Reference: (Maheshwari and Williams 2001) [Fig. 8]

Emsley modified Gullstrand's simplified schematic eye for easier calculation purposes (*Gullstrand – Emsley simplified schematic eye*) and further introduced the *Emsley standard reduced 60-diopter eye* (Emsley 1952). This is one of the simplest models and often used for educational purpose: it consists of only one refracting surface (Figure 2-16).

Bennet and Rabbetts simplified eye is a modification of the relaxed Gullstrand – Emsley simplified eye. The authors also provide a reduced eye using only one refracting surface just as the Emsley standard reduced 60-diopter eye (Bennett and Rabbetts 1989). Rabbetts introduced further data for accommodation levels and age levels (Rabbetts and Bennett 1998). Most of the above paraxial eye models use discrete accommodation levels. Blaker introduced a variable accommodative schematic eye together with age levels (Blaker 1980). Atchison and Smith extend Gullstrand's exact schematic eye to allow for simulation of variable accommodation levels (Atchison and Smith 2000) [p. 46].

Finite Schematic Eyes

Lotmar's eye model is based on Le Grand full theoretical eye. He replaced the anterior corneal spherical surface by a polynomial representation and replaced the posterior lens surface by a paraboloid (Q = -1) (Lotmar 1971). However this schematic is no accurate representation of real eyes (Atchison and Smith 2000) [p. 171].

Drasdo and Fowler modified a schematic eye similar to Gullstrand – Emsley simplified eye by adding asphericity to the corneal surface and exchanging the planar retina by a sphere (Drasdo and Fowler 1974). Their purpose was to determine the retinal projection from the visual field.

Pomerantzeff et al. constructed wide-angle eye models based on biological and physical measured characteristics of sample eyes to model the spherical aberration (Pomerantzeff, Fish et al. 1971; Pomerantzeff, Pankratov et al. 1984).

Another model was introduced to predict retinal illumination (Kooijman 1983). This one is also based on Le Grand full theoretical eye. All four surfaces are aspherical. The retina is either spherical or aspherical.

Navarro et al. provided a model also based on Le Grand full theoretical eye by refining it with asphericities. They modeled the accommodation of the eye: the parameters for the lens curvatures and asphericities, lens thickness, lens refractive index and anterior chamber depth (ACD) are functions of the level of accommodation provided as diopters (Navarro, Santamaria et al. 1985).

Liou and Brennan created a schematic eye with two aims: firstly to resemble the anatomy of real eyes as closely as possible and secondly to correctly model the spherical and chromatic aberration of real eyes (Liou and Brennan 1997). They provide conicoids to model the cornea and lens and include a gradient index lens. The specification of different axes leads to a non-rotationally symmetric model. No accommodation is modeled and age related parameters are assumed to be from a 45 year old person.

Thibos et al. developed schematic eyes based on Emsley standard reduced 60-diopter eye with an aspherical surface. They do not focus on anatomical correctness but are intended to model the chromatic aberration of real eyes. The *chromatic eye* is not rotationally symmetric, various alignment axes are provided (Thibos, Ye et al. 1992), while their *Indiana eye* is rotationally symmetric (Thibos, Ye et al. 1997).

Popiolek-Masajada et al. designed a schematic eye using four refracting surfaces and a alternative description of the lens profile with a combination of hyperbolic cosine functions and hyperbolic tangent functions (Popiolek-Masajada and Kasprzak 1999). This representation ensures the continuity of the radius of curvature along the whole lens profile. This is generally not the case when constructing anterior and posterior lens surface using two conicoids. The parameters of the lens are varied by the level of accommodation. The authors extended their model eye by using an accommodation dependent gradient refractive index (Popiolek-Masajada and Kasprzak 2002). However their model eye is focused on the lens and they used a paraxial ray tracing schema together with a paraxial cornea for analysis purpose of their model. The authors claim to present a complete finite schematic eye with finite ray tracing analysis in future.

Siedlecki et al. proposed a model eye with aspherical surfaces and a radially varying refractive index distribution of the crystalline lens. They analyzed their model eyes with ray tracing and compared the results to other model eyes, especially regarding spherical aberration (Siedlecki, Kasprzak et al. 2004).

Recently, Norrby took up the extensive analysis of the shape of real eyes of Dubbelman et al. to construct the *Dubbelman eye model* (Norrby 2005). It uses conicoids and is rotationally symmetric. Similar to Navarro's eye model it uses a functional dependency of the lens parameters (including an equivalent constant refractive index) from accommodation level and age, in addition. Norrby analyzed the eye model by means of real ray tracing and found similar spherical aberration compared to real eyes.

Navarro et al. proposed a method for obtaining optical schematic models of individual eyes (Navarro, Gonzalez et al. 2006). They used measurements of real eyes to model the crystalline lens with a gradient-index lens so that the individual eye models give a high-fidelity reproduction of the monochromatic wavefront aberration.

Smith et al. do not focus on the construction of a complete schematic eye but investigated mathematical models for the refractive index distribution of the crystalline lens (Smith, Pierscionek et al. 1991; Atchison and Smith 2000; Smith 2003) [p. 170].

2.3 Methods for Measuring the Human Eye

2.3.1 Keratometry

Keratometry is a basic method to measure the curvature of the central anterior corneal surface. Devices are called *keratometers*, or sometimes *ophthalmometers* (although this name is misleading, because an ophthalmometer typically measures more than the cornea). There are two basic types of keratometers: the instrument based on Hermann von Helmholtz and the one according to Javal-Schiotz. Helmholtz built his laboratory device 1854 and included a doubling device to eliminate eye movements (Helmholtz, Gullstrand et al. 1909) [p. 259 ff.]; this device uses two adjustable prisms to measure two axes perpendicular to each other (one position device). Javal and Schiotz modified Helmholtz instrument in 1881 and built a device

for clinical use (Javal and Schiötz 1881) that uses only one prism (two position device). Since then, the keratometer became the most popular instrument for measuring corneal curvature. Since it is important for the device to stay in focus when measuring, often the *Scheiner principle* is used to guarantee a focused image. Today many different keratometers are sold commercially, but the principle remained unchanged. A popular commercial version of the keratometer according to Helmholtz principle was built by Bausch & Lomb, Inc. (USA); a popular version of the Javal-Schiotz is the keratometer of Haag-Streit AG (Switzerland). In 1950 Hans Littmann developed a keratometer based on Helmholtz design that was produced by Carl Zeiss AG (Germany).

2.3.2 Placido-Videotopography

Placido-videotopography systems are capable of measuring the complete anterior corneal surface and therefore overcome the limitation of keratometers measuring only the central corneal curvature. This method is also known as *(photo)keratoscopy* or *videokeratography*; measuring devices are also called *(placido) videokeratometers* or *videotopometers*. The principle is named after the Portuguese ophthalmologist Antonio Placido, who 1880 studied the shape of the cornea by observing the reflections of a disk containing concentric black and white rings, now called *Placido's disk* (Duke-Elder and Abrams 1970) [p. 128]. In 1896, Allvar Gullstrand built the first photokeratoscope by incorporating a Placido disk into his ophthalmometer. He was able to manually determine the corneal curvature by analyzing the photographs of the cornea (Gullstrand 1966). In the 1970s and 1980s the first photokeratoscopes were developed for clinical use. Early systems used Polaroid cameras and images had to be hand-digitized. But with the propagation of personal computers systems soon became more automated by using cameras attached to computers that automatically analyzed the images. Since the 1990s computerized videotopography systems from a number of suppliers were commercially available and Placido-videotopography came into widespread clinical use.

Videotopography has two major applications in clinical every day use: refractive laser surgery and contact lens fitting (Salmon 1999) [p. 21]. In refractive laser surgery, corneal topographies are used for the identification of corneal shape anomalies like keratoconus as a contraindicating factor, for the quantitative assessment of the corneal shape when planning surgery as well as for the postoperative evaluation. For contact lens fitting the exact corneal contour is important for selecting best-fit contact lenses. Apart from these applications corneal topography is crucial when investigating optical properties of the human eye in general. In the context of this thesis, measurements from Placido-videotopography systems play a fundamental role.

2.3.3 Ultrasound

Ultrasound A-Scan echo-impulse technique (US) has been first used to measure the human eye in 1956 (Mundt and Hughes 1956), and has been steadily improved and is a common measuring method today. Sonic waves are sent into the eye; the echo from the structures of interest is recorded and from the time the echo took the geometric length is calculated. This technique is capable of measuring the axial length as well as other intraocular distances, as the ACD or lens thickness. Principally there has to be a contact between the eye and the instrument; regarding this contact two methods are distinguished. Using the *applanation method* (AUS), there has to be a direct contact of the transducer to the cornea. In this case, the cornea actually is indented and therefore the eye is slightly shortened (which is operator dependent). This is avoided with the *water-immersion technique* (IUS). Here the eye does not come into direct contact with the transducer, instead uses a coupling fluid in between preventing compression. IUS is therefore more accurate than AUS, but slightly more

complicated in application because the patient has to be in horizontal position and some coupling device is needed (Kiss, Findl et al. 2002a).

2.3.4 Partial Coherence Interferometry

In 2000 the IOLMaster (Carl Zeiss Meditec AG, Germany) was introduced. This device measures three quantities: the anterior chamber depth, corneal curvature and axial length. The anterior chamber depth is determined as the distance between the optical sections of the crystalline lens and the cornea produced by lateral slit illumination. The corneal curvature is determined with conventional keratometry. The axial length is measured with *partial coherence interferometry* (PCI). This is a non-contact optical biometry method that is principally used by *optical coherence tomography* (OCT), too. The velocity of light is too high for direct measurement of echo delay times as done for example with ultrasound. Therefore the effect of interference of coherent light is used instead. A diode laser of 780 nm delivers a beam of light of short coherence length. This beam is split into two beams in a *Michelson interferometer*. The interference of the reference beam and the beam reflected by the cornea and the retina is detected by a photodetector. The signals are recorded as a function of the position of a mirror. This mirror position determines the axial length as the distance from the cornea to the retinal pigment epithelium (Kiss, Findl et al. 2002a; Kiss, Findl et al. 2002b). The results of the axial length measurement are recalculated with a statistical calibration function to be comparable to ultrasonic immersion measurements; this is discussed in more detail in section 4.2.

2.3.5 Wavefront-Analyzing Instruments

The two most widely used techniques for objectively measuring the wavefront aberrations of human eyes are instruments based on Hartmann-Shack and instruments based on Tscherning.
The *Hartmann-Shack sensor* that is widely used in the field of astronomy and adaptive optics has been initially used to measure aberrations of the human eye by Liang et al. (Liang, Grimm et al. 1994). A point source is generated on the retina. The light that emerges from this point source travels through the optical components and leaves through the pupil. In some distance a Hartmann-Shack sensor is positioned that consists of an array of small lenses. Each lenslet focuses its part of the wavefront to a spot in its focal plane. From the position of each spot the corresponding local slope of the wavefront can be calculated. Recorded with a *charge-coupled device* (CCD) matrix the whole wavefront can be calculated.
In 1894 Marius Tscherning studied the monochromatic aberrations of the human eye (Tscherning 1894). In 2000 an instrument for automatic wavefront analyzing based on *Tscherning's aberroscope* was introduced (Mrochen, Kaemmerer et al. 2000a). The device uses a collimated laser beam that illuminates a mask with regular matrix pin holes. This mask produces thin parallel rays that are sent through the eye and strikes the retina. The resulting retinal spot pattern is distorted according to the optical errors of the eye. With a CCD camera this spot pattern is recorded and the deviations of the spots from their ideal positions are evaluated to calculate the optical aberrations.
A compact review about wavefront-analyzing instruments is given by Applegate et al. (Applegate, Thibos et al. 2001); Biedermann provides some background information and historical outline (Lohmann and Caulfield 2002).

2.4 Current Surgical Procedures

An eye that needs no correction is called *emmetropic*. In this case the eye has the ideal length relative to the refractive power of the cornea and the lens. A sharp image can be focused onto the retina. If the eye is too long or short, the sharp image does not fall onto the retina, the patient suffers from so called *ametropia*; the eye has some amount of *refractive error*. If the eye is too long it results in *myopia* or *nearsightedness*. If the eye is too short it leads to

hyperopia or *farsightedness*. A myopic patient only sees sharp when looking at near objects, a hyperopic patients only when looking at objects located far away. *Astigmatism* is a refractive error of the eye in which there is a difference of refractive error in different meridians. This occurs, when the lens or cornea is no surface of revolution. If the meridians are perpendicular to each other this is called a *regular* astigmatism (with-the-rule, against-the-rule and oblique – depending on the axis), correctable with cylinders. If the meridians are not perpendicular, it is an *irregular* astigmatism. Ametropia is typically quantified by the amount of correcting glasses needed to restore emmetropia, the so called *eyeglass prescription* or *spectacle refraction*. This spectacle refraction consists of sphere and cylinder in diopters and the axis in degrees (SPH / CYL x AX). Two ways of describing the cylinder are popular: the plus-cylinder and the minus-cylinder writing. For example, +2.0 / +1.0 x 90° in plus-cylinder notation is equivalent to +3.0 / -1.0 x 180° in minus-cylinder notation and both of them specify a power of 2.0 diopters at the 90 degree axis and 3.0 diopters at the 180 degree axis. The spectacle refraction is typically determined using an automated refractor (also called *autorefractor*) or with a manual refractor (also called *phoropter*) at a vision chart. The refraction obtained the latter way is the most reliable one and called *subjective manifest refraction*.
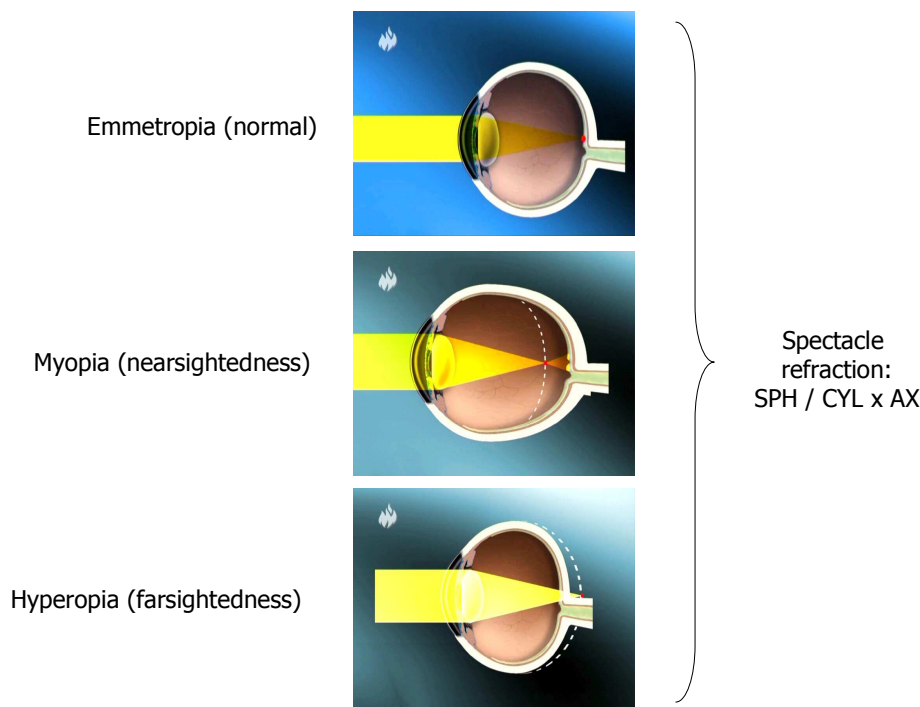
Figure 2-17: Emmetropia and Ametropia
Reference: Prometheus Wissenschafts-Fernsehen, Klarner Medien GmbH (Germany)

2.4.1 Corneal Refractive Surgery

Corneal refractive surgery is an alternative to glasses or contact lenses to permanently correct ametropia. There are several methods that all have in common that they modify the shape of the cornea.

One of the early methods is *radial keratotomy* (RK). The central cornea is flattened using a series of peripheral radial cuts (incisions) performed with a hand-held knife with a diamond cutting tip. The incisions are made from the edge of the marked optical zone out to the edge of the cornea; the cutting tip is extended to the appropriate length relative to the measured corneal thickness. This method is applicable for low myopia and astigmatism. This method was initially developed by Sato et al. (Sato, Akiyama et al. 1953), later refined by Yenaliev

(Enaliev 1979) and Fyodorov et al. (Fyodorov and Durnev 1979; Fyodorov and Durnev 1981) and firstly introduced in the United States by Bores et al. (Bores, Myers et al. 1981).

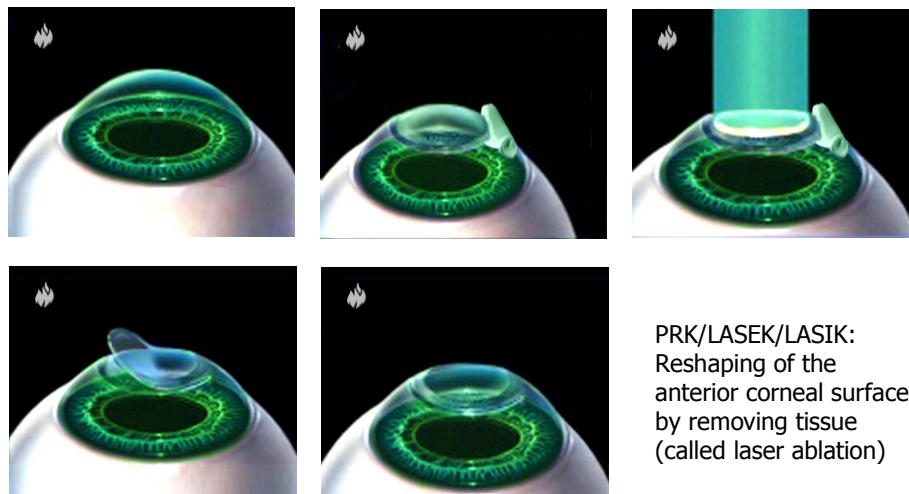PRK/LASEK/LASIK: Reshaping of the anterior corneal surface by removing tissue (called laser ablation)

Figure 2-18: Corneal refractive surgery
Reference: Prometheus Wissenschafts-Fernsehen, Klarner Medien GmbH (Germany)

In *photorefractive keratectomy* (PRK) the epithelium is removed and the anterior corneal surface is reshaped with an excimer laser. This is a cool light laser working with ultra-violet light at a wavelength of 193 nm that has the ability of removing corneal tissue. While early lasers used one broad beam, modern systems use the so called flying spot technique. Many single laser beams are combined to result in a desired ablation pattern. After the laser treatment, the epithelium heals within a few days. The excimer laser was introduced into ophthalmology by Trokel et al. (Trokel, Srinivasan et al. 1983) who treated cow eyes. The first treatments of in vivo rabbit eyes and human eyes were done by Seiler et al. (Seiler and Wollensak 1986; Seiler, Bende et al. 1988).

Laser in situ keratomileusis (LASIK) is the most widely used method performed today. In this method a flap is cut either mechanically with a microkeratome or with a femtosecond-laser (FEMTO-LASIK). This flap is lifted and the laser ablation is done just as for PRK with the same excimer laser systems in the stroma. Afterwards the flap is repositioned. The cut inside the stroma does not heal, but the epithelium overgrows it again within one or two days. Keratomileusis refers to any corneal procedure that uses subtraction of tissue. Fundamental contributions were made by Jose Barraquer in the 1960s (Nordan 1989). He introduced the first successful techniques for keratomileusis and invented the first microkeratome for cutting a corneal flap. One of the first introducing the term LASIK for their treatments on rabbit and human eyes with an excimer laser and a corneal flap were Pallikaris et al. (Pallikaris, Papatzanaki et al. 1990; Pallikaris, Papatzanaki et al. 1991).

Laser epithelial keratomileusis (LASEK) and *epithelial laser in situ keratomileusis* (EPI-LASIK, named by Pallikaris et al. (Pallikaris, Katsanevaki et al. 2003)) are advancements of PRK. In both methods the epithelium is removed. For LASEK this is done mechanically after applying a few drops of a weak alcohol solution to a circumscribed area on the surface of the cornea. For EPI-LASIK this is done with a microkeratome, just as for LASIK – with the difference, that only the epithelium is removed. Therefore the name EPI-LASIK, although the method is actually closer related to PRK. After the laser treatment the epithelium is laid back

into place and acts like some natural bondage and may serve to facilitate healing of new epithelium. Some more historical information is given by Kusserow (Kusserow 2006).

2.4.2 Cataract Surgery

A cataract is the clouding of the crystalline lens of the eye. Normally, light travels through the clear lens and is focused onto the retina. As a result of the natural aging process, the lens gradually becomes cloudy. This opacity results in distorted or blurred vision and can finally lead to blinding. The common treatment of cataract is to surgically remove the cloudy lens. There are principally two types of cataract surgery: intra-capsular and extra-capsular surgery. In both cases the human lens is removed and replaced with an artificial *intraocular lens* (IOL). In intra-capsular surgery, the entire lens including the lens capsule is removed. In extra-capsular surgery, the majority of the lens capsule is left intact and only the lens is removed. This is typically done by using ultrasonic waves to emulsify the nucleus of the crystalline lens and to remove it afterwards (*phacoemulsification*). This is the preferred method used in modern practice because only a small incision is needed. After removing the lens, an intraocular lens is typically inserted through a small incision using a foldable IOL (made of silicone or acrylic material), or through an enlarged incision using a polymethylmethacrylate (PMMA) lens (Figure 2-19). In most cases, the lens implant is placed into the capsular bag within the posterior chamber (posterior chamber intraocular lens).
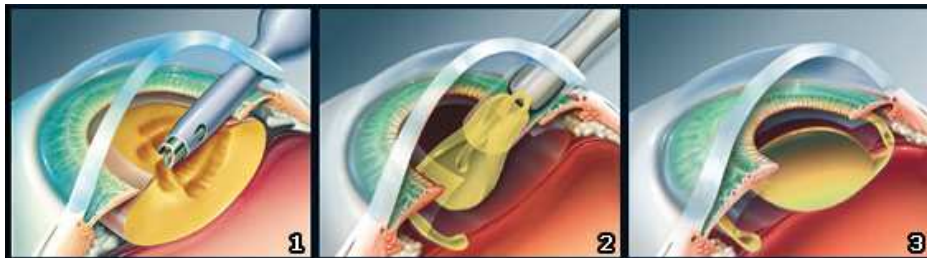
Figure 2-19: Cataract Surgery
Reference: http://www.gesundheitssprechstunde.ch

Phakia is the presence of the natural crystalline lens. *Aphakia* is the absence of the natural crystalline lens, either from natural causes or because it has been removed. *Pseudophakia* is the state of the eye after the natural lens has been substituted by an artificial intraocular lens. Cataract surgery has been practiced for over 2000 years – the human lens was extracted, leaving the eye aphakic. Modern cataract surgery started with the first implantation of an IOL by Sir Harold Ridley in the year 1949. A review of the evolution of intraocular lenses is given by Auffarth et al. (Auffarth and Apple 2001).

2.4.3 Lens Based Refractive Surgery

Intraocular lenses can also be used for correcting ametropia. If the crystalline lens is removed and replaced with an intraocular lens similar to cataract surgery, the procedure is called *clear lens extraction* (CLE). This is typically done for elder patients with high refractive errors and has the same side effects as cataract surgery such as loss of accommodation. The other possibility is to implant a lens in addition to the crystalline lens (Figure 2-20). These lenses are called *phakic intraocular lenses* (P-IOLs); they have the advantage that the eye still can accommodate. According to their position and fixation strategy there are different types of phakic lenses. There are phakic anterior chamber IOLs that are placed in between the posterior cornea and the iris, either angle-supported or iris-supported. The iris-supported lenses are attached by claws to the iris by a technique called enclavation (e.g. Verisyse, Advanced Medical Optics, Inc. (USA) and Artisan, Ophtec Inc. (USA), respectively). And there are phakic posterior chamber IOLs that are positioned in between the iris and the crystalline lens (e.g. Visian ICL[2], STAAR, USA). The first phakic intraocular lenses were implanted in the 1950s by Strampelli (Strampelli 1961) and Barraquer (Barraquer 1958). Due to severe complications the method was discontinued until Baikoff et al. revived the method in 1987 (Baikoff and Joly 1990). An overview about P-IOLs is given by Kohnen et al. (Kohnen, Baumeister et al. 2005).
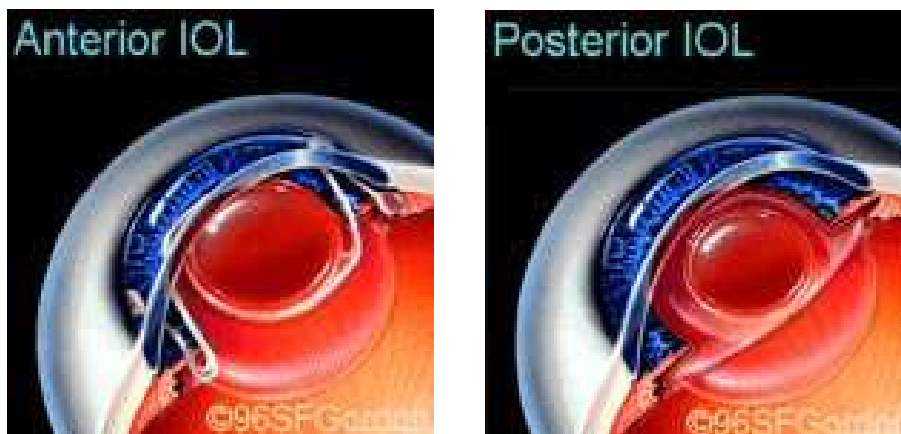
Figure 2-20: Lens based refractive surgery (phakic IOLs)

2.5 Ray Tracing in Ophthalmology

Ray tracing has been used in ophthalmology to address various issues. First of all one has to distinguish between investigations using paraxial ray tracing in contrast to real ray tracing. Maguire et al. used paraxial ray tracing in combination with measured corneal topography to assess optical properties (Camp, Maguire et al. 1990; Maguire, Zabel et al. 1991). Popiolek-Masajada et al. used paraxial ray tracing to analyze their model eye (Popiolek-Masajada and Kasprzak 2002). Theoretical simulations concerning ablation profiles without measured

---

[2] Some confusion seems to exist in the current use of the abbreviation ICL. In this product name, the abbreviation likely stands for "implantable collamer lens" and refers to the lens material. However, most authors seem to abbreviate "intraocular contact lens" with ICL as a synonym for P-IOLs; also "implantable contact lens" or "internal contact lens" occurs.

topography were done by Manns et al. based on paraxial optics (Manns, Ho et al. 2002). Ishikawa et al. used paraxial ray tracing for IOL calculation (Ishikawa, Hirano et al. 1998; Ishikawa, Hirano et al. 2000a; Ishikawa, Hirano et al. 2000b; Ishikawa, Hirano et al. 2000c), as well as Norrby et al. (Norrby 2004; Norrby, Lydahl et al. 2005). Langenbucher et al. provided calculation methods based on paraxial ray tracing for calculation of toric and phakic IOLs and the assessment of other optical properties (Langenbucher, Reese et al. 2004; Langenbucher and Seitz 2004; Langenbucher, Szentmary et al. 2007; Langenbucher, Viestenz et al. 2007). Bueeler et al. used paraxial ray tracing to assess shifts of ocular reference axes in model eyes in the context of refractive surgery (Bueeler, Iseli et al. 2005).

Also real ray tracing has been used and actually became more popular in the past few years since modern personal computers easily provide the computational power needed for realistic simulations. There is literature about actually calculating optical components with real ray tracing like calculating IOLs (Pomerantzeff, Pankratov et al. 1985; Naeser 1997; Preussner and Wahl 2000; Horiuchi and Akagi 2001b; Horiuchi and Akagi 2001a; Preussner, Wahl et al. 2001; Preussner, Wahl et al. 2002; Preussner, Wahl et al. 2003; Preussner, Wahl et al. 2005). The studies of Preussner et al. are principally based on measured corneal topography data. This will be discussed more detailed in the context of IOL calculation in section 5.1.

Since advanced IOL designs like aspherical IOLs are investigated more literature is emerging using real ray tracing to assess the optical properties of pseudophakic eyes with special regard to the wavefront aberration. There is literature investigating IOL designs (mainly spherical versus aspherical) with real ray tracing without use of corneal topography data (Atchison 1991; Werner and Roth 1999; Altmann, Nichamin et al. 2005; Dietze and Cox 2005; Marcos, Barbero et al. 2005; Franchini 2006; Tabernero, Piers et al. 2007) while others explicitly use measured corneal topographies (Holladay, Piers et al. 2002; Wang and Koch 2005; Tabernero, Piers et al. 2006; Marcos, Rosales et al. 2007; Piers, Weeber et al. 2007; Rosales and Marcos 2007); some studies additionally included polychromatic effects (Franchini 2006; Piers, Weeber et al. 2007). Franchini et al. used real ray tracing to study different lens edge designs by analyzing reflected glare images (Franchini, Gallarati et al. 2003). Ho et al. investigated accommodating IOLs using real ray tracing (Ho, Manns et al. 2006). IOL related literature using real ray tracing is discussed in more detail in the context of aspherical IOL calculation in section 5.2.

Real ray tracing has also been used in the context of corneal refractive surgery. Klonos et al. did some early investigation of PRK ablation profiles in a model eye with a gradient-index distribution of the lens analyzed with real ray tracing (Klonos, Pallikaris et al. 1996). Ortiz et al. used real ray tracing for choosing the optimal ablation parameters from individualized eye models (Fernandez del Cotero, Moreno et al. 2001; Ortiz, Saiz et al. 2002; Ortiz, Saiz et al. 2003). Most studies using real ray tracing in the context of simulating and analyzing ablation profiles for refractive surgery are mainly focused on corneal wavefront aberration and all include measured corneal topography data (Schwiegerling and Snyder 2000; Marcos, Barbero et al. 2001; Viestenz, Seitz et al. 2001; Marcos, Cano et al. 2003; Preussner and Wahl 2003; Cano, Barbero et al. 2004; Somani, Tuan et al. 2004; Yi, Iskander et al. 2006; Tabernero, Klyce et al. 2007). They are discussed in more detail in the corresponding section 5.3.

There are other studies not directly IOL or refractive surgery related. Greivenkamp et al. used real ray tracing for the analysis of schematic eyes (Greivenkamp, Schwiegerling et al. 1995). Also Liou et al. used real ray tracing to analyze their schematic eye (Liou and Brennan 1997). Fink et al. simulated human optics with real ray tracing (Fink, Frohn et al. 1996a; Fink, Frohn et al. 1996b; Fink and Micol 2006). Others did investigations using real ray tracing based on measured corneal topography data (Garcia 2000; Barbero, Marcos et al. 2002; Carvalho 2002; Langenbucher, Sauer et al. 2003). Sarver et al. also used corneal topography data and are

principally capable of calculating optical components with their Visual Optics Lab[3] program (Sarver and Applegate 2000). Norrby recently analyzed the Dubbelman model eye using real ray tracing (Norrby 2005). Only few authors did real ray tracing calculations including a gradient index model of the human crystalline lens (Klonos, Pallikaris et al. 1996; Davis 1999; Breidegard, Gustafsson et al. 2000; Siedlecki, Kasprzak et al. 2004; Seiler and Koller 2005; Navarro, Gonzalez et al. 2006).

While some authors use own programs for ray tracing, others use commercially available optical design programs from technical optics for their calculations. Popular examples are ASAP (Breault Research Organization, Inc., USA), CODE V (Optical Research Associates, USA), OSLO (Lambda Research Corporation, USA), or ZEMAX (ZEMAX Development Corporation, USA). These programs are especially useful when needing advanced features like ray tracing a gradient index lens for simulating a human crystalline lens. When only pseudophakic eyes with IOLs providing a homogeneous refractive index are considered, this feature is not needed.

---

[3] Commercial variants based on this as VOL-Pro and VOL-CT (former CTView) are sold by Sarver and Associates, Inc. (USA; http://saavision.com).

3 Development of the Individual Virtual Eye

This section describes the construction of a computer model of the human eye. The purpose of this virtual eye is to analyze and simulate the optical properties of the eye as well as each of its optical elements. The computer technical implementation of the optical components is described as well as the methods for calculations and optimizations based on real ray tracing. Using measured biometric geometry of human eyes an individual virtual eye can be constructed.

3.1 Components

3.1.1 Anterior Cornea

The anterior cornea is the most dominant refracting surface of the human eye. For the virtual eye, this surface can either be a theoretical model surface or it can be based on measured patient data. The latter is more relevant in view of the upcoming era of individualized surgery.

Model

As discussed on page 17, there are several mathematical options to describe the corneal surface. To be able to model both, toricity and asphericity, a biconic surface was used for the virtual eye:

$$z(x,y) = \frac{\frac{x^2}{R_x} + \frac{y^2}{R_y}}{1 + \sqrt{1 - \frac{(1+Q_x)x^2}{R_x^2} - \frac{(1+Q_y)y^2}{R_y^2}}} = \left[\frac{f(x,y)}{g(x,y)} \right] \tag{3-1}$$

R_x: radius of curvature in x direction
R_y: radius of curvature in y direction
Q_x: asphericity in x direction
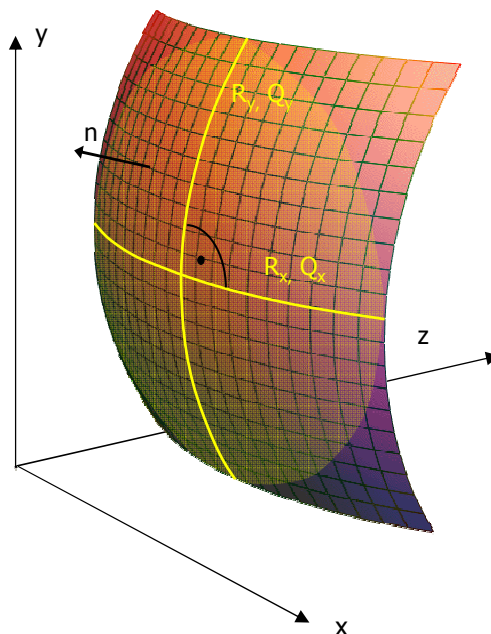Q_y: asphericity in y direction

Figure 3-1: Biconic surface

33

Two radii of curvatures and two corresponding asphericities are used for specification (Figure 3-1). Each pair of radius and asphericity describes one conic section (marked yellow); the two conic sections are perpendicular to each other. For $R_x = R_y$ and $Q_x = 0$ and $Q_y = 0$, the formula describes a sphere. For $R_x \neq R_y$ and $Q_x = 0$ and $Q_y = 0$, the formula is similar (though not identical) to a part of a torus. For $R_x = R_y$ and $Q_x = Q_y$ and $Q_y \neq 0$, the formula is identical to a conicoid. The axis of an astigmatic eye does not have to lie exactly on the x or y axis; this is handled by simple variable substitution that is equal to a local coordinate transformation by a rotation matrix. The numerator $f(x,y)$ and denominator $g(x,y)$ of the biconic formula can both be derived. Partial derivative after x:

$$\frac{f'(x,y)}{\partial x} = \frac{2x}{R_x} \tag{3-2}$$

$$\frac{g'(x,y)}{\partial x} = \frac{-(1+Q_x)x}{R_x^2 \sqrt{1 - \frac{(1+Q_x)x^2}{R_x^2} - \frac{(1+Q_y)y^2}{R_y^2}}} \tag{3-3}$$

Partial derivative after y:

$$\frac{f'(x,y)}{\partial y} = \frac{2y}{R_y} \tag{3-4}$$

$$\frac{g'(x,y)}{\partial y} = \frac{-(1+Q_y)y}{R_y^2 \sqrt{1 - \frac{(1+Q_x)x^2}{R_x^2} - \frac{(1+Q_y)y^2}{R_y^2}}} \tag{3-5}$$

By use of the quotient rule

$$z' = \left(\frac{f}{g}\right)' = \frac{f'g - g'f}{g^2} \tag{3-6}$$

the biconic formula can easily be derived using $f'(x,y)$ and $g'(x,y)$. This enables the calculation of the surface normal at oblique positions, which is crucial for the ray-surface intersection calculations necessary in the ray tracing process.

Measured Data

The anterior cornea can be alternatively constructed from measured data from videotopography measurements. This is of particular clinical relevance. Common to all topography systems using Placido rings is the analysis of the ring positions from the center of the topography along meridians. In this thesis, data from a C-Scan (Technomed GmbH, Germany) and a prototype of a new topography system developed in cooperation with the University eye hospital (Division "Experimental Ophthalmic Surgery") was used, soon commercially available as OphthaTOP (OphthaSWISS AG, Switzerland). Both systems use 360 meridians (1-degree steps) and analyze 30 respectively 32 ring edges. The raw measurement data of the corneal elevation is thereafter given as values at discrete measurement positions, aligned along meridians as shown in Figure 3-2. For the ray-tracing procedure, there has to be the possibility to determine the surface elevation and the surface normal at oblique positions – not only at the discrete measured positions. The interpolation schema used is described in the next paragraphs.
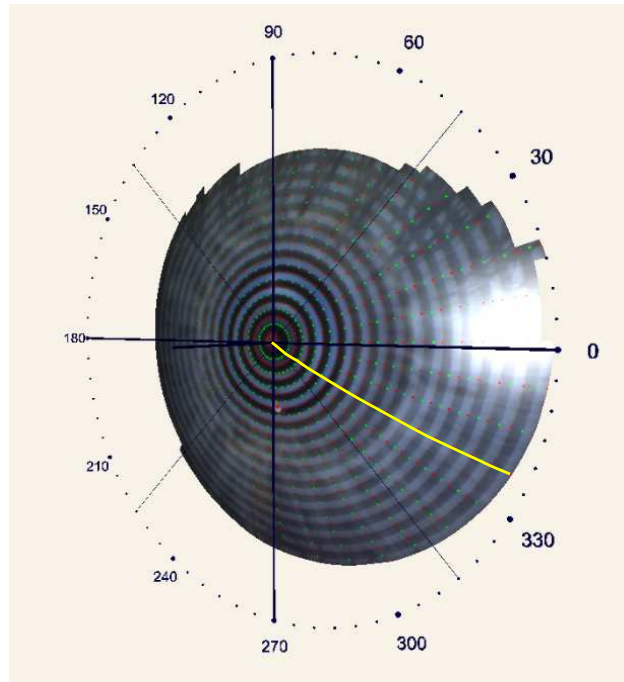
Figure 3-2: Discrete measurement point distribution along meridians

Figure 3-3 shows one semi-meridian consisting of measured points. At $r = 0$ the vertex point is added. Without loss of generality only two rings are shown. A functional cubic spline interpolation is performed for each single semi-meridian. Two constraints are set: at the vertex point the first derivative of the spline function is set to zero; at the last ring edge the second derivative is set to zero. As a result of the first constraint the surface normal at the vertex always coincides with the z-axis. This spline interpolation leads to a function $z_{spline}(r)$ and their derivative $z_{spline}'(r)$ that can be evaluated at oblique radii r.
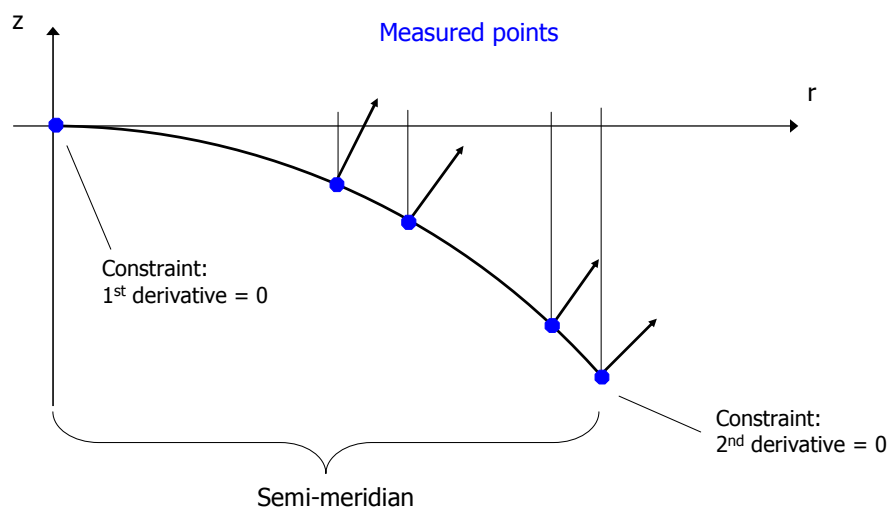
Figure 3-3: Spline interpolation of semi-meridian

35

Figure 3-4 outlines the calculation of an *elevation z* at an oblique position:
1. Calculation of the elevations z_1 and z_2 via $z_{spline}(r)$ of adjacent meridians with the same radius r (This is important, because the measurement points are usually not aligned at the same radius r – this would be only the case when the cornea is exactly rotationally symmetric.)
2. Calculation of the elevation z as a linear interpolation along the circular arc
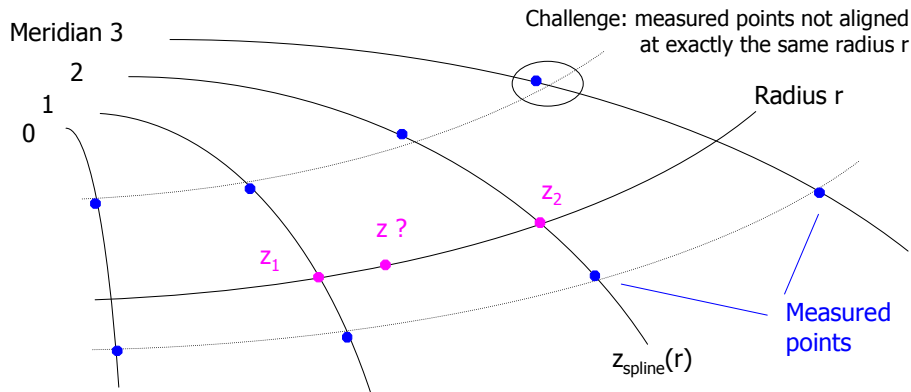
Figure 3-4: Calculation of surface elevation

Figure 3-5 outlines the calculation of a *surface normal* **n** at an oblique position:
1. Calculation of the surface normals **n₁** and **n₂**:
    a. Meridonal: via the derivative $z_{spline}'(r)$ of adjacent meridians
    b. Radial: via a parabolic interpolation of adjacent elevations
2. Calculation of the surface normal **n** as a linear vector-interpolation of **n₁** and **n₂**
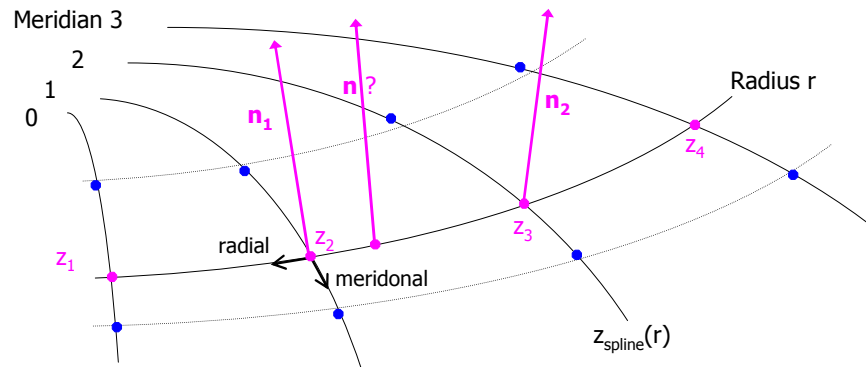
Figure 3-5: Calculation of surface normal

This interpolation schema was used for several reasons. For visualization properties the corneal measurement points can be used to construct a triangle mesh. Rendering of this triangle mesh can be easily done; for shading purpose the triangle normals and vertex normals are calculated in a straight forward manner: the vertex normals are calculated by averaging the adjacent triangle normals – fast and sufficient for rendering purpose. However this approximation of surface normals turned out to be not exact enough for ray-tracing purpose with respect to the optical properties of such a corneal surface. Apart from that the surface elevation and normal were only available in the measurement points. For these reasons the simple triangle mesh approximation was not applicable. Another approach would be the approximation of the elevation data by Zernike polynomials, for example. Once fitted, these functions provide elevation and normals in a fast and elegant way. However it has to be assured, that enough Zernike-coefficients are used so that die approximation is exact enough. Anyway it remains an approximation. For these reasons the outlined interpolation schema was used to stick as close to the measured values as possible. The spline interpolation of the semi-meridians is done in a pre-processing step once. No computationally expensive calculations are necessary in time-critical procedures. This is an important issue since ray-surface intersection calculations dominate the ray-tracing calculations.

3.1.2 Posterior Cornea

The difference of refraction indices at the anterior corneal surface between air and stroma is much bigger than the difference between stroma and aqueous humor at the posterior cornea (Figure 3-6). Talking in terms of paraxial optics, in an average human eye the anterior cornea has an approximate refractive power of +48 D while the posterior has -6 D (Atchison and Smith 2000) [p. 13]. Therefore the anterior cornea is very dominant with respect to the posterior – but nevertheless the posterior cornea is not negligible. In the virtual eye, it is modeled just as the anterior cornea: either as a theoretical biconic surface or as spline-interpolated measured data.

+48 D

-6 D

Air
1,0

Stroma
1,376

Aqueous humor
1,337   <- Indices of refraction

Corneal
thickness

Anterior cornea
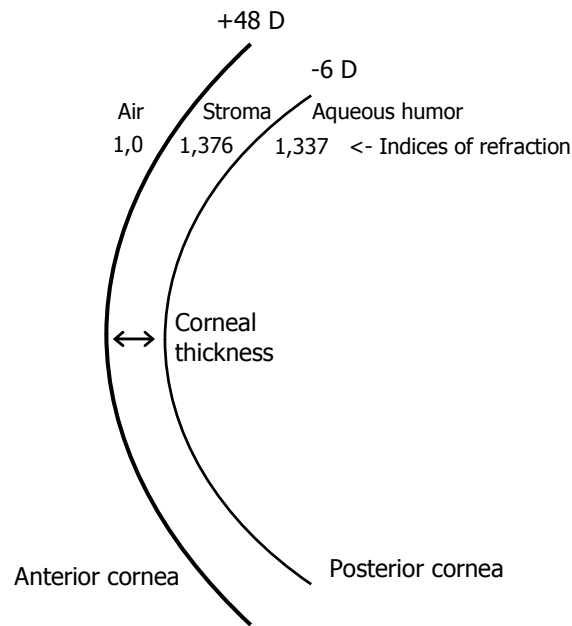
Posterior cornea

Figure 3-6: Posterior cornea

3.1.3 Pupil

The virtual pupil restricts the number of light rays entering the virtual eye. In principle, the pupil could be represented by modeling the iris. However it is more practical to use the entrance pupil as described in the context of the ray-tracing procedure in section 3.2.1.

3.1.4 Lens

The virtual lens is defined by two refracting surfaces, a thickness and the refractive index of the lens' material (Figure 3-7). The surfaces are both modeled by the already introduced formula for a biconic surface. While a standard spherical lens is restricted to consist of spherical surfaces, the modeling with a biconic surface allows for various possibilities:

- Toric lenses can be modeled by using different radii R_x and R_y.
- Aspherical lenses result from using non-zero values for Q.
- Design issues can be assessed, like biconvex or planoconvex lens design.

Toric and aspherical surfaces can be used for the anterior surface, the posterior surface – or both. Lenses can be designed either symmetric or asymmetric and so on. The direction of the toricity, the axis, is controlled by variable substitution as for the theoretical cornea.

38
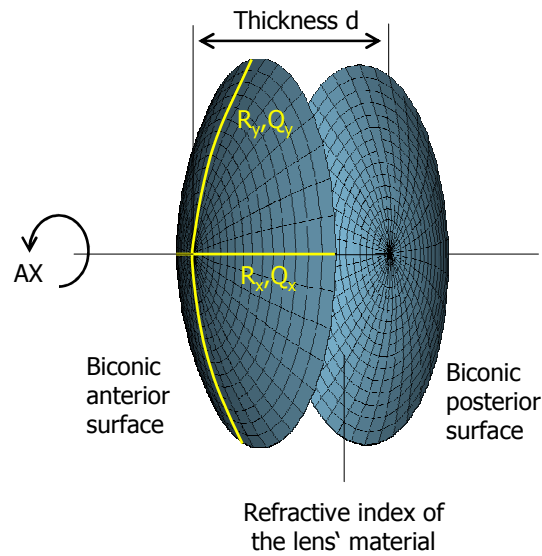
Figure 3-7: Virtual lens

As it is an important issue how well an intraocular lens is positioned in a pseudophakic eye, the position of the lens is not only defined by the distance from the cornea, but additionally a tilt and decentration of lens can be defined, if desired (see Figure 3-8). The decentration is defined by two offset values, one for the *x* and one for the *y* direction. The tilt is defined by a rotation around the tilt axis by an angle *β*. This tilt axis is the axis parallel to the *x* axis traveling through the midpoint of the lens – optionally rotated by an angle *α* around the *z* axis. (Note that if a lens is both decentered and tilted at a time, the tilt is still a rotation around the lens' midpoint.)
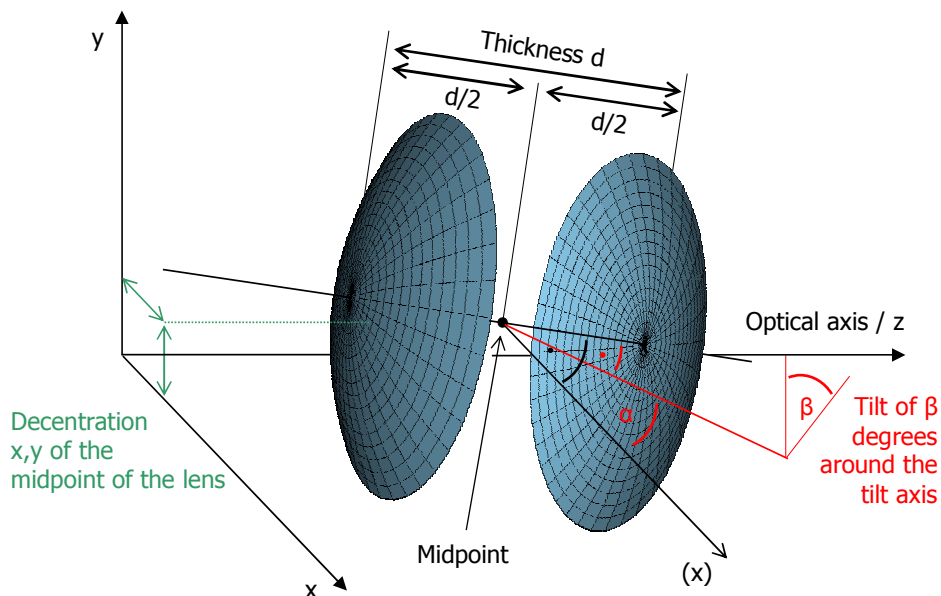
Figure 3-8: Tilt and decentration of the virtual lens

39

The human crystalline lens is more sophisticated than this model, since it has no uniform refractive index and it has the ability to accommodate. Thus if it is the goal to simulate a human crystalline lens, this representation would be only a rough approximation. However this representation of the lens is fine for artificial intraocular lenses; this is at the same time highly relevant as virtually everyone will once be a cataract patient.

3.1.5 Spectacles

Virtual spectacles are in principle modeled the same way as the virtual lens, consisting of two refracting surfaces, a thickness d_{spec} and refractive index n_{spec}. The anterior surface is constraint to be purely spherical with a radius R_{sph}. The posterior surface is modeled as a biconic just as the virtual lens with one radius R_{cyl} in a direction specified by AX in degrees, while the radius perpendicular is very large near infinity – this results in a purely cylindrical surface (Figure 3-9). This spectacle is positioned in front of the anterior cornea at vertex distance. The clinical spectacle refraction (*SPH / CYL x AX*, see page 24) can be transformed into geometric quantities needed for this virtual spectacle with the following formulae derived from paraxial optics:

$$R_{sph} = \frac{n_{spec} - 1}{SPH} \tag{3-7}$$

$$R_{cyl} = \frac{(n_{spec} - d_{spec})(n_{spec} - 1)}{-n_{spec} AST} \tag{3-8}$$

R_{sph} [m]: radius of curvature of anterior surface
R_{cyl} [m]: radius of curvature of anterior surface
d_{spec} [m]: thickness of spectacle
n_{spec}: refractive index of spectacle
SPH / CYL x AX: spectacle refraction

This conversion is applicable for both, plus- and minus-cylinder notation and AX for the virtual spectacle is the same as from spectacle refraction.
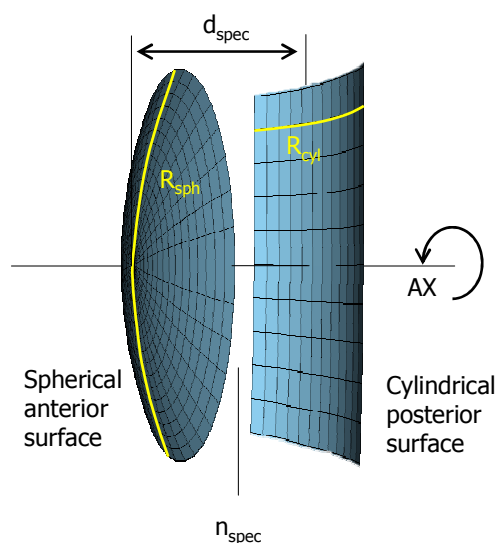
Figure 3-9: Virtual spectacles

40

3.2 Ray Tracing for Optical Quality Assessment

A point in object space is projected onto the virtual retina. This is done by sending a number of light rays through the virtual eye. Each ray is traced, and at every surface the ray is refracted according to Snell's law. Finally all rays hitting the virtual retina form a spot diagram and the size of the spot can be quantified. Alternatively the wavefront error can be calculated and used for quantification of the optical properties.

3.2.1 Ray Distribution and Pupil

The light rays are emitted from a light point source. In principle, this light source can be located anywhere in object space. However it is the most common case that this light source is assumed to be located in infinite distance from the eye; this corresponds to the simulation of distance viewing. In this case, the light rays can be assumed as a bunch of rays parallel to the *z*-axis. These rays are uniformly square sampled and first pass the optional virtual spectacles before they hit the anterior cornea. The pupil limits the amount of light entering the eye. As discussed on page 21 the entrance pupil is the image of the real pupil in object space. In the virtual eye these entrance pupil dimensions are used to determine whether a light ray is allowed to enter the eye or not. These dimensions can be either direct measurements (from a topography system, for example) or theoretical values. All rays falling outside this entrance pupil are neglected.

The Stiles-Crawford effect (Stiles and Crawford 1933) refers to the directional sensitivity of the cone photoreceptors of the human eye and can be simulated by an apodization filter placed at the pupil. Therefore the rays are weighted depending on their distance from the pupil center as a reasonable approximation according to equation (3-9) (Atchison and Smith 2000) [p. 125]. This weighting factor carried by each ray is considered when calculating the spot size or the wavefront error.

$$w(r) = \exp\left(-\beta \cdot r^2\right) \tag{3-9}$$

r [mm]: ray distance from pupil center
β: Stiles-Crawford coefficient

3.2.2 Ray-Surface Intersections and Refraction
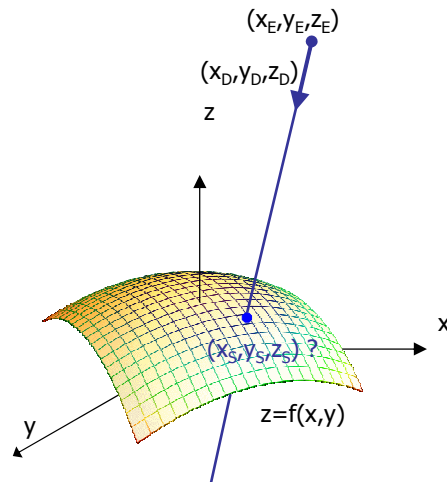
Figure 3-10: Ray-surface intersection

As the light rays travel through the virtual eye, the dominant task is to calculate intersections between rays and surfaces, calculating the surface normals and to finally determine the new direction of the ray according to Snell's law of refraction. All surfaces used in the virtual eye are described by a function $f(x,y)$ (Figure 3-10). A light ray emerging from a position E and traveling in the direction D can be written in parametric form as a function of t:

$$x(t) = x_E + tx_D$$
$$y(t) = y_E + ty_D \qquad \textbf{(3-10)}$$
$$z(t) = z_E + tz_D$$

The calculation of the parameter t_S that satisfies the following equation results in the intersection:

$$\text{Sought - after}: t_S$$
$$\underbrace{z(t_S) - f\big(x(t_S), y(t_S)\big)}_{g(t_S)} = 0 \qquad \textbf{(3-11)}$$
$$\Rightarrow \text{intersection } \big(x(t_S), y(t_S), z(t_S)\big)$$

When the surface specified by f is a sphere, the solution of equation (3-11) leads to a quadratic equation and can therefore be calculated algebraically in an efficient way. When f is the biconic formula, this leads to a 4th degree polynomial. The solution of this polynomial is a large formula and therefore a general numeric method was preferred: numeric root-finding via *Van Wijngaarden-Dekker-Brent's Method* (Press 1992) [p. 359 ff.]. This method needs no derivative of the function g what makes it applicable even when the function f results from a spline-interpolated measured cornea (as described on page 34). In this case the derivative of the function g is not directly available.

Once the intersection with a surface is determined, the surface normal is calculated. With the direction of the ray before refraction **i**, the surface normal **n** and the refractive indices n_1 and

n_2 of the two media that are separated by the surface, the new direction **o** of the ray after refraction can be calculated (Figure 3-11). Therefore the vectorial form of Snell's law is used:

$$\mathbf{o} = \left(\frac{n_1}{n_2}\right)\mathbf{i} + \left(\cos\theta_2 - \frac{n_1}{n_2}\cos\theta_1\right)\mathbf{n}$$

$$\cos\theta_1 = \mathbf{i} \cdot \mathbf{n} \qquad\qquad \textbf{(3-12)}$$

$$\cos\theta_2 = \sqrt{1 - \left(\frac{n_1}{n_2}\right)^2\left(1 - (\cos\theta_1)^2\right)}$$

This representation has the advantage that the cosines of the angles do not have to be calculated making it an elegant way of calculating Snell's law in three dimensional space.
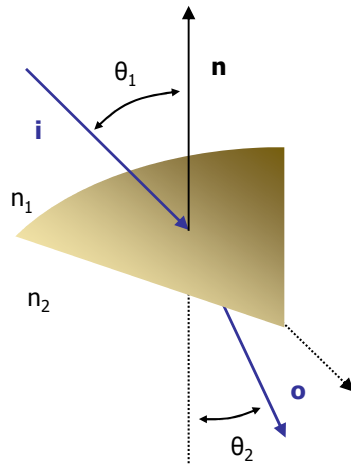
Figure 3-11: Snell's law in three dimensions

3.2.3 Calculation of Spot Size
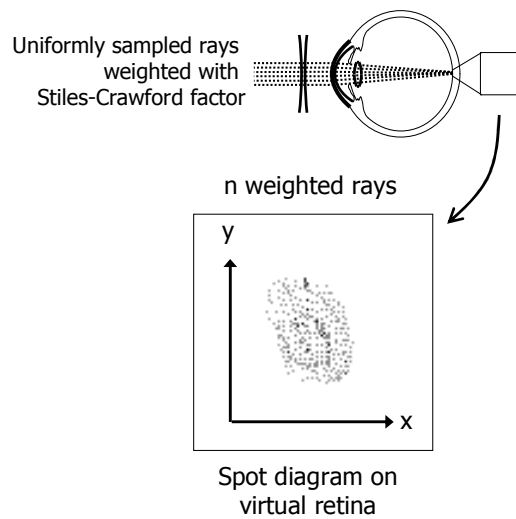
Figure 3-12: Spot diagram

Once the rays traced through the virtual eye have passed all refracting surfaces (spectacles, cornea and lens) they finally hit the virtual retina. While a real retina has some radius of curvature, the virtual retina is assumed to be a plane as a reasonable approximation. The intersections of all rays with this retinal plane form a spot diagram (Figure 3-12). In case of a perfect optical system (in terms of geometrical optics) free from aberrations a point in object space would be projected onto a point in image space (the retina). Therefore all rays emerging from the point light source, then traced through the virtual eye would finally strike the retina in one point of infinitesimally small size. The more the optical system deviates from the ideal state the bigger the spot size is. From the two-dimensional spot diagram the RMS spot size (see also section 2.1.3) can be calculated ("OSLO Manual" 2001) [p. 178 f.]:

$$\text{RMS spot size}: \sigma = \sqrt{\sigma_x^2 + \sigma_y^2}$$

$$\text{Variances}: \sigma_x^2 = \frac{1}{W} \sum_{i=1}^{n} w_i (x_i - \bar{x})^2$$

$$\sigma_y^2 = \frac{1}{W} \sum_{i=1}^{n} w_i (y_i - \bar{y})^2$$

$$\text{Weighted averages}: \bar{x} = \frac{1}{W} \sum_{i=1}^{n} w_i x_i$$

$$\bar{y} = \frac{1}{W} \sum_{i=1}^{n} w_i y_i$$

$$\text{Summed weights}: W = \sum_{i=1}^{n} w_i$$

(3-13)

n: number of rays traced
w_i: weighting factor for each ray

The weights for each ray according to equation (3-9) enables the incorporation of the Stiles-Crawford factor as described.

3.2.4 Calculation of Wavefront Aberration

Another often used quantification of the optical quality is the wavefront aberration or the RMS wavefront error (see section 2.1.3). The wavefront aberration is the offset of a spherical reference wavefront and the true aberrated wavefront (Figure 3-13). This wavefront aberration can be calculated as follows: first, the intersections of the rays with a sphere representing the reference wavefront are calculated. Then the *optical path length* (OPL) to these intersections is calculated as the geometric path length multiplied with the refractive index of the corresponding medium. The difference of the OPL of each ray is calculated with respect to a reference OPL. This results in a wavefront aberration function that can be used to calculate the RMS wavefront error or that can be approximated by Zernike polynomials via least square fitting. In both latter cases a weighting of the rays is possible just as in the case of calculating the RMS spot size.
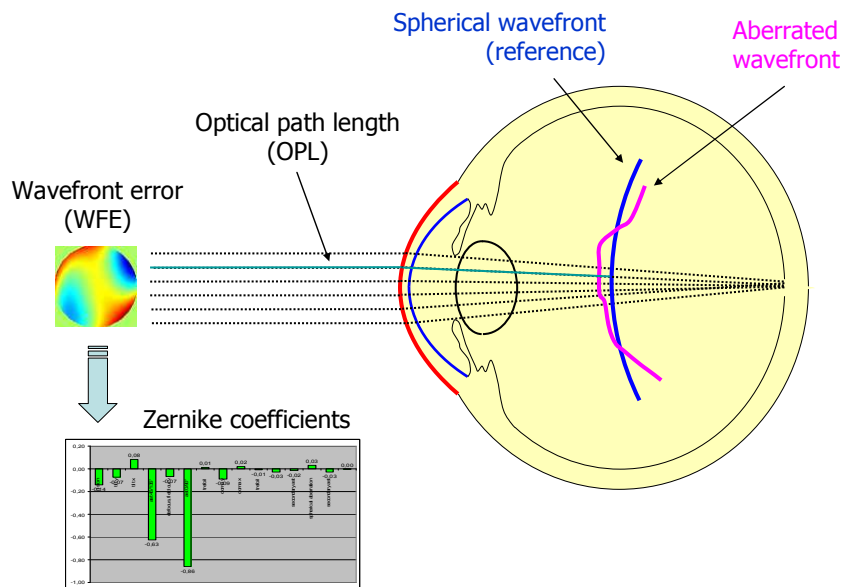
Figure 3-13: Calculation of the wavefront aberration

3.3 Optimization for Optical Component Calculation

The optimization procedure is the key process for the calculation of optical components in the virtual eye. A function $F(v_1, v_2, ...)$ is constructed that receives some input variables v_i. These are the quantities that should be calculated. Each function evaluation is a complete ray-tracing iteration as described in the preceding section 3.2. The output of the function is the optimization criterion, either the RMS spot size or wavefront error. In an optimization process this function F is minimized, and therefore the aberrations are minimized. A general schematic overview of the optimization procedure using real ray tracing in the individual virtual eye is shown in Figure 3-14.
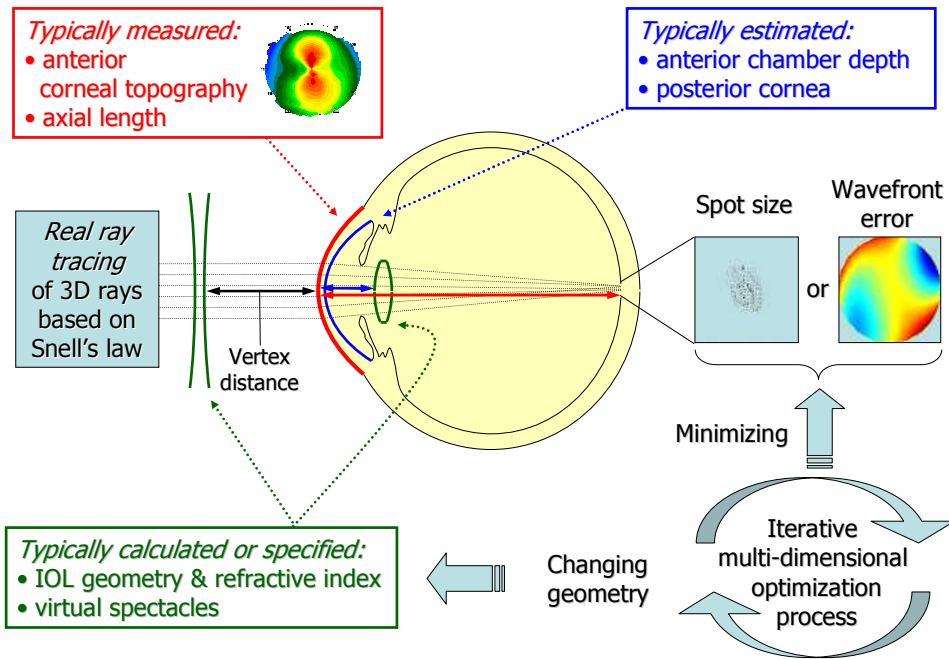
Figure 3-14: Real ray tracing in the individual virtual eye

If only one quantity needs to be calculated, this optimization procedure is one-dimensional. But sometimes more than one quantity has to be calculated; in this case a multi-dimensional optimization is to be performed. This is illustrated by the example of calculating an intraocular lens in Figure 3-15. Calculating a spherical lens results in the determination of only one radius thus in a one-dimensional optimization. Calculating an aspherical lens results in the determination of a radius and an asphericity, thus in a two-dimensional optimization. In the case of a toric lens two radii and one axis are to be determined, resulting in a three-dimensional optimization.
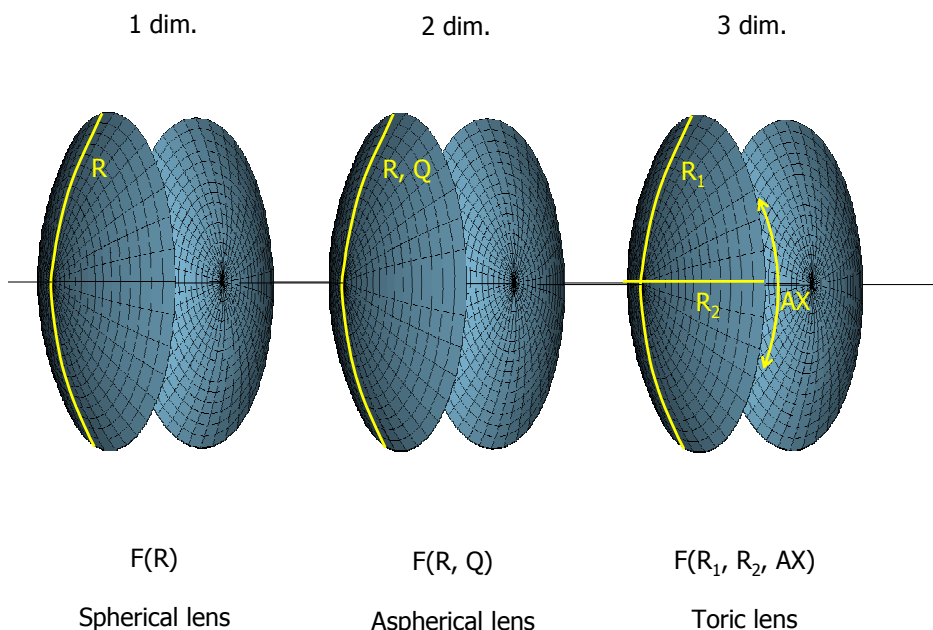
Figure 3-15: Example of one- and multi-dimensional optimization tasks

The function *F* that has to be minimized is nonlinear and no derivative is directly available. In general, the task of finding a global minimum of such a function is very difficult (Press 1992) [p. 394]. Sophisticated solution attempts include methods like genetic algorithms or adaptive simulated annealing and are, for example, implemented for the purpose of optimizing complex optical systems in commercial ray-tracing packages such as OSLO (Lambda Research Corporation, USA) ("OSLO Manual" 2001) [p. 220 ff.]. Although no formal proof is presented, it turned out that for the purpose of all calculations performed in this thesis an algorithm for finding the local minimum of the function *F* was sufficient. For the one-dimensional case *Brent's method* (Press 1992) [p. 402 ff.] was used. This algorithm combines a parabolic interpolation with the golden section algorithm and needs no derivative of the function *F*. The multi-dimensional minimization is done with *Powell's method* (Press 1992) [p. 412 ff.]. This method uses Brent's method as a sub-algorithm, thus also needs no derivative of *F*.

3.4 Technical Details and Calculation Time

The ray-tracing program was developed in the programming language C++, using Microsoft Visual Studio .NET 2003 and the operating system Microsoft Windows XP (Microsoft Corporation, USA) and is integrated in a videotopometer software (see Figure 1-1). All calculations were performed with a standard personal computer equipped with an Intel Pentium 4 2.6 GHz processor (Intel Corporation, USA).

Optimization Task 50 x 50 = 2500 rays per iteration	Cornea [1] & Lens (4 refracting surfaces)		Spectacle, Cornea [1] & Lens (6 refracting surfaces)	
	Iterations	Time [sec]	Iterations	Time [sec]
1 dim (spherical lens)	36	1.3	36	2.1
2 dim (aspherical lens)	53	2.1	55	3.5
3 dim (toric lens)	191	6.6	166	9.6
4 dim (toric aspherical lens)	240	9.0	258	15.6
	=> approx. 40 ms per iteration		=> approx. 60 ms per iteration	

[1] The cornea consists of two spline-interpolated surfaces.

Table 3-1: Example of calculation time for typical optimization tasks

The calculation time is highly dependent on the starting conditions, the number of rays traced, the number of refracting surfaces and the number of variables in the optimization process. Table 3-1 shows the typical number of iterations and calculation time for the example of calculating toric aspherical IOLs as in section 5.2.

4 Verification of the Individual Virtual Eye

4.1 Introduction

The capabilities of RRT in the individual virtual eye were first tested with the geometry data of real eyes. Pseudophakic eyes were chosen to eliminate the unknown factor crystalline lens. The goal of this chapter is to see, if the manifest refraction can be simulated or predicted by RRT in the individual virtual eye using the measured geometry. This is the precondition of further applications of the RRT method.

4.2 Methods

	30 Eyes of 28 Patients
	Mean ± SD (Range)
Age	69.2 ± 9.3 (46-82) years
Axial length (IOLMaster)	23.65 ± 1.03 (21.04-25.77) mm
Axial length (optical, retransformed)	23.82 ± 0.98 (21.34-25.84) mm
Pre-op ACD (IOLMaster)	3.28 ± 0.43 (2.25-4.32) mm
Sim K [1] (C-Scan 1.0-1.5 mm)	7.80 ± 0.27 (7.15-8.41) mm
K-readings [1] (manual keratometer)	7.77 ± 0.25 (7.11-8.33) mm
K-readings [1] (IOLMaster)	7.74 ± 0.28 (7.11-8.39) mm
Corneal astigmatism (sim K)	0.84 ± 0.74 (0.05-2.82) D
Corneal asphericity Q (flat axis, 3.5 mm diameter)	0.22 ± 0.63 (-0.90 to 1.70)
Power of implanted IOL (SA60AT)	20.95 ± 2.18 (17-27) D
Post-op ACD (predicted, including corneal thickness)	4.52 ± 0.20 (4.01-4.92) mm

[1] mean values of flat and steep meridian

Table 4-1: Baseline patient data

30 eyes of 28 patients who had cataract surgery without any complications at the University Eye Hospital Tübingen were evaluated. This set of patients does not include eyes with abnormalities like refractive treatment (see Table 4-1 for statistics). In all cases an AcrySof SA60AT (Alcon Laboratories, Inc., USA) intraocular lens was implanted. The anterior corneal surface was measured postoperatively with a C-Scan (Technomed GmbH, Germany) videotopography system. The posterior corneal surface is approximated from the anterior surface by a simple transformation of the axial curvature map using a constant back-to-front ratio. Refractive indices were assumed according to Gullstrand's model eye; for other ray-tracing parameters see Table 4-2. The attempt to measure the pseudophakic lens position exactly with the IOLMaster (Carl Zeiss Meditec AG, Germany) failed. This is in agreement with the manual (IOLMaster user's guide 2004) [p. 74] and has been observed by others, too (Auffarth, Martin et al. 2002; Kriechbaum, Findl et al. 2003). Therefore the postoperative lens position was estimated from axial length using regression data based on PCI measurements of the SA60AT lens (Preussner, Wahl et al. 2004) (in contrast to Preussner et al, who exclude corneal thickness, the more common definition of ACD to be the distance from the anterior cornea to the anterior lens surface is used in this thesis). The geometry of the IOL was used according to the manufacturer's specification consisting of anterior and posterior radius of curvature, thickness and refractive index. Axial length was measured preoperatively with the IOLMaster. According to the manual, the axial length output of the IOLMaster is calibrated

against acoustic measurement devices (immersion ultrasound) which measure the length to the inner limiting membrane. For ray tracing the optical length to the retinal pigment epithelium is needed (see Figure 2-9), which is in fact measured internally by the IOLMaster with PCI and therefore can be retransformed from acoustical length (Haigis, Lege et al. 2000; Preussner, Wahl et al. 2002; Olsen 2007). For the following calculations the retransformation according to Olsen et al. is used (Olsen and Thorwest 2005). When comparing to the manifest refraction the ray-tracing simulation must ideally use the exact pupil dimensions at the time of refraction. Due to the lack of this information ray-tracing calculations were performed with three different pupil sizes using feasible values of 3.5, 3.0 and 2.5 mm in diameter (Atchison and Smith 2000) [p. 24]; (Mester, Dillinger et al. 2003). A virtual spectacle was placed in front of the cornea. The iterative three-dimensional minimizing process of the RMS spot size as described in section 3.3 and shown schematically in Figure 3-14 results in the geometry of best corrected spectacles. From the spectacle geometry the values for sphere, cylinder and axis (SPH, CYL and AX) can be calculated as described on page 40. These values obtained from ray tracing will be further referred to as *predicted refraction* and compared to the *manifest refraction* determined several weeks postoperatively with a manual refractor. The relative difference is named *refraction difference*.

Parameter	Value
Refractive index cornea / aqueous humor / vitreous humor	1.376 / 1.336 / 1.336 (Helmholtz, Gullstrand et al. 1909) [p. 300]
Corneal back-to-front ratio	0.81 (Atchison and Smith 2000) [p. 12]
Corneal thickness	0.50 mm
Number of rays traced per iteration	50 * 50 = 2500
Spectacle vertex distance	12.00 mm
Stiles-Crawford weighting factor	according to equation (3-9) with β = 0.12

Table 4-2: Ray-tracing parameters

4.3 Results

Results of predicted versus manifest refraction are summarized in Table 4-3. Figure 4-1 shows scatter plots of SPH, CYL and AX and the *spherical equivalent refraction* (SEQ) for the 3.0 mm pupil. For AX only 22 eyes having a CYL > 0.5 D were compared. All variables show linear dependence and significant correlation. The refraction difference shows noticeable standard deviation but no great bias. The predicted refraction shows slightly more myopia than the manifest refraction for 3.5 and 3.0 mm pupil. For the 2.5 mm pupil there is negligible offset observed in the SEQ. The refraction difference for CYL tends to have greater standard deviation than SPH and SEQ. A dependence on the pupil size can be seen in Table 4-3. A widening of the simulated pupil in ray tracing from 2.5 to 3.5 mm in diameter results in an SEQ offset of approximately -0.2 D. On a standard state-of-the-art personal computer such a three-dimensional optimization process calculating SPH, CYL and AX is performed within a few seconds.

Pupil Diameter	3.5 mm		3.0 mm		2.5 mm	
	Mean ± SD (Range)	r [1]	Mean ± SD (Range)	r [1]	Mean ± SD (Range)	r [1]
SEQ (D)	-0.17 ± 0.52 (-1.27 to 1.15)	0.86	-0.13 ± 0.49 (-1.25 to 1.03)	0.88	0.02 ± 0.47 (-1.02 to 1.17)	0.89
SPH (D)	-0.09 ± 0.48 (-1.01 to 1.20)	0.89	-0.05 ± 0.45 (-0.86 to 0.96)	0.91	0.11 ± 0.43 (-0.76 to 1.09)	0.92
CYL (D)	-0.14 ± 0.58 (-1.78 to 1.09)	0.74	-0.17 ± 0.56 (-1.59 to 0.87)	0.76	-0.18 ± 0.52 (-1.57 to 0.71)	0.79
AX (°, n=22)	4.75 ± 27.00 (-39.00 to 67.00)	0.93	5.44 ± 30.07 (-40.00 to 77.00)	0.92	5.13 ± 30.19 (-41.00 to 81.00)	0.91

[1] Pearson's correlation index; all correlations: $P<0.01$ (analyzed with SPSS 13.0 for Windows, SPSS Inc., USA)

Table 4-3: Difference between RRT predicted refraction and manifest refraction
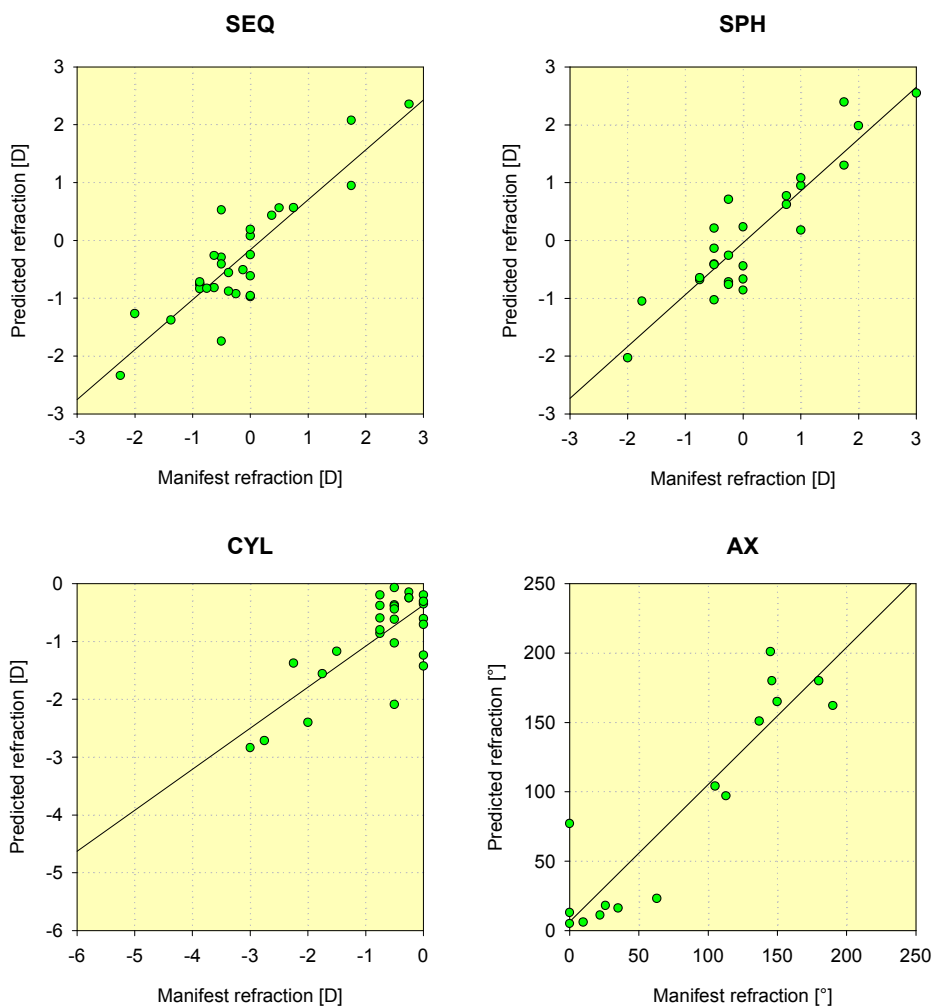

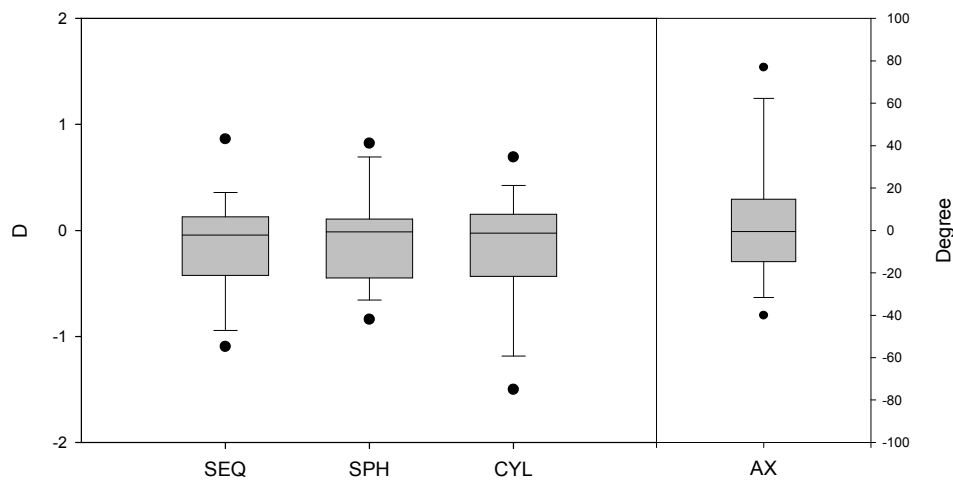**Figure 4-1: RRT3.0 predicted vs. manifest refraction**

Figure 4-2: Difference between RRT3.0 predicted and manifest refraction

4.4 Discussion

The ray-tracing implementation was tested by comparing the predicted refraction to the manifest refraction for a number of patients. Since the geometry of the implanted IOL is known the only estimated parameter is the lens position. Ideally the exact pupil dimensions at the time of manifest refraction have to be used in ray-tracing simulation. Due to the lack of this information, calculations were performed with three different pupil sizes using feasible values. Dependent on the pupil size slightly different results are observed. This is not surprising: The normal cornea has a positive spherical aberration. However implanting a standard IOL having positive spherical aberration (like the SA60AT) amplifies the resulting positive spherical aberration of the whole eye. The bigger the pupil is, the bigger the effect of positive spherical aberration resulting in a more myopic eye when simulated by ray tracing.

A general issue affecting the outcome of ray tracing calculations is the criterion chosen for minimization during the optimization process: the calculations in this section used the common approach of technical optics of minimizing the RMS spot size, which is similar to the RMS wavefront error (though not identical, see section 5.2). Apart from including the Stiles-Crawford factor no physiological factors are taken into account. Which criterion the human eye actually uses for optimum focusing is unknown (Atchison and Smith 2000) [p. 152]. Furthermore, assessing visual acuity or contrast sensitivity – including physiological factors from the retina and brain – is in general not possible from geometrical optical quantities alone. However, according to Applegate et al. there was a significant correlation between RMS wavefront error and the visual performance regarding contrast sensitivity as well as high and low visual acuity (Applegate, Hilmantel et al. 2000) – in a later study they confined their findings to relatively high levels of aberration, and found the RMS wavefront error to be no good predictor of visual acuity for low levels of aberration (Applegate, Marsack et al. 2003). Thibos et al. evaluate the influence of using different metrics when predicting a patient's subjective refraction based on wavefront measurements (Thibos, Hong et al. 2004). Further investigation is necessary to identify a potential benefit of using alternative metrics in ray tracing.

However, it is encouraging that the predicted refraction based on pure geometrical optics shows a correlation with the manifest refraction including physiological factors. Looking at the results in Table 4-3 the smallest mean refraction difference is near zero, observed at a pupil of 2.5 mm. But even at the other pupil sizes the results show a bias less than a quarter

52

diopter. The agreement of the manifest and predicted refraction showing no substantial offset is a precondition for the use of this method to calculate IOLs exactly. Furthermore this shows the capability of this ray-tracing implementation doing a multi-dimensional optimization which is the basis for the calculation of advanced IOL geometries with multiple degrees of freedom – like toricity and/or asphericity.

5 Applications of the Individual Virtual Eye

Three applications of the individual virtual eye and the RRT calculations will be provided in this chapter. The first two deal with the calculation of intraocular lenses while the third investigates ablation profiles used in laser refractive surgery.

5.1 Spherical Intraocular Lenses

5.1.1 Introduction

There are numerous formulae to calculate the IOL power for a patient undergoing a cataract operation. In the eighties the *SRK I* and *II* formulae were published (Retzlaff 1980; Sanders, Retzlaff et al. 1988). These are sometimes referred to as *first and second generation formulae* and are linear regression formulae based on empirics. The so-called *third generation formulae* are theoretical optical ones based on paraxial optics, more precise to the thin lens formula published by Fyodorov in the late sixties (Fedorov, Kolinko et al. 1967) and introduced in the german speaking area by Gernet et al. in 1970 (Gernet, Ostholt et al. 1970; Gernet 1990; Gernet 2001; Gernet 2003), therefore also known as *GOW70 formula*:

$$DL = \frac{n}{L-d} - \frac{n}{\frac{n}{z}-d}$$

$$\text{with } z = DC + \frac{ref}{1 - ref \cdot dBC}$$

$$\text{and } DC = \frac{nC - 1}{RC}$$

(5-1)

DL: IOL power
DC: corneal power
RC: corneal radius of curvature
nC: (fictious) corneal refractive index
ref: target refraction
dBC: spectacle vertex distance
d: optical ACD
L: axial length
n: refractive index of aqueous and vitreous humor

Popular examples principally relying on this thin lens formula are *SRK/T* (Retzlaff, Sanders et al. 1990), *Hoffer Q* (Hoffer 1993), *Haigis* (Haigis 1993a; Haigis 1993b) and *Holladay 1* (Holladay, Prager et al. 1988). Another current formula is the *Holladay 2* formula that is included in a software package sold commercially called Holladay IOL Consultant (Holladay Consulting, Inc., USA; http://www.docholladay.com). It is not published and therefore not included in the further comparisons. The goal of all formulae is to calculate an IOL power that leads to a desired target refraction for the patient after surgery. All these formulae are based on few input parameters: the central corneal power, the axial length and – in case of the Haigis formula – the preoperative anterior chamber depth.

These IOL calculation formulae are easy to use and produce satisfying results for normal eyes. The performance of the classical formulae is getting worse for corneas with an abnormal shape, for example resulting from previous refractive surgery. Implanting IOLs calculated with standard formulae for a patient with previous correction of myopia by LASIK, LASEK or PRK typically results in a *hyperopic shift* compared to the target refraction (Seitz, Langenbucher et al. 1999; Gimbel, Sun et al. 2000; Seitz and Langenbucher 2000; Gimbel and Sun 2001; Seitz, Langenbucher et al. 2002; Aramberri 2003; Hamilton and Hardten 2003; Jarade and Tabbara 2004; Langenbucher, Haigis et al. 2004; Wang, Booth et al. 2004). There

are several formulae trying to correct the outcome of the standard formulae in these cases. The most popular is the *clinical history method* (Hoffer 1995) but there are other established methods like the *Feiz and Mannis method* (Feiz, Mannis et al. 2001) or *Double-K method* (Aramberri 2003) which have in common that they use a clinical history of the patient. Other current methods not using clinical history are the *hard contact lens method* (Haigis 2003), the *modified maloney method* (Koch and Wang 2003; Wang, Booth et al. 2004) or the *regression method of Rosa* (Rosa, Capasso et al. 2002). The great number of correction methods reflects the medical need for corneas treated by refractive surgery as well as that there seems to be no perfect solution of this problem so far. The usage of correcting formulae becomes even more complicated when additionally considering hyperopic LASIK/LASEK/PRK and RK, since different types of refractive surgery modify the cornea in a different manner and may require specific corrections. This problem dealing with abnormally shaped corneas will become even more relevant in the future due to the growing number of refractive surgeries performed. This can be also seen when looking at the increasing number of recent publications dealing with this issue (Langenbucher, Torres et al. 2004; Sonego-Krone, Lopez-Moreno et al. 2004; Schafer, Kurzinger et al. 2005; Jin, Crandall et al. 2006; Mackool, Ko et al. 2006; Masket and Masket 2006; Walter, Gagnon et al. 2006; Qazi, Cua et al. 2007; Savini, Barboni et al. 2007; Shammas and Shammas 2007).

There is not very much literature using ray tracing for IOL calculation. Langenbucher et al. used paraxial ray tracing for the calculation of toric IOLs and toric phakic IOLs (Langenbucher, Reese et al. 2004; Langenbucher and Seitz 2004; Langenbucher, Szentmary et al. 2007). Ishikawa et al. used paraxial ray tracing for IOL calculation (Ishikawa, Hirano et al. 1998; Ishikawa, Hirano et al. 2000a; Ishikawa, Hirano et al. 2000b; Ishikawa, Hirano et al. 2000c), as well as Norrby et al. (Norrby 2004; Norrby, Lydahl et al. 2005). While there were early attempts to overcome the limits of paraxial IOL calculation like the study of Pomerantzeff et al. who used their wide-angle schematic eye for IOL calculation (Pomerantzeff, Pankratov et al. 1985), recent literature dealing with IOL calculation using real ray tracing is even more limited. Naeser et al. used real ray tracing for calculating IOLs (Naeser 1997). Horiuchi et al. also calculated IOL power with real ray tracing according to their publication's abstracts (Horiuchi and Akagi 2001b; Horiuchi and Akagi 2001a) (the publications themselves were unfortunately not available in a language readable by the author). Mainly Preussner et al. published investigations how to use geometry data of real eyes and real ray tracing to calculate an individual IOL (Preussner and Wahl 2000; Preussner, Wahl et al. 2001; Preussner, Wahl et al. 2002; Preussner, Wahl et al. 2003; Preussner, Wahl et al. 2005). A computer program based on the work of Preussner et al. called OKULIX (der Leu, Germany; http://www.okulix.de) is sold commercially and recently been tested in clinical practice (Rabsilber, Reuland et al. 2006).

In this section, RRT in the individual virtual eye as presented in this thesis will be used to calculate the geometry of spherical intraocular lenses and show that it could replace the classical IOL calculation formulae with the potential of also handling difficult cases like refractive treated corneas as well as calculating the geometry of IOLs rather than only its dioptric power.

5.1.2 Methods

	Normal Group 30 Eyes of 28 Patients	Refractive Group 12 Eyes of 7 Patients
	Mean ± SD (Range)	Mean ± SD (Range)
Age	69.2 ± 9.3 (46-82) years	44.6 ± 6.7 (35-54) years
Ablation parameters (SEQ)	-	-8.25 ± 2.6 (-11.25 to -3.50) D, 4 LASEK and 8 PRK
Axial length (IOLMaster)	23.65 ± 1.03 (21.04-25.77) mm	25.00 mm (assumed)
Axial length (optical, retransformed)	23.82 ± 0.98 (21.34-25.84) mm	25.11 mm
Pre-op ACD (IOLMaster)	3.28 ± 0.43 (2.25-4.32) mm	3.50 mm (assumed)
Sim K [1] (C-Scan 0-1.5 mm) before refractive surgery	-	7.65 ± 0.11 (7.50-7.87) mm
Sim K [1] (C-Scan 1.0-1.5 mm)	7.80 ± 0.27 (7.15-8.41) mm	8.98 ± 0.43 (8.40-10.03) mm
K-readings [1] (manual keratometer)	7.77 ± 0.25 (7.11-8.33) mm	-
K-readings [1] (IOLMaster)	7.74 ± 0.28 (7.11-8.39) mm	8.92 ± 0.43 (8.34-9.97) mm (simulated)
Corneal astigmatism (sim K)	0.84 ± 0.74 (0.05-2.82) D	0.64 ± 0.28 (0.22-1.21) D
Corneal asphericity Q (flat axis, 3.5 mm diameter)	0.22 ± 0.63 (-0.90 to 1.70)	2.50 ± 2.48 (-0.82 to 7.5)
Power of implanted IOL (SA60AT)	20.95 ± 2.18 (17-27) D	-
Post-op ACD (predicted, including corneal thickness)	4.52 ± 0.20 (4.01-4.92) mm	4.71 mm

[1] mean values of flat and steep meridian

Table 5-1: Patient data for the normal and refractive group

Normal Group

The calculation of IOLs by classical formulae was compared to the results of the calculation of ray tracing for the normal group of patients (see Table 5-1, left column). IOL power was calculated with classical formulae using axial length, ACD (only for Haigis) and corneal curvature measurements from the IOLMaster (Carl Zeiss Meditec AG, Germany) (mean value of the flat and steep meridian). Formula specific lens constants for the AcrySof SA60AT (Alcon Laboratories, Inc., USA) lens optimized for the IOLMaster were taken from the Library User Group for Laser Interference Biometry (ULIB; http://www.augenklinik.uni-wuerzburg.de/eulib/). For the same eyes IOLs were calculated using RRT (general parameters see Table 5-2). Therefore the cornea was measured with a C-Scan (Technomed GmbH, Germany) videotopometer. The posterior corneal surface is approximated from the anterior surface using a constant back-to-front ratio. The optical axial length was obtained from the IOLMaster measurements that were retransformed according to Olsen et al. (Olsen and Thorwest 2005). The postoperative lens position was estimated from axial length (Preussner, Wahl et al. 2004). (The posterior surface approximation, the axial length retransformation and the lens position estimation is done the same way as described in more detail in section 4.2.) The geometry of a spherical biconvex IOL was calculated for three different pupil sizes. This was done as described by minimizing the RMS spot size – this time depending on the lens geometry (Figure 3-14). To allow a comparison to classical IOL power values the paraxial power of the lens was calculated using the standard thick lens equation (2-7).

Parameter	Value
Refractive index cornea / aqueous humor / vitreous humor	1.376 / 1.336 / 1.336 (Helmholtz, Gullstrand et al. 1909) [p. 300]
Corneal back-to-front ratio	0.81 (Atchison and Smith 2000) [p. 12]
Corneal thickness	Normal group: 0.50 mm, refractive group: 0.40 mm
Number of rays traced per iteration	50 * 50 = 2500
Spectacle vertex distance	12.00 mm
Stiles-Crawford weighting factor	according to equation (3-9) with $\beta = 0.12$

Table 5-2: Ray-tracing parameters

The *prediction error* is the difference between the refractive outcome and the predicted spherical equivalent refraction. The average prediction error is commonly calculated from the numerical differences resulting in a signed *mean numerical error* (MNE) and from the absolute differences resulting in an unsigned *mean absolute error* (MAE). The calculation in this case is done the following way: with the known implanted IOL power and the manifest refraction an optical lens position can be calculated with the thin lens formula (5-1) resolved for d (second solution of quadratic equation) for each eye.

$$d = \frac{L + \frac{n}{z} - \sqrt{\left(-L - \frac{n}{z}\right)^2 - 4\left(L\frac{n}{z} - \frac{n}{DL}\left(\frac{n}{z} - L\right)\right)}}{2} \tag{5-2}$$

Taking an IOL power calculated with a formula of interest together with this optical lens position d makes it possible to recalculate the refraction that this patient would have expected using this formula:

$$ref = \frac{DC - z}{DC \cdot dBC - z \cdot dBC - 1}$$

$$\text{with } z = \frac{n}{\frac{n}{\frac{n}{L-d} - DL} + d} \tag{5-3}$$

$$\text{and } DC = \frac{nC - 1}{RC}$$

The refraction differences to the target refraction (emmetropia in this case) result in the MNE, the absolute differences in the MAE.

Refractive Group

The refractive group consists of 12 eyes of 7 patients who underwent refractive surgery (LASEK and PRK for myopia correction). An IOL calculation for a fictious cataract surgery was performed; see Table 5-1, right column for patients' data. The topography was measured; for the axial length and ACD feasible values were assumed. For the calculation with ray tracing the axial length was retransformed to optical values as before. Postoperative ACD was estimated as for the normal group. The posterior corneal surface was approximated by a theoretical surface. The curvature of this surface was estimated from the simulated K-readings of a C-Scan topography taken *before* refractive surgery by the same constant back-to-front ratio as for the normal group.

For the IOL calculation in the normal group with the classical formulae the K-readings measured with the IOLMaster were used since the lens constants used are optimized for the IOLMaster. In the refractive group only C-Scan topographies were available and no IOLMaster measurements. The IOLMaster measures the corneal curvature at a distance of

1.3 mm from the optical axis for an eye of mean size (Preussner, Wahl et al. 2004). Therefore simulated K-readings were calculated out of the C-Scan topography in a similar range of radii from 1.0 to 1.5 mm. An offset of 0.06 mm can be seen in the normal group of patients (Table 5-1, left column) between IOLMaster K-readings and simulated K-readings which is a difference in power around 0.34 D. Therefore an offset of 0.06 mm was added to the simulated K-readings to get "simulated" IOLMaster K-readings for IOL calculation with the classical formulae.

For both, the normal and refractive group, the asphericity in a diameter of 3.5 mm on the flat axis of all corneas was determined by a least square fit method.

5.1.3 Results

Normal Group

Results are summarized in Table 5-3. For every formula the mean power for all IOLs together with standard deviation and range was calculated (column 1). As expected the range of powers is big (reaching from approx. 15 to 30 D) since absolute power values are considered. But it can be seen, that all formulae as well as RRT calculate very similar IOL powers in average showing small offset. The MNE is small for all formulae: the biggest for the Hoffer Q formula, the smallest for ray tracing with a 2.5 mm pupil (see Figure 5-2). The biggest MAE is 0.49 D with the SRK II formula; all other formulae including RRT perform better resulting in similar values ranging from 0.36 to 0.40 D. The smallest MAE of 0.36 D is seen with the Hoffer Q formula and RRT with a 2.5 mm pupil (see Figure 5-1).

	Normal Group			Refractive Group
		Difference between Refractive Outcome and Predicted Refraction (SEQ)		
	Mean Power ± SD (Range)	MNE ± SD (Range)	MAE ± SD (Range)	Mean Power ± SD (Range)
SRK II	20.57 ± 2.59 (15.58 to 29.10)	-0.04 ± 0.64 (-1.22 to 1.47)	0.49 ± 0.41 (0.03 to 1.47)	21.87 ± 1.57 (19.56 to 25.52)
Holladay 1	20.36 ± 3.04 (14.71 to 30.33)	0.17 ± 0.45 (-0.90 to 0.90)	0.38 ± 0.28 (0.01 to 0.90)	22.85 ± 1.94 (19.92 to 27.29)
SRK/T	20.70 ± 3.10 (15.26 to 30.39)	-0.05 ± 0.48 (-1.26 to 0.74)	0.39 ± 0.27 (0.06 to 1.26)	22.48 ± 1.78 (19.80 to 26.58)
Haigis	20.40 ± 3.16 (15.01 to 30.81)	0.14 ± 0.46 (-0.93 to 0.87)	0.39 ± 0.28 (0.01 to 0.93)	23.69 ± 2.31 (20.24 to 29.02)
Hoffer Q	20.33 ± 3.22 (14.58 to 30.94)	0.19 ± 0.42 (-0.80 to 0.88)	0.36 ± 0.29 (0.01 to 0.88)	23.52 ± 2.28 (20.11 to 28.76)
RRT 3.5	20.36 ± 3.02 (15.57 to 29.76)	0.17 ± 0.52 (-1.05 to 1.19)	0.40 ± 0.36 (0.01 to 1.19)	24.08 ± 2.51 (19.65 to 28.72)
RRT 3.0	20.42 ± 3.07 (15.34 to 29.84)	0.13 ± 0.47 (-0.96 to 1.01)	0.37 ± 0.32 (0.03 to 1.01)	24.70 ± 2.45 (20.77 to 29.59)
RRT 2.5	20.60 ± 3.12 (15.26 to 30.22)	0.01 ± 0.46 (-1.11 to 0.79)	0.36 ± 0.29 (0.01 to 1.11)	25.03 ± 2.48 (21.23 to 30.34)

Table 5-3: IOL calculation results

Computationally the calculation of a spherical IOL is a simpler task than calculating best corrected spectacles to predict refraction, since this is a one-dimensional minimizing process (depending only on the radius of curvature of the lens); calculation time lies within a fraction of a second.
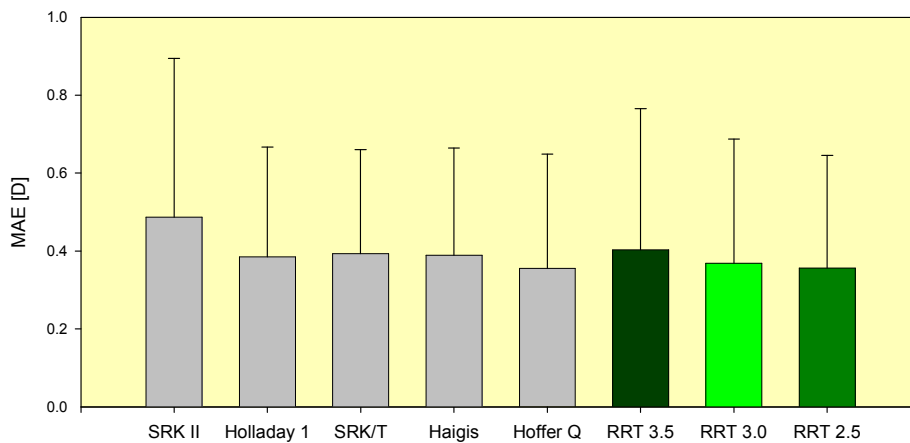
Figure 5-1: IOL calculation for the normal group (MAE)
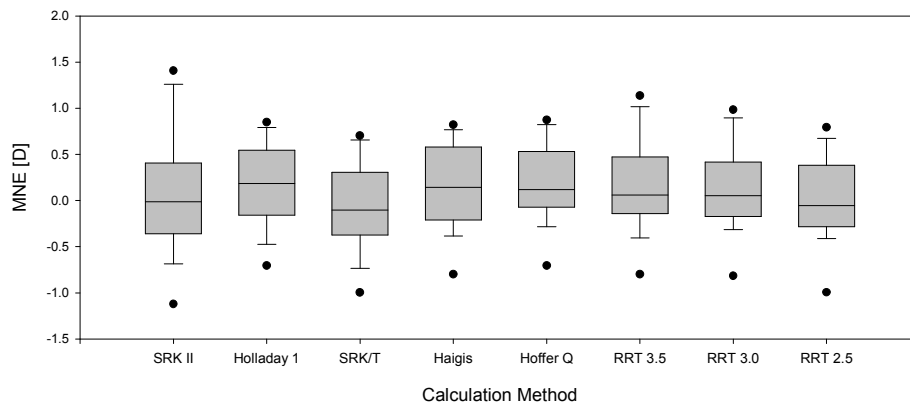
Figure 5-2: IOL calculation for the normal group (MNE)

Refractive Group

Results are summarized in Table 5-3. A much greater discrepancy is seen when comparing different formulae. The average power of SRK II is clearly the smallest with 21.87 D. Holladay 1, SRK/T, Haigis and Hoffer Q range from 22.48 to 23.69 D. RRT delivers higher values than any other formula ranging from 24.08 to 25.03 D depending on pupil size.

Figure 5-3 compares the absolute power of the IOLs calculated with ray tracing to the ones calculated with the classical formulae. An average of the newer Holladay 1, SRK/T, Haigis and Hoffer Q was calculated excluding the older SRK II formula. For the normal group the difference is – depending on the assumed pupil size – between -0.08 and 0.16 D. For the refractive group the difference is much higher ranging from 0.95 to 1.90 D.
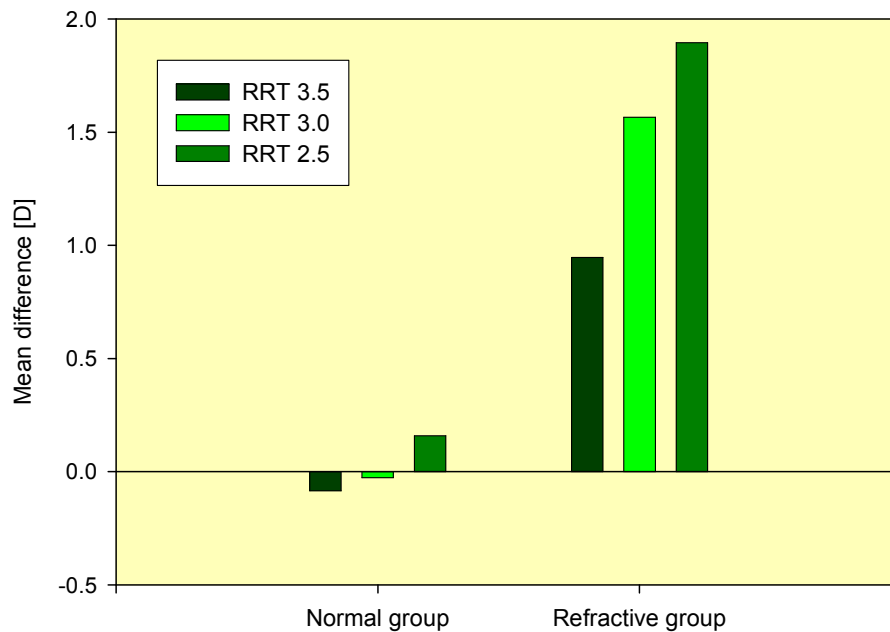
Figure 5-3: RRT vs. classical formulae

5.1.4 Discussion

IOL Calculation: State-of-the-Art

IOL specific constants are necessary for each of the classical formulae. These are the *A-constants* of the SRK formulae; Hoffer uses *pACD*, Haigis three constants *a0, a1, a2*, Holladay a *surgeon factor sf*. These constants mainly reflect IOL properties and the lens position after implantation. To improve outcomes these constants have to be personalized to take into account surgical technique, diagnostic instruments, preoperative and postoperative medications (Holladay 2004). Nevertheless the reliability of IOL calculation in general is limited. First of all there cannot be a perfect calculation scheme that guarantees target refraction with ultimate precision because of the fact that the individual postoperative position of the implanted IOL cannot be known exactly at the time of IOL calculation. The postoperative lens position is therefore predicted for IOL calculation. As the SRK I and II formulae are purely empirical they use an implicit prediction controlled by the A-constant. The third generation formulae typically use the axial length and corneal curvature together with their lens constants for explicit prediction of the IOL position while the Haigis formula additionally includes information about the preoperative ACD. By proper adjustment of the lens constants the *average* lens position can be determined accurately, but the *individual* post operative lens position remains predictive. Another general problem is inaccurate measurement of the central corneal curvature and axial length. The central corneal power is typically measured by keratometry (manual or automated) or simulated keratometry with a videotopometer. The axial length and ACD is measured by ultrasound or optical coherence tomography. When simulated by RRT a dislocation of the IOL of 0.1 mm in axial direction typically alters the patient's refraction by an amount of 0.13 diopters for an eye of normal length. For shorter eyes the change is bigger, for longer eyes smaller. A change of corneal power in the magnitude of 1 D typically results in a refraction difference of nearly the same amount (0.98 D). A change of the axial length of 0.1 mm typically alters the refraction by 0.26 diopters; more for shorter, less for longer eyes (own calculations confirmed results found

by others (Preussner and Wahl 2000)). Wrong predictions of the lens position or relying on false measurements will result in offset errors relative to the target refraction in similar orders of magnitude. A comprehensive review of IOL power calculation was provided recently by Olsen (Olsen 2007).

The mentioned IOL calculation formulae are easy to use and produce satisfying results for normal eyes. Results are getting worse if eyes differ from the average having extreme values for corneal curvature or axial length, especially when using the first generation SRK I formula. The SRK II formula is a modification of the SRK I for better handling of longer and shorter eyes. The theoretical optical formulae perform even better when calculating extreme eyes; nevertheless there are still differences between formulae when calculating very short or very long eyes (Sanders, Retzlaff et al. 1990; Hoffer 1993; Hoffmann, Hutz et al. 1997).

Hoffer compares all formulae used in the present investigation (except the Haigis formula) and reports similar performance for the theoretical optical formulae (SRK/T, Holladay 1, Hoffer Q) showing a MAE between 0.3 and 0.4 D and less accuracy for the empirical SRK formulae showing a MAE slightly higher than 0.5 D (Hoffer 1993). Hoffmann et al. report similar performance of all those formulae including the Haigis formula (Hoffmann, Hutz et al. 1997); however they quantify the error regarding the IOL power (not the refraction difference) resulting in higher absolute values than Hoffer. These two studies used ultrasound measurements of the axial length. The axial length may be the most critical parameter in IOL calculation (Hoffmann, Hutz et al. 1997). At around 2000 the IOLMaster was introduced using the optical measurement technique PCI showing highly reproducible measurements of axial length. The accuracy of IOL calculation using PCI measurements seems to be at least equal to conventional immersion ultrasound (IUS) (Olsen and Thorwest 2005). For example, Kiss et al. compared IOL calculations using the Holladay 1 formula with both PCI and IUS measurements and report an equal MAE of 0.46 D (Kiss, Findl et al. 2002b).

The Challenge of Abnormally Shaped Corneas

The theoretical optical IOL calculation formulae rely on paraxial optics. This in only an approximation of Snell's law for small angles and therefore results in considering only paraxial rays − that means only rays near the optical axis − and is only valid for spherical surfaces. For a sphere the asphericity (Q) is zero. A negative asphericity stands for a prolate shape, a positive for an oblate shape. An average cornea is prolate; a cornea after LASIK/LASEK/PRK correction of myopia is typically oblate (Hersh, Shah et al. 1996; Holladay and Janes 2002; Anera, Jimenez et al. 2003a; Anera, Jimenez et al. 2003b; Hersh, Fry et al. 2003; Marcos, Cano et al. 2003; Cano, Barbero et al. 2004; Somani, Tuan et al. 2004; Anera, Villa et al. 2005; Preussner, Wahl et al. 2005; Koller, Iseli et al. 2006) (compare to the discussion in the context of ablation profiles for refractive surgery on page 108 and details summarized in Table 5-10). If there is an equal central corneal power but different asphericities, this leads to a different focus when analyzed with RRT. Two problems arise when calculating an IOL for a cornea with unusual asphericity (Figure 5-4). On the one hand the measurement by keratometry introduces an error by under- or overestimating the central corneal power (Seitz, Langenbucher et al. 1999). On the other hand the IOL calculation introduces an error because the formulae are assuming the asphericity of an average cornea since the lens constants are optimized for normal corneas having an average asphericity.
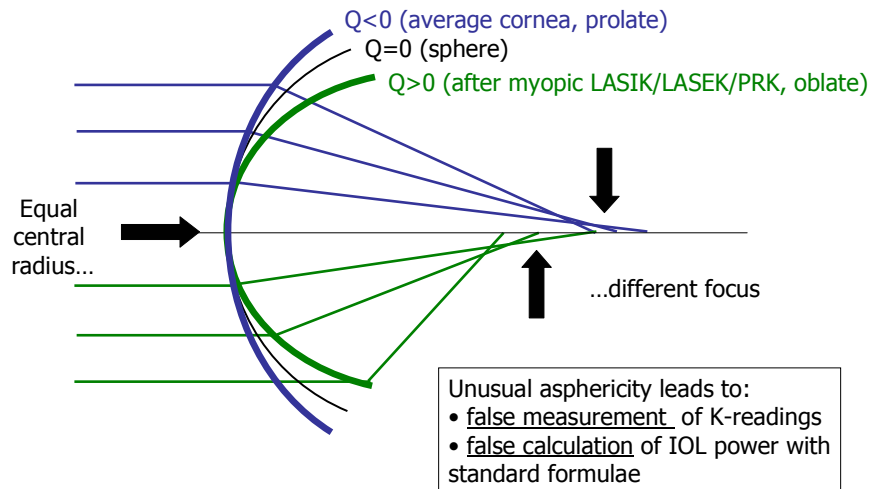
Figure 5-4: Influence of corneal asphericity on IOL calculation

There is another challenge concerning corneas that had previous refractive surgery (LASIK/LASEK/PRK). The cornea principally consists of two refracting surfaces: the anterior and posterior surface. When looking at the geometry, there is a high linear correlation of the anterior and posterior radius of curvature for an average cornea with a back-to-front ratio of 0.81 according to Atchison et al. (Atchison and Smith 2000) [p. 12], recently validated in a large population-based study (0.819) (Fam and Lim 2007). At the anterior corneal surface the refractive indices differ much more than at the posterior surface. Therefore the influence of the posterior surface is much less. Talking in terms of paraxial optics the total corneal refraction of around 42 D is the result of values around 48 D from the anterior and - 6 D from the posterior corneal surface for an average eye (Figure 3-6). Keratometry and videotopography only measure the radius of curvature of the anterior corneal surface. A fictious refractive index for a single refractive surface is used when calculating refractive power from the anterior radius of curvature (e.g. 1.3375 is a commonly used fictious refractive index; compare to the real refractive indices according to Gullstrand in Table 5-2). This reflects an estimation of the posterior radius of curvature with a constant back-to-front ratio and is reasonable and satisfying for normal eyes. In refractive surgery the anterior corneal surface is modified without affecting the posterior surface (at least not directly). As a result the back-to-front ratio for normal eyes is no longer valid for refractive treated eyes (Figure 5-5). Therefore an error occurs in the calculation of corneal power that seems to increase with ablation depth (Seitz, Langenbucher et al. 1999).
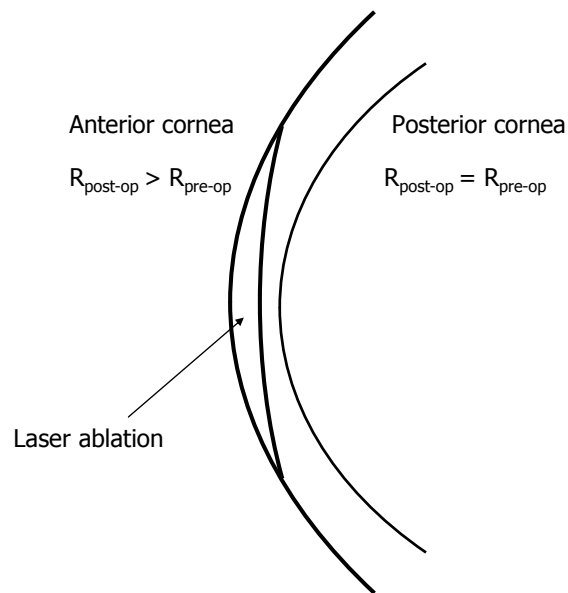
Figure 5-5: Changed back-to-front ratio after refractive surgery

Benefits of RRT

All classical formulae only use the central corneal power as a description of the cornea's refractive property. This power is described by K-readings and reflects no information about the shape of the cornea beyond sphere and cylinder – e.g. no individual asphericity. Nor do they consider a possibly changed back-to-front ratio of corneal curvatures. The IOL calculation using real ray tracing overcomes these limitations of the classical formulae by having the ability to consider the complete topography of the anterior and posterior corneal surface. Additionally, in contrast to classical formulae, ray tracing does not only calculate a paraxial power value for an IOL, but its geometry.

Thus ray tracing is not limited to calculate spherical IOLs. Not only design issues like symmetry of the anterior and posterior surfaces can be assessed, for example optical properties of biconvex vs. planoconvex IOLs. Also toric and aspherical lenses can be calculated – or a combination of both, whatever desired. See Figure 5-6 for a comparison of input parameters of RRT and state-of-the-art formulae.

	State-of-the-art formulae	Real Ray Tracing
Axial length	✓ Measurement	✓ Measurement
ACD post-op	✓ Estimation	✓ Estimation
Corneal power	K-Readings (combined power of front & back surface)	Complete corneal topography • Consideration of toricity & asphericity • Separation of front & back surface Both relevant after refractive surgery
IOL design	-	✓ Directly influences calculation: • Toric lenses • Aspheric lenses • biconvex/planoconvex etc.
Pupil	-	✓ Directly influences calculation

Figure 5-6: Comparison of input parameters for IOL calculation

A systematic offset can be seen when comparing the mean IOL powers calculated by ray tracing for different pupil sizes: because the whole eye has a positive spherical aberration, a bigger pupil assumed in ray tracing, leads to a shift of the focus towards the cornea. The result is the calculation of a weaker IOL to assure that the patient has the desired target refraction. This effect can be seen in both groups (see Figure 5-3): moving from 2.5 to 3.5 mm pupil size resu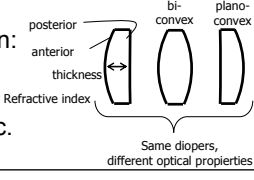lts in a difference of approximately 0.25 D in the normal group and 1.0 D in the refractive group. The reason is the different asphericity of the corneas: in the normal group the average asphericity is 0.22 (slightly oblate). The asphericity of the refractive group is much higher: 2.5 in average (oblate). Moving towards bigger positive asphericity leads to increasing positive spherical aberration. So the spherical aberration of clearly oblate corneas is higher than for normal corneas leading to higher dependence of pupil size when analyzed by ray tracing – at least in case of simulating a spherical IOL. (The asphericity for the average cornea reported in literature is somewhat lower around $Q = -0.2$ according to several investigations (Atchison and Smith 2000) [p. 15]; (Liou and Brennan 1997). But – see Figure 5-7 – even this prolate cornea has a positive spherical aberration, so the argumentation stays the same.)

Real ray tracing identifies the pupil size to be an important factor when simulating human optics or calculating IOLs. When predicting refraction as in chapter 4 it may have been desirable to know the exact pupil size. However when calculating IOLs the patient's refraction preferably has to be guaranteed at all occurring pupil sizes. The results of ray tracing using spherical IOLs show that the refraction difference is only moderate for normal eyes, but much higher for refractive treated patients. Regarding spherical aberration, independence of pupil size can only be achieved by calculating an individual aspherical IOL. All calculations in this section are limited to spherical IOLs – but the ray-tracing implementation presented is not limited and can also calculate advanced IOL geometries (see section 5.2).

To see if ray tracing has the potential to replace the classical formulae it has to perform at least equally when calculating IOLs for normal eyes. To assess this issue the results for IOL power between the different formulae and ray tracing were compared for the normal group. If lens constants are used that are optimized for a specific subset of patients, the MNE becomes zero (Hoffer 1993; Olsen 2007). Since in this case the lens constants of ULIB were used for

the formulae without recalculating them for this subset MNEs slightly differing from zero are observed. The MAEs are similar compared to those found by other authors for larger numbers of eyes as cited before. Even with the relatively small number of eyes a slightly higher MAE for the SRK II formula compared to the others can be seen. The MAE of all other formulae is very similar ranging from 0.36 to 0.40 D – including the RRT calculation. This agreement of ray tracing and classical formulae known to perform well for normal eyes is a promising result of the new method.

In the refractive group there is a greater discrepancy when comparing the different formulae (Table 5-3), maybe as a result of the higher axial length and higher K-readings compared to the normal group. As discussed before in cases of myopia correction with refractive ablation techniques a resulting hyperopic shift is often reported when using classical formulae without further corrections. As the power value calculated by ray tracing is significantly higher this leads to the suggestion that this hyperopic shift possibly can be avoided when using ray tracing. In this evaluation the information of the K-readings before refractive surgery was used to estimate the posterior corneal surface. Even if that information is not available an average posterior surface can be assumed resulting in very similar IOL powers. So ray tracing has the potential to calculate IOLs in difficult cases even if no clinical history is available. Although this analysis is restricted to the case of myopic LASIK/LASEK/PRK, ray tracing is principally ready to handle eyes treated by hyperopic corrections or RK, too.

Apart from inaccurate measurements of the anterior cornea and optical axial length, factors affecting the accuracy of the ray-tracing calculation in this thesis are the estimation of the posterior cornea (including corneal thickness) and the prediction of the postoperative intraocular lens position. There are recent investigations that measure the posterior corneal surface using different measurement techniques, ranging from different variants of Scheimpflug imaging to OCT (Dubbelman, Weeber et al. 2002; Langenbucher, Torres et al. 2004; Ciolino and Belin 2006; Tang, Li et al. 2006), indicating that obtaining accurate individual measurements is not trivial, especially after refractive surgery – but if once available in clinical practice, ray tracing will directly benefit from including accurate measurements of the posterior cornea. It will also benefit from using improved algorithms for prediction of the intraocular lens position. Sasaki et al. proposed an improved prediction based on Scheimpflug imaging (Sasaki, Sakamoto et al. 2002). Norrby et al. introduced the "lens haptic plane concept" that separates the prediction of the postoperative position from the calculation itself (Norrby and Koranyi 1997; Norrby 2004; Norrby, Lydahl et al. 2005). Although they focus on paraxial ray tracing, this concept may be suitable for real ray tracing as well. Also interesting for the use with ray tracing is the prediction of the effective lens position by Olsen, who used a multi-variable regression method (Olsen 2006).

Conclusion

It has been show that it is possible to use RRT for IOL calculation. In contrast to state-of-the-art IOL calculation formulae, RRT does not use empirical adjustment factors despite of the prediction of the post-op ACD. Main input parameters are the retransformed optical axial length and the complete corneal topography regarding potential individual irregularities – not only K-readings (Figure 5-6). Different than current formulae, RRT actually calculates the geometry of an IOL and can therefore address properties beyond a simple dioptric power. It has been shown that the ray-tracing calculation can compete with state-of-the-art IOL calculation formulae for normal eyes (Figure 5-1, Figure 5-2 and Table 5-3). Furthermore it has been shown that ray tracing can possibly avoid a hyperopic shift often reported when using standard formulae for IOL calculation for eyes with previous refractive treatment without knowledge about clinical history (Figure 5-3).

5.2 Customized Aspherical Intraocular Lenses

5.2.1 Introduction

It is well known, that the human cornea is no perfect sphere. Besides toricity and other irregularities the average cornea is a prolate ellipsoid. The asphericity is a quantity that is usually used to describe the shape of an aspherical ellipsoid as introduced in section 2.2. The asphericity is a geometrical quantity that results in spherical aberration (SA) in terms of wavefront error. It is known from technical optics that a spherical lens hat some amount of positive spherical aberration. Only one asphericity depending on the refractive index leads to zero spherical aberration:

$$Q_{optimal} = -\frac{1}{n^2} \tag{5-4}$$

n: refractive index

The human cornea is known to be prolate with an average asphericity somewhere around Q = -0.2 according to several investigations (Atchison and Smith 2000) [p. 15]; (Liou and Brennan 1997). The corneal spherical aberration is therefore less than that of a sphere, but not zero. When assuming a corneal refractive index of 1.376 the asphericity leading to zero SA would have to be Q = -0.53 according to formula (5-4).
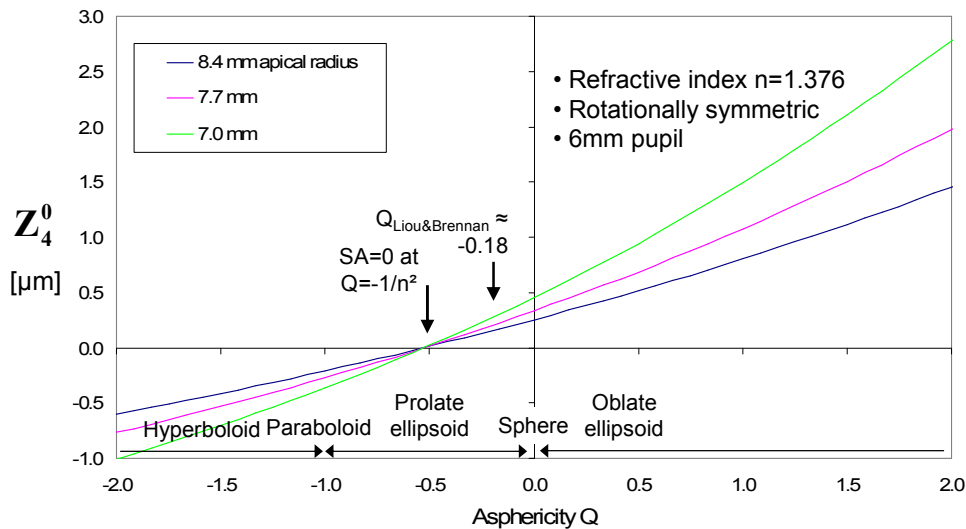
Figure 5-7: Corneal asphericity and spherical aberration (model calculation)

The spherical aberration can be quantified from the wavefront aberration. If the wavefront aberration is approximated by Zernike polynomials as described on page 10, the Z(4,0) quantifies the spherical aberration. Figure 5-7 shows a model calculation that illustrates the relation of asphericity and spherical aberration: one rotationally symmetric corneal surface with three different apical radii was considered. The Z(4,0) coefficient from the resulting wavefront aberration was calculated with RRT for varying asphericities.

Total ocular wavefront aberrations are the result of corneal and internal wavefront aberrations. This total ocular wavefront can be measured directly with wavefront measuring devices (see section 2.3). However it is not easy to measure the corneal and internal aberrations separately.

Corneal aberrations come from the anterior and posterior corneal surface. The posterior surface is often neglected and corneal wavefront aberration therefore is typically calculated from corneal topography of the anterior cornea. Barbero et al. measured the corneal wavefront aberration directly for the special case of an aphakic patient (Barbero, Marcos et al. 2002). The internal wavefront aberration comes mainly from the crystalline lens. Artal et al. used salt water filled goggles to separately measure the internal aberration of human eyes and show, that corneal and internal aberration compensate each other (Artal, Guirao et al. 2001). Others have similar results based on measurement of corneal and total aberrations (Mrochen, Jankov et al. 2003; Kelly, Mihashi et al. 2004). Regarding spherical aberration this means, that in a young phakic patient the positive corneal spherical aberration is compensated to some degree by a negative spherical aberration of the crystalline lens. The corneal SA tends to be not age depended. If a patient is undergoing a cataract surgery, the crystalline lens is replaced by an IOL. If this IOL has spherical surfaces it has positive SA and therefore does not compensate but amplifies the positive SA of the pseudophakic eye. The SA has influence on the contrast sensitivity, particular with big pupil size. Increased SA leads to decreased contrast sensitivity. To address this issue, it may be beneficial to use IOLs with reduced SA. Smith et al. determined an optimum shape of an IOL (still consisting of spherical surfaces) to achieve minimal SA (Smith and Lu 1988). Atchison investigated the use of aspherical surfaces for IOLs (Atchison 1991). Ushio et al. investigated the spherical aberration of spherical IOLs of different designs (Uchio, Ohno et al. 1995). Werner et al. did experiments with actually manufactured aspherical IOLs (Werner and Roth 1999). Holladay et al. proposed the use of aspherical IOLs with a prolate anterior surface to reduce the SA of pseudophakic eyes (Holladay, Piers et al. 2002). Today most manufacturers sell aspherical IOLs, therefore there is an increasing number of publications investigating the potential advantages of aspherical IOLs (Packer, Fine et al. 2002; Kershner 2003; Mester, Dillinger et al. 2003; Bellucci, Morselli et al. 2004; Packer, Fine et al. 2004b; Bellucci, Scialdone et al. 2005; Kasper, Buhren et al. 2005; Chen, Ye et al. 2006; Denoyer, Roger et al. 2006; Franchini 2006; Kasper, Buhren et al. 2006a; Kasper, Buhren et al. 2006b; Munoz, Albarran-Diego et al. 2006; Padmanabhan, Rao et al. 2006; Tabernero, Piers et al. 2006; Beiko 2007; Bellucci and Morselli 2007; Bellucci, Morselli et al. 2007; Caporossi, Martone et al. 2007; Denoyer, Le Lez et al. 2007; Kurz, Krummenauer et al. 2007; Marcos, Rosales et al. 2007; Tzelikis, Akaishi et al. 2007). While they tend to agree on the fact that aspherical IOLs reduce the SA of the pseudophakic eyes the positive impact on the patient's vision is still discussed controversially.

In section 5.1 RRT was used to calculate spherical IOLs. In this section RRT will be used to calculate more advanced IOL geometries like customized toric and/or aspherical IOLs. The term "customized" means, that the IOLs are calculated for an individual patient. This is in contrast to the current concept used in clinical practice, to implant IOLs providing a fixed value of negative spherical aberration that is intended to correct the positive average corneal SA. After calculating customized IOLs the remaining wavefront aberration is analyzed with RRT and the results are compared for the different kinds of IOLs.

5.2.2 Methods

For the calculations and simulations the measurements of 45 eyes of 45 Caucasian patients undergoing cataract surgery without complications at the University Eye Hospital Tübingen were used. The anterior corneal surface was measured post-op with a prototype videotopometer OphthaTOP (OphthaSWISS AG, Switzerland) and with a C-Scan (Technomed GmbH, Germany) videotopometer. Axial length was measured with an IOLMaster (Carl Zeiss Meditec AG, Germany). Posterior corneal surface and ACD were estimated as described in section 5.1.2. Table 5-4 gives an overview of the patients' statistics.

	45 Eyes of 45 Patients (20 OD, 25 OS)
	Mean ± SD (Range)
Age	73.5 ± 7.4 (47-88) years
Sim K power	43.45 ± 1.53 (39.63-46.91) D (OphthaTOP) 43.71 ± 1.63 (39.80-47.75) D (C-Scan)
Sim K astigmatism	1.10 ± 1.04 (0.06-4.87) D (OphthaTOP) 1.03 ± 1.04 (0.17-4.77) D (C-Scan)
Axial length (IOLMaster)	23.98 ± 1.90 (20.64-31.08) mm 24.13 ± 1.81 (20.95-30.90) mm (retransformed optical)
Post-op ACD (estimated Preussner)	4.56 ± 0.33 (3.98-5.80) mm

Table 5-4: Baseline patient data

Investigation of Reference Axes
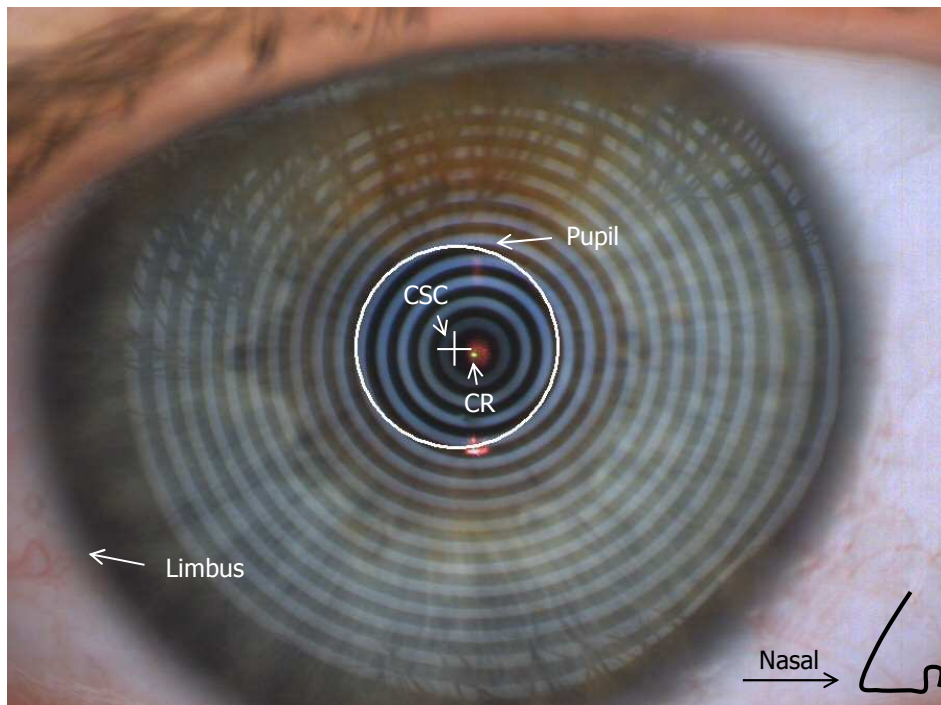
Figure 5-8: Example of a video image (RE) of OphthaTOP with pupil, corneal sighting center and corneal reflex

Figure 5-8 shows a typical video image of the OphthaTOP topography system. From these raw video images the topographical elevation is calculated after edge detection. Additionally the system is capable of detecting the pupil. The *corneal reflex* (CR) and the pupil centroid also known as *corneal sighting center* (CSC) were recorded for assessment of the reference axes of the eye as discussed later. This was done for preoperative and postoperative topographic video images. The use of the *line of sight* (LOS) for reference axis is achieved by rotating the incoming rays by the angle β (Figure 5-28). The angle β in degrees is estimated based on the standard formula for a circular arc:

$$\beta = \frac{180 \cdot \|\mathbf{CSC} - \mathbf{CR}\|}{\pi \cdot \|\mathbf{F} - \mathbf{CR}\|}$$

(5-5)

CSC: corneal sighting center [3D position vector in mm]
CR: corneal reflex [3D position vector in mm]
F: fixation target [3D position vector in mm]

The distance $\|\mathbf{F} - \mathbf{CR}\|$ is given by the videokeratometer and was 85 mm for the OphthaTOP unit. With the information of these reference points the corneal wavefront aberration was calculated with respect to different reference axes. The results are compared and the impact of using different reference axes was investigated.

Corneal Asphericity and Spherical Aberration

For the assessment of corneal asphericity, a biconic surface was fitted to each corneal elevation map. This was done by the following steps:
(a)   approximation of the apical radii R_{steep} and R_{flat}
(b)   determination of best-fitting Q_{steep} and Q_{flat} from Baker's equation (2-16) of a conic section using 4 and 6 mm diameter
Corneal wavefront with respect to the *videokeratometric axis* (VK axis) was calculated using only the anterior corneal surface with RRT in the exit pupil plane. The cornea was assumed to have a refractive index of 1.76. Zernike polynomials were fitted to the wavefront with special regard to the Z(4,0) coefficient. For each topography Z(4,0) was calculated in two different ways: first using the spline-interpolated raw elevation data (page 34) and second using a theoretical biconic surface (equation (3-1)) constructed of the values determined in step (a) and (b). Both, OphthaTOP and C-Scan topographies were evaluated.

Customized IOLs

The following types of IOLs were calculated (see Figure 5-9):
    (a) a spherical IOL (calculation of R =>1-dimensional optimization)
    (b) an aspherical IOL (calculation of R & Q => 2-dim. optimization)
    (c) a toric IOL (calculation of $R1$ & $R2$ & AX => 3-dim. optimization)
    (d) a toric aspherical IOL (calculation of $R1$ & $R2$ & AX & Q => 4-dim. optimization)
The radius of curvature of the posterior surface is held constant (R_{post} = -25 mm). When optimizing aspherical IOLs (b and d) it is crucial to optimize the radius R (respectively $R1$ and $R2$) and the asphericity Q simultaneously.
First, a "model eye" was constructed from the topographical analysis of the OphthaTOP using a biconic surface with the average values found for the 45 patient eyes and the average axial length and ACD. For this model eye the four types of IOLs are calculated and the residual wavefront aberration is analyzed. Second, the four types of IOLs are calculated for each patient eye using the individual spline-interpolated OphthaTOP elevation data, axial length and ACD. These will be referred to as "real eyes". The geometry of the IOLs is calculated with the multi-dimensional optimization process as described in section 3.3 and shown schematically in Figure 3-14; as optimization criterion both, RMS WFE and RMS spot size were used. For assessment of the optical properties the residual wavefront aberration relative to the VK axis is calculated and fitted to Zernike polynomials.
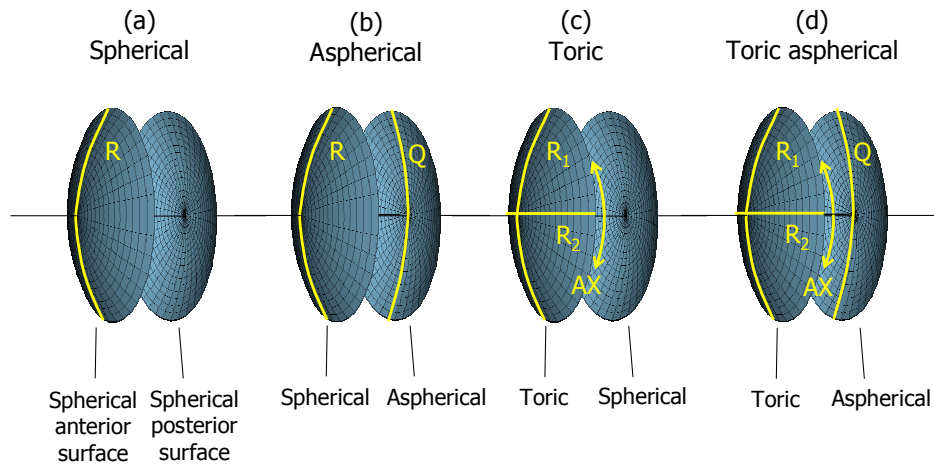
Figure 5-9: Types of customized IOLs

Tilt and Decentration

After the calculation of customized IOLs the behavior of the toric and toric aspherical IOLs with tilt and decentration was investigated. The IOLs were tilted and decentered in the according patient eyes and the change in wavefront aberration for a 6 mm pupil evaluated. Refer to Figure 5-10 for the definition of the sign convention used. According to the OSA standards the same right handed coordinate system is used for both, right and left eyes, when specifying wavefront aberrations and Zernike coefficients. There is no difference in direction for the specification of vertical tilt and decentration: superior tilt means that the distance of the superior edge of the IOL to the cornea is increased (implemented as a rotation around the x-axis and specified in positive degrees). Superior decentration means a shift of the IOL in upward direction (specified in positive millimeters). To enable the comparison of right and left eyes the directions are defined in mirror symmetry for horizontal tilt and decentration: nasal tilt means that the distance of the nasal edge of the IOL to the cornea is increased (implemented as a rotation around the y-axis and specified in positive degrees for right and left eyes). Nasal decentration is defined as a shift of the IOL in nasal direction (specified in positive millimeters for right and left eyes). Tilt and decentration are specified relative to the VK axis.
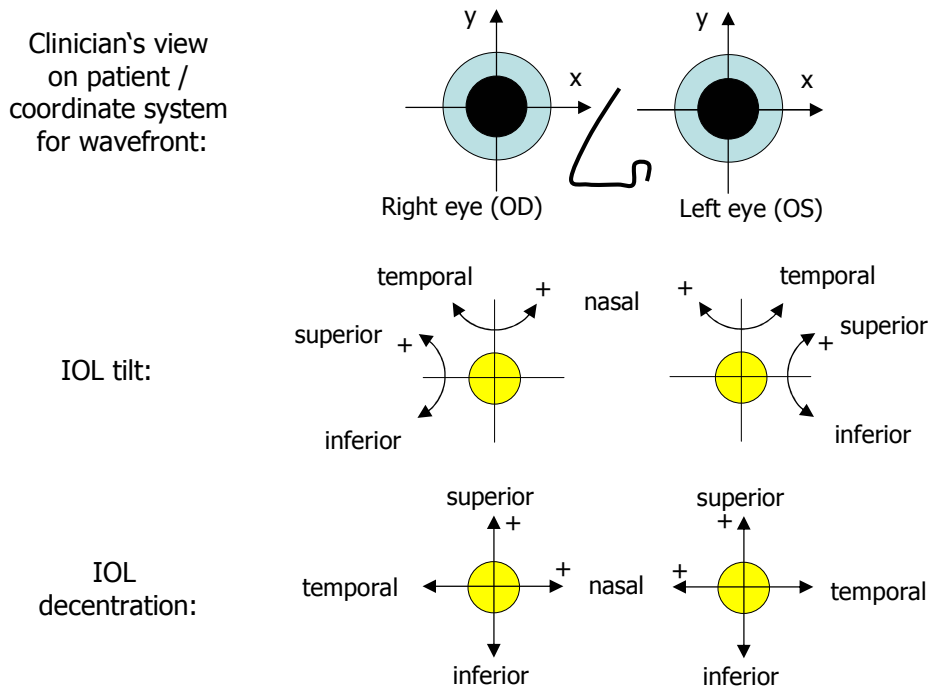
Figure 5-10: Tilt and decentration; definition of directions for right and left eyes

5.2.3 Results

Investigation of Reference Axes
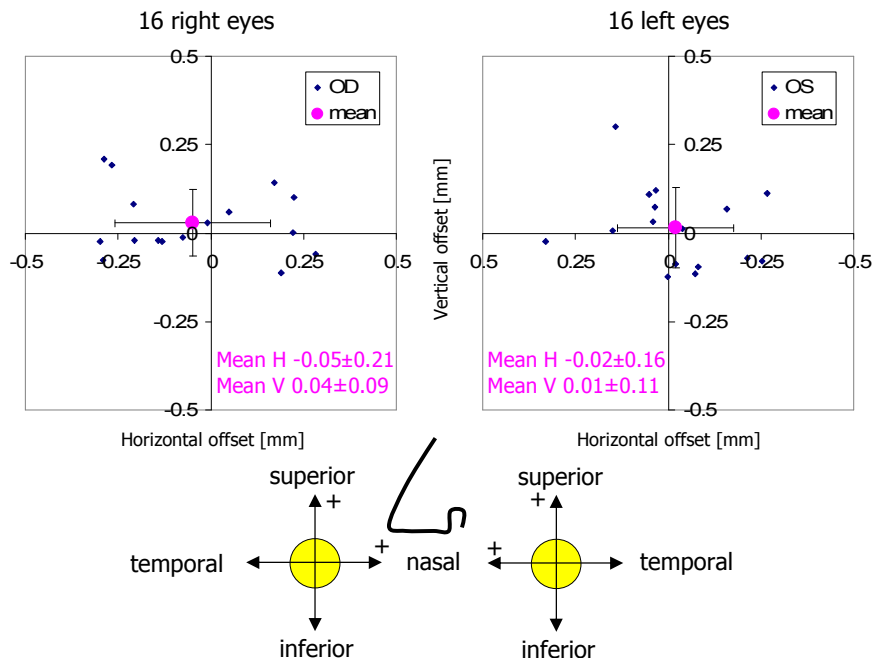
Figure 5-11: Offset of the CSC relative to the corneal reflex

The pupil was properly detectable in 32 out of 45 topographies. The CSC relative to the corneal reflex is shown in Figure 5-11. Sign convention of the offset corresponds to the definition of IOL decentration in Figure 5-10. The pupil position shows a large variation and the CSC shows a small average offset in superior/temporal direction. The pupil was detectable

in both, preoperative and postoperative video images in 22 eyes. Figure 5-12 shows the scatter plot of the offset CSC to CR indicating that there seems to be no systematic difference.
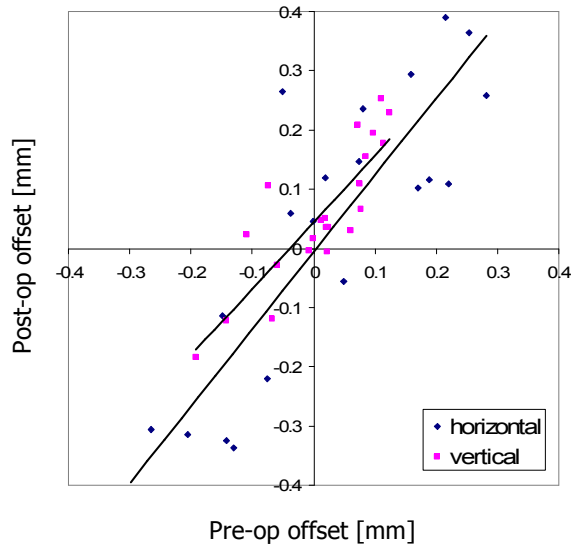
Figure 5-12: Offset of the CSC to the CR preoperative vs. postoperative (22 eyes)

Figure 5-13 and Figure 5-14 show the corneal wavefront aberration calculated for different reference axes: first, relative to the VK axis; second, relative to the LOS; third, relative to the LOS simulated with a temporal offset of the CSC of 0.2 mm.

	AST RMS	HOA RMS	Coma RMS	SA like RMS	Ast +-45	Ast 0/90	Tre-foil	Coma v	Coma h	Tre-foil	Qua-dra-foil	2nd Ast	SA Z40	2nd Ast	Qua-dra-foil
☐ VK axis	0.94	0.46	0.26	0.12	-0.35	-0.14	-0.03	-0.11	-0.11	0.12	0.02	-0.02	0.09	0.01	-0.03
☐ LOS	0.96	0.46	0.26	0.13	-0.36	-0.09	-0.05	-0.09	-0.11	0.12	0.02	-0.03	0.11	0.01	-0.05
☐ LOS sim	0.96	0.48	0.31	0.14	-0.31	-0.08	-0.04	-0.09	-0.18	0.14	0.01	-0.02	0.12	0.02	-0.06

Zernike mode
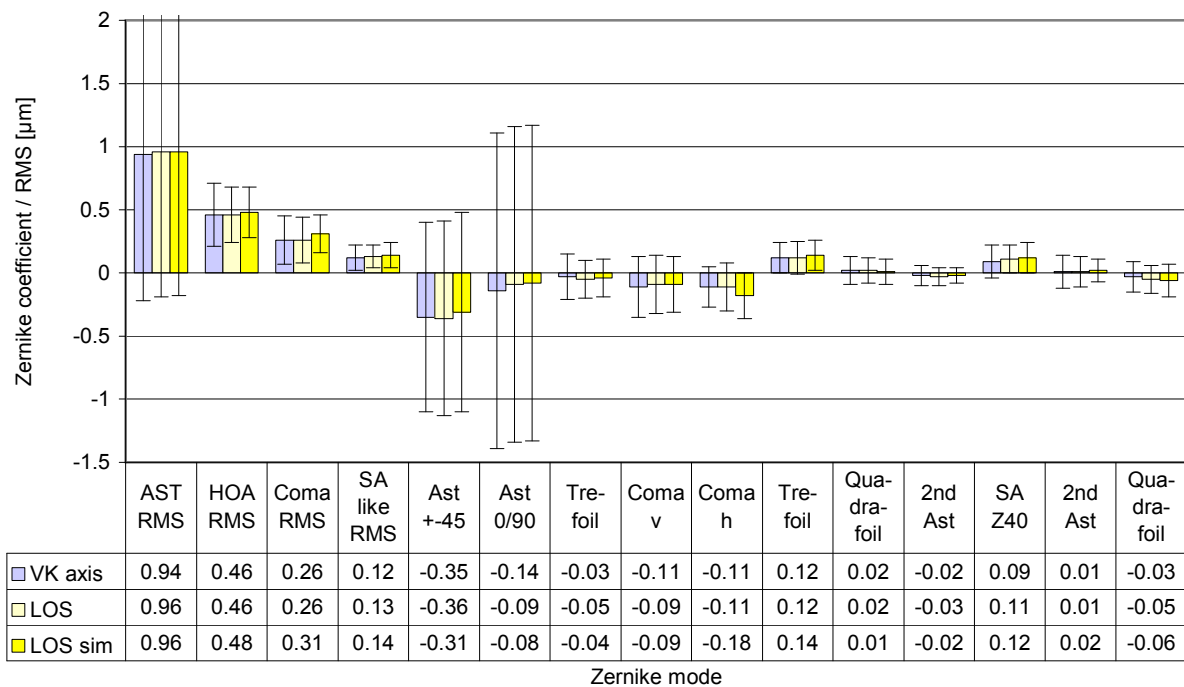
Figure 5-13: Corneal wavefront aberration calculated for different reference axes; 16 post-op right eyes, 6 mm pupil

	AST RMS	HOA RMS	Coma RMS	SA like RMS	Ast +-45	Ast 0/90	Tre-foil	Coma v	Coma h	Tre-foil	Qua-dra-foil	2nd Ast	SA Z40	2nd Ast	Qua-dra-foil
☐ VK axis	1.04	0.5	0.24	0.13	-0.08	0	-0.08	-0.12	0.12	-0.12	0.01	0.01	0.11	0.02	-0.07
☐ LOS	1.06	0.52	0.27	0.13	-0.09	0	-0.08	-0.09	0.13	-0.11	0.01	0.02	0.11	0.04	-0.08
☐ LOS sim	1.04	0.56	0.33	0.14	-0.14	0.02	-0.08	-0.09	0.21	-0.13	0.03	0.01	0.13	0.04	-0.11

Zernike mode
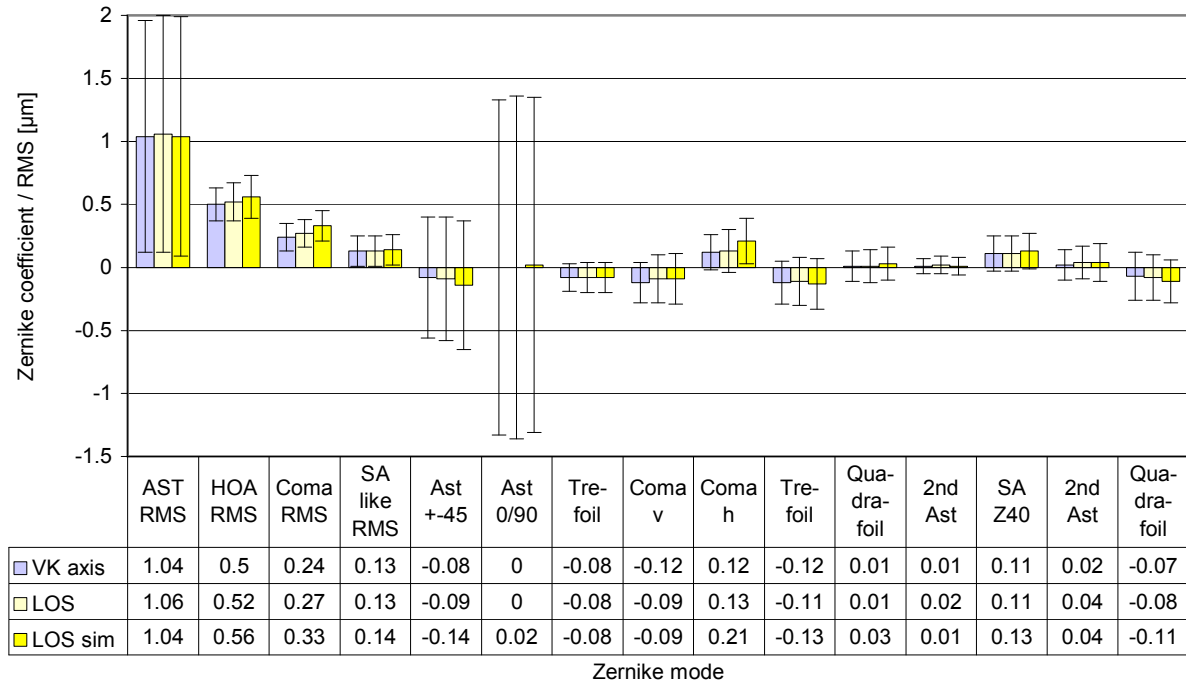
Figure 5-14: Corneal wavefront aberration calculated for different reference axes; 16 post-op left eyes, 6 mm pupil

Corneal Asphericity and Spherical Aberration

Figure 5-15 shows the values of the biconic surface fits. The apical radii show an offset of approximately 0.05 mm between C-Scan and OphthaTOP; however the difference between steep and mean axis is equally 0.18 mm. The asphericities determined with the two systems are very similar. The mean asphericity Q calculated for 6 mm diameter is -0.16 with the C-Scan and -0.22 for the OphthaTOP system. For 4 mm corneal diameter the asphericities were small, the cornea therefore almost spherical. In both systems the asphericities of the flat axis were significantly lower than those of the steep axis for 6 mm corneal diameter.
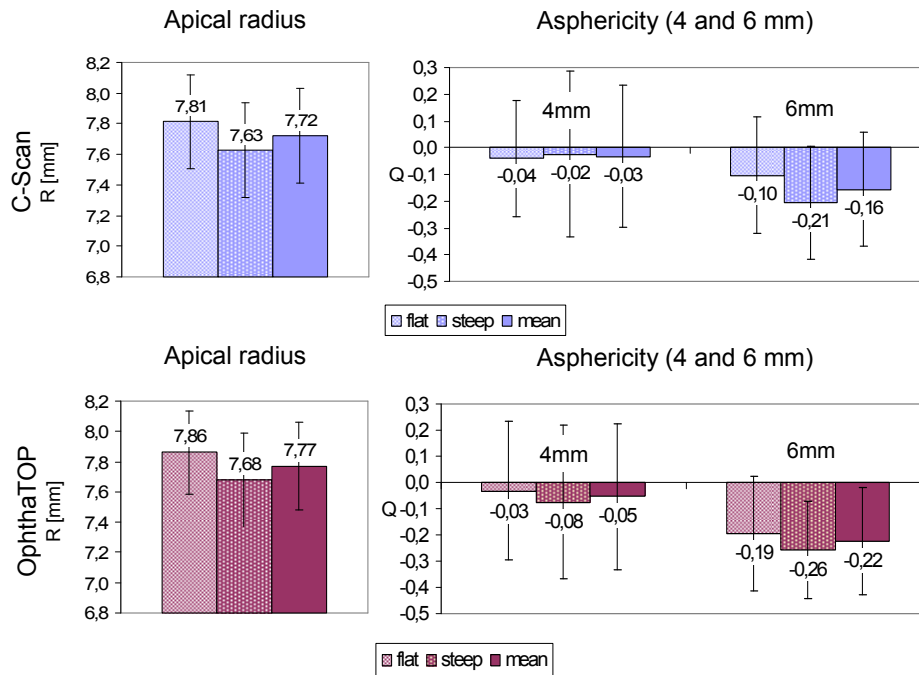
Figure 5-15: Biconic surface fits for C-Scan & OphthaTOP

Figure 5-16 shows the results for the SA obtained from RRT and quantified as Zernike $Z(4,0)$ coefficient. On the left side SA is shown as calculated from the elevation data (with standard deviation) and for the biconic surfaces (for both topography units). On the right side, theoretical values are provided for the Liou and Brennan model eye (Liou and Brennan 1997) and for a sphere for the purpose of comparison.

It can be seen, that for a diameter of 4 mm all variants including the sphere result in roughly the same SA ranging from 0.04 to 0.06 µm. For 6 mm diameter there are bigger differences: similar values around 0.2 µm are found for the biconic surfaces and the Liou and Brennan model eye. However smaller values around 0.1 µm are found when the elevation data is used for calculation. Both, 4 and 6 mm diameters show a big standard deviation for the elevation data. No big difference is seen between the C-Scan and OphthaTOP systems. Figure 5-17 shows the scatter plot of measured $Z(4,0)$ coefficient from real eyes (OphthaTOP) over the corneal asphericity (mean of flat and steep meridian, OphthaTOP).

Corneal spherical aberration (4mm)

Corneal spherical aberration (6mm)
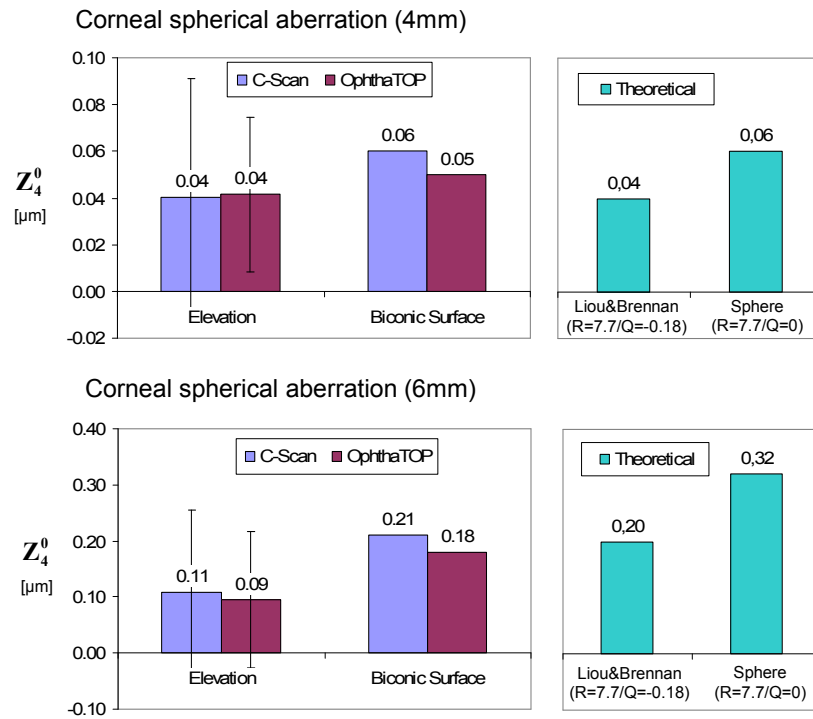
Figure 5-16: Corneal spherical aberration from elevation and biconic fit compared to theoretical surfaces

$$y = 0.1642x^2 + 0.4302x + 0.1775$$
$$R^2 = 0.1988$$

Figure 5-17: Corneal asphericity and spherical aberration (real eyes, 6 mm diameter)

Customized IOLs

Table 5-5 shows the model eye parameters derived from the OphthaTOP biconic surface fits and other measurements.

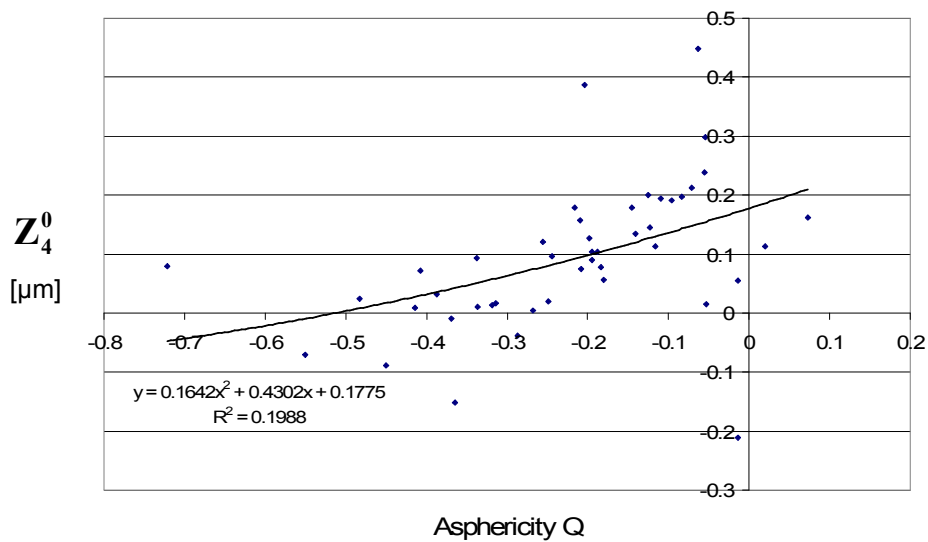|	Average from 45 Eyes of 45 Patients
Apical radii	R_{flat} = 7.86 mm R_{steep} = 7.68 mm => 1.10 D astigmatism (axis was set to 0°)
Asphericities	Q_{flat} = -0.18 Q_{steep} = -0.26
ACD	4.56 mm
Axial length	24.13 mm
Corneal thickness	0.5 mm
Corneal back2front ratio	0.81

Table 5-5: Model eye parameters

General information regarding the diagrams from Figure 5-18 to Figure 5-22: These diagrams show the Zernike analysis of the wavefronts (see also Figure 2-4 and the description of Zernike polynomials on page 10). Actually Zernike polynomials up to the 6th order (28 terms) were fitted to the wavefront. However the diagrams only show the Zernike modes up to the 4th order (omitting 13 terms including the Z(6,0) coefficient) for the sake of simplicity without hiding important information, because the 5th and 6th order coefficients are rather small. Piston and tilt are not shown; piston is only a constant offset without further relevance. Tilt causes a displacement of image away from the center of the fovea that can be compensated by the eye by adjusting the fixation angle (Bueeler, Iseli et al. 2005). Thus the individual Zernike coefficients start in the 5th column ranging from astigmatism to quadrafoil. All Zernike coefficients refer to RMS microns, as they are calculated according to the OSA standards (Thibos, Applegate et al. 2002). The left four columns give RMS error values for combined Zernike modes: total RMS gives the total RMS error (excluding piston and tilt). LOA RMS combines the 2nd order (lower order) aberrations astigmatism and defocus. HOA RMS combines 3rd to 6th order (higher order) aberrations. SA RMS combines primary spherical aberration Z(4,0) and secondary spherical aberration Z(6,0). Note that, per definition, the individual Zernike coefficients are relative and do have a numerical sign, while the combined RMS values are absolute and thus always positive. When interpreting the diagrams also keep in mind, that the combined RMS errors can be calculated directly from the individual Zernike coefficients by the square root of the sum of the squared coefficients, e.g. $SA\ RMS = \sqrt{\left(Z_4^0\right)^2 \cdot \left(Z_6^0\right)^2}$ (Salmon and van de Pol 2006).

The results of the residual wavefront aberration for the model eye with the different types of IOLs are shown in Figure 5-18 when optimizing RMS WFE and in Figure 5-19 when optimizing RMS spot size. When optimizing RMS WFE all IOL types lead to a defocus of almost zero. The toric IOLs completely compensate the astigmatism. The aspherical and toric aspherical IOLs reduce the Z(4,0) and the SA RMS to almost zero. The toric aspherical IOL leads to almost aberration free optics with a total RMS of almost zero. Optimizing RMS spot size shows very similar results for the aspherical and toric aspherical IOLs, but differences for the spherical and toric IOLs: in presence of SA the RMS spot size seems to be smaller when there is some amount of defocus left.
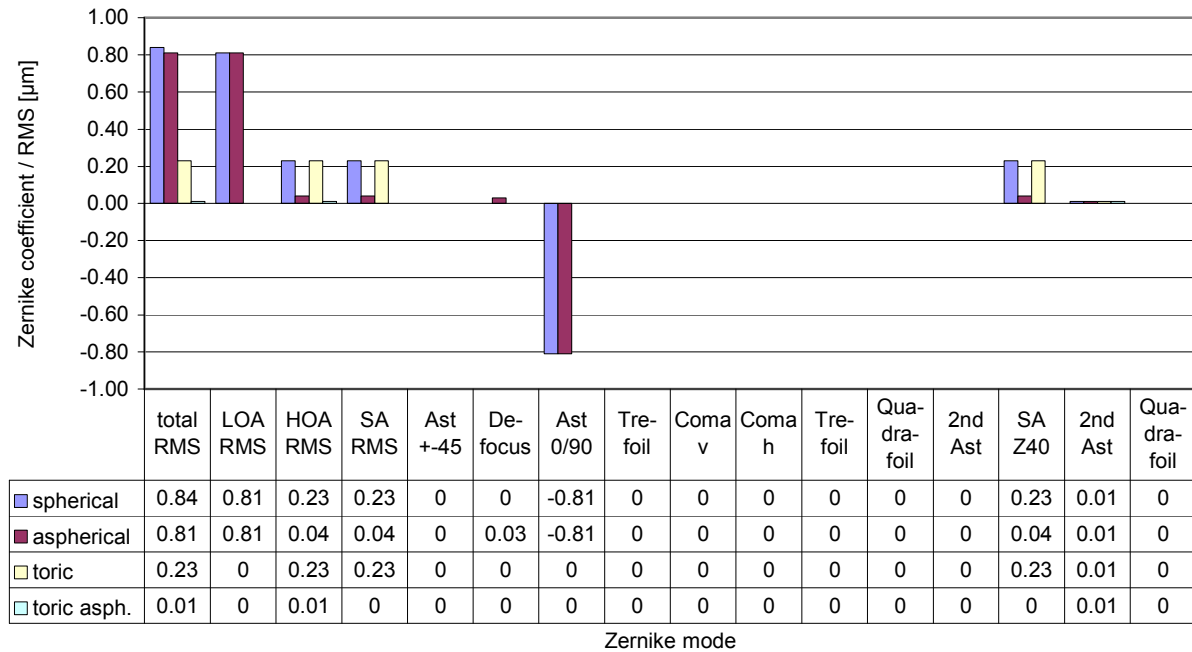
	total RMS	LOA RMS	HOA RMS	SA RMS	Ast +-45	De-focus	Ast 0/90	Tre-foil	Coma v	Coma h	Tre-foil	Qua-dra-foil	2nd Ast	SA Z40	2nd Ast	Qua-dra-foil
spherical	0.84	0.81	0.23	0.23	0	0	-0.81	0	0	0	0	0	0	0.23	0.01	0
aspherical	0.81	0.81	0.04	0.04	0	0.03	-0.81	0	0	0	0	0	0	0.04	0.01	0
toric	0.23	0	0.23	0.23	0	0	0	0	0	0	0	0	0	0.23	0.01	0
toric asph.	0.01	0	0.01	0	0	0	0	0	0	0	0	0	0	0	0.01	0

Zernike mode

Figure 5-18: Wavefront aberration of the model eye with different IOL types optimized for minimal RMS WFE

	total RMS	LOA RMS	HOA RMS	SA RMS	Ast +-45	De-focus	Ast 0/90	Tre-foil	Coma v	Coma h	Tre-foil	Qua-dra-foil	2nd Ast	SA Z40	2nd Ast	Qua-dra-foil
spherical	0.93	0.9	0.23	0.23	0	-0.39	-0.81	0	0	0	0	0	0	0.23	0.01	0
aspherical	0.81	0.81	0.02	0.01	0	0	-0.81	0	0	0	0	0	0	-0.01	0.01	0
toric	0.45	0.39	0.23	0.23	0	-0.39	-0.02	0	0	0	0	0	0	0.23	0.01	0
toric asph.	0.03	0.02	0.02	0.02	0	-0.01	-0.02	0	0	0	0	0	0	-0.02	0.01	0

Zernike mode
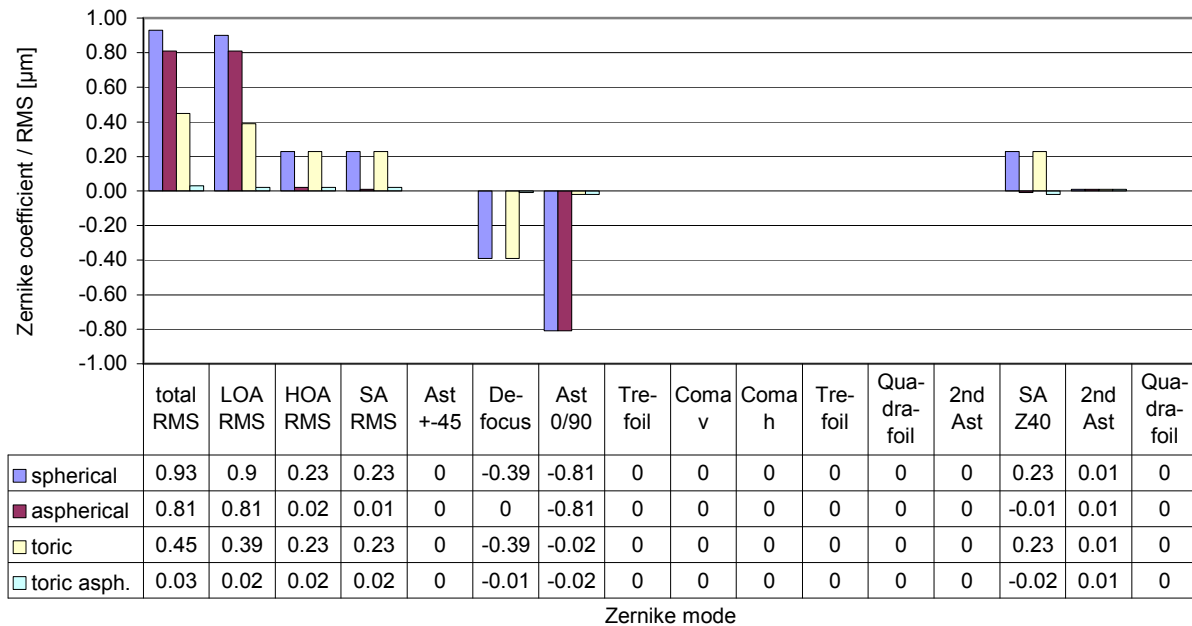
Figure 5-19: Wavefront aberration of the model eye with different IOL types optimized for minimal RMS spot size

Figure 5-20 shows the results for the real eyes optimized for RMS WFE. The bars and numbers refer to the mean values while the error bars specify the standard deviation. The mean defocus is around zero for all types of IOLs and the standard deviation is small. The big standard deviation of the astigmatism is almost completely eliminated by the toric IOLs; this can also be seen when looking at the LOA RMS. The SA RMS is reduced by the aspherical and toric aspherical IOLs, but not completely to zero. When looking at the results when optimizing RMS spot size for the same eyes in Figure 5-21 the values are similar, though not

identical to the case when optimizing RMS WFE. As for the model eye, there is an interaction of SA and defocus.

	total RMS	LOA RMS	HOA RMS	SA RMS	Ast +-45	De-focus	Ast 0/90	Tre-foil	Coma v	Coma h	Tre-foil	Qua-dra-foil	2nd Ast	SA Z40	2nd Ast	Qua-dra-foil
☐ spherical	1	0.83	0.47	0.17	-0.2	0.04	-0.1	-0.07	-0.09	0.03	0.01	0.02	0.01	0.16	0.01	-0.04
☐ aspherical	0.99	0.83	0.44	0.09	-0.2	0.05	-0.1	-0.07	-0.09	0.03	0.01	0.02	0.01	0.08	0.01	-0.04
☐ toric	0.49	0.08	0.47	0.17	0.01	0.04	-0.02	-0.07	-0.09	0.03	0.01	0.02	0.01	0.16	0.01	-0.04
☐ toric asph.	0.45	0.07	0.43	0.07	0.01	0.02	-0.02	-0.07	-0.09	0.03	0.01	0.02	0.01	0.02	0.01	-0.04

Zernike mode

Figure 5-20: Wavefront aberration of real eyes with different IOL types optimized for minimal RMS WFE

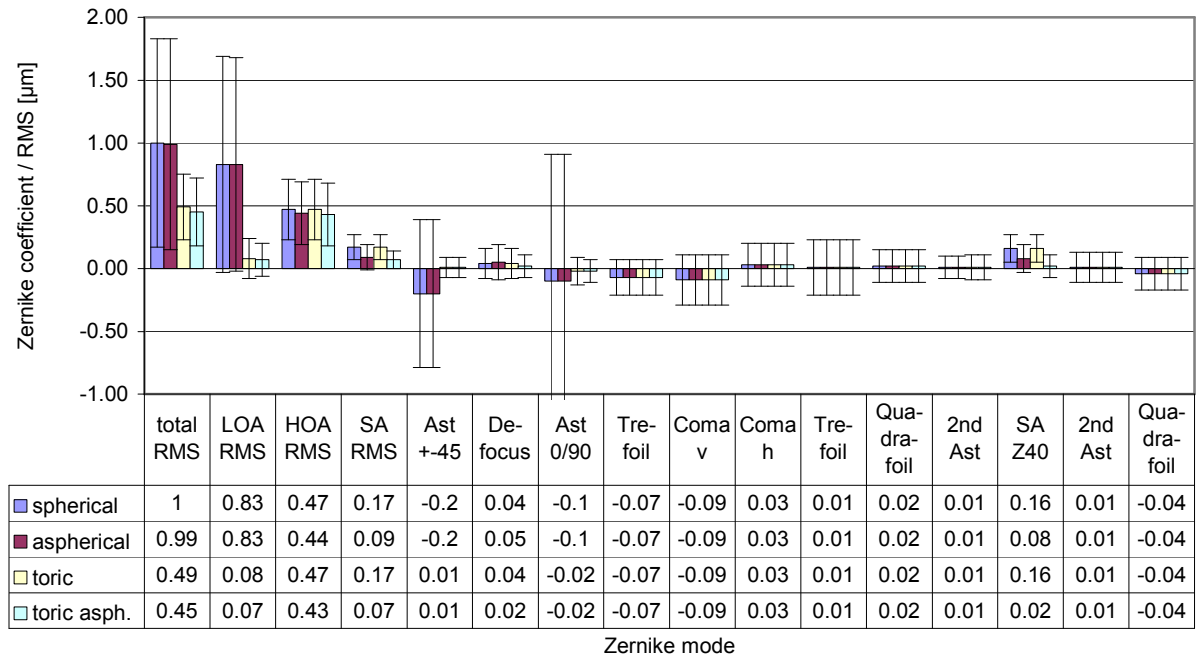|	total RMS	LOA RMS	HOA RMS	SA RMS	Ast +-45	De-focus	Ast 0/90	Tre-foil	Coma v	Coma h	Tre-foil	Qua-dra-foil	2nd Ast	SA Z40	2nd Ast	Qua-dra-foil
☐ spherical	1.04	0.89	0.47	0.17	-0.2	-0.2	-0.1	-0.07	-0.09	0.03	0.01	0.02	0.01	0.16	0.01	-0.04
☐ aspherical	0.98	0.83	0.43	0.06	-0.2	0.02	-0.1	-0.07	-0.09	0.03	0.01	0.02	0.01	0.02	0.01	-0.04
☐ toric	0.58	0.33	0.47	0.17	-0.04	-0.2	-0.03	-0.07	-0.09	0.03	0.01	0.02	0.01	0.16	0.01	-0.04
☐ toric asph.	0.47	0.18	0.43	0.05	-0.03	0.01	-0.03	-0.07	-0.09	0.03	0.01	0.02	0.01	0.01	0.01	-0.04

Zernike mode

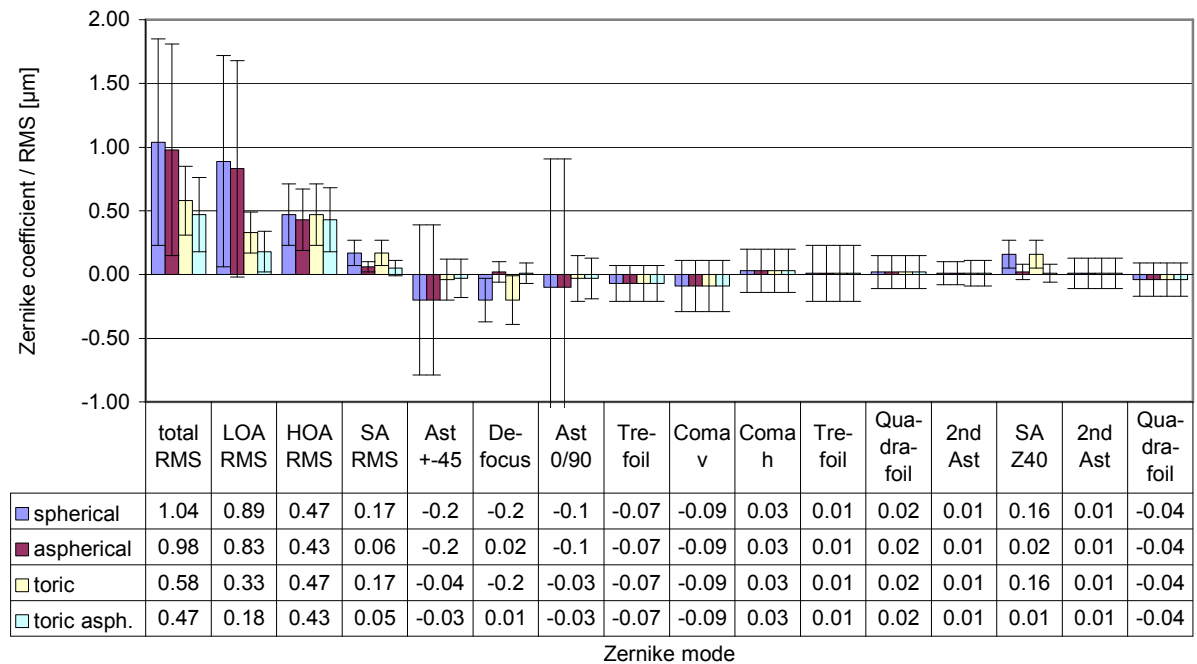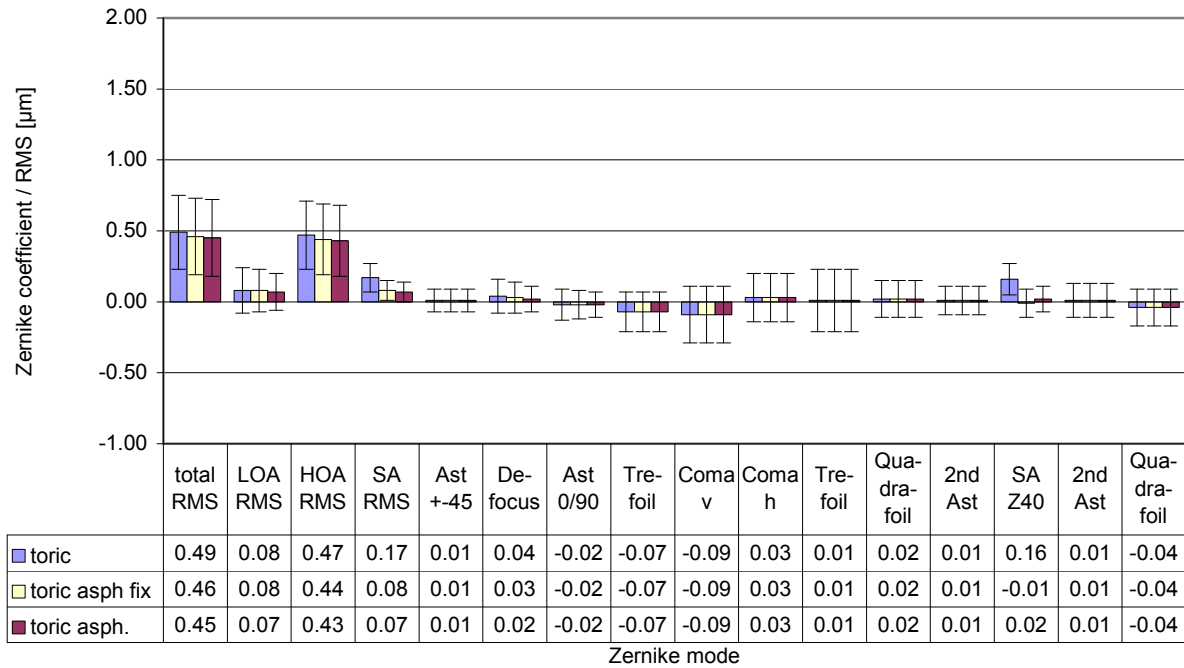**Figure 5-21: Wavefront aberration of real eyes with different IOL types optimized for minimal RMS spot size**

	total RMS	LOA RMS	HOA RMS	SA RMS	Ast +-45	De-focus	Ast 0/90	Tre-foil	Coma v	Coma h	Tre-foil	Qua-dra-foil	2nd Ast	SA Z40	2nd Ast	Qua-dra-foil
□ toric	0.49	0.08	0.47	0.17	0.01	0.04	-0.02	-0.07	-0.09	0.03	0.01	0.02	0.01	0.16	0.01	-0.04
□ toric asph fix	0.46	0.08	0.44	0.08	0.01	0.03	-0.02	-0.07	-0.09	0.03	0.01	0.02	0.01	-0.01	0.01	-0.04
■ toric asph.	0.45	0.07	0.43	0.07	0.01	0.02	-0.02	-0.07	-0.09	0.03	0.01	0.02	0.01	0.02	0.01	-0.04

Zernike mode

Figure 5-22: Wavefront aberration of real eyes with different toric IOL types optimized for minimal RMS WFE

Figure 5-23 shows a comprehensive chart for comparison of the model eye and the real eyes. As in the model eye there are no higher order aberrations except for spherical aberration, the elimination of the SA RMS leads to an elimination of the total HOA. For the real eyes the SA RMS is reduced by the aspherical IOL by some degree, too. However since the real eyes do have various other higher order aberrations the reduction of the total HOA is significant, but limited.
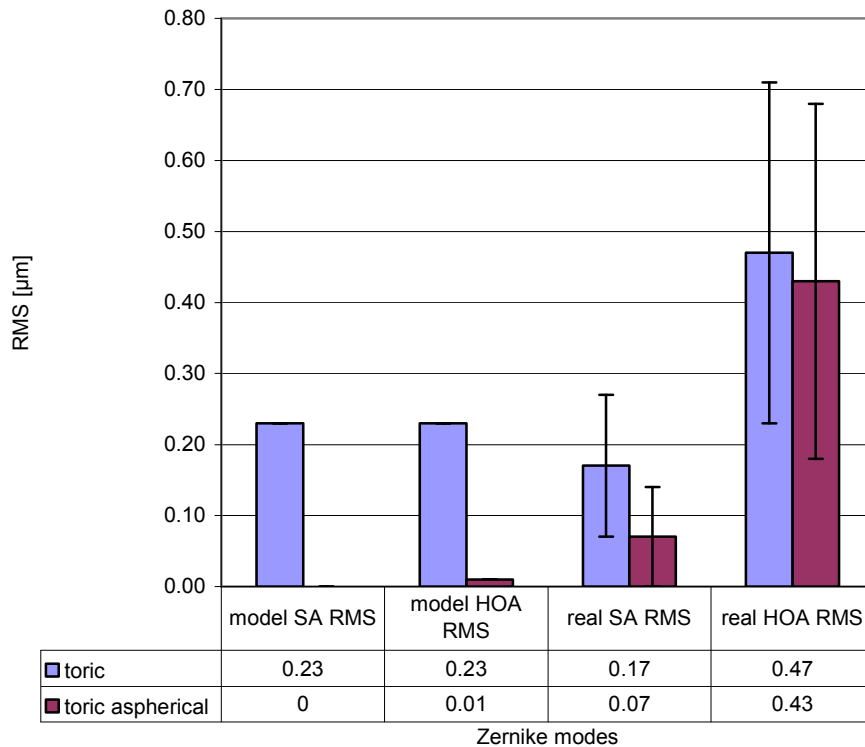

	model SA RMS	model HOA RMS	real SA RMS	real HOA RMS
□ toric	0.23	0.23	0.17	0.47
■ toric aspherical	0	0.01	0.07	0.43

Zernike modes

Figure 5-23: Wavefront aberration of the model eye compared to the real eyes with toric and toric aspherical IOLs optimized for minimal RMS WFE

Table 5-6 shows the geometries of the different IOLs calculated. When comparing the spherical and aspherical IOLs, the following interrelation can be observed: when some asphericity is added to the posterior surface, the radius of curvature of the anterior surface needs to be changed, too. The asphericities of the posterior surface for the IOLs of the model eyes are hyperbolic in the range from -54.1 to -78.4. For real eyes the values are not as negative in average but most are hyperbolic in shape; a big standard deviation is observed.

	IOL type [1]	Anterior Surface Q = 0.00	Posterior Surface R = -25.00 mm [2]	
		R_{flat} [mm] Mean ± SD (Range)	R_{steep} [mm] Mean ± SD (Range)	Q Mean ± SD (Range)
Model Eye (RMS WFE)	spherical	21.82	-	0.00
	aspherical	19.91	-	-54.1
	toric	23.29	20.52	0.00
	toric aspherical	20.83	18.58	-68.7
Model Eye (RMS spot size)	spherical	22.80	-	0.00
	aspherical	19.47	-	-76.4
	toric	24.37	21.43	0.00
	toric aspherical	20.56	18.42	-78.4
Real Eyes (RMS WFE)	spherical	25.90 ± 24.80 (13.04 to 167.49)	-	0.00
	aspherical	24.61 ± 23.37 (13.49 to 162.75)	-	-21.81 ± 26.18 (-75.91 to 0.16)
	toric	28.36 ± 30.56 (14.63 to 203.92)	24.05 ± 20.79 (13.49 to 142.10)	0.00
	toric aspherical	26.15 ± 27.50 (14.42 to 189.13)	22.51 ± 19.19 (13.33 to 135.13)	-31.90 ± 22.57 (-88.73 to 1.71)
Real Eyes (RMS spot size)	spherical	26.98 ± 27.14 (14.26 to 179.45)	-	0.00
	aspherical	24.01 ± 22.78 (13.57 to 158.89)	-	-36.86 ± 31.26 (-94.70 to 18.16)
	toric	29.87 ± 34.55 (14.96 to 226.51)	25.00 ± 22.21 (13.66 to 148.63)	0.00
	toric aspherical	25.46 ± 24.87 (14.12 to 172.35)	22.11 ± 17.39 (12.95 to 123.15)	-37.08 ± 25.06 (-90.36 to 17.70)

[1] refractive index of the IOL is 1.5542; center thickness is 0.65 mm

[2] 4 patient eyes were excluded because they needed a different posterior surface curvature

Table 5-6: Geometries of the IOLs calculated

Tilt and Decentration

Results of the analysis of tilt is shown in Figure 5-24 and Figure 5-25; analysis of decentration in Figure 5-26 and Figure 5-27. Horizontal and vertical tilt leads to an increase of HOA, LOA and thus total RMS for an increasing tilt angle. In both groups of IOLs the increase of aberrations are similar, thus the aspherical toric IOLs preserve their better performance compared to the toric IOLs for all calculated tilt angles in average. This situation changes for decentration: the toric aspherical IOLs induce more total RMS aberration compared to the toric IOLs at some degree of decentration around 0.4 to 1.0 mm. This is mainly because of the larger increase of LOAs when decentered more than approximately 0.4 mm. The change of HOAs strongly depends on the direction of decentration. Nasally decentered aspherical toric IOLs increase HOAs more than toric IOLs, while temporally decentered aspherical toric IOLs increase HOAs less. Similar, the benefit of toric aspherical IOLs is preserved when decentered superior and lost when decentered inferior in terms of HOAs.
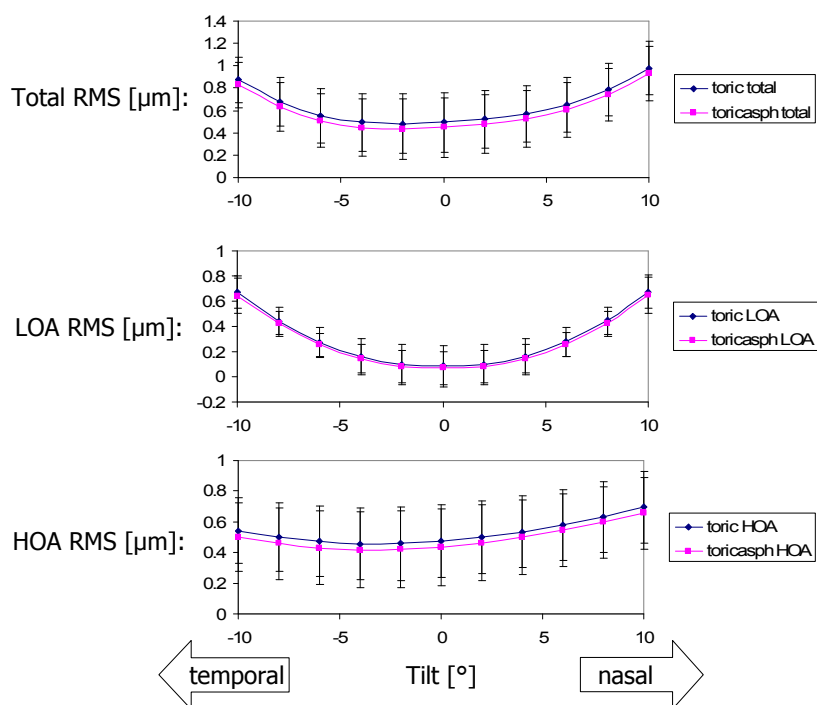
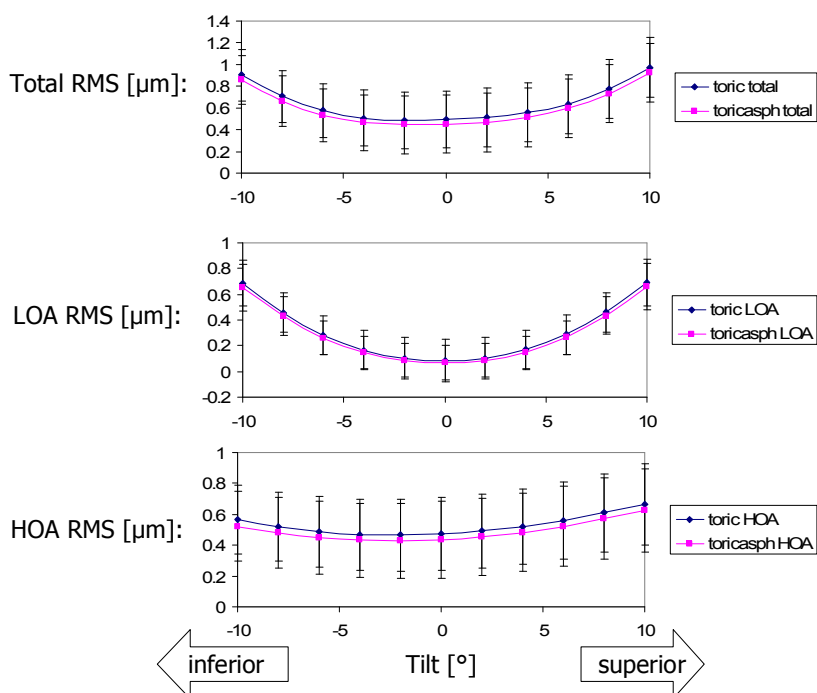**Figure 5-24: Horizontal tilt (6 mm pupil)**
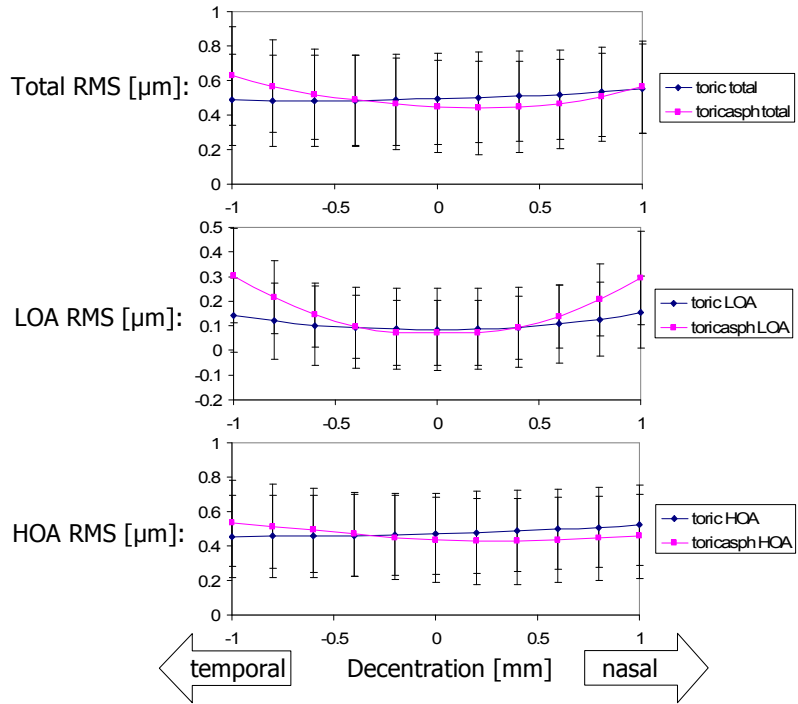

Figure 5-25: Vertical tilt (6 mm pupil)

Figure 5-26: Horizontal decentration (6 mm pupil)
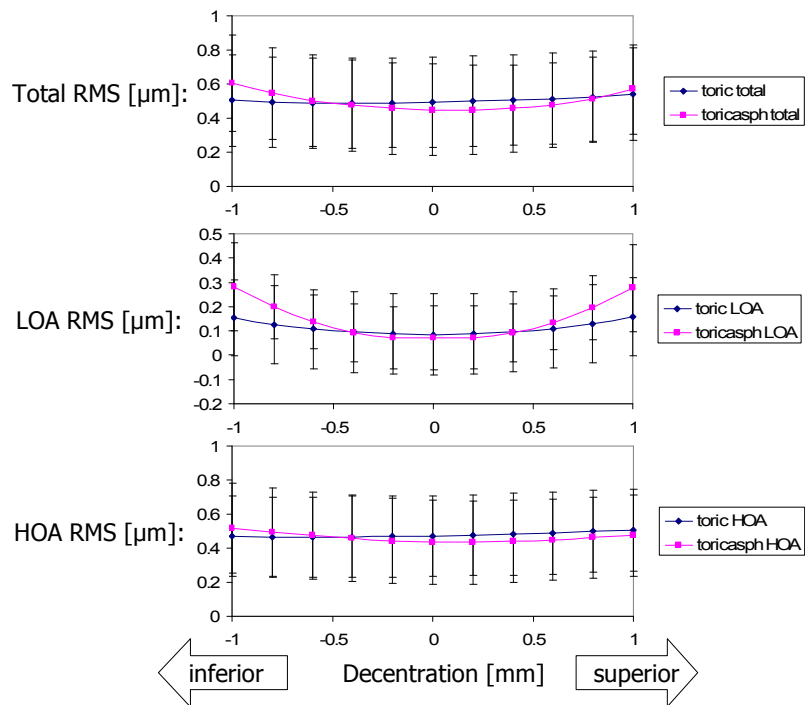

Figure 5-27: Vertical decentration (6 mm pupil)

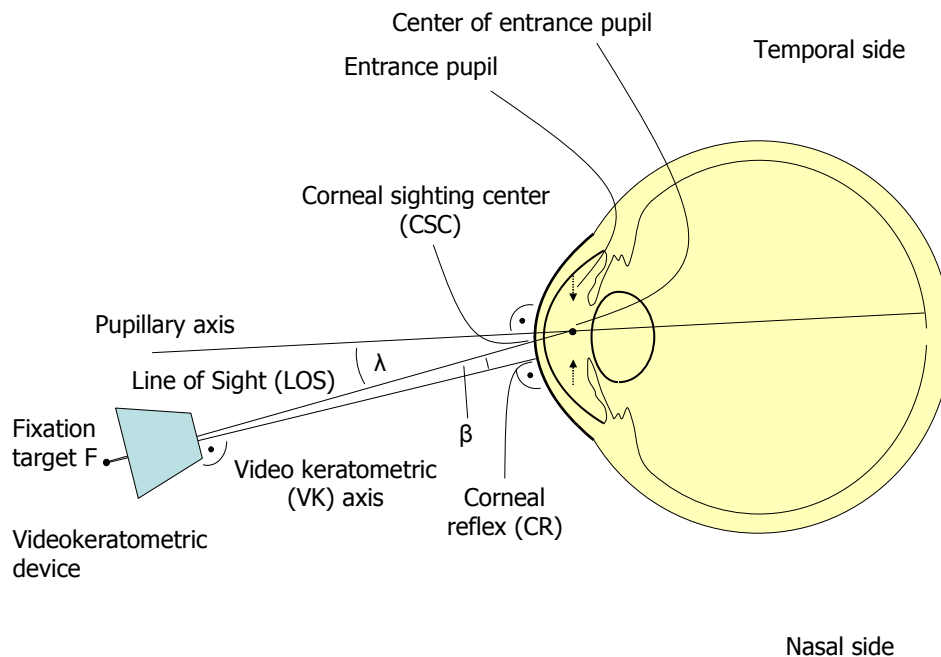## 5.2.4 Discussion

Investigation of Reference Axes

Figure 5-28: Schematic view of reference axes

Many different reference axes of the eye have been defined; a comprehensive review is given by Atchison et al. (Atchison and Smith 2000) [p. 30 ff.]. The important axes and points for the purpose of this investigation are shown in Figure 5-28. The terms and definitions of Atchison et al. are referred to as they are widely accepted. The LOS is the line joining the fixation point and the center of the entrance pupil. It is the most important axis from the point of view of visual function and has been established as the reference axis for reporting aberrations of the eye (Applegate, Thibos et al. 2000; Thibos, Applegate et al. 2000; Thibos, Applegate et al. 2002). As the pupil's position depends on the size (resulting from different illumination levels) this is also the case for the LOS. The LOS intercepts the cornea in the point CSC (Mandell 1995; Mandell, Chiang et al. 1995). The *pupillary axis* (PA) is the line passing through the center of the entrance pupil which is normal to the cornea. The VK axis is the axis of a videokeratometer. When a videokeratometer is used in standard mode the VK axis is normal to the cornea. It is normally not coincident with the LOS and neither passes through the CSC, nor does it pass through the *corneal apex* (Mandell 1994; Mandell, Chiang et al. 1995; Mandell and Horner 1995). The VK axis strikes the cornea at the corneal reflex CR (sometimes also called *corneal vertex*) – that is the first Purkinje image of the fixation light. (This point must not be confused with the corneal apex that is defined as the position of maximum corneal curvature.) The LOS and PA define the angle λ while the LOS and VK axis define the angle β. It has been reported that for most patients the PA is temporal with respect to the LOS; that means the angle lambda is positive (Atchison and Smith 2000) [p. 36]. This would imply that also the CSC is displaced in temporal direction relative to the CR (see Figure 5-8). The present results do not show this in the measured sample of patient eyes as there is only a negligible small average temporal displacement of the CSC of -0.05 and -0.02 mm (Figure 5-11). To ensure that this is not the result of a possibly changed fixation behavior of the patients due to the cataract surgery and the implanted IOL, the CSC positions from postoperative topographies were compared to those measured preoperatively – no

obvious offset was found (Figure 5-12). Studies found that the pupil center moves in temporal direction with increasing size (Atchison and Smith 2000) [p. 23] – as long as natural dilatation is assessed, this may be different for pharmacologically dilated pupils (Porter, Yoon et al. 2006). Sobaci et al. found no difference between pupil size and centroid shift between phakic and pseudophakic eyes (Sobaci, Erdem et al. 2007). Yang et al. studied the pupil location under different light conditions and reported a temporal offset of the CSC with respect to the CR of 0.202 mm in photopic conditions (with a mean pupil diameter of 4.06 mm) (Yang, Thompson et al. 2002). They also found a "small but significant" average temporal shift of 0.13 mm from photopic to mesopic conditions and even more to pharmacologically dilated conditions. The average pupil size of the patients in the present investigation was only 2.52 mm; it might be one possible explanation of the contrary results that small pupils move nasally.

Corneal wavefront aberration was calculated for right and left eyes separately with respect to different reference axes (Figure 5-13 and Figure 5-14). The difference between the VK axis and LOS is rather small; horizontal coma is slightly increased. To take into account that the pupil diameters in this study were very small and eventually move temporally when dilated, additionally a LOS simulating a dilated pupil was calculated by adding a temporal offset of 0.2 mm to the actually measured locations. As a result the horizontal coma is increased by approximately 0.1 µm. SA in special is not greatly influenced by the different reference axes. Salmon et al. proposed that "for small angles of angle lambda […] the VK-tilt problem can probably be safely ignored" (Salmon and Thibos 2002). As there are no great differences for the patient eyes of this study, the VK axis was used as a reference for the further calculations.

Corneal Asphericity and Spherical Aberration

The geometrical quantity asphericity is well-defined according to Baker's equation (2-16) with an apical radius and asphericity. However the determination of the asphericity out of corneal topography maps is not trivial for several reasons. This discussion will focus on the determination of asphericity from corneal elevation maps, though it is in principle possible to extract the asphericity from other display variants as axial curvature maps, too. First of all, since the cornea in general is not rotationally symmetric, there can principally be a different asphericity for each meridian, respectively for each semi-meridian. Second, the term asphericity is defined for an ellipsoid – since the cornea in general will never be a perfect ellipsoid, the description with radius and asphericity will be a simplification in most cases. When the asphericity is determined from a meridian of corneal elevation, typically some kind of mathematical fit is used over a specified corneal diameter. When the cornea is no perfect ellipsoid, the choice of corneal fit diameter has a direct impact on the resulting asphericity. Another very critical issue is the determination of the apical radius. From the mathematical and optical definition, the apical radius is the radius of curvature at the apex. The determination of this apical radius needs to be very exact, because the asphericity depends directly on it. Additionally complicating is the fact, that most measuring devices like videotopometers based on Placido rings do have an inherent difficulty in measuring the apical radius because the first measurement point (e.g. first ring) already has some distance to the apex. It is further of importance to hold the apical radius constant, when determining the asphericity for different corneal diameters. Having different apical radii for different corneal diameters obtained by some mathematical fit does not stick to the geometrical definition of the apical radius. Apart from these computational details, all calculations, of course, rely on the correctness of the elevation data used as input. Since there are many different measuring devices using different algorithms or even different measurement principles (e.g. Placido, Scheimpflug) the choice of measurement device has surely an impact on the results, too.

As stated in the introduction, the refraction at an aspherical surface specified by the geometric quantity asphericity leads to spherical aberration in the wavefront. When considering the (in-

focus) wavefront aberration of rotationally symmetric ellipsoids according to Baker's equation (as done in Figure 5-7) the only resulting aberration is the $Z(4,0)$. If apical radius and asphericity of a real cornea are used, the SA can be calculated from these values. However, if the SA is determined this way, it will include all critical issues in the determination of asphericity discussed in the preceding paragraph. A probably more robust method is directly using the raw elevation data for the calculation of SA by RRT. This avoids the critical determination of asphericity; however, the impact of different measurement devices is still present.

Some of these issues around asphericity and spherical aberration were addressed in the present analysis. Two corneal topography units were used; however they rely on the same basic principle (Placido disk) and similar algorithms for determination of the corneal elevation. To assess apical radius and asphericity the raw elevation maps were fitted to biconic surfaces (Figure 5-15). Besides the offset in the apical radii (that is not critical for the calculations in this section) there were no big differences between the two systems. Both set of topographies showed the tendency of increasing negative asphericity with increasing corneal diameter, as found by others (Holladay 2006; Koller, Iseli et al. 2006; Gonzalez-Meijome, Villa-Collar et al. 2007). Mean asphericities of both systems for 6 mm ($Q = -0.22$ and -0.16) are comparable to Liou and Brennan's model eye that claims to simulate the correct amount of spherical aberration of real eyes and has an asphericity of $Q = -0.18$ (Liou and Brennan 1997). It is therefore no surprise that the spherical aberration using the biconic surface and the average values of the topographies show a very similar SA as a biconic surface using Liou and Brennan's model eye parameters (Figure 5-16). The correctness of the SA obtained with RRT from (theoretical) biconic and spherical surfaces was verified with the optical design program OSLO EDU Edition 6.4.2 (Lambda Research Corporation, USA). Since the spherical aberrations are very similar for elevation and biconic surfaces (including the sphere) the following discussion is referred to 6 mm corneal diameter. The values for this corneal diameter obtained from raw elevation are significantly lower than those from the biconic surface fits, approximately only half in average. Holladay reported lower SA calculated from raw elevation than from conic surface fits, too, and proposes the use of figured conics (Holladay 2006). The values for $Z(4,0)$ recently reported in literature are somewhat higher than those found in this study, ranging around $+0.25$ µm (Holladay, Piers et al. 2002; Wang, Dai et al. 2003; Guirao, Tejedor et al. 2004; Kasper, Buhren et al. 2006a; Beiko, Haigis et al. 2007; Piers, Weeber et al. 2007). Different topography systems and different calculation methods were used. According to Salmon there are principally three main approaches to calculate corneal wavefront aberration from topography data: Fermat's principle, the surface aberration method and ray tracing (Salmon 1999) [p. 69]. Ray tracing is referred to as the "gold standard" since it is based directly on Snell's law – this is the method also used in the present thesis. Fermat's principle and surface aberration methods are somewhat simpler to implement, for example because they do not explicitly need surface normals, but therefore introduce some approximations. Guirao et al. proposed a surface aberration method for calculating corneal wavefront aberration that is often used in literature (Guirao and Artal 2000); this method was used by some of the cited studies for determining corneal SA (Holladay, Piers et al. 2002; Guirao, Tejedor et al. 2004; Piers, Weeber et al. 2007). Another popular method for obtaining the SA is the commercial program VOL-Pro (Sarver and Associates, Inc., USA) that is able to import topography files from different corneal topographers (see page 32 and footnote 3). According to the user's manual the calculation of the wavefront is based on some ray tracing approach with explicit use of surface normals (CTView user's guide 2001) [p. 105 ff.]. Most other studies cited were based on this approach (Wang, Dai et al. 2003; Kasper, Buhren et al. 2006a; Beiko, Haigis et al. 2007). For validation purpose of the used algorithms, some representative elevation data from the present study was imported into VOL-Pro and the wavefront aberrations were compared to the ones obtained by

the analysis with RRT – the results were similar, no systematic offset was found (however it was crucial to setup the correct corneal diameter for the Zernike fit in VOL-Pro to get correct values). The difference of $Z(4,0)$ therefore obviously arises from the input elevation data. Since the OphthaTOP system was successfully tested in measuring aspherical test surfaces (own tests), one remaining possible reason for this discrepancy is the relatively small subset of only 45 (elderly) patients that may be not exactly meet the average SA of the population. Figure 5-17 shows the dependency of spherical aberration and asphericity for real eyes (just as Figure 5-7 shows it for a model eye). It can be seen that the polynomial fit shows a similar characteristics than the model curve with a spherical aberration of zero around an asphericity of -0.5. However the individual values show quite big deviations from theoretically expected ones for conic surfaces – so using only asphericity calculated from topography as an indicator for spherical aberration may not be sufficient (this is in agreement to (Holladay 2006)).

Customized IOLs

The first goal of cataract surgery (besides the reconstruction of lens transparency) is to restore a patient's Snellen visual acuity; that means to correctly choose the IOLs refractive power in terms of diopters to correct a patient's sphere and eventually cylinder in terms of spectacle correction. (The cylinder has to be corrected either by a toric IOL of by additional toric spectacles.) With the introduction of advanced measuring techniques as videotopography or especially wavefront measuring devices the knowledge about human optics increased and today additional efforts are made to increase the quality of vision for post cataract patients. As described in the introduction a second goal of cataract surgery has to be achieved, that is to reestablish a patient's contrast sensitivity by compensating the positive spherical aberration of the cornea. The current concept used in clinical practice is to implant aspherical IOLs with a fixed amount of negative spherical aberration intended to correct the average positive corneal spherical aberration by some degree. The first commercially available aspherical IOL was the Tecnis Z9000 (Advanced Medical Optics, Inc., USA; former Pharmacia, Netherlands) (Altmann 2004; Packer, Fine et al. 2004a) inducing a negative SA of -0.27 µm for a 6 mm pupil (Holladay, Piers et al. 2002) intended to completely eliminate total ocular SA to zero. Piers et al. used adaptive optics to show the potential benefit of completely eliminating the SA (Piers, Fernandez et al. 2004). The AcrySof IQ (Alcon Laboratories, Inc., USA) IOL has a negative SA of -0.20 µm for 6 mm (personal communication with Alcon) intended not to completely eliminate the total SA but leaving some amount of positive SA what should be advantageous for a patient. The SofPort (Bausch & Lomb, Inc., USA) IOL claims to have a SA of zero according to the manufacturer with the goal to not increase the SA of a patient and to be not as sensitive to tilt and decentration as other aspherical IOLs. Although there are others, too, these three IOLs are the most popular aspherical ones used today. Choosing an IOL to correct SA implies knowledge about the SA of the cornea beyond simple K-readings that are used in state-of-the-art IOL calculation formulae (see section 5.1.4). The corneal SA has to be determined what is typically done based on measurements with a videotopometer as described in the preceding paragraph. Therefore, in a design process for an IOL with a fixed SA typically a large number of corneas have been analyzed to determine an average corneal SA for general use. Since it has been shown that the corneal SA varies greatly between individuals (Mrochen, Jankov et al. 2003; Wang, Dai et al. 2003; Guirao, Tejedor et al. 2004; Iseli, Jankov et al. 2006; Lombardo, Lombardo et al. 2006; Gonzalez-Meijome, Villa-Collar et al. 2007; Piers, Weeber et al. 2007) one might agree with Beiko et al. who state "Without [individual] measurement, the implantation of an IOL with a given spherical aberration aimed at correcting the mean value for a population is akin to placing an IOL with a power of +19.00 diopters in all cataract patients because it is the mean power for the population." (Beiko, Haigis et al. 2007). However it might not be sufficient to only consider the corneal SA alone but it may be necessary to include the full spectrum of corneal HOAs when aiming for the

optimum aspherical IOL, as indicated by theoretical investigations of Wang et al. (Wang and Koch 2007) as well as practical measurements using adaptive optics by Piers et al. (Piers, Manzanera et al. 2007).

In the present study customized aspherical IOLs were calculated based on individual measurements – including all corneal HOAs – and their optical performance evaluated in terms of Zernike approximations of the resulting ocular wavefronts. Two optical quality criterions were used in the optimization process, RMS WFE and RMS spot size. Which criterion the human eye actually uses is unknown (see page 52). A difference in the resulting IOL geometry was found when using the two criterions – so minimizing RMS WFE or minimizing RMS spot size is not generally the same. When using RMS spot size the results of all calculations show that there is some interaction between SA and defocus (e.g. Figure 5-19): when there is some positive SA left, optimizing spot size leads to negative defocus, while optimizing WFE guarantees zero defocus. However when aspherical IOLs are used, there tends to be only minor difference between optimizing RMS WFE and RMS spot size.

Calculating the different IOL types for the model eye nicely leads to the expected results in wavefront aberration (Figure 5-18). The spherical IOL corrects the defocus; the aspherical IOL corrects defocus and SA. The toric IOL corrects the defocus and astigmatism; and the toric aspherical IOL finally corrects defocus, astigmatism and SA – since there are no HOAs in the model eye the total RMS is almost zero. Note that the correction of the toric anterior surface of the IOL can alternatively be corrected by spectacles – thus the results of the toric aspherical IOL can, in principle, be achieved with an aspherical IOL and toric spectacles, too.

The results for the real eyes are not as easy to interpret (Figure 5-20). The difference between the model eye and the real eyes is that the real eyes have additional HOAs besides SA. The great variation of the Zernike coefficients can be seen at the error bars – in average most of the coefficients are around zero (because they are randomly distributed). However the average SA for the spherical and toric IOL is positive, as expected (positive average corneal SA plus positive SA of the IOL). Although the individual higher order Zernike coefficients are around zero in average, the average RMS HOA is far away from zero. The defocus shows small standard deviation while those of the uncorrected astigmatism (non-toric IOL) coefficients are huge. With the toric IOLs the astigmatism is well corrected – RMS LOAs are greatly reduced. In contrast to the model eye, the SA RMS and $Z(4,0)$ are not identical, because of the secondary SA. With the aspherical and toric aspherical IOLs the SA RMS is reduced, but not to zero. (When SA RMS would be used as the minimization criterion, it would surely be possible to reduce it to almost zero – but this will lead to an increased total RMS what is not desirable.) As a result of the smaller SA RMS the HOA RMS are also reduced – but still remain large. Let's keep in mind, that it is the total RMS that should be minimal at the end. The toric aspherical IOL gives the smallest total RMS that is not much larger than the HOA RMS (the SA RMS is smaller by over a factor of 6 and thus plays a minor role) – that means that the optical performance is limited by the HOAs of the cornea that cannot be further reduced with that type of IOL.

An aspherical IOL with intended negative spherical aberration needs a prolate, parabolic or hyperbolic surface. Values for asphericities found in literature are rare: Gerste et al. cites a model calculation for an average eye done by W. Fiala that results in an asphericity for one surface of $Q = -6.31$ (Gerste 2004). Werner et al. propose one aspherical surface with $Q = -6.5$ (Werner and Roth 1999). Kurz et al. speak of values $Q = -5$ and -8 (Kurz, Krummenauer et al. 2007). Dietze et al. propose a bi-aspherical surface with anterior $Q = -30.29$ and posterior $Q = -12.79$ (Dietze and Cox 2005). In theory, there are various possibilities to design an IOL with negative spherical aberration. Asphericity can be provided in the anterior and/or posterior surface and depends strongly on the refractive index of the lens material and the apical radii of curvature of the anterior and posterior surfaces (that are highly variable depending on the lens design, too). Since most cited studies do not provide the complete geometry data of the IOLs

the pure specification of a Q value is of limited information. Holladay et al. describe the shape of the Z9000 IOL that has a modified prolate anterior surface, a figured conic with polynomials of 4th and 6th (see equation (2-19)) without providing absolute values (Holladay, Piers et al. 2002). Altmann et al. gives some absolute values for a 22 diopter version of the Z9000 and the Sofport IOLs (Altmann, Nichamin et al. 2005): the Z9000 IOL is equiconvex with an aspherical anterior surface (Q = -1.04 and two additional polynomials of 4th and 6th order; the small absolute value of Q is somewhat misleading, own calculations with RRT show that very similar results can be achieved with slightly changed anterior radius of curvature and an approximate Q = -22); the SofPort IOL is biconvex with both surfaces aspherical (Q = -1.09) and claims to have no SA (verified by own calculations with RRT). As written in the methods section it is crucial to optimize the radius R and the asphericity Q simultaneously during the optimization process of an aspherical IOL. For example, Kurz et al. propose to first calculate the apical radius and then – in a separate step with unchanged radius – optimize the asphericity. This is not recommended because it leads to bigger spot sizes and wavefront aberration. Table 5-6 shows the geometries of the IOLs calculated by RRT. This, of course, is only one of many ways to design aspherical IOLs. However the Q-values for the anterior surface with an apical radius of 25 mm calculated with RRT are far more negative as those from the cited literature.

The crucial role of the HOAs of the real eyes is summarized in Figure 5-23: With the toric aspherical IOL the smallest total RMS WFE is achieved with completely eliminated SA RMS = HOA RMS in the model eye. In the real eyes the smallest total RMS WFE that can be achieved with an aspherical toric IOL by reducing SA RMS is slightly smaller than with the toric IOL. However, the HOA RMS is still large.

Unfortunately there are no measurements with some wavefront measuring device available of the patient eyes used in this study for comparison purpose with the theoretically calculated values from RRT. But the present results can be compared to literature of others who measured wavefront aberration of phakic and pseudophakic eyes. Whenever Zernike values are compared among studies it is absolutely crucial to ensure that all general conditions are equal. First of all the standards proposed in 2001 for reporting the aberrations of the eye should be maintained (Thibos, Applegate et al. 2002); as this was a serious problem in the early times of wavefront measuring most current devices stick to the OSA standards (Mrochen 2002). Important things like the numbering schema and the normalization factor of the Zernike polynomials are defined by those standards (see page 10). Second, it has to be kept in mind that – even if they report the aberration according to the OSA standard – there may be substantial differences between commercial available wavefront measuring devices, especially if they use different principles as introduced on page 26 (Burakgazi, Tinio et al. 2006). And finally, as the wavefront greatly depends on pupil diameter, only Zernike values obtained from the same pupil diameters are comparable. When reviewing statistics, especially average values, let's keep in mind that RMS values are always unsigned while Zernike coefficients are signed. There are numerous studies measuring the wavefront aberration of normal phakic eyes; at this point only one outstanding study is cited for comparison: Salmon et al. recently published a study that collected data from 10 laboratories that measured HOAs in normal, healthy adult eyes. Various commercial devices were used, all relying on Hartmann-Shack aberrometry and a "good agreement between the different data sets" was found. 2560 eyes were evaluated and they found at 6 mm pupil HOA RMS (3rd to 6th order) of 0.327 ± 0.130 µm; SA RMS (Z(4,0) and Z(6,0)) of 0.133 ± 0.094 µm and Z(4,0) of 0.128 ± 0.096 µm (Salmon and van de Pol 2006). There are also several studies measuring the wavefront of pseudophakic eyes[4], but not all are suitable for comparison with this study

---

[4] Measurements of multifocal IOLs are not included since this is not of interest in the context of this section. Furthermore, though attempts were made, it remains doubtful if refractive and especially diffractive multifocal IOLs can be properly measured with wavefront measurement devices (Charman, Montes-Mico et al. 2007).

(Miller, Anwaruddin et al. 2002; Barbero, Marcos et al. 2003; Mester, Dillinger et al. 2003; Taketani, Matuura et al. 2004; Vilarrodona, Barrett et al. 2004; Choi, Kim et al. 2005; Marcos, Barbero et al. 2005; Rocha, Chalita et al. 2005; Chen, Ye et al. 2006; Iseli, Jankov et al. 2006; Tabernero, Piers et al. 2006; Bellucci, Morselli et al. 2007; Caporossi, Martone et al. 2007; Kurz, Krummenauer et al. 2007; Oshika, Sugita et al. 2007; Piers, Weeber et al. 2007). In this context only a few meet the requirements of obeying the OSA standard and providing data for total HOA RMS for a 6 mm pupil that can be compared to the values calculated by RRT: these are summarized in Table 5-7.

Study	Setting	Spherical IOLs			Aspherical IOLs		
		Number of Eyes (IOL type [1])	HOA RMS (3rd to 6th) [µm] Mean ± SD	Z(4,0) [µm] Mean ± SD	Number of Eyes (IOL type [1])	HOA RMS (3rd to 6th) [µm] Mean ± SD	Z(4,0) [µm] Mean ± SD
(Bellucci, Morselli et al. 2004) [2]	Italy	n = 5 (911Edge)	0.75 ± 0.10 [3]	0.20 ± 0.10 [3]	n = 5 (Z9000)	0.60 ± 0.30 [3]	0.02 ± 0.02 [3]
		n = 5 (SA60AT)	0.65 ± 0.20 [3]	0.45 ± 0.08 [3]			
		n = 5 (MA60BM)	0.75 ± 0.20 [3]	0.50 ± 0.10 [3]			
		n = 5 (AR40e)	0.60 ± 0.15 [3]	0.28 ± 0.12 [3]			
(Taketani, Matsuura et al. 2004) [2]	Japan	n = 24 (H60M)	0.80 ± 0.23	-	-	-	-
		n = 25 (MA30BA)	1.00 ± 0.54				
(Taketani, Yukawa et al. 2005) [2]	Japan	n = 30 (60BB)	1.00 ± 0.38	-	-	-	-
		n = 34 (MA60AC)	0.97 ± 0.33				
(Pesudovs, Dietze et al. 2005) [4]	United Kingdom	n = 20 (722C)	0.42 ± 0.17	0.24 ± 0.09	-	-	-
		n = 21 (MA30BA, MA60BM)	0.54 ± 0.25	0.32 ± 0.17			
		n = 16 (MA30BA, MA60BM)	0.66 ± 0.23	0.42 ± 0.15			
(Kasper, Buhren et al. 2006a) [5]	Germany	n = 21 (AR40e)	0.66 (3rd to 5th)	0.37	n = 21 (Z9000)	0.50 (3rd to 5th)	0.09
(Padmanabhan, Yoon et al. 2006) [6]	USA	n = 62 (MA60BM)	0.67 ± 0.34	0.37 ± 0.16	-	-	-
(Padmanabhan, Rao et al. 2006) [6]	USA	n = 32 (MA60BM)	0.70 [3]	0.29 ± 0.21	n = 32 (Z9000)	0.70 [3]	0.07 ± 0.12
		n = 16 (AR40e)	0.65 [3]	0.20 ± 0.09			
(Nishi, Nawa et al. 2006) [2]	Japan	n = 44 (SA60AT)	0.78 ± 0.20	0.53 ± 0.28	-	-	-
(Munoz, Albarran-Diego et al. 2006) [2]	Spain	n = 15 (AR40e)	1.10 ± 0.50 [3]	0.15 ± 0.17 [3]	n = 30 (Z9000)	1.10 ± 0.50 [7]	-0.03 ± 0.29
		n = 15 (Stabibag)	1.50 ± 1.50 [3]	0.21 ± 0.21 [3]			
(Awwad, Lehmann et al. 2007) [8]	USA	n = 13 (SN60AT)	0.56 ± 0.13	-	n = 15 (SN60WF)	0.44 ± 0.14	-
(Tzelikis, Akaishi et al. 2007) [5]	Brazil	n = 25 (SN60AT)	0.90 ± 0.27 (3rd to 5th)	0.19 ± 0.10 ("mean SA")	n = 25 (SN60WF)	0.66 ± 0.37 (3rd to 5th)	0.03 ± 0.03 ("mean SA")

[1] full names of the IOLs: Acryfold 60BB (HOYA, Japan); AcrySof SA60AT, SN60WF, MA60BM, MA60AC and MA30BA (Alcon Laboratories, Inc., USA); CeeOn 911Edge (Advanced Medical Optics, Inc., USA); Hydroview H60M (Bausch & Lomb, Inc., USA); Sensar AR40e (Advanced Medical Optics, Inc., USA); Stabibag (Ioltech, France); Tecnis Z9000 (Advanced Medical Optics, Inc., USA); 722C PMMA (Pharmacia, Netherlands);
[2] measured with Hartmann-Shack principle (KR-9000PW, Topcon, Japan)
[3] approximate values read from diagram
[4] measured with Hartmann-Shack principle
[5] measured with Hartmann-Shack principle (Zywave, Bausch & Lomb, Inc., USA)
[6] measured with Tscherning principle (ALLEGRETTO WAVE Analyzer, WaveLight AG, Germany)
[7] approximate values read from diagram, two Z9000 groups combined
[8] measured with Hartmann-Shack principle (LADARWave, Alcon Laboratories, Inc., USA)

Table 5-7: Wavefront measurements of pseudophakic eyes reported for a 6 mm pupil according to the OSA standard

The total RMS calculated by RRT is 0.47 µm for the spherical and 0.44 µm for the aspherical IOLs (Figure 5-23). Despite of Awwad et al. who exactly measure 0.44 µm for their aspherical IOLs, the other actually measured values are all somewhat higher. One reason can be that the IOLs calculated in RRT are perfectly aligned while the measured eyes surely suffer from some tilt and decentration. But the order of magnitude predicted by RRT lies in the same range than the actually measured. What is essential and can be seen comparing the different studies: the Z(4,0) is reduced by the aspherical IOLs; but the total RMS is only slightly reduced compared to the spherical IOLs. The biggest reduction had Awaad et al. from 0.56 to

0.44 µm, while Munoz et al. only have a reduction in the Stabibag group. Bellucci et al. tested five different IOLs. Three groups of spherical IOLs result in slightly higher values for total RMS, while one group performed just as good as the aspherical group. Padmanabhan et al. found a reduction of Z(4,0) for the Z9000 but "no significant differences in the RMS of the total higher order aberrations among all three groups of IOLs" (Padmanabhan, Rao et al. 2006). Also interesting is the study of Denoyer et al. that provides wavefront measurement data of 20 eyes with a CeeOn Edge 911 (Advanced Medical Optics, Inc., USA) and 20 eyes with a Z9000 measured with a Hartmann-Shack device (Wavescan, VISX, USA) (Denoyer, Le Lez et al. 2007). The results are not included in Table 5-7 because they refer to a 5 mm pupil: HOA RMS for the Edge 911 was 0.33 ± 0.18 µm and for the Z9000 was 0.32 ± 0.08 µm – almost the same (similar results also in (Denoyer, Roger et al. 2006)). Dietze et al. also measured pseudophakic eyes with a Hartmann-Shack device. Based on their measurements they conclude that the total HOA RMS might be reduced by the elimination of SA by 19-20 % (Dietze and Cox 2005). With RRT customized aspherical IOLs were calculated with ideal geometries for minimizing the total HOA RMS. SA RMS is not totally eliminated and based on the calculations on RRT the total HOA RMS might be reduced by 8.5 %. Since the studies cited measured pseudophakic eyes with non-customized aspherical IOLs providing a fixed value of SA the reduction may be even less. Most measured total RMS values verify this theoretically predicted limited benefit. Because the potential gain is small for the wavefront aberration, this may also be the reason for some controversial discussion (Packer, Fine et al. 2006b) and the discrepancy in literature between studies clinically investigating the benefit of aspherical IOLs regarding the patient's contrast sensitivity. The studies supported by the aspherical lens manufacturer (Packer, Fine et al. 2002; Mester, Dillinger et al. 2003; Bellucci, Morselli et al. 2004; Packer, Fine et al. 2004b; Bellucci, Scialdone et al. 2005) as well as other studies (Kershner 2003; Kennis, Huygens et al. 2004; Denoyer, Roger et al. 2006; Caporossi, Martone et al. 2007; Denoyer, Le Lez et al. 2007) reported better contrast sensitivity of patients with an aspherical Z9000 IOL than of those with a spherical IOL. Other studies found no benefit of the aspherical Z9000 IOL (Kasper, Buhren et al. 2006b; Munoz, Albarran-Diego et al. 2006). Caporossi found a benefit in terms of photopic and mesopic contrast sensitivity not only for the Z9000 but also for two other aspherical IOL models (AcrySof IQ and Sofport) compared to spherical IOLs (Caporossi, Martone et al. 2007). Tzelikis recently reported better contrast sensitivity in mesopic conditions for the AcrySof IQ lens compared to a spherical (Tzelikis, Akaishi et al. 2007). Kurz et al. found no benefit testing the aspherical Acri.Smart 36 A IOL (Acri.Tec AG, Germany) (Kurz, Krummenauer et al. 2007).

It is obvious to think about IOLs that not only correct for the SA. This would lead to the design of customized IOLs that correct other higher order aberration beyond spherical aberration as recently simulated theoretically (Wang and Koch 2005; Piers, Weeber et al. 2007). If it once becomes possible to manufacture such IOLs this may be an interesting future application for RRT. However, the question of the correct positioning of such IOLs will still be an important issue, as discussed next.

Tilt and Decentration

The effects of displacement of IOLs have been studied for spherical IOLs (Atchison 1989a; Atchison 1989b; Erickson 1990; Korynta, Bok et al. 1994; Korynta, Bok et al. 1999). As long as aspherical IOLs are considered there is also the discussion that they may be more sensible to tilt and decentration. Atchison already investigated the influence of tilt and decentration of IOLs and concluded that the aspherical IOLs have to be well centered in order to outperform spherical IOLs (Atchison 1991). With the proposal of their new lens design Holladay et al. simulate the performance of the IOL for a 5 mm pupil and state, that if the aspherical IOL is centered within 0.4 mm and tilted less than 7 degrees it will exceed the performance of a

conventional spherical IOL (Holladay, Piers et al. 2002); referred to by others (Packer, Fine et al. 2002; Packer, Fine et al. 2004b). Preussner et al. concludes that "the sensitivity against decentration is generally greater the more "customized" the optical properties are" (Preussner and Wahl 2003). Dietze et al. studied their aspherical IOL model in contrast to a spherical one and found similar sensitivity of the different lenses to tilt; however if the aspherical IOL is decentered more than approximately 0.5 mm it will perform less good as the spherical IOL for a 4.4 mm pupil (Dietze and Cox 2005). Altmann et al. studied the influence of decentration for three different IOL models (spherical IOL vs. aspherical with negative SA IOL vs. aspherical with zero SA IOL) (Altmann, Nichamin et al. 2005). Sarver et al. used the geometries provided by Altmann and also studied the effect of decentration in some model eyes (Sarver, Wang et al. 2006). Tabernero et al. recently presented an eye model to address "the problem of IOL misalignments with a completely realistic approach" (Tabernero, Piers et al. 2006). All those studies mentioned so far rely on considerations of monochromatic light. Recently, Piers et al. did simulations for the Z9000 IOL using polychromatic eye models that in addition to spherical aberration also include higher order aberrations representative for the population mean. Based on their model the tolerances are significantly higher than from previous studies. They predict a better performance of the aspherical IOL compared to a spherical IOL as long as the decentration is less than 0.8 mm and the tilt is less than 10° (for a 4 mm pupil) (Packer, Fine et al. 2006a; Piers, Weeber et al. 2007). However they did not specify the direction they tilted and decentered their IOLs.

As Piers et al. the investigation of tilt and decentration with RRT in this study includes all aberrations of the pseudophakic eyes. The analysis was done for a 6 mm pupil. Toric and toric aspherical IOLs were compared. Toric IOLs were used to have the astigmatism corrected for the eyes. In principle, it is possible to achieve the same correction with the combination of toric spectacles to correct the astigmatism and use non-toric spherical and aspherical IOLs, as well. Therefore, in the remaining discussion "spherical IOL" will be used for the toric IOL and "aspherical IOL" will be used for the toric aspherical IOLs for simplicity. The residual wavefront aberration was summed up in HOA RMS, LOA RMS and the combined total RMS (without piston and tilt). The reason of increased LOAs due to tilt and decentration are both, defocus and astigmatism. The reason for increased HOAs is mainly because of the induction of coma. For the IOL tilt there was no greater sensitivity found for the aspherical than for the spherical IOLs (Figure 5-24 and Figure 5-25). For all calculated tilt degrees up to (and may be beyond) 10° the benefit of the aspherical IOLs was preserved. The LOAs show more increase than the HOAs and this increase tends to be symmetrical with respect to the tilt direction. The HOAs show a slight tendency to be more increased in the nasal and superior tilt direction. This can be explained from Figure 5-20: the eyes have a mean vertical coma of -0.09 μm (no matter if right or left eye). Both, spherical and aspherical IOLs induce negative vertical coma when tilted superior. Such a superior tilt induces negative vertical coma (amplifying the already existing) while an inferior tilt induces positive coma that compensates existing coma to some degree. In Figure 5-20 right and left eyes are merged, the resulting average horizontal coma is +0.03 μm – however separating leads to an average of horizontal coma for right eye of -0.10 μm and +0.13 μm for left eyes (for all types of IOLs). The analysis of the subset of 32 eyes (with pupils) shows similar values of -0.11 μm for right and +0.12 μm for right eyes (Figure 5-13 and Figure 5-14). Thus, a nasal tilt of the IOL amplifies the preexisting coma (resulting in more negative coma for right and more positive coma for the left eyes having the rotation directions specified in Figure 5-10 in mind), while the temporal compensates. Greater sensitivity for the aspherical IOL was found for decentration (Figure 5-26 and Figure 5-27). The increase of LOAs is significantly higher for the aspherical IOL; both curves are symmetric with respect to the direction of decentration. Let's keep in mind that these LOAs can be corrected by means of spectacles, if desired – so if the patient needs them anyway this would be only a shift of sphere and cylinder. The HOAs show an interesting behavior. Model

calculations have shown that aspherical IOLs are more sensitive than spherical IOLs, specifically inducing more coma. RRT was used to simulate a spherical and an aspherical IOL when decentered in the same direction by the same magnitude: the aspherical IOL induces approximately 4 times as much coma as the spherical IOL – but with opposite sign. This explains the curve in Figure 5-27: the preexisting average negative vertical coma of -0.09 μm of the patient eyes is amplified by the additional induced negative coma of the superior decentered spherical IOL while it is compensated by the superior decentered aspherical IOL – preserving the benefit of the aspherical IOL even beyond 1.0 mm decentration. In the inferior direction this is the other way round destroying the benefit of the aspherical IOL for more than 0.4 mm decentration. This is similar for the horizontal decentration Figure 5-26: the negative horizontal coma is amplified by the nasally decentered spherical IOL and compensated by the aspherical for right eyes – and with opposite decentration direction and sign of coma the same happens to left eyes. So for nasal decentration the benefit of the aspherical IOL is preserved beyond 1.0 mm while it is lost around 0.4 mm decentered temporally. The asymmetry of the HOA curves is reflected in the total RMS curve for horizontal and vertical decentration. In terms of total RMS, the benefit of the aspherical IOL is preserved when not decentered more than approximately 0.4 mm in temporal and inferior direction, and not more than around 0.9 mm in nasal and superior direction.

This is the first investigation to the knowledge of the author that studies the effects of tilt and decentration of spherical and aspherical IOLs using measured pseudophakic eyes including topography and considering different directions of displacement. The study found that aspherical IOLs are not more sensitive to tilt. They neither loose their benefit when tilted, nor does the direction of tilt play a major role. On the other side the aspherical IOLs are more sensitive to decentration. They loose their benefit compared to the spherical IOLs when decentered too much. The magnitude of this limit depends on the direction of decentration, both vertically and horizontally. This is the result of two factors: first, the patient eyes evaluated had average corneal vertical and horizontal coma different from zero. This is not unusual: corneal mirror symmetry has been reported in literature, in particular for horizontal coma (Wang, Dai et al. 2003) (unfortunately no average Zernike coefficients separated for right and left eyes given there). Wu et al. recently measured average corneal horizontal coma of -0.16 μm in right eyes and +0.16 μm in left eyes for 6 mm diameter excellently supporting the results of the present study (Wu, Lu et al. 2006). Padmanabhan et al. measured average ocular vertical coma of -0.11 μm (and trefoil -0.13 μm) for 6 mm pupil in their pseudophakic eyes comparable to the present results in Figure 5-20 (Padmanabhan, Yoon et al. 2006). The second factor is that this existing coma is either amplified or partially compensated by the induced additional coma of the decentered IOLs – with the remarkable difference that the sign of induced coma is opposite between aspherical and spherical IOLs when decentered in the same direction. This behavior was not only found with the aspherical IOLs of the design used in this study described in Figure 5-9 – it was also found when using other aspherical IOL geometries with an anterior aspherical surface, both surfaces aspherical, and also with the geometry of the Z9000. Thus, these findings are likely to be applicable to common commercial aspherical IOLs. Before drawing clinical consequences keep in mind that the simulated tilt and decentration in these calculations were specified with respect to the VK axis. With zero tilt and decentration the IOL is aligned perfectly on the VK axis. Although there was no systematic offset in the present study, some other studies found an average temporal tilt of the pupillary axis to the LOS (positive angle lambda) (Atchison and Smith 2000) [p. 36]. This is an indication that the whole eye is rotated temporally – however this is no proof because it only refers to the entrance pupil and not to the lens position. The potential temporal eye rotation is supported by Yang et al. who found that the CR has an average offset with respect to the geometric corneal center (defined as the limbus center) in nasal superior direction (Yang, Thompson et al. 2002). This is a strong indication of a tilt of the whole eye in

temporal/inferior direction with respect to the VK axis (as drawn schematically in Figure 5-28). It is likely that the "neutral" crystalline and IOL position is tilted temporally/inferior, too. This tilt would lead to a compensation of the corneal coma what can be nicely seen in Figure 5-24 and Figure 5-25: The minimum HOAs seem to be at an estimated temporal tilt around 3° and inferior tilt around 2°. So if the corneal coma is already compensated from the physiological tilt of the IOL the simulated decentration curves in Figure 5-26 and Figure 5-27 of the IOL will be symmetrical – however their different behavior of the spherical and aspherical IOLs inducing coma of opposite signs are still there.

Study	Setting	Number of eyes	IOL [1]	Tilt [mm] Mean ± SD (Range)	Decentration [°] Mean ± SD (Range)	Measurement methods
(Akkin, Ozler et al. 1994)	Turkey	n = 42	foldable	1.13	0.15	-
(Hayashi, Harada et al. 1997)	Japan	n = 225	PMMA & silicone & acryl	2.45	0.33	EAS-1000 [3]
(Kim and Shyn 2001)	Korea	n = 65	MZ60BD	2.67 ± 0.48	0.31 ± 0.15	EAS-1000 [3]
		n = 47	SI-30NB	2.61 ± 0.83	0.32 ± 0.18	
		n = 25	MA60BM	2.69 ± 0.87	0.33 ± 0.19	
(Taketani, Matsuura et al. 2004)	Japan	n = 24	H60M	4.00 ± 2.76	0.42 ± 0.19	EAS-1000 [3]
		n = 25	MA30BA	3.83 ± 2.25	0.44 ± 0.34	
(Taketani, Matuura et al. 2004)	Japan	n = 40	MA30BA	3.43 ± 1.55	0.30 ± 0.17	EAS-1000 [3]
(Taketani, Yukawa et al. 2005)	Japan	n = 30	60BB	2.22 ± 1.44	0.35 ± 0.21	EAS-1000 [3]
		n = 34	MA60AC	3.18 ± 1.84	0.37 ± 0.17	
(Mutlu, Erdurman et al. 2005)	Turkey	n = 45	MA30BA	2.72 ± 0.55 (2.0-3.6)	0.39 ± 0.13 (0.1-0.8)	Purkinje / photographic
		n = 43	SA30AL	2.70 ± 0.84 (2.0-6.1)	0.34 ± 0.08 (0.2-0.6)	
(Hayashi and Hayashi 2005)	Japan	n = 30	MA60BM	1.67 ± 0.94	0.22 ± 0.13	EAS-1000 [3]
		n = 30	SA30AL	1.64 ± 1.00	0.24 ± 0.18	
(Baumeister, Neidhardt et al. 2005)	Germany	n = 106	3-piece foldable	2.74 ± 1.68 [2]	0.25 ± 0.14 [2]	Scheimpflug / anterior eye segment analysis system
(Becker, Holzer et al. 2006)	Germany	n = 43	Z9000	-	0.36	Digital slitlamp photographs
(de Castro, Rosales et al. 2007)	Spain	n = 21	aspherical	< 2.6	< 0.4	comparative: Purkinje (custom built) & Scheimpflug [4]

[1] full names of the IOLs: Acryfold 60BB (HOYA, Japan); AcrySof MA60BA, MA60BM, MA60AC, SA30AL and MA30BA (Alcon Laboratories, Inc., USA); Hydroview H60M (Bausch & Lomb, Inc., USA); MZ60BD (Alcon Laboratories, Inc., USA); SI-30NB (Allergan, Inc., USA); Tecnis Z9000 (Advanced Medical Optics, Inc., USA)
[2] mean of four groups of IOLs
[3] EAS-1000 Anterior Eye Segment Analysis System (Nidek, Japan); based on Scheimpflug principle
[4] Pentacam (OCULUS Optikgeräte GmbH, Germany)

Table 5-8: Studies that measured tilt and decentration of IOLs implanted using state-of-the-art technique (CCC)

It is possible to measure tilt and decentration in vivo with different principles. A review of measurements published in literature was done to compare the limits of dislocation calculated with RRT with the magnitudes that occur in real patient eyes. With older techniques of IOL implantation there were values reported in literature showing a mean tilt of larger than 5.6 degrees and a mean decentration of more than 0.64 mm (Auran, Koester et al. 1990; Kozaki, Tanihara et al. 1991; Akkin, Ozler et al. 1994). Techniques improved and the currently most widely used procedure is *continuous curvilinear capsulorhexis* (CCC) and IOLs are placed *in-the-bag*. So tilt and decentration are much lower today, Table 5-8 gives an overview of some

studies that collected in-vivo measured data. All those studies report similar values; the IOL's material (e.g. PMMA, silicone or acryl) seems to have minor influence on tilt and decentration (Hayashi, Harada et al. 1997; Kim and Shyn 2001). It has to be noted, that the tilt and decentration are typically specified relative to the pupillary axis and the pupil center, respectively, often with dilated pupils. The results of RRT (although specified against the VK axis) show that the decentration direction plays a crucial role. It may therefore be interesting if there are systematic directions for tilt and decentration of the IOLs. Unfortunately, few studies that measured decentration provide a direction. The very few eyes measured by Tabernero et al. do show a slight average decentration in temporal direction (Tabernero, Piers et al. 2006). Rosales et al. clearly show a nasal decentration for their eyes (Rosales and Marcos 2007). De Castro et al. provides measurements that indicate that the average decentration tends to be in nasal superior direction (de Castro, Rosales et al. 2007). With the results of RRT the following conclusions can be drawn: Considering the values in Table 5-8 it can be seen that an IOL will never be positioned ideally as there is always some tilt and decentration inducing aberrations for any type of IOL. However the mean tilt is around 2.7 degrees and the maximum reported value 6 degrees. The results of RRT propose that the IOLs may be even tilted more than 10 degrees without loosing their benefit. The conclusion can be drawn, that tilt is in general no bigger problem for the aspherical than for spherical IOL. Decentration is more critical: Mutlu et al. report a mean decentration of nearly 0.4 mm and a maximum value of around 0.8 mm. From the simulation of others and the results of RRT it can be seen that the aspherical IOL may loose their benefit already around 0.4 mm. However, RRT also showed that tilt as well as decentration induce coma and therefore depend on each other. The direction of decentration is important regarding the opposite signs of induced coma for spherical and aspherical IOLs. Therefore, for proper assessment of the optical properties the tilt and decentration – together with their directions – have to be known with respect to the pupillary axis (that depends on illumination state) and the angle lambda to the LOS. There are only two studies to the knowledge of the author that incorporated some of those quantities in their eye models (Tabernero, Piers et al. 2006; Rosales and Marcos 2007).

Conclusion

For the clinical data in this study only a slight temporal offset of the corneal sighting center relative to the corneal reflex was found (Figure 5-11), what leads to a minor relevance of choosing different reference axes (e.g. line of sight vs. videokeratometric axis) on the calculation of corneal wavefront aberration (Figure 5-13 and Figure 5-14). No systematic difference in the relative position of the corneal sighting center and the corneal reflex was detected when comparing eyes before and after cataract surgery (Figure 5-12).

The assessment of corneal asphericity showed similar values for the two topography devices used in this study using biconic surface fits (Figure 5-15). However, the determination of asphericity turned out to be critical depending on corneal diameter and calculation methods. As a result, the calculation of corneal spherical aberration turned out to result in different – somewhat smaller – values when on using raw elevation data compared to biconic surface fits (Figure 5-16). The clear dependency of corneal asphericity and spherical aberration shown for model calculations based on conic surfaces (Figure 5-7) is principally also seen for elevation data of real eyes (Figure 5-17) – however using the corneal asphericity as an indicator for the corneal spherical aberration may not result in precise values. It is therefore recommended to determine the corneal spherical aberration from the raw elevation data obtained from videokeratography.

RRT has been used to calculate the exact geometry of customized toric aspherical IOLs with the goal of providing smallest possible wavefront aberration. For a model eye with no higher order aberration besides spherical aberration it is possible to completely eliminate higher order aberration. For real eyes the spherical aberration is significantly reduced – and therefore

also the total higher order aberrations (Figure 5-23). However, the potential benefit was somewhat limited, as the reduction of total higher order aberrations was below 10 %. This result of the present theoretical calculations is supported by having a look at the limited reduction of higher order aberrations actually measured in pseudophakic eyes with spherical and aspherical IOLs found in literature (Table 5-7).

The dislocation of spherical and aspherical IOLs was simulated and compared to amounts of clinically measured tilt and decentration reported in literature (Table 5-8). RRT predicts that, in terms of wavefront aberration, aspherical IOLs will likely preserve their potential benefit compared to spherical IOLs for typical clinically occurring values (Figure 5-24 and Figure 5-25). In contrast, the aspherical IOLs may induce more wavefront aberration than spherical IOLs for amounts of decentration around approximately 0.4 mm (Figure 5-26 and Figure 5-27) – this is in an order of magnitude that will likely be exceeded in many eyes as the measurements in literature show. However, for more improved assessment of the wavefront aberration induced it would be necessary to use individual values for tilt and decentration, since they may amplify or compensate each other, depending on the direction. Clinical studies providing comprehensive data with respect to those quantities beyond mean values are rare – once available, they can be easily included in the individual virtual eye to further refine simulation outcome.

5.3 Ablation Profiles for Refractive Surgery

5.3.1 Introduction

Refractive surgery procedures such as LASIK, LASEK or PRK (see section 2.4) have shown to effectively correct the sphere and cylinder error of human eyes. However clinical studies found decreased visual quality regarding contrast sensitivity (Verdon, Bullimore et al. 1996; Applegate and Howland 1997; Schlote, Kriegerowski et al. 1997; Holladay, Dudeja et al. 1999; Schlote, Derse et al. 1999; Seiler, Kaemmerer et al. 2000; Marcos 2001; Anera, Jimenez et al. 2003a; Lee, Hu et al. 2003). This decrease in visual quality is especially observed regarding contrast sensitivity with large pupil diameters and is increasing with the amount of diopters corrected. The result is reduced performance in night vision. Often visual symptoms as halos, glare or starburst are reported that seem to correlate with measured wavefront aberration (Chalita, Chavala et al. 2004). The corneal and total ocular wavefront aberration is typically also increased after corneal refractive surgery as has been reported by many studies as discussed later in detail. Corneal refractive surgery is used to correct for both, hyperopia and myopia – however the investigation in this section restricts on the case of myopia correction if not denoted otherwise.

The classical formula for calculating an ablation profile is *Munnerlyn's formula* (Munnerlyn, Koons et al. 1988). It is based on paraxial optics and easy to calculate. Since then efforts were made to optimize profiles. Patel et al. made calculations in a model eye and propose an optimal shape of the cornea after refractive surgery with regard to the spherical aberration (Patel, Marshall et al. 1993). Seiler et al. made real treatments comparing a standard spherical an an aspherical ablation profile and found a reduced spherical aberration (Seiler, Genth et al. 1993). Klonos et al. predicted visual performance after PRK with real ray tracing in a model eye (Klonos, Pallikaris et al. 1996). Klein proposed optimized ablation profiles based on total ocular aberrations from Hartmann-Shack devices and claims that the neglect of corneal shape introduces an error below approximately 0.05 μm regarding the optimal ablation depth (Klein 1998). Schwiegerling et al. made proposals for custom PRK treatments (Schwiegerling and Snyder 1998) and investigated pre- and postoperative corneas after PRK and found an increased SA. They concluded that the ideal ablation profile has to provide a deeper central ablation depth to correct for spherical aberration (Schwiegerling and Snyder 2000). MacRae et al. proposed the use of corneal topography to model ablation profiles in order to reduce spherical aberration (MacRae, Schwiegerling et al. 1999). Mrochen et al. presented early results of wavefront-guided treatments of real eyes and reported a reduction of 3rd and 4th order higher order aberrations about 27 % (Mrochen, Kaemmerer et al. 2000b). Munger proposed an optimized ablation profile based on theoretical calculations with a slightly decreased central ablation depth compared to Munnerlyn's formula (Munger 2000) – regarding the ablation depth this is contrary to Schwiegerling et al. (Schwiegerling and Snyder 2000). Manns et al. proposed the use of corneal topography and wavefront information to optimize profiles. Based on theoretical calculations he proposed optimized ablation profiles that reduce spherical aberration (central ablation depth is higher or lower than Munnlerlyn based on the preoperative asphericity of the cornea) (Manns, Ho et al. 2002). Ortiz et al. did simulations and proposed a calculation method for a customized ablation for LASIK based on real ray tracing – however they focus on individually choosing the correction height of otherwise standard "sphere-cylinder surgical correction" rather than customizing the ablation profile itself (Fernandez del Cotero, Moreno et al. 2001; Ortiz, Saiz et al. 2002; Ortiz, Saiz et al. 2003). Gatinel et al. found no increased oblateness of postoperative corneas in their model calculations using Munnerlyn's general formula (5-6) (Gatinel, Hoang-Xuan et al. 2001). They proposed ablation profiles with the goal to target for a specific postoperative asphericity and found increased central ablation depth for an intended increase in negative asphericity

(Gatinel, Malet et al. 2002). Both studies emphasize the discrepancy between theoretical prediction and clinical findings regarding asphericity and spherical aberration. Contrary to these two studies Jiménez et al. did some analytically model calculation with the parabolic approximation (5-7) of Munnerlyn's formula. They found an increase of asphericity to oblateness with increased correction height and claimed this to be the explanation of clinically observed increased spherical aberration (Jimenez, Anera et al. 2003). They supported their findings by analyzing pre- and postoperative corneas and postulate an increase of asphericity due to Munnerlyn's paraxial approximation by 87.2 % (Anera, Jimenez et al. 2003a). Marcos et al. investigated real measured topographies after LASIK and compared the results with simulated ablations using both, general and parabolic approximation of Munnerlyn's formula (Marcos, Cano et al. 2003); they extended their investigation to account for *variable beam fluence* (VBF) in a later study (Cano, Barbero et al. 2004). They found a decrease using the general formula while there is an increase of asphericity using the parabolic approximation – this explains the discrepancy between Gatinel et al. and Jiménez et al. and was finally reinvestigated by the authors (Jimenez, Anera et al. 2004a). Hersh et al. made simulated ablation calculations with two different models for beam fluence and compared to clinical findings after LASIK (Hersh, Fry et al. 2003). With a *homogeneous beam fluence* (HBF) model they found a decrease in asphericity while they found a strong increase with the variable beam fluence model what they claim to be possibly the explanation of the oblateness found clinically. Preussner et al. provides a proposal for customized ablations based on corneal topography but points out that expectations "should not be viewed with too much optimism as long as the accuracy of the implementation in surgical procedures is limited" (Preussner and Wahl 2003; Preussner 2004). Mrochen et al. proposed a theoretical method for calculating wavefront-optimized ablation profiles to precompensate for the spherical and higher order aberrations (Mrochen, Donitzky et al. 2004). Yoon et al. simulated Munnerlyn ablations with and without variable beam fluence and compared it to clinically findings (Yoon, Macrae et al. 2005). According to them the variable beam fluence accounted for approximately half of the clinically observed amount of induced spherical aberration. Anera et al. compared simulated ablations with real ablations using a known ablation algorithm. Even with variable beam fluence they found "that the postsurgical shape of the cornea truly differs from the predicted shape" (Anera, Villa et al. 2005). Koller et al. compared clinically outcome of a Q-factor customized and wavefront-guided ablation profiles (Koller, Iseli et al. 2006). While both methods performed similar there is still some discrepancy between theoretically predicted and clinical outcome regarding corneal asphericity and spherical aberration, they are still higher. Yi et al. studied the performance of wavefront-only corneal ablation based on the profile proposed by Klein (Klein 1998). They concluded that wavefront-only corneal ablation "could potentially lead to significantly better visual outcomes" but did not include any biological factors (Yi, Iskander et al. 2006). Following Mrochen et al. who give an overview of the state-of-the-art two main approaches may be categorized (Mrochen, Hafezi et al. 2006): *topography based* ablations relying on corneal properties and *wavefront based* ablations relying on the whole eye's properties. Both approaches may either use the information for generic ablation profile optimization to correct for systematic errors (e.g. *wavefront-optimized*) or they can use the information of individual patient eyes to create individual ablation profiles (e.g. *wavefront-guided*).

Various studies recognized a discrepancy between simulations and clinical findings especially regarding the postoperative increased spherical aberration (Marcos, Barbero et al. 2001; Gatinel, Malet et al. 2002; Anera, Jimenez et al. 2003a; Anera, Jimenez et al. 2003b; Hersh, Fry et al. 2003; Jimenez, Anera et al. 2003; Marcos, Cano et al. 2003; Cano, Barbero et al. 2004; Mrochen, Donitzky et al. 2004; Anera, Villa et al. 2005; Yoon, Macrae et al. 2005; Koller, Iseli et al. 2006). The possible reasons included the following factors: decentration, type of the laser, laser nomogram departure from Munnerlyn's formula, technical procedures,

effect of corneal hydration on beam fluence, low accuracy of the videotopography systems, change of the posterior corneal surface and the optical role of the flap in case of LASIK. However, summarized, three factors have been identified to play the major roles: *variable beam fluence*, *wound healing* and *corneal biomechanics* (the latter two are sometimes combined and referred to as *biological response*).

First, the efficacy of the laser has an influence on the ablation process. There is always some reflection loss of the laser energy. If it is assumed to be constant, it was spoken of homogeneous beam fluence. However this reflection loss is increasing for non-normal incidence what occurs when a laser spot moves to the periphery of the cornea, depending on its curvature. Additionally the illumination area is increased. This was called variable beam fluence. While some authors considered variable beam fluence may be not negligible early (Blaker and Hersh 1994; Hersh, Burnstein et al. 1996; Gatinel, Hoang-Xuan et al. 2001; Gatinel, Malet et al. 2002) Mrochen et al. first provided a quantitative estimation (Mrochen and Seiler 2001) followed by others (Jimenez, Anera et al. 2002; Anera, Jimenez et al. 2003b; Hersh, Fry et al. 2003). The effect of laser polarization has also been studied (Jimenez, Anera et al. 2004b; Anera, Villa et al. 2005).

Second, corneal wound healing (like epithelial hyperplasia and stromal remodeling) influences the ultimate corneal shape. Huang et al. developed a mathematical model of corneal surface smoothing (Huang, Tang et al. 2003). They mathematically modeled epithelial thickness modulations to explain regression and induction of the aberrations clinically observed after laser ablation.

Third, the biomechanical response of the cornea may affect the corneal shape. Roberts et al. suggests that the natural mechanical forces of the cornea are affected by the severing and removing of cornea lamellae. Thus the tension on the remaining lamellae is weakened and an outward peripheral force pulls laterally on the cornea. As a result, the central cornea is flattened while the peripheral is bulged (Roberts 2000; Dupps and Roberts 2001; Roberts 2002).

This study uses RRT to investigate the discrepancy between theoretical expectations and clinically found outcome. A simulation of PRK/LASEK using Munnerlyn's formula and real measured topographies is performed. A homogeneous and a variable beam fluence model considering reflection loss and non-normal laser beam incidence are simulated. The results in terms of corneal shape and wavefront aberration calculated with RRT are compared to the real outcome.

5.3.2 Methods

34 eyes of 25 patients who had refractive laser surgery at the University Eye Hospital Tübingen were analyzed. All treatments were LASEK procedures (page 27) for myopia correction without any astigmatism correction. None of the ablations were significantly decentered. All patients were treated by the same surgeon with an ESIRIS (SCHWIND eye-tech-solutions GmbH, Germany) laser system (Excimer flying spot). Before and after surgery, topographies of the anterior cornea were made with a C-Scan (Technomed GmbH, Germany) videotopometer. For details see Table 5-9.

	34 Eyes of 25 Patients (15 OD, 19 OS)
	Mean ± SD (Range)
Age	42.5 ± 8.6 (22 to 56) years
Gender	13 female, 12 male
Sim K [1], pre-op (C-Scan)	7.64 ± 0.21 (7.29 to 8.18) mm
Corneal astigmatism, pre-op (sim K)	0.65 ± 0.36 (0.17 to 1.63) D
Laser system	ESIRIS, Software Version 2.6 and 2.7
Operation method	9 ORK-CAM, 25 LASEK/PRK (all pure sphere correction without astigmatism)
Laser correction (spectacle)	-6.26 ± 2.52 (-11.00 to -2.50) D
Laser correction (cornea)	-5.75 ± 2.16 (-9.72 to -2.40) D
FCZ diameter	1x 6.25 mm,18x 6.50 mm, 15x 7.00 mm
Central ablation depth	98.76 ± 33.83 (44.00 to 153.00) µm
Post-op topography time delay	24.50 ± 34.09 (2 to 200) weeks

[1] mean values of flat and steep meridian

Table 5-9: Baseline patient data
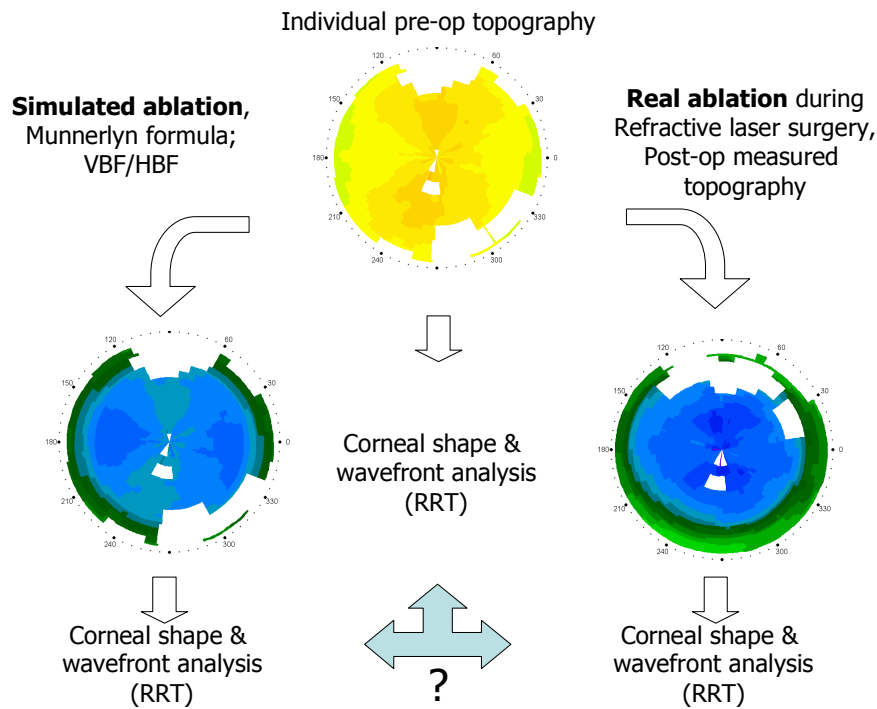
Figure 5-29: Comparison of simulated and real ablation results

For all patient eyes the result of refractive surgery in terms of corneal shape and wavefront aberration is compared between the preoperative state, theoretically predicted and real outcome (Figure 5-29). There was no pupil information available from the topographies and therefore the reference axis for all calculations is the VK axis. From the results of the previous section 5.2 (Figure 5-13 and Figure 5-14) it is assumed that referencing on the LOS would not greatly change outcomes. The corneal shape in terms of apical radius and asphericity is determined with a biconic surface fit and the anterior corneal wavefront aberration is calculated and quantified as Zernike coefficients as described in section 5.2.2. This analysis

starts with the shape and wavefront analysis of the preoperative corneal topography. Then a laser ablation is simulated. It is referred to the terminology proposed by Tabernero et al. (Tabernero, Klyce et al. 2007): *full correction zone* (FCZ) is the corneal region of full intended refractive correction; the transitional treatments outside the FCZ is called the *transition zone* (TSZ); the *functional optical zone* (FOZ) describes the area of the cornea that provides reasonable quality of vision. While FCZ and TSZ are parameters defined by the ablation profile, the FOZ must be determined postoperatively and is the result of all influencing factors including wound healing and biomechanics, for example. First, homogeneous beam fluence is assumed what means that the laser ablates exactly the provided ablation profile. This is done by subtracting an ablation profile *t(Y)* from the measured preoperative topography elevation map. The classical ablation profile for myopia of Munnerlyn is used (Munnerlyn, Koons et al. 1988):

$$t(Y) = \sqrt{R_1^2 - Y^2} - \sqrt{\left(\frac{R_1(n-1)}{n-1+R_1 D}\right)^2 - Y^2} - \sqrt{R_1^2 - \frac{S^2}{4}} + \sqrt{\left(\frac{R_1(n-1)}{n-1+R_1 D}\right)^2 - \frac{S^2}{4}} \qquad \textbf{(5-6)}$$

Y: distance from optical axis [m]
D: correction [D]
S: diameter of FCZ [m]
R_1: initial radius of curvature [m]
n: refractive index of the cornea

The *parabolic approximation* of Munnerlyn's formula is much simpler but can lead to false implications. To show this one data set was calculated with this approximation (Marcos, Cano et al. 2003):

$$t(Y) = \frac{4DY^2}{3} - \frac{DS^2}{3} \qquad \textbf{(5-7)}$$

Y: distance from optical axis [m]
D: correction [D]
S: diameter of FCZ [m]

The same FCZ and correction height is chosen for the simulation as those used in the real treatments. Figure 5-30 shows an example of cross sections of the Munnerlyn ablation profile. All profiles are rotationally symmetric.
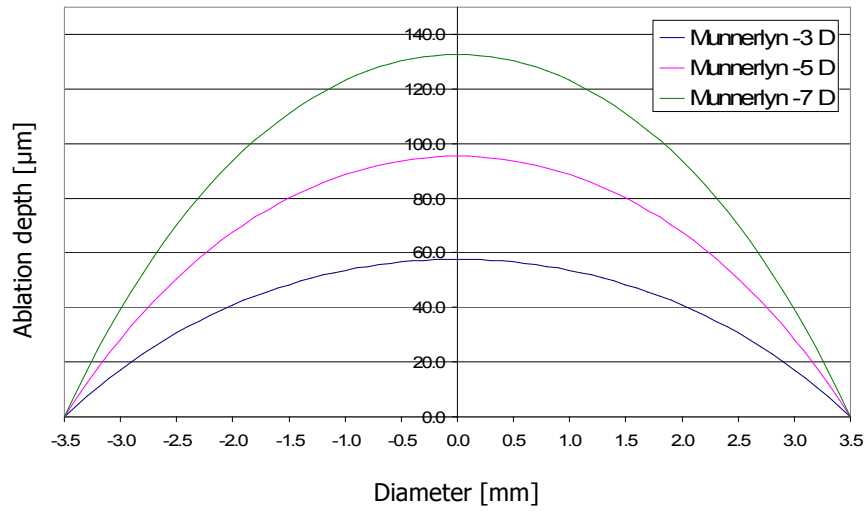
Figure 5-30: The Munnerlyn ablation profile

A second ablation is simulated including the effect of variable beam fluence due to reflection and non-normal incidence. This is done by weighting the Munnerlyn ablation profile with a fluence loss factor *p(Y)* provided by Jiménez et al. (Jimenez, Anera et al. 2002; Anera, Villa et al. 2005):

$$p(Y) = (1 - 0.0435\alpha) - \frac{\alpha Y^2}{2R_1^2} + \frac{\alpha(0.232 - 0.5(Q+1))Y^4}{R_1^4} \tag{5-8}$$

with

$$\alpha = \frac{1}{\ln(F_0 / F_{th})}$$

Y: distance from optical axis [m]
R₁: initial radius of curvature [m]
Q: initial corneal asphericity
F₀: incident exposure of laser [mJ/cm^2]
Fth: threshold exposure of laser [mJ/cm^2]

103

R$_1$ = 7.63 mm
Q = -0.21
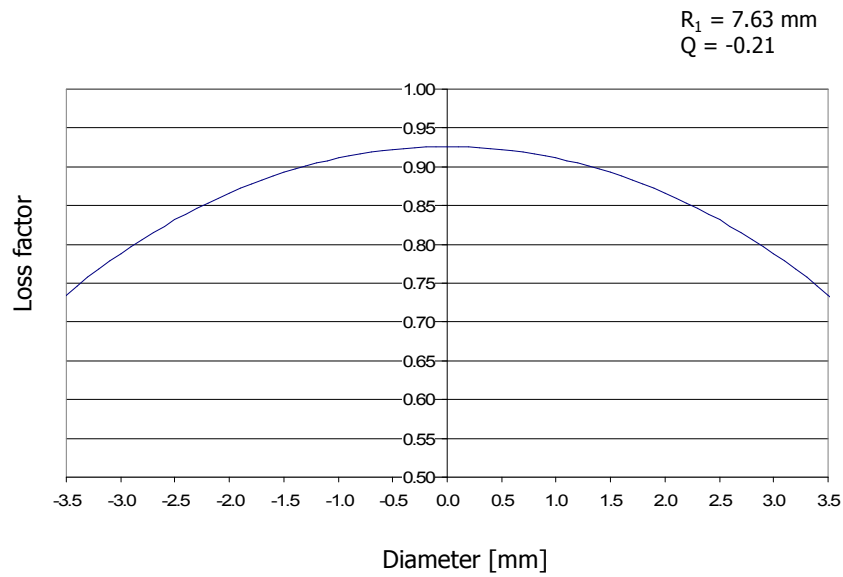
Figure 5-31: The fluence loss factor

An incident exposure $F_0 = 90$ mJ/cm^2 and a threshold exposure $F_{th} = 50$ mJ/cm^2 were used. Figure 5-31 shows the fluence loss factor for a sample cornea while the radius and asphericity are chosen individually for each eye; Figure 5-32 shows the difference in ablation height with and without fluence loss factor for a sample cornea. Corneal shape and wavefront aberration of the topographies resulting from the simulated laser ablation are calculated. Finally, the shape and wavefront aberration of the measured topographies from the real eyes is calculated.

R$_1$ = 7.63 mm
Q = -0.21
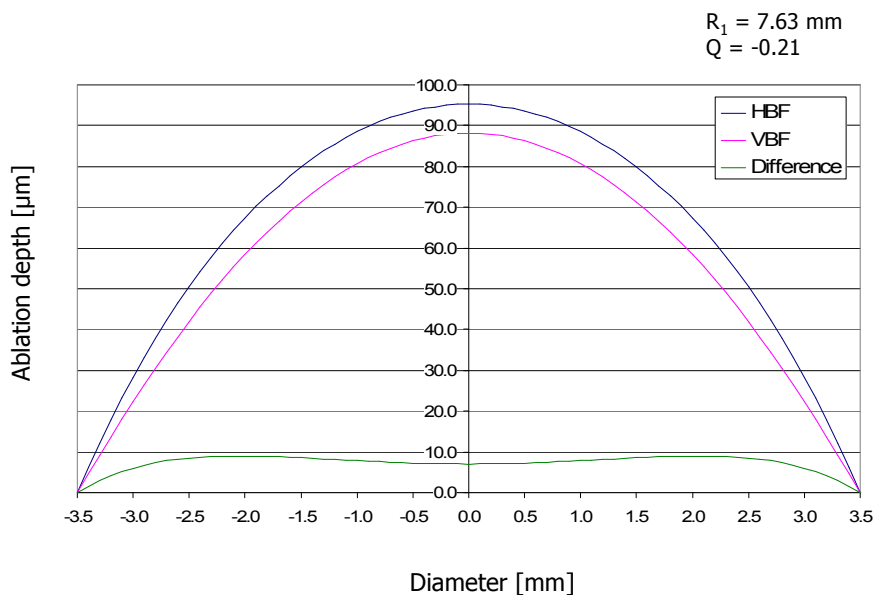
Figure 5-32: Difference of ablation profiles (Munnerlyn -5 D) with homogeneous and variable beam fluence

5.3.3 Results

The shape of the topographies in the different sets is shown in Figure 5-33. The apical radii and asphericities are similar as for the cataract patient eyes analyzed in the previous section 5.2 (Figure 5-15). The asphericities are somewhat more negative, especially for 4 mm. The average asphericity for 6 mm results in a common value of Q = -0.21. The apical radii of the simulated and measured postoperative corneas are similar and much higher than preoperatively around R = 8.55 mm – this is not surprising since flattening the cornea is the main goal of the refractive myopia treatment. The asphericities of the simulated post-op corneas are, however, more negative than before. The simulated post-op corneas are therefore more prolate. In contrast, the measured corneas have a mean asphericity of Q = 0.40 mm for 6 mm diameter; they are clearly oblate and also show a much larger standard deviation.

Apical radius | Asphericity (4 and 6 mm)
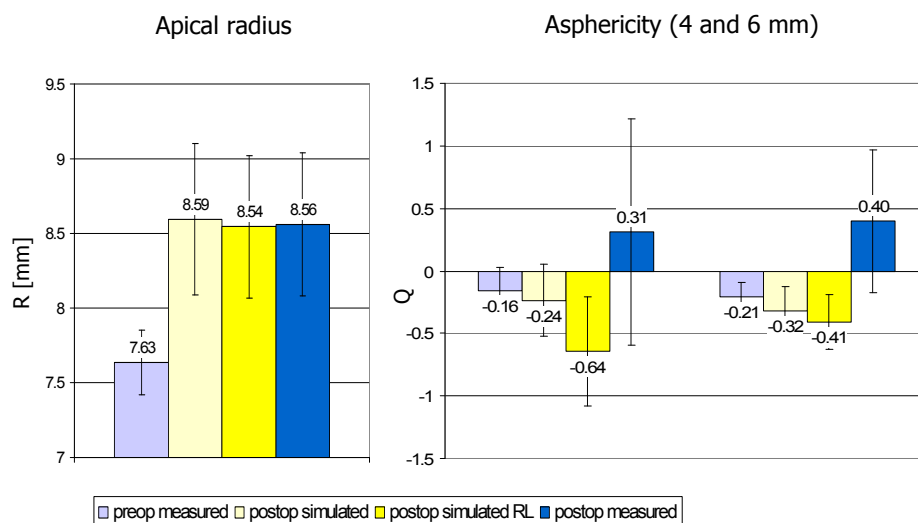
Figure 5-33: Radius and asphericities of the corneas before and after surgery (flat and steep axis averaged)

The corneal wavefront results are shown for 4 mm pupil in Figure 5-34 and for 6 mm pupil in Figure 5-35. For these diagrams the same general description on page 77 for the diagrams in Figure 5-18 to Figure 5-22 in the previous section 5.2 is applicable though those were total wavefront results while these here are corneal wavefront values. On the left, RMS values are provided while on the right the individual Zernike coefficients are shown. Because it is not of interest in the context of this section, the defocus is not included and the LOAs are consisting only of astigmatism and are therefore called AST RMS. For both pupil sizes, the aberrations are not increased with respect to the pre-op state when the laser ablation is simulated. The only Zernike mode that slightly changes is the SA $Z(4,0)$; for 4 mm it actually decreases for the simulated ablation with homogeneous beam fluence and even more with variable beam fluence. For 6 mm SA is decreased homogeneous beam fluence, while it stays approximately the same with variable beam fluence. (Using the parabolic approximation of Munnerlyn's formula (5-7) with variable beam fluence leads to a misleading average $Z(4,0)$ of 0.31 µm – this is twice the value with the exact formula (5-6), but only the result of the too rough approximation.) In contrast, the wavefront aberration from the post-op measured topographies is increased. AST RMS is increased and HOAs are increased. The HOA increase comes from the bigger standard deviations, increased coma RMS and predominantly from a largely

increased Z(4,0). For a 6 mm pupil the SA RMS is increased by a factor of 3 from 0.16 to 0.49 μm compared to the preoperative state.
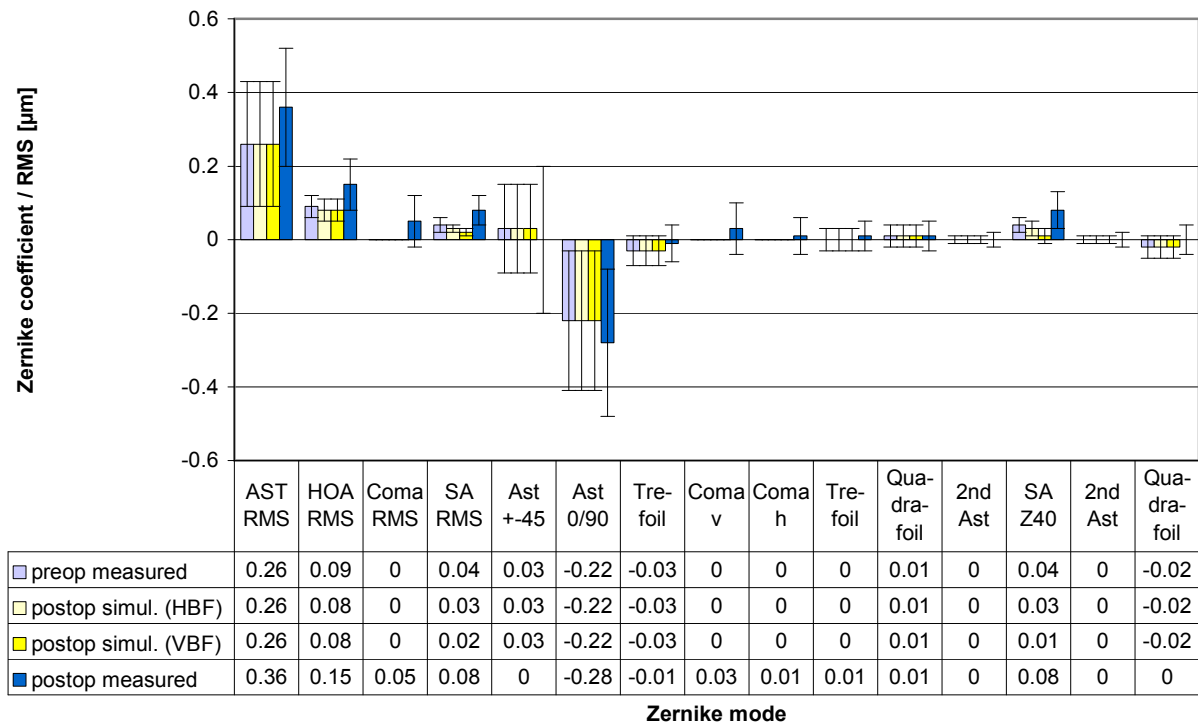

Zernike mode	AST RMS	HOA RMS	Coma RMS	SA RMS	Ast +-45	Ast 0/90	Tre-foil	Coma v	Coma h	Tre-foil	Qua-dra-foil	2nd Ast	SA Z40	2nd Ast	Qua-dra-foil
preop measured	0.26	0.09	0	0.04	0.03	-0.22	-0.03	0	0	0	0.01	0	0.04	0	-0.02
postop simul. (HBF)	0.26	0.08	0	0.03	0.03	-0.22	-0.03	0	0	0	0.01	0	0.03	0	-0.02
postop simul. (VBF)	0.26	0.08	0	0.02	0.03	-0.22	-0.03	0	0	0	0.01	0	0.01	0	-0.02
postop measured	0.36	0.15	0.05	0.08	0	-0.28	-0.01	0.03	0.01	0.01	0.01	0	0.08	0	0

Figure 5-34: Corneal wavefront aberration (4 mm pupil)

Zernike mode	AST RMS	HOA RMS	Coma RMS	SA RMS	Ast +-45	Ast 0/90	Tre-foil	Coma v	Coma h	Tre-foil	Qua-dra-foil	2nd Ast	SA Z40	2nd Ast	Qua-dra-foil
preop measured	0.56	0.34	0.13	0.16	0.07	-0.46	-0.05	-0.01	0.02	0.01	0.02	0	0.15	0.02	-0.06
postop simul. (HBF)	0.57	0.29	0.13	0.08	0.07	-0.47	-0.05	0	0.02	0.01	0.02	0	0.05	0.02	-0.05
postop simul. (VBF)	0.56	0.34	0.13	0.17	0.07	-0.46	-0.05	0	0.02	0.01	0.02	0	0.16	0.02	-0.05
postop measured	0.72	0.64	0.23	0.49	0.02	-0.54	-0.02	0.07	0.01	0	0.03	0.01	0.49	0.04	-0.01

Figure 5-35: Corneal wavefront aberration (6 mm pupil)

106
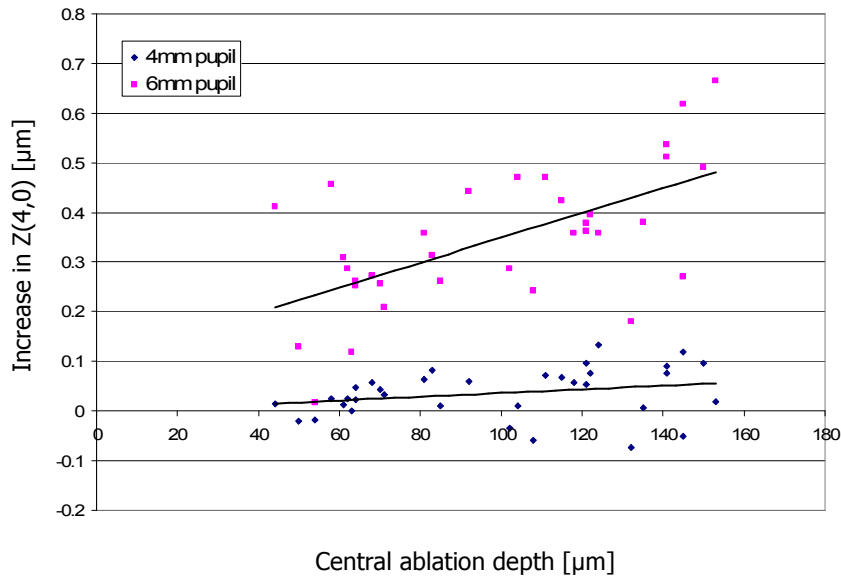
Figure 5-36: Increase of Z(4,0) depending on ablation depth

This increase of SA of the measured topographies shows a dependence on the ablation depth (Figure 5-36), slightly for 4 mm pupil and more evident for the 6 mm pupil. Figure 5-37 shows the increase compared between the simulated and real ablations. For 6 mm simulation with homogeneous beam fluence predicts a decrease in SA. With variable beam fluence RRT simulation predicts that the SA does not change.

	4mm	6mm
☐ postop simulated (HBF)	-0.02	-0.1
■ postop simulated (VBF)	-0.03	0.01
■ postop measured	0.04	0.35
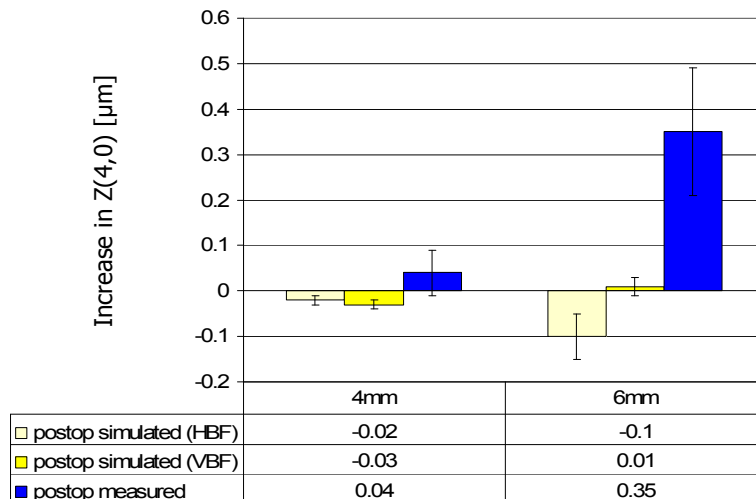
Figure 5-37: Increase of Z(4,0) simulated vs. real

5.3.4 Discussion

This investigation shows that the corneal shape after simulated laser ablations is more prolate than before. This is the case with both, the homogeneous and variable beam fluence model. However, the corneal shape measured after LASEK/PRK showed an oblateness with an average Q = 0.31 for 4 mm and Q = 0.40 for 6 mm (Figure 5-33). This change from prolate to oblate is consistent with the results of various other studies (Hersh, Shah et al. 1996; Anera, Jimenez et al. 2003b; Somani, Tuan et al. 2004; Preussner, Wahl et al. 2005); the results of some studies is shown in Table 5-10. The values for asphericity depend on the correction height, are provided for different corneal diameters and the calculation is critical, so they may not be comparable with ultimate exactness – but they clearly show the overall trend. Most of those provide results for LASIK treatments; all studies report oblate corneal shapes postoperatively – using different laser systems (that use different ablation profiles), different topography units, and finally different diameters and computational procedures for calculating Q-values. The results of Anera et al. doing LASIK with an ESIRIS is very similar to the results of the present study (Anera, Jimenez et al. 2003a).

Study	Set-ting	No. of eyes	Laser [1]	Method	Pre-op MRSE [2] [D] Mean ± SD	Post-op time [month]	Topo-graphy system [3]	Dia-meter [mm]	Pre-op Q Mean ± SD	Post-op Q Mean ± SD
(Holladay and Janes 2002)	USA	n = 39	VISX S2	LASIK	Approx. -5	6	EyeSys	-	-	Approx. +0.75
(Hersh, Fry et al. 2003)	USA	n = 20	LADAR-Vision	8 LASIK, 3 PRK, 9 LASEK	-5.85 ± 1.71	28.7 ± 12.1 days	EyeSys	5.0	-0.17 ± 0.14	+0.92 ± 0.70
(Anera, Jimenez et al. 2003a)	Spain	n = 24	ESIRIS	LASIK	-4.8	3	EyeSys	4.5	-0.12	+0.42
(Marcos, Cano et al. 2003; Cano, Barbero et al. 2004)	Spain	n = 13	Techno-las	LASIK	-6.1 ± 2.70	> 1	Atlas	4.4 to 7.0	-0.14 ± 0.14	+1.1 ± 1.3
(Anera, Villa et al. 2005)	Spain	n = 37	Astra-scan	LASIK	-3.1	3	Orbscan	6	-0.51	+0.43 ± 0.27
(Koller, Iseli et al. 2006)	Suisse	n = 45	Eye-Q	LASIK	-5.13 [4]	1	Kerato-graph	3.25 [4]	-0.21 ± 0.13 [4]	+0.49 ± 0.48 [4]

[1] full names of the laser systems: Astrascan Sight excimer laser (Lasersight Inc., USA); Chiron Technolas 217C excimer laser (Bausch & Lomb, Inc., USA); Eye-Q (Wavelight AG, Germany); ESIRIS (SCHWIND eye-tech-solutions GmbH, Germany); LADARVision excimer laser (Alcon Laboratories, Inc., USA); STAR S2 excimer laser (VISX, USA)

[2] mean refractive spherical equivalent

[3] full names of the topography systems: Atlas (Carl Zeiss Meditec AG, Germany); EyeSys 2000 (EyeSys Vision, USA); Keratograph C (OCULUS Optikgeräte GmbH, Germany); Orbscan II (Bausch & Lomb, Inc., USA)

[4] approximate (groups merged)

Table 5-10: Measured pre- and postoperative corneal asphericities from literature

The *corneal* wavefront aberration calculated from corneal topography measurements reflects the changed geometry in terms of changed aberrations (Figure 5-34 and Figure 5-35). For the simulated ablation no increased HOAs are observed. The only Zernike mode affected is the SA – with homogeneous beam fluence the SA is decreased. This corresponds to the increased prolateness. With variable beam fluence the SA is higher, around the preoperative level. There is some discrepancy to the geometry, since with variable beam fluence the topographies are even more prolate. This may be due to the biconic surface fit that is not able to follow the more complex shape of the cornea. However, using the measured postoperative topographies for a 6 mm pupil for calculation shows that the HOAs are nearly doubled. This is also the result of increased coma – but mainly due to the three times larger SA. In terms of absolute values this means an increase in HOAs of 0.30 µm, coma of 0.10 µm and in SA of 0.33 µm. Coma can be induced by all kinds of decentration, in general. This can be an actually

decentered ablation area or an artifact due to the use of different reference axes (Bueeler, Iseli et al. 2005). In this study the videokeratometric axis is used to calculate the wavefront aberration, while the ablations were likely centered to the pupil during surgery. The largely increased SA is not predicted by Munnerlyn's profile. Some, but not all of the discrepancy can be explained by the variable beam fluence. All ablation zones were 6.5 or 7 mm – the pupil sizes investigated were 4 and 6 mm with the intent to stay in the ablated zone and to not include the somewhat abrupt change at the border of the ablation zone (Hersh, Fry et al. 2003). Although the definition and measurement of the FOZ is ambiguous (Tabernero, Klyce et al. 2007) the trend is observed that the FOZ can be smaller than the ablation diameter (FCZ) used for the laser ablation (Boxer Wachler, Huynh et al. 2002; Holladay and Janes 2002). However, the increase of SA is also seen for the 4 mm pupil – this leads to the suggestion that it is truly a property of the ablated area. Various other studies also measured increased corneal higher order aberrations from topography and especially increased spherical aberration (what is the direct result of the change to oblateness; see Figure 5-7) after refractive surgery (Schwiegerling and Greivenkamp 1997; Martinez, Applegate et al. 1998; Oshika, Klyce et al. 1999; Schwiegerling and Snyder 2000; Marcos 2001; Hersh, Fry et al. 2003; Yoon, Macrae et al. 2005; Koller, Iseli et al. 2006). Some studies providing values are summarized in Table 5-11. As for the asphericities in Table 5-10 different laser systems, surgical procedures, topography units and calculation methods are used – but all show an increase in corneal aberrations compared to the preoperative state. The results of Zhou et al. doing LASIK with an ESIRIS (Zhou, Jin et al. 2007) are similar to the results of the present investigation.

Study	Set-ting	No. of eyes	Laser [1]	Method	Pre-op MRSE [2] [D] Mean ± SD	Post-op time [month]	Topo-graphy system [3]	Dia-meter [mm]	Zernike mode	Pre-op RMS [µm] Mean ± SD	Post-op RMS [µm] Mean ± SD
(Marcos, Barbero et al. 2001) [4]	Spain	n = 14	Techno-las	LASIK	-6.8 ± 2.9	> 1	Atlas	6.5	Z(4,0) [5]	-	Increase of 0.74
(Cano, Barbero et al. 2004) [4]	Spain	n = 13	Techno-las	LASIK	-6.8 ± 2.9	> 1	Atlas	4.4	Z(4,0) [5]	0.08 ± 0.04	0.17 ± 0.10
(Oshika, Miyata et al. 2002)	Japan	n = 100	VISX S2	LASIK	-6.9 ± 2.5	1	TMS-1	6.0	coma like	0.45 ± 0.21	1.60 ± 0.88
									SA like	0.25 ± 0.12	2.02 ± 0.72
(Buzzonetti, Iarossi et al. 2004)	Italy	n = 18	LADAR-Vision	LASEK	-5.7 ± 4.05	3	EyeMap	7.0	2nd AST and 3rd-7th HOAs	3.30 ± 0.9	4.90 ± 1.5
		n = 18		LASIK	-5.4 ± 3.10					2.40 ± 0.8	4.08 ± 1.2
(Lombardo, Lombardo et al. 2006)	Italy	n = 80	Techno-las	PRK	-5.91 ± 1.26	12	Keratron	6.0	SA like [5]	0.32 ± 0.09	0.69 ± 0.15
(Zhou, Jin et al. 2007)	China	n = 56	ESIRIS	wavefront guided LASIK	-4.40 ± 1.83	12	Keratron	6.0	SA like	0.31 ± 0.01	0.66 ± 0.18
									3rd-7th HOAs	0.44 ± 0.84	0.84 ± 0.28

[1] full names of the laser systems: Chiron Technolas Keracor 217C excimer laser (Bausch & Lomb, Inc., USA); ESIRIS (SCHWIND eye-tech-solutions GmbH, Germany), Software 2.6.2; LADARVision 4000 excimer laser (Alcon Laboratories, Inc., USA); STAR S2 excimer laser (VISX, USA)
[2] mean refractive spherical equivalent
[3] full names of the topography systems: Atlas (Carl Zeiss Meditec AG, Germany); EyeMap (CSO Costruzione Strumenti Oftalmici, Italy); Keratron Scout (Optikon 2000, Italy); TMS-1 (Computed Anatomy Inc., USA)
[4] these two studies base on the same clinical data
[5] reported according to the OSA standard

Table 5-11: Measured pre- and postoperative corneal wavefront aberration from literature

There are numerous studies that measured *total* ocular aberrations of eyes before and after refractive treatments with some wavefront measurement device. The results depend on many factors: type of surgery (LASIK, LASEK, PRK; conventional or wavefront-guided), the laser system (proprietary ablation profiles), the operator, treatment heights, optical zones, other

technical procedures (e.g. flap creation), wavefront measurement device (Tscherning vs. Hartmann-Shack) and pupil size during measurement etc. Thus a comprehensive literature review is complex. Only a few representative studies are cited in the following text to give a rough impression of results achieved in the past and today. Early results of PRK (Mierdel, Kaemmerer et al. 1999) and LASIK (Marcos 2001; Moreno-Barriuso, Lloves et al. 2001; Miller, Anwaruddin et al. 2002) found large increase of SA and HOAs in general. Seiler et al. found an increase of HOAs of a factor of around 17 after PRK (Seiler, Kaemmerer et al. 2000); Marcos et al. reported an increase of SA of 0.63 µm (6.5 mm pupil) after LASIK (Marcos, Barbero et al. 2001). Some newer – mostly comparative – studies using various procedures ranging from conventional LASEK to wavefront-guided LASIK found similar increases of SA around 0.2 µm (pupil size around 6 mm) (Aizawa, Shimizu et al. 2003; Phusitphoykai, Tungsiripat et al. 2003; Seo, Lee et al. 2004; Yoon, Macrae et al. 2005; Koller, Iseli et al. 2006). Porter et al. found an increase of HOAs after wavefront-guided LASIK (Porter, Yoon et al. 2006). Remarkably, Awwad et al. found a decrease of HOAs and SA after wavefront-guided LASIK (Awwad, El-Kateb et al. 2004). Chung et al. found no difference between wavefront-guided LASIK and LASEK and is among some recent studies that – though an increase in HOA was still there – found an increase of SA of only 0.01 to 0.08 µm in average (pupil size around 6 mm) (Chung, Lee et al. 2006; Awwad, Bowman et al. 2007; Binder and Rosenshein 2007).

Most ablation profiles are proprietary to the laser companies. That they are not all identical has been shown experimentally for some laser systems (Canals, Elies et al. 2004). However it is likely that all base on Munnerlyn's formula in general. As the profiles likely are optimized in some way one can assume that they perform at least as good as Munnerlyn's basic formula. When simulated, Munnerlyn's ablation profiles show good results without increasing HOAs. The real ablated corneas are worse. This indicates that it's not as easy as providing the theoretically correct ablation profile because of other factors. One potential factor has been identified to be the variable beam fluence that can easily be compensated (and is likely done in most systems). Another factor is that the parabolic approximation of Munnerlyn's formula should not be used. The present investigation shows there are other factors left – wound healing and corneal biomechanics may be some plausible. So the challenge of laser companies is to enhance the profiles and may be technical procedures to precompensate for these factors that cannot be calculated from geometrical optical point of view. The recently published good results indicate that the laser companies seem to be on the right way. The literature review indicates that this increase in quality may be not or not only due to the use of wavefront-guided procedures but to general improvements and better understanding of corneal behavior. In this conclusion the present study is consistent with the recent investigations of Netto et al. (Netto, Dupps et al. 2006).

There are some limitations of the present theoretical investigations. The contribution to the corneal wavefront aberration of a possibly changed posterior corneal surface is not considered. However, this influence is likely to be small (Langenbucher, Torres et al. 2004; Ciolino and Belin 2006; Tang, Li et al. 2006). All calculations are referenced to the VK axis, whereas the ablations are likely centered on the pupil and the wavefront measurements are referenced to the LOS – however one might not expect a fundamental influence on the results of the calculations regarding HOAs and especially SA. Finally, the time delay for the post-op topography measurements was not equal for all patients (Table 5-9); some patients were measured only few weeks after surgery and the corneal wound healing process might not be completely finished. However the delay for most patients is likely to be long enough.

Conclusion

RRT has been used to assess the outcome of refractive corneal surgery on the shape of the cornea. On the basis of individual corneal topographies the laser ablation was simulated and

compared to the actually measured corneal topography after surgery (Figure 5-29). The profiles used for simulation as well as the true corneal ablations were pure corrections of sphere without a cylindrical correction. In simulation of Munnerlyn's ablation profile (Figure 5-30), there was noted neither an increase in oblateness of the cornea, nor a big increase in HOAs. In contrast, the corneas after real surgery show greatly increased oblateness (Figure 5-33) and greatly increased corneal HOAs (Figure 5-34 and Figure 5-35). This increase is consistent with many other studies found in literature (Table 5-10 and Table 5-11). By the simulation of homogeneous and variable beam fluence RRT was able to approve that not considering the fluence loss of the laser (Figure 5-31) has some influence on the post-op corneal SA (Figure 5-37). However, the simulations with RRT suggest that there are other more important factors left which have great influence on the post-op corneal shape, probably wound healing and corneal biomechanics.

6 Conclusion

On the basis of measured geometry data of eyes it has been shown that an individual virtual eye can be constructed with computer scientific methods (chapter 3). To incorporate measured topography data from individual persons a spline-based interpolation method was developed. By means of real ray tracing it is possible to simulate the optical properties and moreover calculate optical components. The latter is possible by formulating optimization problems and by solving them numerically to receive the desired geometry of optical components. In order to do this in a reasonable time it is crucial to efficiently implement the real ray tracing procedure as well as the optimization algorithm. In chapter 4 this individual virtual eye was verified with regard to the ability of predicting a manifest refraction of patient eyes. The good results were the precondition for further applications of the virtual eye in chapter 5.

In section 5.1 it has been shown that spherical intraocular lenses can be computed and that RRT is able to compete with established calculation formulae successfully used for normal eyes in current clinical practice. However, since the calculation in the individual virtual eye is based on the complete geometry of eyes and is not limited to paraxial optics it has the potential to overcome the limitations of current IOL calculation formulae and provide significant benefits for eyes current formulae are known to fail. This includes eyes that do not meet the population average like eyes with irregular corneal surfaces as a result of refractive surgery.

Section 5.2 shows the capability of RRT to calculate customized intraocular lenses with advanced geometry providing asphericity and toricity – calculated to fit an individual patient eye. The individual virtual eye allows for the simulation of different IOL designs by means of wavefront aberration in some kind of virtual cataract surgery. The theoretically achievable minimum wavefront aberration can be predicted for individual patient eyes. Corneal and ocular wavefront aberration can be calculated from the virtual eye separately. The results have been compared to actually measured wavefront aberration with wavefront measurement devices and conclusions of clinical relevance can be drawn. This includes the importance of reference axes used for calculation and measurement as well as questions of how much tilt and decentration affects the overall results of customized IOLs with respect to spherical IOLs, for example. All those calculations require a complete model of the eye and computational power provided by the individual virtual eye and the corresponding calculation methods. Future applications may also include the calculation of multifocal IOLs or customized IOLs correcting higher order aberrations beyond spherical aberration.

The analytical possibilities are further demonstrated in section 5.3. Laser ablations for refractive surgery are simulated with RRT and compared to real treated patient eyes. Different ablation profiles or factors like laser beam fluence loss can be incorporated into the simulations in the virtual eyes and the results have been used to explain discrepancies of predictions and results found clinically. RRT could play a major role not only in analyzing but actually calculating advanced ablation profiles in future.

Another obvious future application is the calculation of phakic intraocular lenses. Combined surgical procedures like the implantation of phakic lenses or intraocular lenses (for correction of defocus and spherical aberration for example) and a refractive ablation on the cornea (for correction of astigmatism) may also be an interesting field where RRT may be a valuable method for analysis and simulation. The accuracy of RRT is directly affected by the input data from measurements of the patient eyes – so it will directly benefit from improvements of the measurement devices, especially regarding corneal elevation. It will also benefit from incorporating measured geometry that is currently not assessed in most cases in clinical practice as the posterior corneal surface. Currently measurements of different devices are used for constructing the individual virtual eye (like those of a videokeratometer and a PCI device for measuring axial length). Once possible – may be due to the combination of different

measurement methods – it would be desirable to have one measurement device that completely measures the geometry of the whole eye including cornea, lens and segmental lengths. The software architecture where the individual virtual eye is embedded in has to receive additional measurement data apart from corneal topography from other sources or manual input at the moment (Figure 1-1). But the architecture itself is ready to receive all data from one hardware unit as soon as the device is able to measure the missing quantities like axial length, what is currently work in progress. One major challenge for extending the capabilities of the individual virtual eye is the proper simulation of the human crystalline lens. Another challenge is the further development towards more realism by incorporating polychromatic issues or additional physical properties beyond geometrical optics like diffraction and scattering. And, finally there is a wide scope when extending the individual virtual eye by addressing issues beyond optics regarding physiology of the retina and brain.

References

1. Aizawa, D., K. Shimizu, et al. (2003). "Clinical outcomes of wavefront-guided laser in situ keratomileusis: 6-month follow-up." J Cataract Refract Surg **29**(8): 1507-13.
2. Akkin, C., S. A. Ozler, et al. (1994). "Tilt and decentration of bag-fixated intraocular lenses: a comparative study between capsulorhexis and envelope techniques." Doc Ophthalmol **87**(3): 199-209.
3. Altmann, G. E. (2004). "Wavefront-customized intraocular lenses." Curr Opin Ophthalmol **15**(4): 358-64.
4. Altmann, G. E., L. D. Nichamin, et al. (2005). "Optical performance of 3 intraocular lens designs in the presence of decentration." J Cataract Refract Surg **31**(3): 574-85.
5. Anera, R. G., J. R. Jimenez, et al. (2003a). "Changes in corneal asphericity after laser in situ keratomileusis." J Cataract Refract Surg **29**(4): 762-8.
6. Anera, R. G., J. R. Jimenez, et al. (2003b). "Changes in corneal asphericity after laser refractive surgery, including reflection losses and nonnormal incidence upon the anterior cornea." Opt Lett **28**(6): 417-9.
7. Anera, R. G., C. Villa, et al. (2005). "Differences between real and predicted corneal shapes after aspherical corneal ablation." Appl Opt **44**(21): 4528-32.
8. Applegate, R. A., G. Hilmantel, et al. (2000). "Corneal first surface optical aberrations and visual performance." J Refract Surg **16**(5): 507-14.
9. Applegate, R. A. and H. C. Howland (1997). "Refractive surgery, optical aberrations, and visual performance." J Refract Surg **13**(3): 295-9.
10. Applegate, R. A., J. D. Marsack, et al. (2003). "Interaction between aberrations to improve or reduce visual performance." J Cataract Refract Surg **29**(8): 1487-95.
11. Applegate, R. A., L. N. Thibos, et al. (2000). "Reference axis selection: subcommittee report of the OSA Working Group to establish standards for measurement and reporting of optical aberrations of the eye." J Refract Surg **16**(5): S656-8.
12. Applegate, R. A., L. N. Thibos, et al. (2001). "Optics of aberroscopy and super vision." J Cataract Refract Surg **27**(7): 1093-107.
13. Aramberri, J. (2003). "Intraocular lens power calculation after corneal refractive surgery: double-K method." J Cataract Refract Surg **29**(11): 2063-8.
14. Arasa, J. and J. Alda (2004) "Real Ray Tracing." Encyclopedia of Optical Engineering **Volume**, 1-10 DOI: 10.1081/E-EOE-120027488
15. Artal, P., A. Guirao, et al. (2001). "Compensation of corneal aberrations by the internal optics in the human eye." J Vis **1**(1): 1-8.
16. Atchison, D. A. (1989a). "Optical design of intraocular lenses. III. On-axis performance in the presence of lens displacement." Optom Vis Sci **66**(10): 671-81.
17. Atchison, D. A. (1989b). "Refractive errors induced by displacement of intraocular lenses within the pseudophakic eye." Optom Vis Sci **66**(3): 146-52.
18. Atchison, D. A. (1991). "Design of aspheric intraocular lenses." Ophthalmic Physiol Opt **11**(2): 137-46.
19. Atchison, D. A. and G. O. Smith (2000). Optics of the human eye. Oxford, Butterworth-Heinemann.
20. Auffarth, G. U. and D. J. Apple (2001). "[The evolution of intraocular lenses]." Ophthalmologe **98**(11): 1017-28.
21. Auffarth, G. U., M. Martin, et al. (2002). "[Validity of anterior chamber depth measurements for the evaluation of accommodation after implantation of an accommodative Humanoptics 1CU intraocular lens]." Ophthalmologe **99**(11): 815-9.
22. Auran, J. D., C. J. Koester, et al. (1990). "In vivo measurement of posterior chamber intraocular lens decentration and tilt." Arch Ophthalmol **108**(1): 75-9.

References

23. Awwad, S. T., R. W. Bowman, et al. (2007). "Wavefront-guided LASIK for myopia using the LADAR CustomCornea and the VISX CustomVue." J Refract Surg **23**(1): 26-38.

24. Awwad, S. T., M. El-Kateb, et al. (2004). "Wavefront-guided laser in situ keratomileusis with the Alcon CustomCornea and the VISX CustomVue: three-month results." J Refract Surg **20**(5): S606-13.

25. Awwad, S. T., J. D. Lehmann, et al. (2007). "A comparison of higher order aberrations in eyes implanted with AcrySof IQ SN60WF and AcrySof SN60AT intraocular lenses." Eur J Ophthalmol **17**(3): 320-6.

26. Baikoff, G. and P. Joly (1990). "Comparison of minus power anterior chamber intraocular lenses and myopic epikeratoplasty in phakic eyes." Refract Corneal Surg **6**(4): 252-60.

27. Baker, T. Y. (1943). "Ray tracing through non-spherical surfaces." Proc Phys Soc **55**: 361.

28. Barbero, S., S. Marcos, et al. (2003). "Optical aberrations of intraocular lenses measured in vivo and in vitro." J Opt Soc Am A Opt Image Sci Vis **20**(10): 1841-51.

29. Barbero, S., S. Marcos, et al. (2002). "Corneal and total optical aberrations in a unilateral aphakic patient." J Cataract Refract Surg **28**(9): 1594-600.

30. Barraquer, J. (1958). An Med Cir **38**: 255-266.

31. Bass, M. (1995). Handbook of optics. New York ; London, McGraw-Hill.

32. Baumeister, M., B. Neidhardt, et al. (2005). "Tilt and decentration of three-piece foldable high-refractive silicone and hydrophobic acrylic intraocular lenses with 6-mm optics in an intraindividual comparison." Am J Ophthalmol **140**(6): 1051-8.

33. Becker, K. A., M. P. Holzer, et al. (2006). "[Accuracy of lens power calculation and centration of an aspheric intraocular lens]." Ophthalmologe **103**(10): 873-6.

34. Beiko, G. H. (2007). "Personalized correction of spherical aberration in cataract surgery." J Cataract Refract Surg **33**(8): 1455-60.

35. Beiko, G. H., W. Haigis, et al. (2007). "Distribution of corneal spherical aberration in a comprehensive ophthalmology practice and whether keratometry can predict aberration values." J Cataract Refract Surg **33**(5): 848-58.

36. Bellucci, R. and S. Morselli (2007). "Optimizing higher-order aberrations with intraocular lens technology." Curr Opin Ophthalmol **18**(1): 67-73.

37. Bellucci, R., S. Morselli, et al. (2004). "Comparison of wavefront aberrations and optical quality of eyes implanted with five different intraocular lenses." J Refract Surg **20**(4): 297-306.

38. Bellucci, R., S. Morselli, et al. (2007). "Spherical aberration and coma with an aspherical and a spherical intraocular lens in normal age-matched eyes." J Cataract Refract Surg **33**(2): 203-9.

39. Bellucci, R., A. Scialdone, et al. (2005). "Visual acuity and contrast sensitivity comparison between Tecnis and AcrySof SA60AT intraocular lenses: A multicenter randomized study." J Cataract Refract Surg **31**(4): 712-7.

40. Bennett, A. G. and R. B. Rabbetts (1989). Clinical visual optics, Butterworths.

41. Binder, P. S. and J. Rosenshein (2007). "Retrospective comparison of 3 laser platforms to correct myopic spheres and spherocylinders using conventional and wavefront-guided treatments." J Cataract Refract Surg **33**(7): 1158-76.

42. Blaker, J. W. (1980). "Toward an adaptive model of the human eye." J Opt Soc Am **70**(2): 220-3.

43. Blaker, J. W. and P. S. Hersh (1994). "Theoretical and clinical effect of preoperative corneal curvature on excimer laser photorefractive keratectomy for myopia." J Refract Corneal Surg **10**(5): 571-4.

44. Bores, L. D., W. Myers, et al. (1981). "Radial keratotomy: an analysis of the American experience." Ann Ophthalmol **13**(8): 941-8.

45. Boxer Wachler, B. S., V. N. Huynh, et al. (2002). "Evaluation of corneal functional optical zone after laser in situ keratomileusis." J Cataract Refract Surg **28**(6): 948-53.

46. Breidegard, B., J. Gustafsson, et al. (2000). "Raytracing in the Compensation of the Peripheral Optics of the Eye." Center for Rehabilitation Engineering Research (Certec), Lund University, Sweden.

47. Bueeler, M., H. P. Iseli, et al. (2005). "Treatment-induced shifts of ocular reference axes used for measurement centration." J Cataract Refract Surg **31**(10): 1986-94.

48. Burakgazi, A. Z., B. Tinio, et al. (2006). "Higher order aberrations in normal eyes measured with three different aberrometers." J Refract Surg **22**(9): 898-903.

49. Buzzonetti, L., G. Iarossi, et al. (2004). "Comparison of wavefront aberration changes in the anterior corneal surface after laser-assisted subepithelial keratectomy and laser in situ keratomileusis: preliminary study." J Cataract Refract Surg **30**(9): 1929-33.

50. Calossi, A. (2007). "Corneal asphericity and spherical aberration." J Refract Surg **23**(5): 505-14.

51. Camp, J. J., L. J. Maguire, et al. (1990). "A computer model for the evaluation of the effect of corneal topography on optical performance." Am J Ophthalmol **109**(4): 379-86.

52. Canals, M., D. Elies, et al. (2004). "Comparative study of ablation profiles of six different excimer lasers." J Refract Surg **20**(2): 106-9.

53. Cano, D., S. Barbero, et al. (2004). "Comparison of real and computer-simulated outcomes of LASIK refractive surgery." J Opt Soc Am A Opt Image Sci Vis **21**(6): 926-36.

54. Caporossi, A., G. Martone, et al. (2007). "Prospective randomized study of clinical performance of 3 aspheric and 2 spherical intraocular lenses in 250 eyes." J Refract Surg **23**(7): 639-48.

55. Carvalho, L. A. (2002). "A Simple mathematical model for simulation of the human optical system based on in vivo corneal data." Brazilian Journal of Biomedical Enginnering.

56. Chalita, M. R., S. Chavala, et al. (2004). "Wavefront analysis in post-LASIK eyes and its correlation with visual symptoms, refraction, and topography." Ophthalmology **111**(3): 447-53.

57. Charman, W. N., R. Montes-Mico, et al. (2007). "Can we measure wave aberration in patients with diffractive IOLs?" J Cataract Refract Surg **33**(11): 1997.

58. Chen, W. R., H. H. Ye, et al. (2006). "Comparison of higher-order aberrations and contrast sensitivity between Tecnis Z9001 and CeeOn 911A intraocular lenses: a prospective randomized study." Chin Med J (Engl) **119**(21): 1779-84.

59. Choi, J., T. I. Kim, et al. (2005). "Comparison of wavefront aberration after cataract surgery with acrylic intraocular lens implantation." J Cataract Refract Surg **31**(2): 324-9.

60. Chung, S. H., I. S. Lee, et al. (2006). "Comparison of higher-order aberrations after wavefront-guided laser in situ keratomileusis and laser-assisted subepithelial keratectomy." J Cataract Refract Surg **32**(5): 779-84.

61. Ciolino, J. B. and M. W. Belin (2006). "Changes in the posterior cornea after laser in situ keratomileusis and photorefractive keratectomy." J Cataract Refract Surg **32**(9): 1426-31.

62. CTView user's guide (2001). Sarver and Associates, Inc.

63. Davis, A. (1999). "Raytracing a Schematic Eye." University of Rochester, Optics 448: Principles of Eye Design.

References

64. de Castro, A., P. Rosales, et al. (2007). "Tilt and decentration of intraocular lenses in vivo from Purkinje and Scheimpflug imaging. Validation study." <u>J Cataract Refract Surg</u> **33**(3): 418-29.

65. Denoyer, A., M. L. Le Lez, et al. (2007). "Quality of vision after cataract surgery after Tecnis Z9000 intraocular lens implantation: effect of contrast sensitivity and wavefront aberration improvements on the quality of daily vision." <u>J Cataract Refract Surg</u> **33**(2): 210-6.

66. Denoyer, A., F. Roger, et al. (2006). "[Quality of vision after cataract surgery in patients with prolate aspherical lens]." <u>J Fr Ophtalmol</u> **29**(2): 157-63.

67. Dietze, H. H. and M. J. Cox (2005). "Limitations of correcting spherical aberration with aspheric intraocular lenses." <u>J Refract Surg</u> **21**(5): S541-6.

68. Drasdo, N. and C. W. Fowler (1974). "Non-linear projection of the retinal image in a wide-angle schematic eye." <u>Br J Ophthalmol</u> **58**(8): 709-14.

69. Dubbelman, M., H. A. Weeber, et al. (2002). "Radius and asphericity of the posterior corneal surface determined by corrected Scheimpflug photography." <u>Acta Ophthalmol Scand</u> **80**(4): 379-83.

70. Duke-Elder, S. and D. Abrams (1970). Ophthalmic Optics and Refraction. <u>System of Ophthalmology</u>. S. Duke-Elder. London, Henry Kimpton.

71. Dupps, W. J., Jr. and C. Roberts (2001). "Effect of acute biomechanical changes on corneal curvature after photokeratectomy." <u>J Refract Surg</u> **17**(6): 658-69.

72. Emsley, H. H. (1952). <u>Visual Optics ... Fifth edition</u>, 2 vol. Hatton Press: London.

73. Enaliev, F. S. (1979). "[Surgical treatment experience in myopia]." <u>Vestn Oftalmol</u>(3): 52-5.

74. Erickson, P. (1990). "Effects of intraocular lens position errors on postoperative refractive error." <u>J Cataract Refract Surg</u> **16**(3): 305-11.

75. Fam, H. B. and K. L. Lim (2007). "Validity of the keratometric index: large population-based study." <u>J Cataract Refract Surg</u> **33**(4): 686-91.

76. Fedorov, S. N., A. I. Kolinko, et al. (1967). "[A method of calculating the optical power of the intraocular lens]." <u>Vestn Oftalmol</u> **80**(4): 27-31.

77. Feiz, V., M. J. Mannis, et al. (2001). "Intraocular lens power calculation after laser in situ keratomileusis for myopia and hyperopia: a standardized approach." <u>Cornea</u> **20**(8): 792-7.

78. Fernandez del Cotero, J. N., F. Moreno, et al. (2001). "Geometric ray tracing analysis of visual acuity after laser in situ keratomileusis." <u>J Refract Surg</u> **17**(3): 305-9.

79. Fink, W., A. Frohn, et al. (1996a). "A ray tracer for ophthalmological applications." <u>Ger J Ophthalmol</u> **5**(2): 118-25.

80. Fink, W., A. Frohn, et al. (1996b). "[Visual image in high ametropia. Computer-assisted simulation with optic ray calculation]." <u>Klin Monatsbl Augenheilkd</u> **208**(6): 472-6.

81. Fink, W. and D. Micol (2006). "simEye: Computer-based simulation of visual perception under various eye defects using Zernike polynomials." <u>J Biomed Opt</u> **11**(5): 054011.

82. Franchini, A. (2006). "Comparative assessment of contrast with spherical and aspherical intraocular lenses." <u>J Cataract Refract Surg</u> **32**(8): 1307-1319.

83. Franchini, A., B. Z. Gallarati, et al. (2003). "Computerized analysis of the effects of intraocular lens edge design on the quality of vision in pseudophakic patients." <u>J Cataract Refract Surg</u> **29**(2): 342-7.

84. Fyodorov, S. N. and V. V. Durnev (1979). "Operation of dosaged dissection of corneal circular ligament in cases of myopia of mild degree." <u>Ann Ophthalmol</u> **11**(12): 1885-90.

85. Fyodorov, S. N. and V. V. Durnev (1981). "Surgical correction of complicated myopic astigmatism by means of dissection of circular ligament of cornea." <u>Ann Ophthalmol</u> **13**(1): 115-8.

86. Garcia, D. D. (2000). CWhatUC: Software Tools for Predicting, Visualization and Simulating Corneal Visual Acuity. <u>Graduate Division</u>. Berkeley, University of California. **Doctor of Philosophy**.

87. Gatinel, D., M. Haouat, et al. (2002). "[A review of mathematical descriptors of corneal asphericity]." <u>J Fr Ophtalmol</u> **25**(1): 81-90.

88. Gatinel, D., T. Hoang-Xuan, et al. (2001). "Determination of corneal asphericity after myopia surgery with the excimer laser: a mathematical model." <u>Invest Ophthalmol Vis Sci</u> **42**(8): 1736-42.

89. Gatinel, D., J. Malet, et al. (2002). "Analysis of customized corneal ablations: theoretical limitations of increasing negative asphericity." <u>Invest Ophthalmol Vis Sci</u> **43**(4): 941-8.

90. Gernet, H. (1990). "[Intraocular lens planning. Geometric-optical and Sanders-Retzlaff-Kraff I and II formulas]." <u>Ophtalmologie</u> **4**(1): 96-101.

91. Gernet, H. (2001). "[Gernet and GOW-70-Program intraocular lens calculation. Significance of the of the position of the principal plane of the lens in phakic and pseudophakic eyes for accuracy of the target refraction of different IOL types]." <u>Ophthalmologe</u> **98**(9): 873-6.

92. Gernet, H. (2003). "Virgin formulas." <u>J Cataract Refract Surg</u> **29**(6): 1056-7.

93. Gernet, H., H. Ostholt, et al. (1970). "Die präoperative Berechnung intraokularer Binkhorst-Linsen." <u>Versammlung der Vereinigung Rheinisch-Westfälischer Augenärzte.</u> **122**: 54-55.

94. Gerste, R. D. (2004). Innovative Intraokularlinsen: Individuelle Aberrationskorrektur bringt Vorteile. <u>Ophthalmo-Chirurgie-Sonderveröffentlichung</u>, Dr. R. Kagen Verlag GmbH & Co. KG.

95. Gimbel, H. V. and R. Sun (2001). "Accuracy and predictability of intraocular lens power calculation after laser in situ keratomileusis." <u>J Cataract Refract Surg</u> **27**(4): 571-6.

96. Gimbel, H. V., R. Sun, et al. (2000). "Accuracy and predictability of intraocular lens power calculation after photorefractive keratectomy." <u>J Cataract Refract Surg</u> **26**(8): 1147-51.

97. Gonzalez-Meijome, J. M., C. Villa-Collar, et al. (2007). "Asphericity of the anterior human cornea with different corneal diameters." <u>J Cataract Refract Surg</u> **33**(3): 465-73.

98. Greivenkamp, J. E., J. Schwiegerling, et al. (1995). "Visual acuity modeling using optical raytracing of schematic eyes." <u>Am J Ophthalmol</u> **120**(2): 227-40.

99. Guirao, A. and P. Artal (2000). "Corneal wave aberration from videokeratography: accuracy and limitations of the procedure." <u>J Opt Soc Am A Opt Image Sci Vis</u> **17**(6): 955-65.

100. Guirao, A., J. Tejedor, et al. (2004). "Corneal aberrations before and after small-incision cataract surgery." <u>Invest Ophthalmol Vis Sci</u> **45**(12): 4312-9.

101. Gullstrand, A. (1966). "Photographic-ophthalmometric and Clinical Investigations of Corneal Refraction." <u>Am J Optom Arch Am Acad Optom</u> **43**: 143-214.

102. Haigis, W. (1993a). "[Critical corneal radii may skew correct IOL calculation by using the SRK/T formula]." <u>Ophthalmologe</u> **90**(6): 703-7.

103. Haigis, W. (1993b). "Occurrence of erroneous anterior chamber depth in the SRK/T formula." <u>J Cataract Refract Surg</u> **19**(3): 442-6.

104. Haigis, W. (2003). "Corneal power after refractive surgery for myopia: contact lens method." <u>J Cataract Refract Surg</u> **29**(7): 1397-411.

105. Haigis, W., B. Lege, et al. (2000). "Comparison of immersion ultrasound biometry and partial coherence interferometry for intraocular lens calculation according to Haigis." <u>Graefes Arch Clin Exp Ophthalmol</u> **238**(9): 765-73.

106. Hamilton, D. R. and D. R. Hardten (2003). "Cataract surgery in patients with prior refractive surgery." <u>Curr Opin Ophthalmol</u> **14**(1): 44-53.

107. Hayashi, K., M. Harada, et al. (1997). "Decentration and tilt of polymethyl methacrylate, silicone, and acrylic soft intraocular lenses." <u>Ophthalmology</u> **104**(5): 793-8.

108. Hayashi, K. and H. Hayashi (2005). "Comparison of the stability of 1-piece and 3-piece acrylic intraocular lenses in the lens capsule." <u>J Cataract Refract Surg</u> **31**(2): 337-42.

109. Hecht, E. (1989). <u>Optik</u>, Addison-Wesley Publishing Company.

110. Helmholtz, H. L. F. v., A. Gullstrand, et al. (1909). <u>Handbuch der physiologischen Optik ... Dritte Auflage, ergänzt und herausgegeben in Gemeinschaft mit Prof. Dr. A. Gullstrand ... und Prof. Dr. J. von Kries ... von Professor Dr. W. Nagel</u>. Hamburg und Leipzig, Verlag von Leopold Voss.

111. Hersh, P. S., Y. Burnstein, et al. (1996). "Excimer laser phototherapeutic keratectomy. Surgical strategies and clinical outcomes." <u>Ophthalmology</u> **103**(8): 1210-22.

112. Hersh, P. S., K. Fry, et al. (2003). "Spherical aberration after laser in situ keratomileusis and photorefractive keratectomy. Clinical results and theoretical models of etiology." <u>J Cataract Refract Surg</u> **29**(11): 2096-104.

113. Hersh, P. S., S. I. Shah, et al. (1996). "Corneal asphericity following excimer laser photorefractive keratectomy. Summit PRK Topography Study Group." <u>Ophthalmic Surg Lasers</u> **27**(5 Suppl): S421-8.

114. Ho, A., F. Manns, et al. (2006). "Predicting the performance of accommodating intraocular lenses using ray tracing." <u>J Cataract Refract Surg</u> **32**(1): 129-36.

115. Hoffer, K. J. (1993). "The Hoffer Q formula: a comparison of theoretic and regression formulas." <u>J Cataract Refract Surg</u> **19**(6): 700-12.

116. Hoffer, K. J. (1995). "Intraocular lens power calculation for eyes after refractive keratotomy." <u>J Refract Surg</u> **11**(6): 490-3.

117. Hoffmann, P. C., W. W. Hutz, et al. (1997). "[Significance of optic formula selection for postoperative refraction after cataract operation]." <u>Klin Monatsbl Augenheilkd</u> **211**(3): 168-77.

118. Holladay, J. T. (2004). "International Intraocular Lens & Implant Registry 2004." <u>J Cataract Refract Surg</u> **30**(1): 207-29.

119. Holladay, J. T. (2006). "Spherical Aberration: The Next Frontier." <u>Cataract & Refractive Surgery Today</u> **6**(11): 95-106.

120. Holladay, J. T., D. R. Dudeja, et al. (1999). "Functional vision and corneal changes after laser in situ keratomileusis determined by contrast sensitivity, glare testing, and corneal topography." <u>J Cataract Refract Surg</u> **25**(5): 663-9.

121. Holladay, J. T. and J. A. Janes (2002). "Topographic changes in corneal asphericity and effective optical zone after laser in situ keratomileusis." <u>J Cataract Refract Surg</u> **28**(6): 942-7.

122. Holladay, J. T., P. A. Piers, et al. (2002). "A new intraocular lens design to reduce spherical aberration of pseudophakic eyes." <u>J Refract Surg</u> **18**(6): 683-91.

123. Holladay, J. T., T. C. Prager, et al. (1988). "A three-part system for refining intraocular lens power calculations." <u>J Cataract Refract Surg</u> **14**(1): 17-24.

124. Horiuchi, I. and Y. Akagi (2001a). "[A new predictive formula for anterior chamber depth for pseudophakia]." <u>Nippon Ganka Gakkai Zasshi</u> **105**(9): 614-8.

125. Horiuchi, I. and Y. Akagi (2001b). "[A new theoretical formula for the intraocular lens power calculation by the Ray Tracing Method]." Nippon Ganka Gakkai Zasshi **105**(9): 619-27.

126. Huang, D., M. Tang, et al. (2003). "Mathematical model of corneal surface smoothing after laser refractive surgery." Am J Ophthalmol **135**(3): 267-78.

127. IOLMaster (Software Version 3.xx), user's guide (2004). Carl Zeiss Meditec.

128. Iseli, H. P., M. Jankov, et al. (2006). "Corneal and total wavefront aberrations in phakic and pseudophakic eyes after implantation of monofocal foldable intraocular lenses." J Cataract Refract Surg **32**(5): 762-71.

129. Ishikawa, T., A. Hirano, et al. (1998). "[Trial of new intraocular lens power calculation following phototherapeutic keratectomy]." Nippon Ganka Gakkai Zasshi **102**(9): 594-600.

130. Ishikawa, T., A. Hirano, et al. (2000a). "Trial for new intraocular lens power calculation following phototherapeutic keratectomy." Jpn J Ophthalmol **44**(4): 400-6.

131. Ishikawa, T., A. Hirano, et al. (2000b). "Intraocular Lens Calculation for Cataract Treated with Photorefractive Keratectomy Using Ray Tracing Method." Jpn J Ophthalmol **44**(5): 575.

132. Ishikawa, T., A. Hirano, et al. (2000c). "[Intraocular lens calculation for cataract treated with photorefractive keratectomy using ray tracing method]." Nippon Ganka Gakkai Zasshi **104**(3): 165-9.

133. Jarade, E. F. and K. F. Tabbara (2004). "New formula for calculating intraocular lens power after laser in situ keratomileusis." J Cataract Refract Surg **30**(8): 1711-5.

134. Javal, L. and H. Schiötz (1881). "Un opthalmomètre pratique." Annales d'oculistique **86**: 5-21.

135. Jimenez, J. R., R. G. Anera, et al. (2004a). "Corneal asphericity after refractive surgery when the Munnerlyn formula is applied." J Opt Soc Am A Opt Image Sci Vis **21**(1): 98-103.

136. Jimenez, J. R., R. G. Anera, et al. (2003). "Equation for corneal asphericity after corneal refractive surgery." J Refract Surg **19**(1): 65-9.

137. Jimenez, J. R., R. G. Anera, et al. (2002). "Effect on laser-ablation algorithms of reflection losses and nonnormal incidence on the anterior cornea." Appl Phys Letters **81**(8): 1521-23.

138. Jimenez, J. R., R. G. Anera, et al. (2004b). "Influence of laser polarization on ocular refractive parameters after refractive surgery." Opt Lett **29**(9): 962-4.

139. Jin, G. J., A. S. Crandall, et al. (2006). "Analysis of intraocular lens power calculation for eyes with previous myopic LASIK." J Refract Surg **22**(4): 387-95.

140. Kasper, T., J. Buhren, et al. (2005). "[Intraindividual comparison of higher order aberrations after implantation of aspherical and spherical IOLs depending on pupil diameter]." Ophthalmologe **102**(1): 51-7.

141. Kasper, T., J. Buhren, et al. (2006a). "Intraindividual comparison of higher-order aberrations after implantation of aspherical and spherical intraocular lenses as a function of pupil diameter." J Cataract Refract Surg **32**(1): 78-84.

142. Kasper, T., J. Buhren, et al. (2006b). "Visual performance of aspherical and spherical intraocular lenses: intraindividual comparison of visual acuity, contrast sensitivity, and higher-order aberrations." J Cataract Refract Surg **32**(12): 2022-9.

143. Kelly, J. E., T. Mihashi, et al. (2004). "Compensation of corneal horizontal/vertical astigmatism, lateral coma, and spherical aberration by internal optics of the eye." J Vis **4**(4): 262-71.

144. Kennis, H., M. Huygens, et al. (2004). "Comparing the contrast sensitivity of a modified prolate anterior surface IOL and of two spherical IOLs." Bull Soc Belge Ophtalmol(294): 49-58.

References

145. Kershner, R. M. (2003). "Retinal image contrast and functional visual performance with aspheric, silicone, and acrylic intraocular lenses. Prospective evaluation." J Cataract Refract Surg **29**(9): 1684-94.

146. Kim, J. S. and K. H. Shyn (2001). "Biometry of 3 types of intraocular lenses using Scheimpflug photography." J Cataract Refract Surg **27**(4): 533-6.

147. Kiss, B., O. Findl, et al. (2002a). "Biometry of cataractous eyes using partial coherence interferometry: clinical feasibility study of a commercial prototype I." J Cataract Refract Surg **28**(2): 224-9.

148. Kiss, B., O. Findl, et al. (2002b). "Refractive outcome of cataract surgery using partial coherence interferometry and ultrasound biometry: clinical feasibility study of a commercial prototype II." J Cataract Refract Surg **28**(2): 230-4.

149. Klein, S. A. (1998). "Optimal corneal ablation for eyes with arbitrary Hartmann-Shack aberrations." J Opt Soc Am A Opt Image Sci Vis **15**(9): 2580-8.

150. Klonos, G. G., J. Pallikaris, et al. (1996). "A computer model for predicting image quality after photorefractive keratectomy." J Refract Surg **12**(2): S280-4.

151. Koch, D. D. and L. Wang (2003). "Calculating IOL power in eyes that have had refractive surgery." J Cataract Refract Surg **29**(11): 2039-42.

152. Kohnen, T., M. Baumeister, et al. (2005). "[Intraocular lenses for the correction of refraction errors. Part 1: phakic anterior chamber lenses]." Ophthalmologe **102**(10): 1003-7; quiz 1018.

153. Koller, T., H. P. Iseli, et al. (2006). "Q-factor customized ablation profile for the correction of myopic astigmatism." J Cataract Refract Surg **32**(4): 584-9.

154. Kooijman, A. C. (1983). "Light distribution on the retina of a wide-angle theoretical eye." J Opt Soc Am **73**(11): 1544-50.

155. Korynta, J., J. Bok, et al. (1994). "Changes in refraction induced by change in intraocular lens position." J Refract Corneal Surg **10**(5): 556-64.

156. Korynta, J., J. Bok, et al. (1999). "Computer modeling of visual impairment caused by intraocular lens misalignment." J Cataract Refract Surg **25**(1): 100-5.

157. Kozaki, J., H. Tanihara, et al. (1991). "Tilt and decentration of the implanted posterior chamber intraocular lens." J Cataract Refract Surg **17**(5): 592-5.

158. Kriechbaum, K., O. Findl, et al. (2003). "Comparison of anterior chamber depth measurement methods in phakic and pseudophakic eyes." J Cataract Refract Surg **29**(1): 89-94.

159. Kurz, S., F. Krummenauer, et al. (2007). "Contrast sensitivity after implantation of a spherical versus an aspherical intraocular lens in biaxial microincision cataract surgery." J Cataract Refract Surg **33**(3): 393-400.

160. Kusserow, I. (2006). "Refractive corneal surgery." from http://www.clario.de/english/refractive_surgery.

161. Langenbach, E. (1993). Ray tracing in gradient-index materials (Proceedings Paper). Lens and Optical Systems Design, SPIE.

162. Langenbucher, A., W. Haigis, et al. (2004). "Difficult lens power calculations." Curr Opin Ophthalmol **15**(1): 1-9.

163. Langenbucher, A., S. Reese, et al. (2004). "Matrix-based calculation scheme for toric intraocular lenses." Ophthalmic Physiol Opt **24**(6): 511-9.

164. Langenbucher, A., T. Sauer, et al. (2003). "[Assessment of the optical image quality of the eye using raytracing technique of corneal topography data]." Klin Monatsbl Augenheilkd **220**(4): 235-46.

165. Langenbucher, A. and B. Seitz (2004). "Computerized calculation scheme for toric intraocular lenses." Acta Ophthalmol Scand **82**(3 Pt 1): 270-6.

166. Langenbucher, A., N. Szentmary, et al. (2007). "Calculating the power of toric phakic intraocular lenses." Ophthalmic Physiol Opt **27**(4): 373-80.

167. Langenbucher, A., F. Torres, et al. (2004). "Consideration of the posterior corneal curvature for assessment of corneal power after myopic LASIK." Acta Ophthalmol Scand **82**(3 Pt 1): 264-9.

168. Langenbucher, A., A. Viestenz, et al. (2007). "Computerized calculation scheme for retinal image size after implantation of toric intraocular lenses." Acta Ophthalmol Scand **85**(1): 92-8.

169. Le Grand, Y. and S. G. El Hage (1980). Physiological optics. Berlin, Springer.

170. Lee, Y. C., F. R. Hu, et al. (2003). "Quality of vision after laser in situ keratomileusis: influence of dioptric correction and pupil size on visual function." J Cataract Refract Surg **29**(4): 769-77.

171. Liang, J., B. Grimm, et al. (1994). "Objective measurement of wave aberrations of the human eye with the use of a Hartmann-Shack wave-front sensor." J Opt Soc Am A Opt Image Sci Vis **11**(7): 1949-57.

172. Liou, H. L. and N. A. Brennan (1997). "Anatomically accurate, finite model eye for optical modeling." J Opt Soc Am A Opt Image Sci Vis **14**(8): 1684-95.

173. Lohmann, A. W. and H. J. Caulfield (2002). Optical information processing : a tribute to Adolf Lohmann. SPIE Press monograph ; PM117. Bellingham, WA, SPIE Optical Engineering Press**:** 123-30.

174. Lombardo, M., G. Lombardo, et al. (2006). "Relative contribution of central and peripheral aberrations to overall high order corneal wavefront aberration." J Refract Surg **22**(7): 656-64.

175. Lotmar, W. (1971). "Theoretical eye model with aspheric surfaces." J Opt Soc Am **61**: 1522-9.

176. Mackool, R. J., W. Ko, et al. (2006). "Intraocular lens power calculation after laser in situ keratomileusis: Aphakic refraction technique." J Cataract Refract Surg **32**(3): 435-7.

177. MacRae, S., J. Schwiegerling, et al. (1999). "Customized and low spherical aberration corneal ablation design." J Refract Surg **15**(2 Suppl): S246-8.

178. Maguire, L. J., R. W. Zabel, et al. (1991). "Topography and raytracing analysis of patients with excellent visual acuity 3 months after excimer laser photorefractive keratectomy for myopia." Refract Corneal Surg **7**(2): 122-8.

179. Maheshwari, A. and D. R. Williams. (2001). "Learning Optics using Vision." from http://textonly.cfao.ucolick.org/EO/resourcesnew/Learn_optics_AO.pdf.

180. Mandell, R. B. (1994). "Apparent pupil displacement in videokeratography." Clao J **20**(2): 123-7.

181. Mandell, R. B. (1995). "Locating the corneal sighting center from videokeratography." J Refract Surg **11**(4): 253-9.

182. Mandell, R. B., C. S. Chiang, et al. (1995). "Location of the major corneal reference points." Optom Vis Sci **72**(11): 776-84.

183. Mandell, R. B. and D. Horner (1995). Alignment of videokeratographs. Corneal topography - the state of the art. A. E. Drummond, D. L. Clarke and J. J. Dyer. Thorofare, Bond, J. H. Slack Incorporated.

184. Manns, F., A. Ho, et al. (2002). "Ablation profiles for wavefront-guided correction of myopia and primary spherical aberration." J Cataract Refract Surg **28**(5): 766-74.

185. Marcos, S. (2001). "Aberrations and visual performance following standard laser vision correction." J Refract Surg **17**(5): S596-601.

186. Marcos, S., S. Barbero, et al. (2005). "Optical quality and depth-of-field of eyes implanted with spherical and aspheric intraocular lenses." J Refract Surg **21**(3): 223-35.

References

187. Marcos, S., S. Barbero, et al. (2001). "Optical response to LASIK surgery for myopia from total and corneal aberration measurements." Invest Ophthalmol Vis Sci **42**(13): 3349-56.

188. Marcos, S., D. Cano, et al. (2003). "Increase in corneal asphericity after standard laser in situ keratomileusis for myopia is not inherent to the Munnerlyn algorithm." J Refract Surg **19**(5): S592-6.

189. Marcos, S., P. Rosales, et al. (2007). "Change in corneal aberrations after cataract surgery with 2 types of aspherical intraocular lenses." J Cataract Refract Surg **33**(2): 217-26.

190. Martinez, C. E., R. A. Applegate, et al. (1998). "Effect of pupillary dilation on corneal optical aberrations after photorefractive keratectomy." Arch Ophthalmol **116**(8): 1053-62.

191. Masket, S. and S. E. Masket (2006). "Simple regression formula for intraocular lens power adjustment in eyes requiring cataract surgery after excimer laser photoablation." J Cataract Refract Surg **32**(3): 430-4.

192. Mester, U., P. Dillinger, et al. (2003). "Impact of a modified optic design on visual function: clinical comparative study." J Cataract Refract Surg **29**(4): 652-60.

193. Mierdel, P., M. Kaemmerer, et al. (1999). "Effects of photorefractive keratectomy and cataract surgery on ocular optical errors of higher order." Graefes Arch Clin Exp Ophthalmol **237**(9): 725-9.

194. Miller, J. M., R. Anwaruddin, et al. (2002). "Higher order aberrations in normal, dilated, intraocular lens, and laser in situ keratomileusis corneas." J Refract Surg **18**(5): S579-83.

195. Moreno-Barriuso, E., J. M. Lloves, et al. (2001). "Ocular aberrations before and after myopic corneal refractive surgery: LASIK-induced changes measured with laser ray tracing." Invest Ophthalmol Vis Sci **42**(6): 1396-403.

196. Mrochen, M. (2002). "Revealing company secrets--please tell the truth and nothing but the truth!" J Refract Surg **18**(5): S644-51.

197. Mrochen, M., C. Donitzky, et al. (2004). "Wavefront-optimized ablation profiles: theoretical background." J Cataract Refract Surg **30**(4): 775-85.

198. Mrochen, M., F. Hafezi, et al. (2006). "[Ablation profiles in corneal laser surgery. Current and future concepts]." Ophthalmologe **103**(3): 175-83.

199. Mrochen, M., M. Jankov, et al. (2003). "Correlation between corneal and total wavefront aberrations in myopic eyes." J Refract Surg **19**(2): 104-12.

200. Mrochen, M., M. Kaemmerer, et al. (2000a). "Principles of Tscherning aberrometry." J Refract Surg **16**(5): S570-1.

201. Mrochen, M., M. Kaemmerer, et al. (2000b). "Wavefront-guided laser in situ keratomileusis: early results in three eyes." J Refract Surg **16**(2): 116-21.

202. Mrochen, M. and T. Seiler (2001). "Influence of corneal curvature on calculation of ablation patterns used in photorefractive laser surgery." J Refract Surg **17**(5): S584-7.

203. Mundt, G. H., Jr. and W. F. Hughes, Jr. (1956). "Ultrasonics in ocular diagnosis." Am J Ophthalmol **41**(3): 488-98.

204. Munger, R. (2000). "New paradigm for the treatment of myopia by refractive surgery." J Refract Surg **16**(5): S651-3.

205. Munnerlyn, C. R., S. J. Koons, et al. (1988). "Photorefractive keratectomy: a technique for laser refractive surgery." J Cataract Refract Surg **14**(1): 46-52.

206. Munoz, G., C. Albarran-Diego, et al. (2006). "Spherical aberration and contrast sensitivity after cataract surgery with the Tecnis Z9000 intraocular lens." J Cataract Refract Surg **32**(8): 1320-7.

207. Mutlu, F. M., C. Erdurman, et al. (2005). "Comparison of tilt and decentration of 1-piece and 3-piece hydrophobic acrylic intraocular lenses." J Cataract Refract Surg **31**(2): 343-7.

208. Naeser, K. (1997). "Intraocular lens power formula based on vergence calculation and lens design." J Cataract Refract Surg **23**(8): 1200-7.

209. Navarro, R., L. Gonzalez, et al. (2006). "On the prediction of optical aberrations by personalized eye models." Optom Vis Sci **83**(6): 371-81.

210. Navarro, R., J. Santamaria, et al. (1985). "Accommodation-dependent model of the human eye with aspherics." J Opt Soc Am A **2**(8): 1273-81.

211. Netto, M. V., W. Dupps, Jr., et al. (2006). "Wavefront-guided ablation: evidence for efficacy compared to traditional ablation." Am J Ophthalmol **141**(2): 360-368.

212. Nishi, T., Y. Nawa, et al. (2006). "Effect of total higher-order aberrations on accommodation in pseudophakic eyes." J Cataract Refract Surg **32**(10): 1643-9.

213. Nordan, L. T. (1989). "Barraquer lecture. Jose Barraquer: father of modern refractive keratoplasty." Refract Corneal Surg **5**(3): 177-8.

214. Norrby, N. E. and G. Koranyi (1997). "Prediction of intraocular lens power using the lens haptic plane concept." J Cataract Refract Surg **23**(2): 254-9.

215. Norrby, S. (2004). "Using the lens haptic plane concept and thick-lens ray tracing to calculate intraocular lens power." J Cataract Refract Surg **30**(5): 1000-5.

216. Norrby, S. (2005). "The Dubbelman eye model analysed by ray tracing through aspheric surfaces." Ophthalmic Physiol Opt **25**(2): 153-61.

217. Norrby, S., E. Lydahl, et al. (2005). "Clinical application of the lens haptic plane concept with transformed axial lengths." J Cataract Refract Surg **31**(7): 1338-44.

218. Olsen, T. (2006). "Prediction of the effective postoperative (intraocular lens) anterior chamber depth." J Cataract Refract Surg **32**(3): 419-24.

219. Olsen, T. (2007). "Calculation of intraocular lens power: a review." Acta Ophthalmol Scand **85**(5): 472-85.

220. Olsen, T. and M. Thorwest (2005). "Calibration of axial length measurements with the Zeiss IOLMaster." J Cataract Refract Surg **31**(7): 1345-50.

221. Ortiz, D., J. M. Saiz, et al. (2002). "Geometric ray tracing for design of customized ablation in laser in situ keratomileusis." J Refract Surg **18**(3 Suppl): S327-31.

222. Ortiz, D., J. M. Saiz, et al. (2003). "[Optimization of an individualized LASIK surgery. Geometric ray tracing model]." Arch Soc Esp Oftalmol **78**(8): 443-9.

223. Oshika, T., S. D. Klyce, et al. (1999). "Comparison of corneal wavefront aberrations after photorefractive keratectomy and laser in situ keratomileusis." Am J Ophthalmol **127**(1): 1-7.

224. Oshika, T., K. Miyata, et al. (2002). "Higher order wavefront aberrations of cornea and magnitude of refractive correction in laser in situ keratomileusis." Ophthalmology **109**(6): 1154-8.

225. Oshika, T., G. Sugita, et al. (2007). "Influence of tilt and decentration of scleral-sutured intraocular lens on ocular higher-order wavefront aberration." Br J Ophthalmol **91**(2): 185-8.

226. "OSLO Optics Software for Layout and Optimization."(2001). from http://www.lambdares.com.

227. Packer, M., I. H. Fine, et al. (2004a). "Wavefront technology in cataract surgery." Curr Opin Ophthalmol **15**(1): 56-60.

228. Packer, M., I. H. Fine, et al. (2006a). "The tilt and decentration of aspheric IOLs: What are the limits of tolerance?" Cataract & Refractive Surgery Today **6**(11): 84-5.

229. Packer, M., I. H. Fine, et al. (2006b). "Aberrations after intraocular lens implantation." J Cataract Refract Surg **32**(2): 184-5; author reply 185-6.

230. Packer, M., I. H. Fine, et al. (2002). "Prospective randomized trial of an anterior surface modified prolate intraocular lens." J Refract Surg **18**(6): 692-6.

231. Packer, M., I. H. Fine, et al. (2004b). "Improved functional vision with a modified prolate intraocular lens." J Cataract Refract Surg **30**(5): 986-92.

232. Padmanabhan, P., S. K. Rao, et al. (2006). "Monochromatic aberrations in eyes with different intraocular lens optic designs." J Refract Surg **22**(2): 172-7.

233. Padmanabhan, P., G. Yoon, et al. (2006). "Wavefront aberrations in eyes with Acrysof monofocal intraocular lenses." J Refract Surg **22**(3): 237-42.

234. Pallikaris, I. G., V. J. Katsanevaki, et al. (2003). "Advances in subepithelial excimer refractive surgery techniques: Epi-LASIK." Curr Opin Ophthalmol **14**(4): 207-12.

235. Pallikaris, I. G., M. E. Papatzanaki, et al. (1991). "A corneal flap technique for laser in situ keratomileusis. Human studies." Arch Ophthalmol **109**(12): 1699-702.

236. Pallikaris, I. G., M. E. Papatzanaki, et al. (1990). "Laser in situ keratomileusis." Lasers Surg Med **10**(5): 463-8.

237. Patel, S., J. Marshall, et al. (1993). "Model for predicting the optical performance of the eye in refractive surgery." Refract Corneal Surg **9**(5): 366-75.

238. Paul, H., Ed. (1999). Lexikon der Optik, Spektrum Akademischer Verlag.

239. Pesudovs, K., H. Dietze, et al. (2005). "Effect of cataract surgery incision location and intraocular lens type on ocular aberrations." J Cataract Refract Surg **31**(4): 725-34.

240. Phusitphoykai, N., T. Tungsiripat, et al. (2003). "Comparison of conventional versus wavefront-guided laser in situ keratomileusis in the same patient." J Refract Surg **19**(2 Suppl): S217-20.

241. Piers, P. A., E. J. Fernandez, et al. (2004). "Adaptive optics simulation of intraocular lenses with modified spherical aberration." Invest Ophthalmol Vis Sci **45**(12): 4601-10.

242. Piers, P. A., S. Manzanera, et al. (2007). "Use of adaptive optics to determine the optimal ocular spherical aberration." J Cataract Refract Surg **33**(10): 1721-6.

243. Piers, P. A., H. A. Weeber, et al. (2007). "Theoretical comparison of aberration-correcting customized and aspheric intraocular lenses." J Refract Surg **23**(4): 374-84.

244. Pomerantzeff, O., H. Fish, et al. (1971). "Wide angle optical model of the human eye." Ann Ophthalmol **3**(8): 815-9.

245. Pomerantzeff, O., M. Pankratov, et al. (1984). "Wide-angle optical model of the eye." Am J Optom Physiol Opt **61**(3): 166-76.

246. Pomerantzeff, O., M. M. Pankratov, et al. (1985). "Calculation of an IOL from the wide-angle optical model of the eye." J Am Intraocul Implant Soc **11**(1): 37-43.

247. Popiolek-Masajada, A. and H. Kasprzak (2002). "Model of the optical system of the human eye during accommodation." Ophthalmic Physiol Opt **22**(3): 201-8.

248. Popiolek-Masajada, A. and H. T. Kasprzak (1999). "A new schematic eye model incorporating accommodation." Optom Vis Sci **76**(10): 720-7.

249. Porter, J., G. Yoon, et al. (2006). "Aberrations induced in wavefront-guided laser refractive surgery due to shifts between natural and dilated pupil center locations." J Cataract Refract Surg **32**(1): 21-32.

250. Press, W. H. (1992). Numerical recipes in C : the art of scientific computing, Cambridge University Press.

251. Preussner, P. R. (2004). "[The practicality of wavefront correction in ophthalmology]." Klin Monatsbl Augenheilkd **221**(6): 456-63.

252. Preussner, P. R. and J. Wahl (2000). "[Consistent numerical calculation of optics of the pseudophakic eye]." Ophthalmologe **97**(2): 126-41.

253. Preussner, P. R. and J. Wahl (2003). "Simplified mathematics for customized refractive surgery." J Cataract Refract Surg **29**(3): 462-70.

254. Preussner, P. R., J. Wahl, et al. (2003). "Corneal model." J Cataract Refract Surg **29**(3): 471-7.

255. Preussner, P. R., J. Wahl, et al. (2002). "Ray tracing for intraocular lens calculation." J Cataract Refract Surg **28**(8): 1412-9.

256. Preussner, P. R., J. Wahl, et al. (2001). "[Consistent IOL calculation]." Ophthalmologe **98**(3): 300-4.

257. Preussner, P. R., J. Wahl, et al. (2005). "Topography-based intraocular lens power selection." J Cataract Refract Surg **31**(3): 525-33.

258. Preussner, P. R., J. Wahl, et al. (2004). "Predicting postoperative intraocular lens position and refraction." J Cataract Refract Surg **30**(10): 2077-83.

259. Qazi, M. A., I. Y. Cua, et al. (2007). "Determining corneal power using Orbscan II videokeratography for intraocular lens calculation after excimer laser surgery for myopia." J Cataract Refract Surg **33**(1): 21-30.

260. Rabbetts, R. B. and A. G. C. v. o. Bennett (1998). Bennett and Rabbetts' clinical visual optics. Oxford, Butterworth-Heinemann.

261. Rabsilber, T. M., A. J. Reuland, et al. (2006). "Intraocular lens power calculation using ray tracing following excimer laser surgery." Eye.

262. Retzlaff, J. (1980). "A new intraocular lens calculation formula." J Am Intraocul Implant Soc **6**(2): 148-52.

263. Retzlaff, J. A., D. R. Sanders, et al. (1990). "Development of the SRK/T intraocular lens implant power calculation formula." J Cataract Refract Surg **16**(3): 333-40.

264. Roberts, C. (2000). "The cornea is not a piece of plastic." J Refract Surg **16**(4): 407-13.

265. Roberts, C. (2002). "Biomechanics of the cornea and wavefront-guided laser refractive surgery." J Refract Surg **18**(5): S589-92.

266. Rocha, K. M., M. R. Chalita, et al. (2005). "Postoperative wavefront analysis and contrast sensitivity of a multifocal apodized diffractive IOL (ReSTOR) and three monofocal IOLs." J Refract Surg **21**(6): S808-12.

267. Rosa, N., L. Capasso, et al. (2002). "A new method of calculating intraocular lens power after photorefractive keratectomy." J Refract Surg **18**(6): 720-4.

268. Rosales, P. and S. Marcos (2007). "Customized computer models of eyes with intraocular lenses." Optics Express **15**(5): 2204-18.

269. Salmon, T. O. (1999). Corneal contribution to the wavefront aberration of the eye, Indiana University.

270. Salmon, T. O. and L. N. Thibos (2002). "Videokeratoscope-line-of-sight misalignment and its effect on measurements of corneal and internal ocular aberrations." J Opt Soc Am A Opt Image Sci Vis **19**(4): 657-69.

271. Salmon, T. O. and C. van de Pol (2006). "Normal-eye Zernike coefficients and root-mean-square wavefront errors." J Cataract Refract Surg **32**(12): 2064-74.

272. Sanders, D. R., J. Retzlaff, et al. (1988). "Comparison of the SRK II formula and other second generation formulas." J Cataract Refract Surg **14**(2): 136-41.

273. Sanders, D. R., J. A. Retzlaff, et al. (1990). "Comparison of the SRK/T formula and other theoretical and regression formulas." J Cataract Refract Surg **16**(3): 341-6.

274. Sarver, E. J. and R. A. Applegate (2000). "Modeling and predicting visual outcomes with VOL-3D." J Refract Surg **16**(5): S611-6.

275. Sarver, E. J., L. Wang, et al. (2006). "The effect of decentration on higher-order aberrations." Cataract & Refractive Surgery Today **6**(11): 82-7.

276. Sasaki, H., Y. Sakamoto, et al. (2002). "Predicting postoperative anterior chamber depth in cataract patients using Scheimpflug slit photography." Ophthalmic Res **34**(5): 265-72.

References

277. Sato, T., K. Akiyama, et al. (1953). "A new surgical approach to myopia." <u>Am J Ophthalmol</u> **36**(6:1): 823-9.

278. Savini, G., P. Barboni, et al. (2007). "Correlation between attempted correction and keratometric refractive index of the cornea after myopic excimer laser surgery." <u>J Refract Surg</u> **23**(5): 461-6.

279. Schafer, S., G. Kurzinger, et al. (2005). "[Comparative results of keratometry with three different keratometers after LASIK]." <u>Klin Monatsbl Augenheilkd</u> **222**(5): 419-23.

280. Schlote, T., M. Derse, et al. (1999). "[Impairment of mesopic vision following photorefractive keratectomy of myopia]." <u>Klin Monatsbl Augenheilkd</u> **214**(3): 136-41.

281. Schlote, T., M. Kriegerowski, et al. (1997). "Mesopic vision in myopia corrected by photorefractive keratectomy, soft contact lenses, and spectacles." <u>J Cataract Refract Surg</u> **23**(5): 718-25.

282. Schwiegerling, J. and J. E. Greivenkamp (1997). "Using corneal height maps and polynomial decomposition to determine corneal aberrations." <u>Optom Vis Sci</u> **74**(11): 906-16.

283. Schwiegerling, J. and R. W. Snyder (1998). "Custom photorefractive keratectomy ablations for the correction of spherical and cylindrical refractive error and higher-order aberration." <u>J Opt Soc Am A Opt Image Sci Vis</u> **15**(9): 2572-9.

284. Schwiegerling, J. and R. W. Snyder (2000). "Corneal ablation patterns to correct for spherical aberration in photorefractive keratectomy." <u>J Cataract Refract Surg</u> **26**(2): 214-21.

285. Seiler, T., T. Bende, et al. (1988). "Excimer laser keratectomy for correction of astigmatism." <u>Am J Ophthalmol</u> **105**(2): 117-24.

286. Seiler, T., U. Genth, et al. (1993). "Aspheric photorefractive keratectomy with excimer laser." <u>Refract Corneal Surg</u> **9**(3): 166-72.

287. Seiler, T., M. Kaemmerer, et al. (2000). "Ocular optical aberrations after photorefractive keratectomy for myopia and myopic astigmatism." <u>Arch Ophthalmol</u> **118**(1): 17-21.

288. Seiler, T. and T. Koller (2005). "[Asphericity of the cornea and astigmatism]." <u>Klin Monatsbl Augenheilkd</u> **222**(12): 977-82.

289. Seiler, T. and J. Wollensak (1986). "In vivo experiments with the excimer laser--technical parameters and healing processes." <u>Ophthalmologica</u> **192**(2): 65-70.

290. Seitz, B. and A. Langenbucher (2000). "Intraocular lens calculations status after corneal refractive surgery." <u>Curr Opin Ophthalmol</u> **11**(1): 35-46.

291. Seitz, B., A. Langenbucher, et al. (2002). "[Pitfalls of IOL power prediction after photorefractive keratectomy for high myopia -- case report, practical recommendations and literature review]." <u>Klin Monatsbl Augenheilkd</u> **219**(12): 840-50.

292. Seitz, B., A. Langenbucher, et al. (1999). "Underestimation of intraocular lens power for cataract surgery after myopic photorefractive keratectomy." <u>Ophthalmology</u> **106**(4): 693-702.

293. Seo, K. Y., J. B. Lee, et al. (2004). "Comparison of higher-order aberrations after LASEK with a 6.0 mm ablation zone and a 6.5 mm ablation zone with blend zone." <u>J Cataract Refract Surg</u> **30**(3): 653-7.

294. Shammas, H. J. and M. C. Shammas (2007). "No-history method of intraocular lens power calculation for cataract surgery after myopic laser in situ keratomileusis." <u>J Cataract Refract Surg</u> **33**(1): 31-6.

295. Siedlecki, D., H. Kasprzak, et al. (2004). "Schematic eye with a gradient-index lens and aspheric surfaces." <u>Opt Lett</u> **29**(11): 1197-9.

296. Smith, G. (2003). "The optical properties of the crystalline lens and their significance." <u>Clin Exp Optom</u> **86**(1): 3-18.

297. Smith, G. and C. W. Lu (1988). "The spherical aberration of intra-ocular lenses." Ophthalmic Physiol Opt **8**(3): 287-94.

298. Smith, G., B. K. Pierscionek, et al. (1991). "The optical modelling of the human lens." Ophthalmic Physiol Opt **11**(4): 359-69.

299. Sobaci, G., U. Erdem, et al. (2007). "Changes in Pupil Size and Centroid Shift in Eyes With Uncomplicated In-the-Bag IOL Implantation." J Refract Surg **23**: 796-9.

300. Somani, S., K. A. Tuan, et al. (2004). "Corneal asphericity and retinal image quality: a case study and simulations." J Refract Surg **20**(5): S581-5.

301. Sonego-Krone, S., G. Lopez-Moreno, et al. (2004). "A direct method to measure the power of the central cornea after myopic laser in situ keratomileusis." Arch Ophthalmol **122**(2): 159-66.

302. Stiles, W. S. and B. H. Crawford (1933). "The luminous efficiency of rays entering the eye pupil at different points." Proc R Soc B **112**: 428-50.

303. Strampelli, B. (1961). "Anterior chamber lenses." Arch Ophthalmol **66**: 12-17.

304. Tabernero, J., S. D. Klyce, et al. (2007). "Functional optical zone of the cornea." Invest Ophthalmol Vis Sci **48**(3): 1053-60.

305. Tabernero, J., P. Piers, et al. (2007). "Intraocular lens to correct corneal coma." Opt Lett **32**(4): 406-8.

306. Tabernero, J., P. Piers, et al. (2006). "Predicting the optical performance of eyes implanted with IOLs to correct spherical aberration." Invest Ophthalmol Vis Sci **47**(10): 4651-8.

307. Taketani, F., T. Matsuura, et al. (2004). "High-order aberrations with Hydroview H60M and AcrySof MA30BA intraocular lenses: comparative study." J Cataract Refract Surg **30**(4): 844-8.

308. Taketani, F., T. Matuura, et al. (2004). "Influence of intraocular lens tilt and decentration on wavefront aberrations." J Cataract Refract Surg **30**(10): 2158-62.

309. Taketani, F., E. Yukawa, et al. (2005). "Effect of tilt of 2 acrylic intraocular lenses on high-order aberrations." J Cataract Refract Surg **31**(6): 1182-6.

310. Tang, M., Y. Li, et al. (2006). "Measuring total corneal power before and after laser in situ keratomileusis with high-speed optical coherence tomography." J Cataract Refract Surg **32**(11): 1843-50.

311. Thibos, L. N. (1999). "Handbook of visual optics, Draft Chapter On Standards For Reporting Aberrations Of The Eye." from http://research.opt.indiana.edu/Library/HVO/Handbook_NF.html.

312. Thibos, L. N., R. A. Applegate, et al. (2000). "Report from the VSIA taskforce on standards for reporting optical aberrations of the eye." J Refract Surg **16**(5): S654-5.

313. Thibos, L. N., R. A. Applegate, et al. (2002). "Standards for reporting the optical aberrations of eyes." J Refract Surg **18**(5): S652-60.

314. Thibos, L. N., X. Hong, et al. (2004). "Accuracy and precision of objective refraction from wavefront aberrations." J Vis **4**(4): 329-51.

315. Thibos, L. N., M. Ye, et al. (1992). "The chromatic eye: a new reduced-eye model of ocular chromatic aberration in humans." Appl Opt **31**: 3594-600.

316. Thibos, L. N., M. Ye, et al. (1997). "Spherical aberration of the reduced schematic eye with elliptical refracting surface." Optom Vis Sci **74**(7): 548-56.

317. Thöniß, T. (2004). "Abbildungsfehler und Abbildungsleistung optischer Systeme." from http://www.winlens.de/pdf/papers/Abbildungsfehler.pdf.

318. Trokel, S. L., R. Srinivasan, et al. (1983). "Excimer laser surgery of the cornea." Am J Ophthalmol **96**(6): 710-5.

319. Tscherning, M. (1894). "Die monochromatischen Aberrationen des menschlichen Auges." Z Psychol Physiol Sinne **6**: 456-471.

320. Tzelikis, P. F., L. Akaishi, et al. (2007). "Ocular aberrations and contrast sensitivity after cataract surgery with AcrySof IQ intraocular lens implantation." J Cataract Refract Surg **33**: 1918-24.

321. Uchio, E., S. Ohno, et al. (1995). "Spherical aberration and glare disability with intraocular lenses of different optical design." J Cataract Refract Surg **21**(6): 690-6.

322. Verdon, W., M. Bullimore, et al. (1996). "Visual performance after photorefractive keratectomy. A prospective study." Arch Ophthalmol **114**(12): 1465-72.

323. Viestenz, A., B. Seitz, et al. (2001). "[Effect of pupil size on longitudinal focal distribution after photorefractive keratectomy]." Klin Monatsbl Augenheilkd **218**(7): 498-502.

324. Vilarrodona, L., G. D. Barrett, et al. (2004). "High-order aberrations in pseudophakia with different intraocular lenses." J Cataract Refract Surg **30**(3): 571-5.

325. Walter, K. A., M. R. Gagnon, et al. (2006). "Accurate intraocular lens power calculation after myopic laser in situ keratomileusis, bypassing corneal power." J Cataract Refract Surg **32**(3): 425-9.

326. Wang, L., M. A. Booth, et al. (2004). "Comparison of intraocular lens power calculation methods in eyes that have undergone laser-assisted in-situ keratomileusis." Trans Am Ophthalmol Soc **102**: 189-96; discussion 196-7.

327. Wang, L., E. Dai, et al. (2003). "Optical aberrations of the human anterior cornea." J Cataract Refract Surg **29**(8): 1514-21.

328. Wang, L. and D. D. Koch (2005). "Effect of decentration of wavefront-corrected intraocular lenses on the higher-order aberrations of the eye." Arch Ophthalmol **123**(9): 1226-30.

329. Wang, L. and D. D. Koch (2007). "Custom optimization of intraocular lens asphericity." J Cataract Refract Surg **33**(10): 1713-20.

330. Werner, W. and E. H. Roth (1999). "[Image properties of spherical as aspheric intraocular lenses]." Klin Monatsbl Augenheilkd **214**(4): 246-50.

331. Wu, J., F. Lu, et al. (2006). "Mirror Symmetry of X-Axis Coma Between Left and Right Eyes in the Cornea and the Whole Eye and Its Association with X-Axis Shift of the Pupil Center." Invest Ophthalmol Vis Sci **E-Abstract 1200**(1200-B65 ARVO-Poster).

332. Yang, Y., K. Thompson, et al. (2002). "Pupil location under mesopic, photopic, and pharmacologically dilated conditions." Invest Ophthalmol Vis Sci **43**(7): 2508-12.

333. Yi, F., D. R. Iskander, et al. (2006). "Computer simulation of visual outcomes of wavefront-only corneal ablation." J Cataract Refract Surg **32**(3): 487-94.

334. Yoon, G., S. Macrae, et al. (2005). "Causes of spherical aberration induced by laser refractive surgery." J Cataract Refract Surg **31**(1): 127-35.

335. Zhou, C., M. Jin, et al. (2007). "Corneal wavefront-guided ablation with the Schwind ESIRIS laser for myopia." J Refract Surg **23**(6): 573-80.

List of Figures

List of Tables

Scientific Presentations and Publications

Non-ophthalmic:

1. M. Meißner, D. Bartz, T. Hüttner, G. Müller, J. Einighammer (1999). "Generation of Subdivision Hierarchies for Efficient Occlusion Culling of Large Polygonal Models", Technical Report WSI-99-13, WSI/GRIS, University of Tübingen

2. J. Einighammer (2001). „Tiled Delaunay Triangulation." In: Saupe, Dietmar (Hrsg.) u.a.: Gesellschaft für Informatik (GI), Fachausschuß 4.1 „Graphische Datenverarbeitung". Graphiktag 2001, Proceedings: Workshop über Trends und Höhepunkte der Graphischen Datenverarbeitung: 56-67

3. M. Meißner, D. Bartz, G. Müller, T. Hüttner, J. Einighammer (2001). "Generation of Decomposition Hierarchies for Efficient Occlusion Culling of Large Polygonal Models." Poster presentation at the 6th International Fall Workshop VISION, MODELING, AND VISUALIZATION 2001, Stuttgart

Ophthalmic:

4. J. Einighammer, T. Oltrup, T. Bende, B. Jean (2005). "A method for analysing corneal topography data." Poster presentation at the Association for Research in Vision and Ophthalmology (ARVO) Annual Meeting: Program#845/Poster#B819

5. J. Einighammer, T. Bende, T. Oltrup, B. Jean (2006). "Von der Näherungsrechnung zum Raytracing – Paradigmenwechsel in der IOL Berechnung." Vortrag auf der 90. Jahrestagung der Württembergischen Augenärztlichen Vereinigung, Ophthalmologie 2006 Therapie-Update, Tübingen

6. J. Einighammer, T. Oltrup, T. Bende, B. Jean (2006). "Exact Raytracing Based on Geometry Data of Real Pseudophakic Eyes." Poster presentation at the Association for Research in Vision and Ophthalmology (ARVO) Annual Meeting: Program#305/Poster#B502

7. J. Einighammer, T. Bende, B. Jean (2006). "Calculating IOL Geometry by Real Ray Tracing." E-Poster presentation at the International Society of Refractive Surgery of the American Academy of Ophthalmology (ISRS/AAO) Subspecialty Day: #100832-2006 (available at http://aao.scientificposters.com)

8. J. Einighammer (2006). "Ray Tracing – mehr als eine Alternative zur IOL Berechnung." Vortrag auf dem Tübinger Augenärzteabend "Zur Konvergenz der individualisierten Refraktiven- und Katarakt Chirurgie", Universitäts-Augenklinik Tübingen

9. J. Einighammer (2007). "The individual virtual Eye – Computer Science meets Ophthalmology." Lecture on the Friday colloquium of the department of Graphical-Interactive Systems at the Wilhelm Schickard Institute for Computer Science (WSI/GRIS), University of Tübingen

10. J. Einighammer, T. Oltrup, T. Bende, B. Jean (2007). "Calculating Wavefront Aberration of Pseudophakic Eyes by Real Ray Tracing." Poster presentation at the Association for Research in Vision and Ophthalmology (ARVO) Annual Meeting: Program#3131/Poster#B994

11. J. Einighammer, T. Oltrup, T. Bende, B. Jean (2007). "Calculating intraocular lens geometry by real ray tracing." J Refract Surg **23**(4): 393-404.

12. J. Einighammer (2008). "The Individual Virtual Eye – a computer model for simulating human optics." Lecture at the Institute Colloquium of the Max Planck Institute for Biological Cybernetics, Department Buelthoff, Tübingen.

Acknowledgements

Curriculum Vitae

Dipl.-Inform. Jens Einighammer,
born 4/11/1975 in Tübingen, Germany

| 1985-1994 | *Wilhelm-Schickhardt-Gymnasium Herrenberg* |
| | • retrieval of university-entrance diploma with the majors mathematics and physics |

1994-2001	*University of Tübingen*
	• study of computer science
	• main focus computer graphics
	• student research project and diploma thesis at the department of Graphical-Interactive Systems (WSI/GRIS)

| 2001-2002 | *MagicMaps GmbH, Tübingen* |
| | • employment as software developer of geographic visualization systems |

Since 2003	*University Eye Hospital, Division "Experimental Ophthalmic Surgery", Tübingen*
	• employment as a scientific assistant
	• main focus: software development of diagnostic medical instruments, research in cataract and refractive surgery

Affirmation

I hereby affirm that I have completed this doctoral thesis entirely on my own and unassisted, and that I have specially marked all of the quotes I have used from other authors as well as those passages in my work that are extremely close to the thoughts presented by other authors, and listed the sources in accordance with the regulations I have been given.

_____   _____

Date   Signature